The Microclimate of Valley Glaciers

by

Johannes Oerlemans

Institute for Marine and Atmospheric Research Utrecht
Utrecht University
Utrecht
The Netherlands

Cover: Ice cave at the Vadret da Morteratsch, Switzerland, October 2009

The microclimate of valley glaciers

A crevasse damaged this AWS on Storbreen (photo by Liss Andreassen).

1. Microclimate and mass balance

1.1 Background and historical note

Glaciers have fascinated mankind throughout history. Glaciers look solid and robust, but observing them for only a couple of years shows that they are dynamic and change shape all the time. The lower glaciers come, the greater the contrast with the surrounding landscape. Many glaciers in the world enter pastures and forests. It is not surprising that laymen, artists and scientists have reported on the behaviour of large valley glaciers. A wealth of information on glacier fluctuations in historical times has thus become available, notably from the Alps, Norway and Iceland. Combined with the results of geomorphological studies it has become possible to reconstruct the history of an ever growing number of glaciers.

More systematic mapping of glaciers started only 100 years ago. The most comprehensive data set is related to length variations. It is relatively easy to make annual observations regarding the length of a valley glacier. Volunteers from Alpine clubs and other organisations have played an important role in compiling an impressive data set (World Glacier Monitoring Service, University of Zürich). In recent years the possibilities to map and monitor glaciers have increased enormously, mainly due to new remote sensing techniques.

There are many reasons why glaciers are studied. Considered on a global scale, valley glaciers and small ice caps are believed to contribute significantly to sea-level fluctuations on a century time scale (Meier, 1984; Oerlemans et al., 2007). Compared to the large ice sheets of Greenland and Antarctica, the amount of water stored in glaciers and ice caps is really small (about 0.5 m of sea-level equivalent). However, glaciers are located in warmer and wetter climates and therefore have a relatively larger mass turnover. This makes them more sensitive to climate change. Additionally response times are smaller. It is now believed that the retreat of glaciers and ice caps since 1850 has

contributed about 6 centimetres to global sea-level rise (Oerlemans et al., 2007).

Glaciers can also be used as detectors of climate change. The world-wide retreat of many glaciers during the last few decades is frequently quoted as a clear sign of global warming. Since many glacier length records go back further in time than instrumental observations, these records can be used to reconstruct climate change since about 1600 AD. This is of particular interest for glacier regions like New Zealand, Patagonia, Himalayas and Alaska, where systematic meteorological observations started relatively late. Compared to biogenic climate indicators like tree-rings, glacier systems react in a relatively simple way to climate change. The transfer function does not change in time and geometric effects can be dealt with. An interesting aspect of glaciers is that many are found at high elevations. Some of the highest glaciers in the world (in the tropics and subtropics) have median elevations of more than 4000 m. This implies that a climate signal reflected in glacier fluctuations can be studied as a function of height, at least through the lower troposphere.

On a more local scale glaciers can be of great importance as well. Glaciers have peak discharges when the need is largest: in hot summers (e.g. Hock, 2005). Consequently, in many parts of the world glacier melt water is used to supply irrigation systems (Figure 1.1). Cities like Quito (Ecuador), La Paz (Bolivia) and Lima (Peru) draw typically half of their water supply from glacier systems in the high Andes (e.g. Kaser and Osmaston, 2002).

Figure 1.1. Meltwater stream leaving the Vadret da Morteratsch. On a typical summer day, 5 cm of ice is removed from the surface of the lower part of the glacier and discharged through the glacial river.

Figure 1.2. Basecamp close to the front of the Hintereisferner, Austria. In the summer of 1987 a meteorological experiment on this glacier had limited success due to very bad weather with frequent thunderstorms. Note the Little Ice Age trimline on the mountain slope on the left.

Hydropower reservoirs may also benefit from the presence of glaciers. Reservoirs are normally emptied in winter when the need for power is largest. In the summer, melt water from glaciers helps to refill them. In view of this, it is not surprising that hydropower companies (particularly in Switzerland, Iceland and Norway) have supported mass balance studies over the years.

Glaciers, however, also have their negative sides. Sudden events like ice avalanches and outbursts of glacier-dammed lakes can cause catastrophes with many casualties and extensive destruction. Fluctuations of a more regular kind like alterations in glacier extent can threaten roads, constructions and property. Side moraines and rock walls cleared from ice by retreating glaciers can be very unstable and lead to rock avalanches and very large sediment loads in mountain rivers.

The response of the geometry of a glacier to climate change is the outcome of a process that consists of several steps. Changes in the large-scale climate setting will be felt at the glacier surface and will thus affect the mass balance. But it is important to realise that a large-scale climatic signal is filtered by the atmospheric boundary-layer before it reaches the glacier surface. Therefore a mass-balance model that translates weather conditions into net mass gain or loss at the glacier surface needs to account for the characteristics of a glacier's microclimate.

In this book the focus is on the microclimate of valley glaciers. During the past 25 years, the Institute for Marine and Atmospheric Research, Utrecht University (IMAU), has conducted a number of glacio-meteorological experiments, some of these in collaboration with the universities of Amsterdam, Innsbruck and Iceland. The goal of these experiments was to measure the meteorological conditions at the glacier surface. In comparison to earlier pioneering studies (e.g. Björnsson, 1972; Munro and Davies, 1978; Hay and Fitzharris, 1988) the ambition was high,

namely, to operate weather stations at five or more sites simultaneously. This would make it possible to study altitudinal gradients in the components of the surface energy budget. After a try-out in 1986 on the Hintereisferner, with one mast on the glacier and one mast in the forefield, a large-scale experiment was conducted in the summer of 1987 (Figure 1.2). Unfortunately, the weather conditions were desastrous. Heavy rain and frequent thunderstorms caused rock avalanches, land slides and swollen mountain rivers that could not be crossed anymore. In fact, it was a summer of large devastation in the Oetztal and also in northern Italy. The meteorological stations were not sufficiently robust to handle the moist conditions: the mechanical loggers with magnetic tapes, bought in a shop for second-hand electronics, did not work very long. Altogether the scientific outcome of this experiment was limited. In 1989 the experiment was repeated (Figure 1.3), but again the weather was not very good. Nevertheless, some interesting results on the glacier wind and spatial and temporal variation of the albedo were obtained (e.g. Van de Wal et al., 1992). Although the Hintereisferner experiments were not a big success, the development was irreversible. One of the important things we learned was that masts standing freely on the ice with four legs (Figure 1.4) are remarkably stable. They stay in place even after 5 to 10 m of melt in a summer and the tilting remains limited. The legs melt slightly into the ice and, for permanent stations, this also guarantees a solid start into the winter. The automatic weather station (AWS) on the Vadret da Morteratsch is the champion. It was installed in September 1995 and remained stable ever since. In the period of 14 years that has passed since the AWS started working there are only 20 days of missing data. Meanwhile a layer of ice of about 80 m thick has melted away.

Figure 1.3. Louk Conrads on the Hintereisferner in 1989, showing how representative the measurement of a mass-balance stake can be ...

In the nineties new battery technology and the appearance of affordable solid state loggers on the market created new possibilities. Weather stations could now be built that did not demand continuous check-up and replacement of batteries. In addition to this, better instruments became available, like the CNR-1 manufactured by Kipp and Zonen, combining four sensors for shortwave radiation (up and down) and longwave radiation (up and down) into a single unit (the instrument can be seen on the AWS in Figure 1.4 at the right end of the instrument beam). The performance of this instrument appeared to be remarkably good.

In 1990-1991 an experiment was performed in the ablation zone of the Greenland ice sheet (GIMEX; for an overview see Oerlemans and Vugts, 1993), along what is now known as the Kangerlussuaq transect (K-transect). GIMEX was carried out in collaboration with the Free University, Amsterdam, under the guidance of Hans Vugts. A new element was the operation of a cable balloon system just in front of the ice margin, delivering profiles of temperature, humidity and wind up to 800 m above the surface. GIMEX also marked the beginning of measuring the surface mass balance along the K-transect. The measurements have been continued until today, and now constitute the longest series of *in situ* mass balance observations on the Greenland Ice Sheet (Van de Wal et al., 2008).

Figure 1.4. On a glacier with strong ablation, one should not anchor weather stations but let them stand freely on the ice surface. A construction with four legs attached to each other by steel cables performs well. The tripod with the sonic ranger is drilled into the ice, of course. We owe many smart ideas to technician Wim Boot, here working on the Vadret da Pers (September 2000).

Figure 1.5. Operating a helium balloon of 11 m^3 on the Pasterzen Kees, Austria, summer 1994. The red arrow points to the sensor. A profile mast was used to probe the lower boundary layer (blue arrow). Photo made by Carleen Tijm-Reijmer.

The logical next step was to operate the cable balloon *on* a glacier. In combination with a profile mast the dream of probing the entire katabatic flow over a melting glacier came true. In the summer of 1994 a very successful experiment was carried out on the Pasterzen Kees in Austria, in collaboration with the Free University under the leadership of Hans Vugts. The Pasterzen Kees is a large, gently sloping valley glacier (10 km long) in the eastern Alps. In addition to the operation of standard meteorological stations at 5 sites on the glacier, a profile mast and a cable balloon system (Figure 1.5) were used to probe the boundary layer in more detail. The data from the weather station were tapped by radio telemetry, a system to be abandoned in later expeditions. From the experiment on the Pasterzen Kees a great deal was learned about the valley wind - glacier wind system, about the turbulent exchange between air and glacier surface, and also about gradients in meteorological quantities along the flow line of the glacier (Van den Broeke, 1997a, b; Greuell et al., 1997; Smeets et al., 1998).

The climax of the summer experiments was the expedition to Vatnajökull, Iceland, in 1996. With substantial funding from the European Union, a large number (12) of weather stations could be operated on this 8000 km^2 large ice cap. Cable balloons and radiosondes were used to probe the vertical structure of the boundary layer. Four research institutions were involved, namely, the Institute for Marine and Atmospheric Research, Utrecht University; the Science Institute, University of Iceland; the Department of Earth Sciences, Free University Amsterdam; and the Institute for Meteorology and Geophysics, University of Innsbruck. One of the unexpected results was that katabatic flow shapes the microclimate of the glacier to a large extent, in spite of the fact that the ice cap is very much exposed to depressions travelling in the North Atlantic storm track (Oerlemans et al., 1999). Another remarkable feature was the very strong increase of global radiation with altitude, related to the relative frequent occurrence of low clouds.

With the further development of glacier mass balance models that integrate the surface energy budget continuously (e.g. Oerlemans, 1992), the wish to have year-round data from weather stations on glaciers became stronger. The IMAU has now installed automatic weather stations

(AWS) in the melting zones of the following glaciers: Vadret da Morteratsch, Switzerland (since 1995); Breidamerkurjökul, Iceland (since 1996); Hardangerjøkulen, Norway (since 2000); Storbreen, Norway (since 2001); Langfjordjøkulen, Norway (since 2007). In addition to this the IMAU operates AWS on the ice sheets of Greenland and Antarctica.

1.2 Gain, loss, and the balance rate

Glaciers are often classified according to their geometrical appearance. However, physical processes that determine the magnitude and character of the mass flow through the system may also be of great relevance. For instance, a distinction is made between temperate glaciers and polythermal glaciers. In temperate glaciers the ice temperature is at the (pressure) melting point almost everywhere, allowing extensive sliding motion at the glacier base and facilitating the development of internal drainage systems for meltwater. Virtually all glaciers in mid- and low latitudes are temperate glaciers. In the subpolar regions temperate glaciers are only found in maritime climates, like on Iceland.

In a polythermal glacier there are large zones where the ice temperature is well below the freezing point. Parts of the glacier are frozen to the bed, which has implications for the dynamics of the glacier. Many glaciers in the arctic and sub-arctic regions are polythermal. An example of a well studied polythermal glacier is Storglaciären in northern Sweden (e.g. Petterssen et al., 2003).

Cold glaciers are only found in dry and cold climates, like on the Antarctic continent.
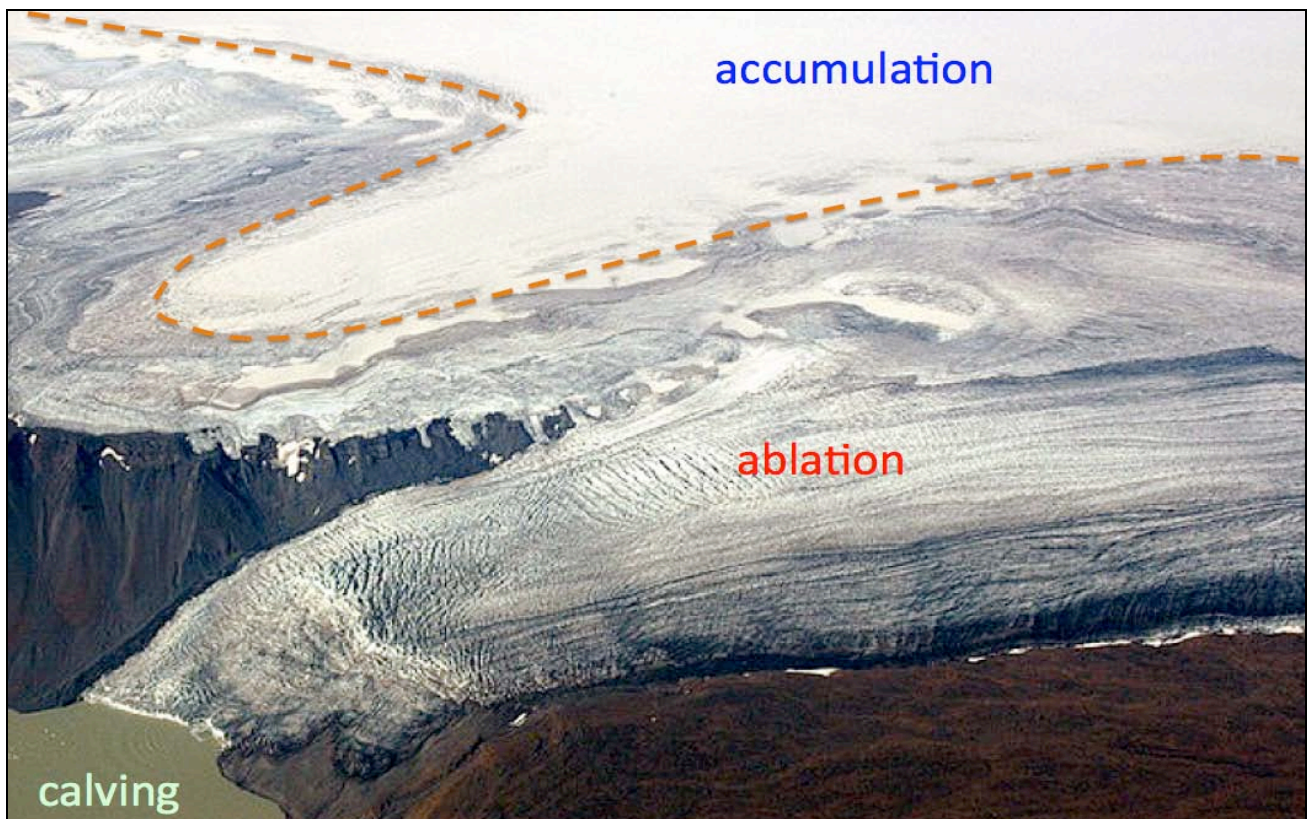

Figure 1.6. The major components of the mass budget of a glacier. The accumulation and ablation zones are separated by the equilibrium line (dashed). This glacier is part of Vatnajökull, Iceland (photo Loftmyndir).

Another way to distinguish between different types of glaciers is the nature of the mass budget (Figure 1.6). The evolution of any glacier is determined by conservation of mass. In many applications the density of a glacier can be considered constant, which implies that conservation of mass is equivalent to conservation of volume. We may therefore write

$$\frac{dV}{dt} = B + B_b + C \qquad (1.1)$$

Here V is the total ice volume, B and B_b are the gain or loss of mass at the surface and at the base of the glacier, respectively, and C the calving flux. The calving flux is the loss of ice in the form of icebergs per unit of time. Glaciers with $C \neq 0$ are called calving glaciers, and calving glaciers that end in the sea, in a fjord or in an estuary are normally referred to as tidewater glaciers. Apart from the outlets of the Greenland and Antarctic ice sheets, tidewater glaciers are very common in the Arctic (e.g. Northern Canada, Svalbard, Severnaya Zemlya), but also in the maritime climate of Alaska. Large glaciers calving into lakes are common in Patagonia.

For all glaciers, B_b is much smaller than B. However, floating ice tongues and ice shelves, which only occur in the coldest climates on earth, can have large values of B_b, with either sign (basal melting as well as accretion of ice can reach values of many meters per year).

Snowfall during a storm, typically lasting a few days, is the most obvious process that adds mass to a glacier. The counterpart is melt and runoff on a warm summer day. The net result of these and other processes after one year, expressed in net mass gain or loss, is called the specific balance rate $\dot{b}$ (e.g. Kaser et al., 2003). It is expressed in kg m^2 a^{-1}, or in mwe a^{-1} (mwe = meters of water equivalent). By definition we have

$$B = \int\limits_{glacier} \dot{b}\, dx\, dy \qquad (1.2)$$

Here x and y are map coordinates. It should be noted that the specific balance rate is always defined with respect to the vertical (i.e. not perpendicular to the glacier surface).

The accumulation zone of a glacier is the zone where $\dot{b} > 0$. Here none or only part of the accumulated snow melts and runs off in summer. It should be noted that meltwater refreezing in a cold underlying snowpack does not represent a loss of mass. The accumulation zone is normally the highest part of a glacier. When going downglacier sooner or later the ablation zone is found where $\dot{b} < 0$. Here the winter snowpack is melted in late spring and early summer, and then the underlying ice is exposed to high air temperatures and a positive radiation balance throughout the summer.

It is instructive to consider the cumulative balance $b_{cum}(t)$, which describes how the mass gain or loss evolves in time. It has unit kg m^2, or mwe. Although there is not a strict definition on when a balance year starts, in this text we will use the 1st of October (Northern Hemisphere) for this purpose.

An example of the cumulative balance for one balance year is shown in Figure 1.7. The measurements are from the sonic ranger on the snout of the Vadret da Morteratsch, which measures the actual surface elevation relative to a material surface within the glacier (strictly speaking relative to the lower ends of the stakes of the tripod on which the sonic ranger is mounted). The data are for the balance year 1 October 2000 – 30 September 2001.
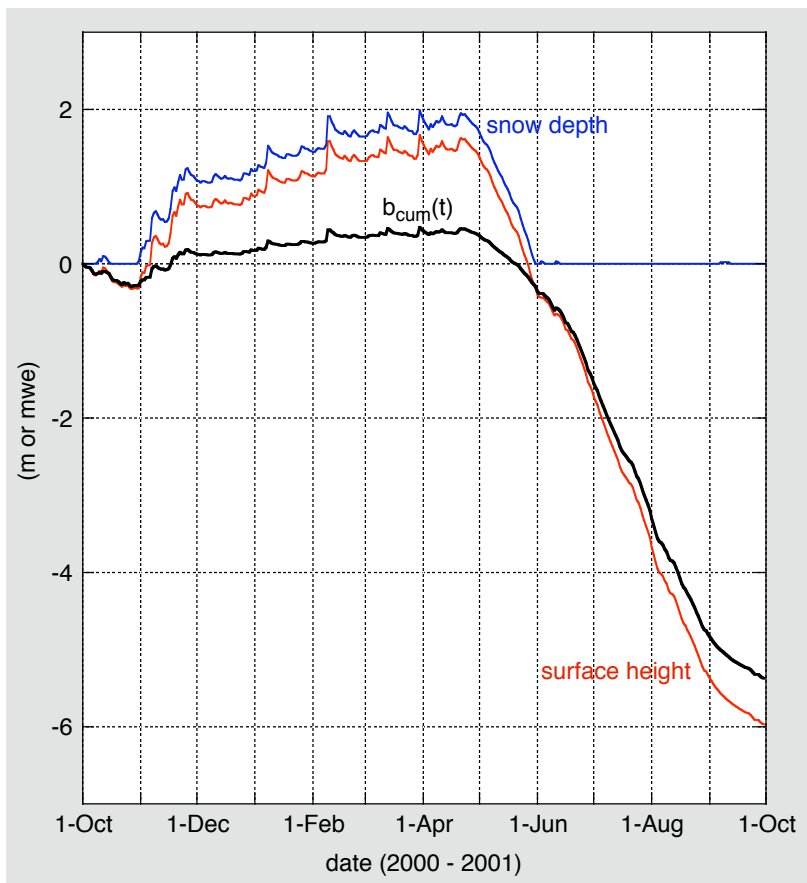
Figure 1.7. Surface height (in m), snow depth (in m), and calculated cumulative balance (in mwe) for a balance year, as measured at the AWS site on the snout of the Vadret da Morteratsch.

To obtain $b_{cum}(t)$, the height measured by the sonic ranger has to be converted into mass. This implies some manipulation of the data. A reduction of the distance between the sonic ranger and the surface can only be brought about by snow accumulation, which makes it easy to determine the snow depth (blue curve in Figure 1.7). At the AWS site three snow pit studies were done during this winter. The average snow density measured was 382 kg m^{-3}. Together with a value of 900 kg m^{-3} for ice density, the cumulative balance can be calculated (black curve in Figure 1.7, in mwe).

Note that in this case there is no need to consider the amount of snow if the interest is in $\dot{b}$. In the beginning and at the end of the balance year the glacier surface consists of ice, and a direct comparison of the ice levels delivers the balance rate (-5.37 mwe a^{-1}).

The conventional way of measuring the balance rate is to use stakes in the ablation zone and to dig snowpits in the accumulation zone (Østrem and Brugman, 1991). The issue of how many data points are needed to obtain a representative net balance for a particular glacier is still a subject of debate (e.g. Cogley, 1998; Hock and Jensen, 1999; Kaser et al., 2003). Except for small and smooth glaciers, many complicating factors exist. For instance, it is difficult to measure the specific balance in regions with strong crevassing. Yet it is to be expected that such regions will have a different balance: they probably accumulate more snow. Lower down on the glacier crevasse regions are likely to have larger melt rates because the effective area subject to heat exchange with the air is larger. Among other factors that introduce errors into the mass-balance measurements are steep slopes and refreezing (important on glaciers with little mass turnover).

It is general practice to measure the annual balance at the end of the ablation season, that is, in early autumn. This then also marks the beginning of the new balance year. It is clear, however, that the balance year will start on a different date for different glaciers. In the Alps early October is the

turning point, but for subarctic glaciers the end of August is more appropriate. In fact, the concept of a balance year is somewhat problematical anyway, because many maritime glaciers are subject to ablation on the lower parts during autumn and spring as well. It is also clear that year-to-year variations in the specific balance can be the result of different dates of measurements. Corrections can be made for this by reducing the measurements to a reference date, but in many cases some ambiguity cannot be avoided.

Figure 1.8. Anders Sirevaag carrying out a snowpit study on Hardangerjøkulen, Norway. The density has been determined by taking 10 cm samples. A temperature profile is measured with thermistors. Photo Carita Knudsen.

Digging snow pits (Figure 1.8) and measuring the density profile is laborious, but it is still the most widely used method to determine the specific balance in the accumulation region. Experience is needed to interpret the layering in a snow pit correctly and to find last year's summer horizon. Snow radar is now becoming more popular to map the accumulation over larger reasons, but in many cases the interpretation of the layering seen in the radar records is difficult.

At a number of glaciers the so-called winter balance is also measured. This is done shortly before melting starts to become significant. Researchers in Norway and Austria, for instance, measure the winter balance in May. Once the winter balance is known the summer balance follows from a comparison with the annual balance. It is clear that the winter balance is also a concept involving some difficulties. Traditionally, the winter balance is seen as a quantity that contains information about the mass accumulation on a glacier. In principle this is correct of course, but the relation is not simple. Mid-latitude glaciers accumulate most of their mass during the winter half year, but this is not necessarily the case with drier and more arctic glaciers. Nevertheless, measuring the balance twice during the balance year is very useful, because this gives insight into the processes at work and offers more possibilities for testing mass balance models.

1.3 Balance profiles

The balance rate depends first of all on altitude. There are a number of reasons reasons for this. The most obvious one is the decrease of air temperature with altitude, about 6 to 7 degrees K per kilometer. Lower air temperatures imply a smaller turbulent heat flux to the surface as well as a reduced amount of downwelling longwave radiation from the atmosphere. The amount of ablation will therefore decrease strongly with altitude. Lower air temperatures also imply that a larger fraction of the precipitation falls as snow, which contributes to the balance gradient as well. Moreover, the total precipitation generally increases with altitude. In mountain regions the annual precipitation on the higher parts can easily be twice as large as in the valleys. However, above a certain level (typically 3500 m) the precipitation starts to decrease with altitude and the balance gradient may become smaller.

We define the balance gradient β as

$$\beta = \frac{d\dot{b}}{dz} \ , \tag{1.3.1}$$

where z is altitude. The balance gradient is an important quantity characterizing the climatic setting of a glacier. It is also one of the parameters that determine the response time of a glacier. Because glaciers with a large balance gradient have higher ice velocities, they react faster to climate change (Oerlemans, 2001).
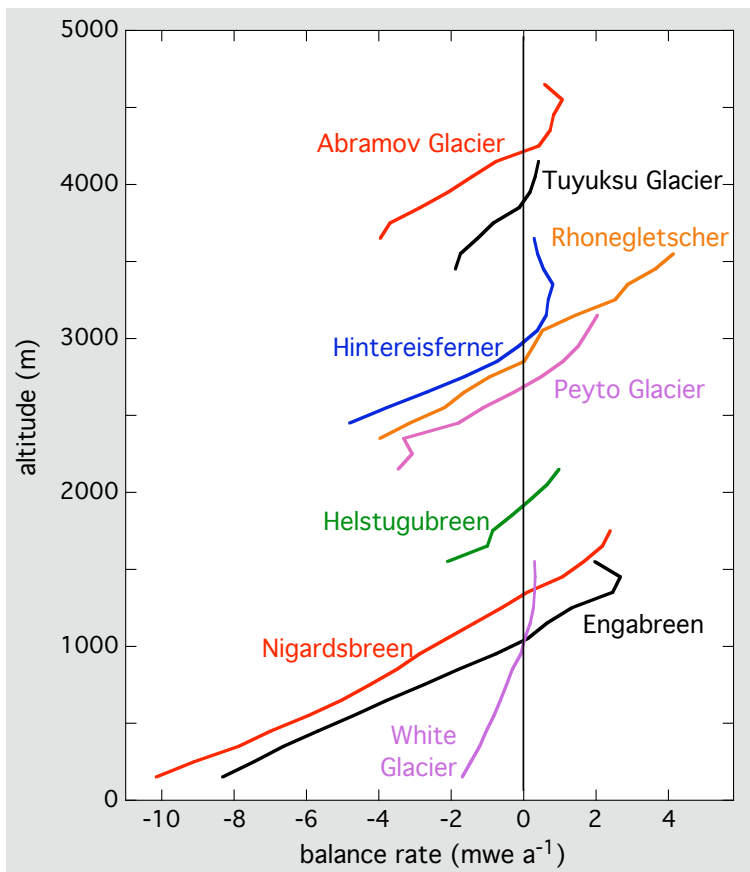

Figure 1.9. Measured balance profiles for a set of glaciers (averages over many years). Based on data from the World Glacier Monitoring Service (Zürich).

The selection of observed balance profiles in Figure 1.9 gives an impression of the typical differences to be found in different climates. Glaciers in the drier polar and subpolar regions, like White Glacier in the Canadian Arctic, have small balance gradients. In contrast, Engabreen and Nigardsbreen, situated in Norway, have a tremendous mass turnover and large balance gradients. Consequently, in spite of the fact that the equilibrium line for White Glacier and Engabreen is at about the same altitude, one must expect these glaciers to show a totally different degree of activity. The mass turnover of Hintereisferner (Austrian Alps) is moderate. This also applies to Hellstugubreen, which is located in the drier part of southern Norway. Another example of a fairly active glacier is Peyto Glacier in the central Rocky Mountains in Canada. Abramov Glacier and Tuyuksu Glacier represent the class of continental glaciers. They are located in central Asia and have high equilibrium lines.

Typical values of β range from 0.003 mwe a^{-1} m^{-1} on glaciers in a dry (sub)arctic climate to 0.01 mwe a^{-1} m^{-1} on glaciers in an extreme maritime climate. As a consequence, ablation rates on maritime glaciers that push their snouts far down can be quite large. On the lower parts of Vatnajökull (Iceland) and Nigardsbreen (Norway) ice ablation is typically 10 mwe a^{-1} (Østrem et al., 1977). On the snout of Franz Josef Glacier, New Zealand, ablation is estimated to be larger than 20 mwe a^{-1} (Oerlemans, 1997a; Anderson et al., 2006).

By definition, the accumulation and ablation zones are separated by the equilibrium line, at which $\dot{b}=0$ (Figure 1.6). One could think of the equilibrium line as the intersect of a mountain topography with a wavy surface (the equilibrium surface) that runs around the world. At any place where the earth surface orography sticks upward through this equilibrium surface, glaciers will form. The equilibrium-line altitude E ranges from a few hundred meters above sea level on some arctic islands to over 6000 m in the drier regions of the subtropics. In large parts of the Antarctic continent it drops below sea level, and the concept of the equilibrium line becomes rather meaningless.

1.4 The energy budget of the upper layer of a glacier

For the melt process the surface energy budget is decisive. The mechanisms of heat transfer thought to be important for glaciers are shown in Figure 1.10. The largest fluxes are the radiative fluxes, typically a few hundred Watts per square metre. A large part of the solar radiation reaching the glacier surface is reflected - more in the case of fresh snow, less in the case of old snow or bare ice, very little when the surface is covered by morainic material. Solar radiation penetrates into the snow and ice. In fact, the reflection as measured at the surface is the result of a complicated scattering process at the ice or snow crystals in the upper metres of the glacier. For longwave radiation the surface is very dense. It has an emissivity (and absorptivity) of about one. The amount of longwave radiation reflected by the surface is negligible - it is all absorbed. Incoming and outgoing longwave radiation compensate each other to a large degree. Normally the amount emitted by the surface is slightly larger (a few tens of Watts per metre squared) than the amount coming in from the atmosphere, making the net longwave balance negative. However, when the air is warm and humid, and clouds are present, the longwave balance may be positive.

The effect of clouds on the shortwave and longwave radiation budgets is of opposite sign. More clouds implies less shortwave radiation and more longwave radiation. The net effect depends on the surface albedo and on the cloud transmissivity (Ambach, 1974; Brock, 2004). For a high surface albedo (e.g. fresh snow) the net change in longwave radiation for a given increase in cloudiness is

larger than the net change in the solar radiation. Consequenty, the net radiation balance increases. For lower albedo (e.g. ice) the solar radiation effect dominates and the net radiation budget decreases with cloudiness.

Turbulent exchange of heat and moisture can be quite significant, especially in winter (when the sun is low) or in summer when air temperature is high. The fluxes are in the direction of the gradients in the mean temperature and humidity profiles. When air temperature is above freezing point the sensible heat flux is always towards the surface. In such conditions the latent heat flux can go in both directions, depending on the humidity of the air. The saturation vapour pressure for a melting glacier surface is 610.8 Pa. If an air mass has a temperature of 10°C, the gradient in vapour pressure and hence the vapour flux changes sign at a relative humidity of about 50%. At lower humidity evaporation cools the surface, at higher humidity condensation heats the surface.

The temperature of precipitation may differ from the temperature at the surface. This implies that precipitation may add or remove heat from the existing snowpack or ice surface. However, the energy fluxes involved are small.

The fluxes inside the glacier are much smaller than those between atmosphere and glacier surface, except for the flow of melt water, which represents a latent heat flux. When glacier ice is at the surface, molecular conduction is the only important process (note, however, that in the interior of cold glaciers conduction, frictional heating and advection due to ice motion have a similar order of magnitude).

In snow and firn, convection by air motion transports heat and water vapour. The fluxes are small but important for the metamorphosis of snow crystals. The vapour transport is determined mainly by the density of the snow and the temperature gradient. Fairly comprehensive models have been developed to describe the metamorphosis of snow in different climatic conditions; most of these models are connected with avalanche research.
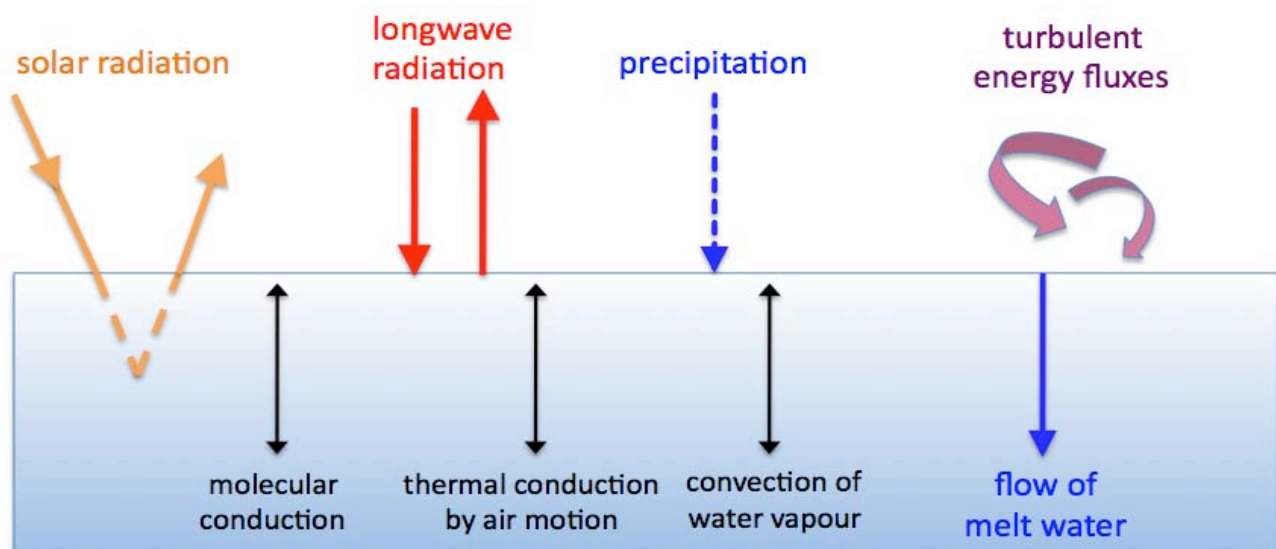

Figure 1.10. The most important processes determining the energy flux at the glacier-atmosphere interface and the thermal structure in the upper layer of the glacier. On temperate glaciers, the flow of melt water and associated refreezing are more important than the other internal processes.
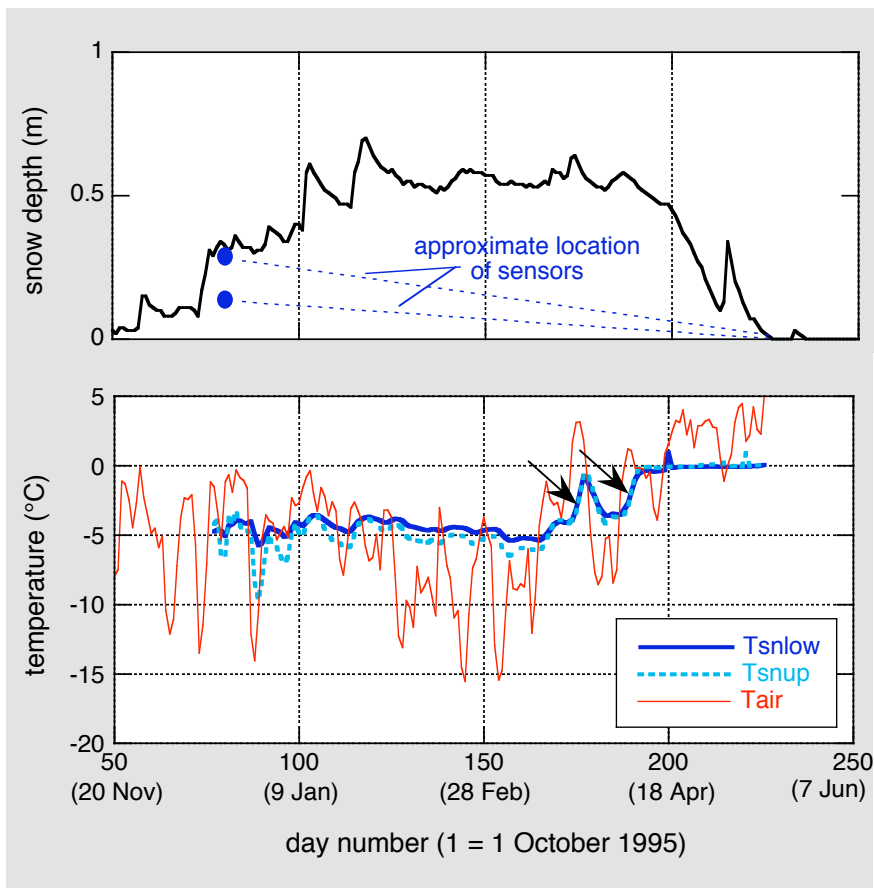
Figure 1.11. The evolution of the snowpack temperature, as measured in the winter of 1995/96 at the AWS site on the Vadret da Morteratsch. Refreezing events are marked (arrows).

The effect of refreezing can be seen in records of the snow temperature in springtime. Figure 1.11 shows an example. Two temperature sensors were inserted in the snow, 15 and 30 cm above the ice surface, after the first major snowfall. It can be seen that snow temperature follows the fluctuations in air temperature, but with a phase lag and smaller amplitude. Later in winter the snow temperature fluctuates less because the distance between snow surface and sensors is larger.

The first melt water occurs on March 23rd (first arrow in Figure 1.11) but it is not enough to raise the temperature of the snowpack to melting point. This happens on April 10th (second arrow). When the snowpack has been heated up and the ice underneath is not cold, runoff may start and the amount of snow diminishes rapidly. In the case shown the entire snow cover disappears within some weeks (in spite of the fact that 25 cm of fresh snow fell on May 3rd).

The importance of refreezing in the heat budget of a snowpack can be illustrated by a simple calculation. The latent heat of melt, denoted by L_m, is $3.34 \cdot 10^5$ J kg^{-1}. Because the specific heat is about 2100 J kg^{-1} K^{-1}, heating of 1 kg of snow (or ice) by 1 K requires the same amount of energy as melting 0.0063 kg of snow. A 2 m winter snowpack of uniform density at -10 °C can therefore be brought to the melting point by the melting and refreezing of only 12.5 cm of the snowpack.

1.5 The structure of the upper layer of a glacier

Because the temperature in the atmosphere decreases with altitude, snow settling on the higher parts of glaciers is generally colder than snow settling further down. The density of freshly fallen snow depends on temperature and wind conditions. A typical value for fresh snow on mid-latitude

glaciers is 100 kg m^{-3}. Then a complicated process starts in which the snow crystals change their shape due to mechanical action by the wind, water vapour transport in the snowpack and melting and refreezing. After many cycles of melting and refreezing the snow turns into firn. According to the official terminology, firn is snow that is at least one year old. However, skiers know better. In spring and early summer sunny slopes have good firn produced from snow that has fallen months or even only weeks earlier. The crystals are large and rounded and the density is typically 500 kg m^{-3}. On mid-latitude and tropical glaciers, firn takes one to five years to change into ice, depending on the local micro-meteorological conditions. This is in sharp contrast to the hundreds of years needed to transform snow into ice on the Greenland and Antarctic ice sheets.

The structure of the upper layers of a glacier is intimately related to the thermal regime (Figure 1.12). The 'simple zones' are the dry snow zone, where no melt water is ever produced, and the lower ablation zone, where the winter snow melts away rapidly and ice melts over a long period of time. The data shown in Figure 1.11 are from the lower ablation zone. In between are the 'complex zones', where refreezing of melt water occurs to form superimposed ice. Depending on the climatic conditions, part or all of this superimposed ice may melt later in the ablation season. If all the superimposed ice melts away, the snow line should be close to the equilibrium line at the end of the summer. This is practical, because a quick estimate of the location of the equilibrium line can then be made on the basis of satellite images or aerial photographs. However, when part of the superimposed ice survives during the melt season, the snow line can be much higher up than the equilibrium line. This is the rule rather than the exception on (sub)polar glaciers. The classical paper on surface stratigraphy of glaciers is Benson (1962).

Most valley glaciers outside the Arctic and Antarctic regions are temperate. Temperatures below melting point are found only in very high places. Just below the equilibrium line temperatures a few degrees below freezing point may occur in a thin layer just below the surface.
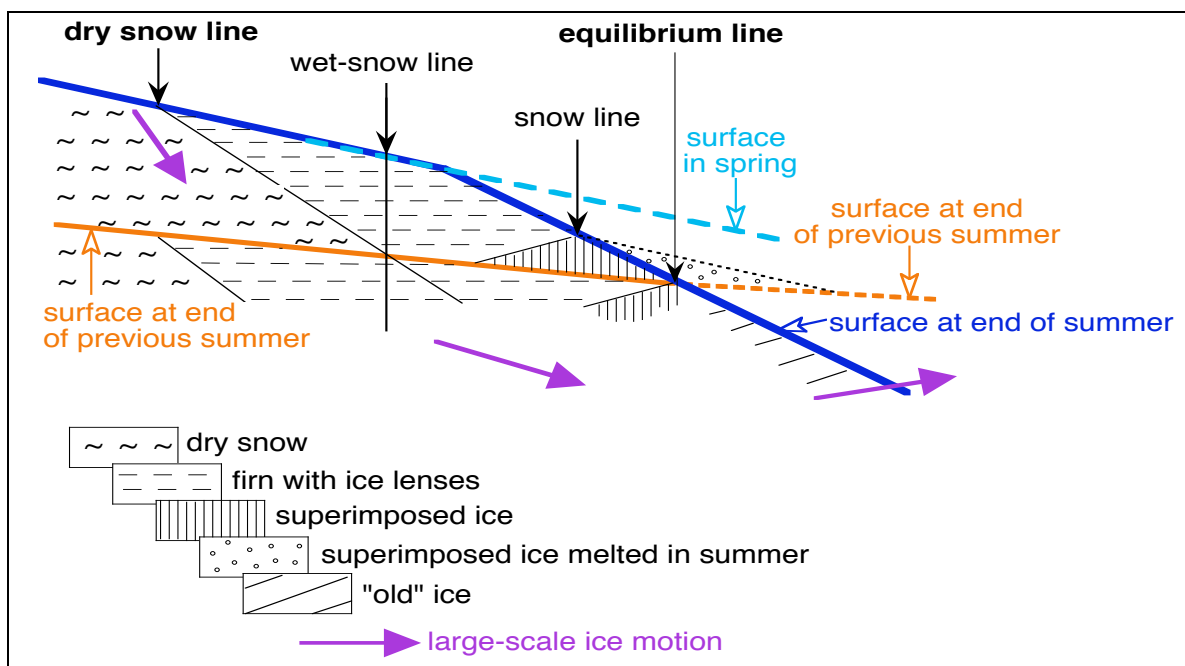

Figure 1.12. The different zones on a glacier. Note that the horizontal scale is typically a hundred times larger than the vertical scale. If the glacier is close to a steady state, large-scale ice motion keeps the surface in place.

1.6 The glacier microclimate

The surface of a glacier differs from its surroundings. The contrast may be small in winter when the landscape is totally covered by snow. However, in summer the differences can become very large. Those parts of a glacier that are not covered by debris have a relatively high albedo. As a consequence, less solar energy is absorbed. The temperature of the glacier surface cannot rise above melting point, so on warm days it is a sink of energy for the overlying air.

On warm summer days alpine valleys heat up considerably. Slope winds help to distribute the warm air generated at the valley walls that face the sun. This process is quite effective and the air in a valley is rapidly mixed (characteristic time scale: 15 minutes). Due to differential heating along the valley axis, an up-valley flow is normally established: the valley wind (e.g. Defant, 1949; Egger, 1987). The layer of air involved is typically 1 km thick and blows up-valley.

The cooling of air over a melting and sloping glacier surface generates a downward katabatic flow, frequently termed the glacier wind (Hoinkes, 1954; Kuhn, 1987; Van den Broeke, 1997a). As we will see later from an analysis of observational data, the glacier wind layer is shallow (~20 m). A typical wind speed is 5 m s^{-1}. Altogether, local wind systems on a spatial scale of hundreds of meters to kilometers play an important role in shaping the microclimate of a glacier (Figure 1.13). One of the central questions is how a climate signal in the free atmosphere is 'filtered' by the glacier boundary layer before it affects the surface.

At night the air is cooled and a mountain wind flows down the valley. It is much weaker and shallower than the valley wind, because turbulent exchange between surface and air is suppressed by the stable stratification.
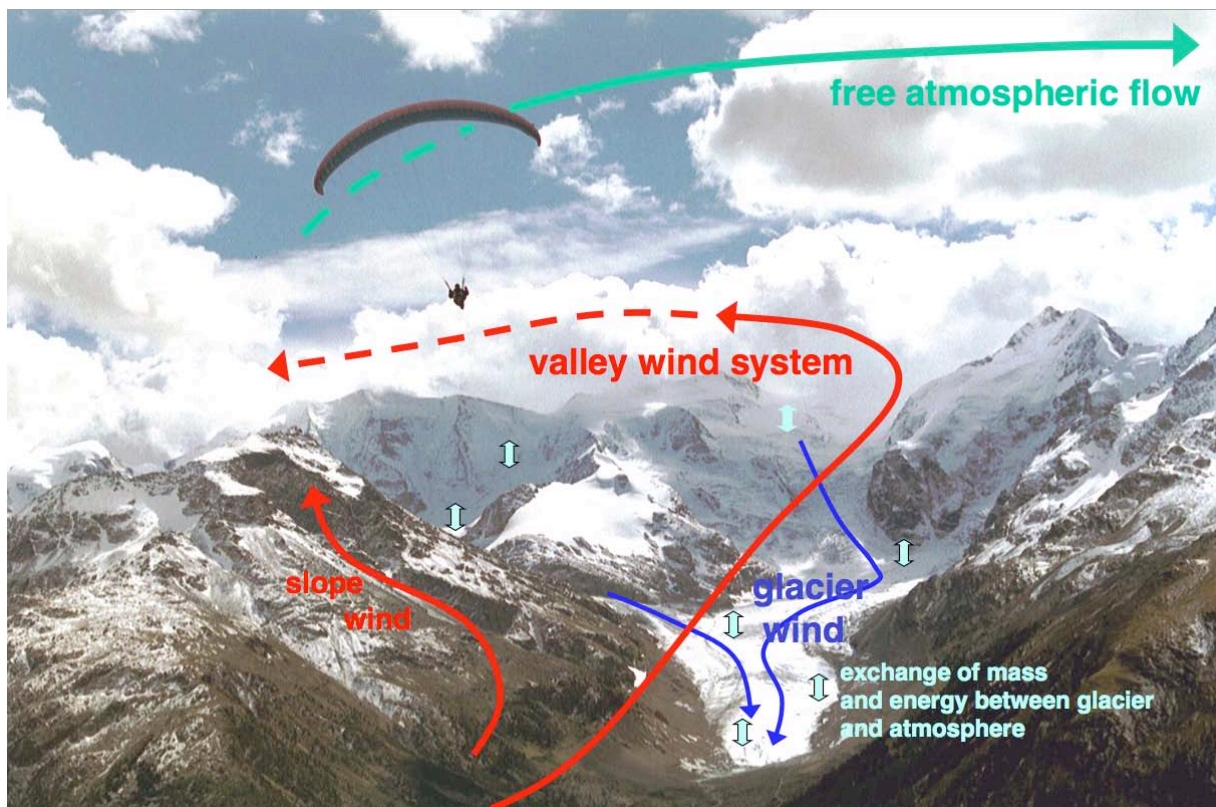

Figure 1.13. An overview of daytime circulation systems in a glacierised valley. The valley wind and the glacier wind have opposite directions.

The valley wind - glacier wind system is the driving force for the turbulent exchange of heat between the glacier surface and the atmosphere. If we want to find out how temperature changes in the atmosphere affect the surface energy flux (and, consequently, the melt rate), we have to understand the physical properties of this system. A special chapter is therefore devoted to the theory of the glacier wind (Chapter 3).

A glacier surface is a very dynamic surface: the albedo and the surface roughness vary strongly in space and time (Figure 1.14). As outlined above, cloudiness and surface albedo are the most important parameters that determine the amount of solar radiation absorbed at he surface (apart from geometric effects like shading). The surface roughness affects the turbulent exchange, but also the absorption of solar radiation. A heavily crevassed zone on a glacier absorbs more radiation than a smooth glacier surface with the same slope and aspect.

The high spatial variability of the surface albedo suggests that the use of photographs and satellite images could be very helpful. In practice there are some obstacles that limit the application of satellite images: instruments with a high resolution have a long repeat time (e.g. Landsat Thematic Mapper), only cloud-free scenes are useful, and many geometric and atmospheric corrections have to be made. In spite of this, a great deal of research has been done to study this aspect of the glacier microclimate from space (e.g. Knap et al., 1999a,b; Greuell and De Ruyter de Wildt, 1999; Klok and Oerlemans, 2002).

Figure 1.14. An illustration of rapid changes in topographic roughness that may occur on a glacier. The photograph at the left was made on the Pasterze in June 1994. The photograph at the right shows the same weather station a few weeks later, after the snow had melted.

Sensors of the AWS on the Vadret da Morteratsch, October 2006.

2. A basic survey of data

2.1 Introduction

The climatic setting of glaciers around the world differs widely. Glaciers at high latitudes, like those in Svalbard or in the Canadian Arctic, experience a climate with a very large seasonal cycle and a relatively small daily cycle. In contrast, glaciers in the (sub)tropics are subject to a very large daily cycle in the weather and a moderate seasonal cycle. For tropical glaciers the seasonal cycle in the mass balance conditions is mainly determined by the hydrological conditions, i.e. the alternation of wet and dry seasons (e.g. Kaser and Osmaston, 2002).

Table 2.1 lists basic climatological data from stations with various climatic settings. The selection of six stations, all not too far from regions with glaciers, includes subpolar, continental, maritime and tropical stations.

	latitude	longitude	T_{ann} (°C)	ΔT (K)	P_{ann} (mm)	S_{ann} (hr)
Resolute (18 m), Canada	74°41'N	94°54'W	-16.2	37.8	138	1475
Riksgränsen (508 m), Sweden	68°26'N	18°08'E	1.9	23.5	380	1341
Hólar (17 m), Iceland	64°18'N	15°11'W	4.7	10.9	1621	1197
Zell am See (754 m), Austria	47°19'N	12°48'E	11.7	24.6	1052	1504
Chang-du (3200 m), Tibet	31°11'N	96°59'E	28.6	18.2	556	2284
Cuzco (3312 m), Peru	13°33'S	71°59'W	32.4	3.6	750	2350

Table 2.1. Some climatological information from different stations around the world. T_{ann} is the annual mean temperature reduced to sea level, ΔT the temperature difference between the warmest and the coldest month, P_{ann} the annual precipitation and S_{ann} the annual amount of sunshine hours (data from Müller, 1987).
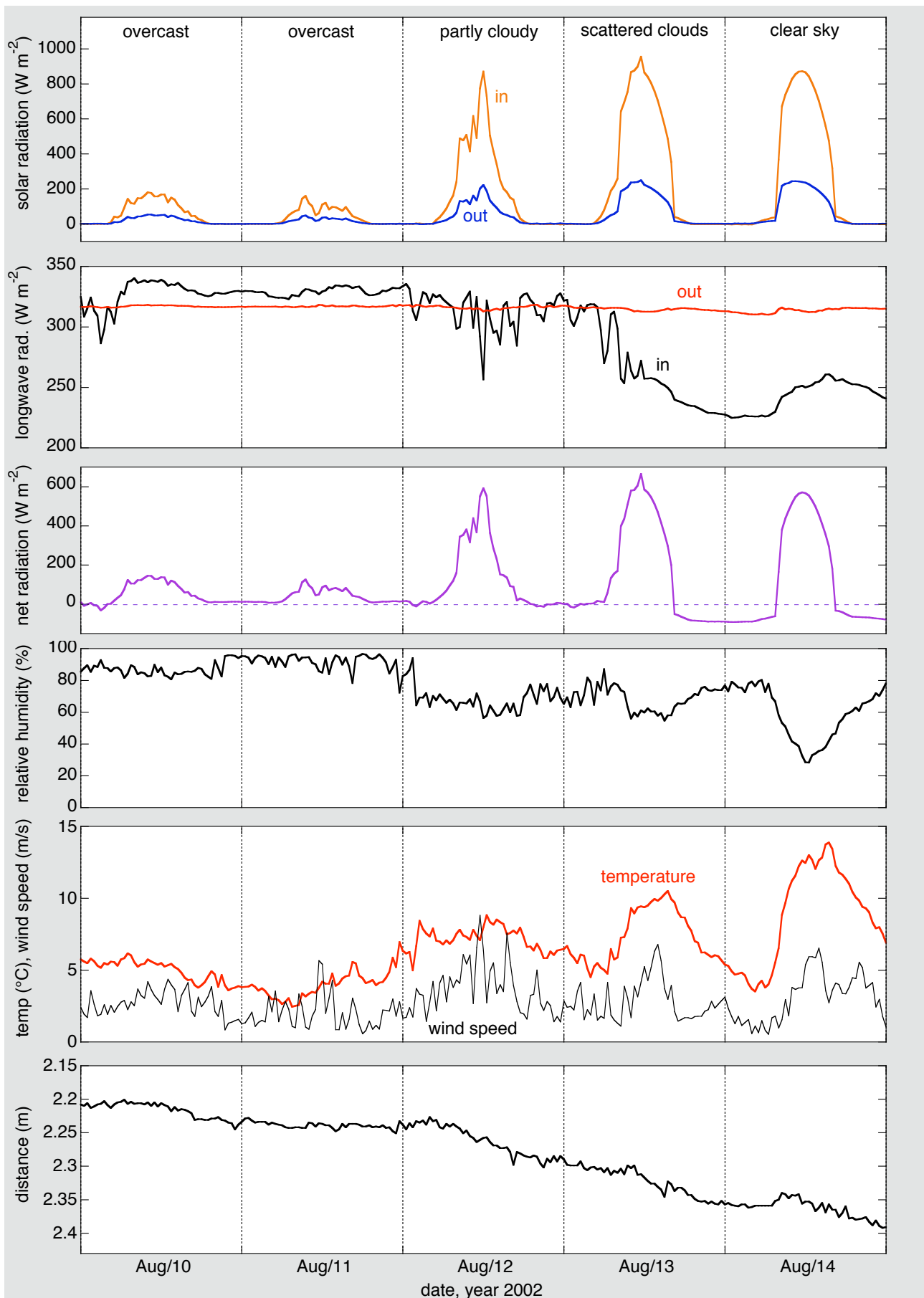
Figure 2.1. A five-day meteorological record (30-min averages) from the Morteratsch AWS, showing typical summer conditions. The lowest panel shows the distance between sonic ranger and surface (scale reversed).

By far the largest temperature difference between summer and winter is seen at Resolute. Values of ΔT of more than 30 K are only found in the high Arctic and the continental parts of North America and Asia. In contrast, a coastal station on Iceland, very close to Vatnajökull, has a seasonal temperature range of only 11 K. In Cuzco, in the tropical Andes, the range is even smaller: 3.6 K. Differences in duration of sunshine and precipitation are also large, of course. It should be noted that the listed values of P_{ann} are not necessarily representative for the glaciers in a particular region. Normally the amount of precipitation falling on a glacier is significantly higher than at weather stations down in the valley or outside the mountain range.

From the discussion above it is clear that a glacier with a 'representative microclimate' is hard to define. Nevertheless, some elements of the glacier microclimate are common to many glaciers around the world. We will start our survey by looking at a few days of observations from the Morteratsch AWS.

2.2 Five days in summer

Figure 2.1 shows solar radiation (incoming and reflected), longwave radiation (incoming and outgoing), relative humidity, air temperature, wind speed and distance of the sonic ranger (SR, also referred to as sonic altimeter) to the surface as measured by the Morteratsch AWS on five days in the summer of 2002. The sensors were at a height of about 3.5 m above the glacier surface. Sampling was every 2 minutes, and 30-min averages were stored on the logger. The interested reader can find a wealth of information on the use of AWS on glaciers in Box et al. (2004).

The radiation components have been measured with the Kipp CNR-1 radiation instrument (see photograph at the beginning of this chapter). This robust and reliable instrument has revolutionised the automatic monitoring of the radiation budget. From the incoming solar radiation the cloud conditions can normally be inferred qualitatively. For the five days considered here it is clear that the first two days are days with overcast conditions: the incoming solar radiation is very small as compared to the last day [Note: We use the term „incoming solar radiation" instead of „global radiation", as the instrument is not absolutely level; because of the tilt of the mast the radiation instrument is normally more or less parallel to the glacier surface]. Interestingly, on the 4th day (August 13), the peak incoming solar radiation is slightly larger than on the clear day. This is related to the strong reflection of solar radiation by small clouds. The clear-sky radiation curve (August 14) is by no means symmetrical around the peak value. This is a consequence of the shading of the AWS site by the surrounding high mountains. Especially in the morning, when the sun rises from behind a high mountain, there is a jump in the incoming solar radiation. On August 12 and 13, the incoming radiation increases earlier in the morning because there is more diffuse radiation due to clouds. The amount of reflected solar radiation is about 30% of the incoming solar radiation, i.e. the albedo is about 0.3 (with somewhat smaller values in the afternoon).

The outgoing longwave radiation is rather constant ($\approx$315 W m^{-2}) as one would expect when the surface is melting all the time. Small fluctuations can be seen because the air between the surface and the sensor makes a small positive contribution to the upward flux measured at 3.5 m. The incoming longwave radiation shows more pronounced variations. In the first half of the record clouds and water vapour (high humidity) make the atmospheric emissivity large. In the last part of the 5-day record the variation in the incoming longwave radiation is mainly a response to air temperature.
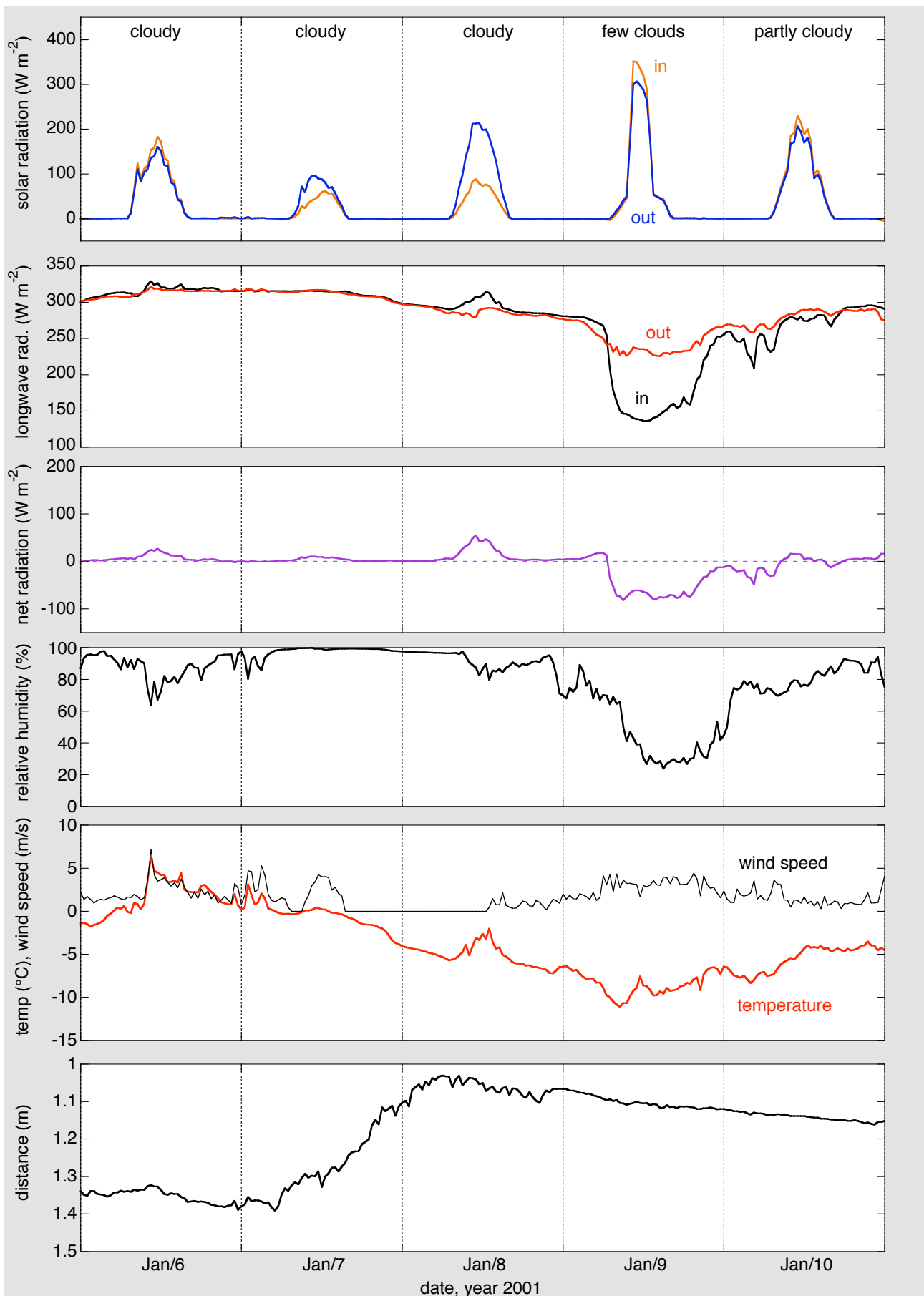
Figure 2.2. As in Figure 2.1 but for five days in winter. On January 7 a major snowfall occurred. During this event the wind speed sensor got stuck and the upward facing radiation sensors became covered by snow.

2 - A basic survey of data

The variation in the net radiation (measured parallel to the glacier surface) is dominated by the incoming solar radiation. The net radiation is only negative during clear nights, when the effective absorptivity/emissivity of the atmosphere is low.

The temperature shows a distinct daily cycle only during the last two days of the record, as a direct response to the solar forcing, of course. The wind speed is correlated with the temperature, a point that will be discussed in detail later.

Since for the five-day period the glacier surface consists of ice, changes in the surface height as measured by the sonic ranger provide a good estimate of the rate of mass loss due to ablation. It is clear that lowering of the surface during the second half of the record is larger than during the first half. This is obviously due to higher air temperatues and a larger amount of incoming solar radiation. During the five-day period about 15 cm of ice has been removed by the melting pocess. The highest ablation rates at this site occur on sunny and warm days in late June / early July. Up to 8 cm of ice can then be removed within a day.

2.3 Five days in winter

Next we consider five days in winter with a day of intense snowfall (Figure 2.2). The record of solar radiation shows a peculiar feature: on January 7 and 8 the amount of reflected radiation is much larger than the amount of incoming radiation. This is due to the fact that the upward facing radiation sensor is covered with snow whereas the downward facing sensor is not. Apparently, on January 9 the sensor is clean of snow and the measurements look as expected. Estimating the incoming radiation during snowfall is therefore best done by dividing the reflected radiation by a fresh snow albedo (e.g. 0.90). This procedure has been used to calculate the net radiation balance (third panel in Figure 2.2).

The measurements also indicate that the snow albedo during cloudy conditions (January 6 and 10) is higher than during clear sky conditions (January 9). This feature will be discussed again later.

During the first three days the net longwave radiation is virtually zero. However, when the sky is clearing (January 9) the incoming longwave radiation drops very rapidly to a low value of about 150 W m^{-2}. In fact, this feature dominates the net radiation balance through the five-day period. Due to the high albedo, the absorbed solar radiation is a small term in the budget.

In the course of January 7, the anemometer stops rotating. From the temperature record it can be seen that at the beginning of the snow event the temperature is going down through the freezing point, which is not a very favourable situation for the instruments.

The sonic altimeter reveals a snow accumulation of about 35 cm. In spite of the low air temperature (about -10 °C) the settling of the snow proceeds quickly. After the snow event the total snow depth at the AWS site was 1.48 m. During the last two days of the five-day record the snow depth decreases by about 10 cm.

It should be noted that the data from the sonic altimeter in Figures 2.1 and 2.2 have not been corrected for the dependence of the travel time of the sound pulse on air density. Temperature and humidity affect the air density, but the corrections are rather small. The problem of applying a correction is that it requires an assumption about the temperature and humidity profiles between the glacier surface and the instrument. If we want to study a daily cyle in the melt rate in detail, the correction can be significant. However, for longer time scales the correction is not important.

The varying height of the sensors is a typical aspect of the winter record. Since the AWS stands freely on the ice, it sinks with the melting surface in summer and the sensor height remains approximately the same. However, when a snowpack forms the distance between the surface and the sensor height decreases. The instrument height is therefore the nominal instrument height (3.5 m in this case) minus the snow depth.

2.4 Annual cycles on different glaciers

In this section we consider daily mean data from three glaciers in a different climatic setting. The glaciers and their characteristics are listed in Table 2.1. Storbreen is a small valley glacier located in southern Norway. Breidamerkurjökull is a large calving glacier in an extreme maritime climate and drains a part of Vatnajökull, Iceland. In contrast, the Vadret da Morteratsch in Switzerland is in a climate of a more transitional character, with less precipitation and, as we will see, with a larger annual temperature range.
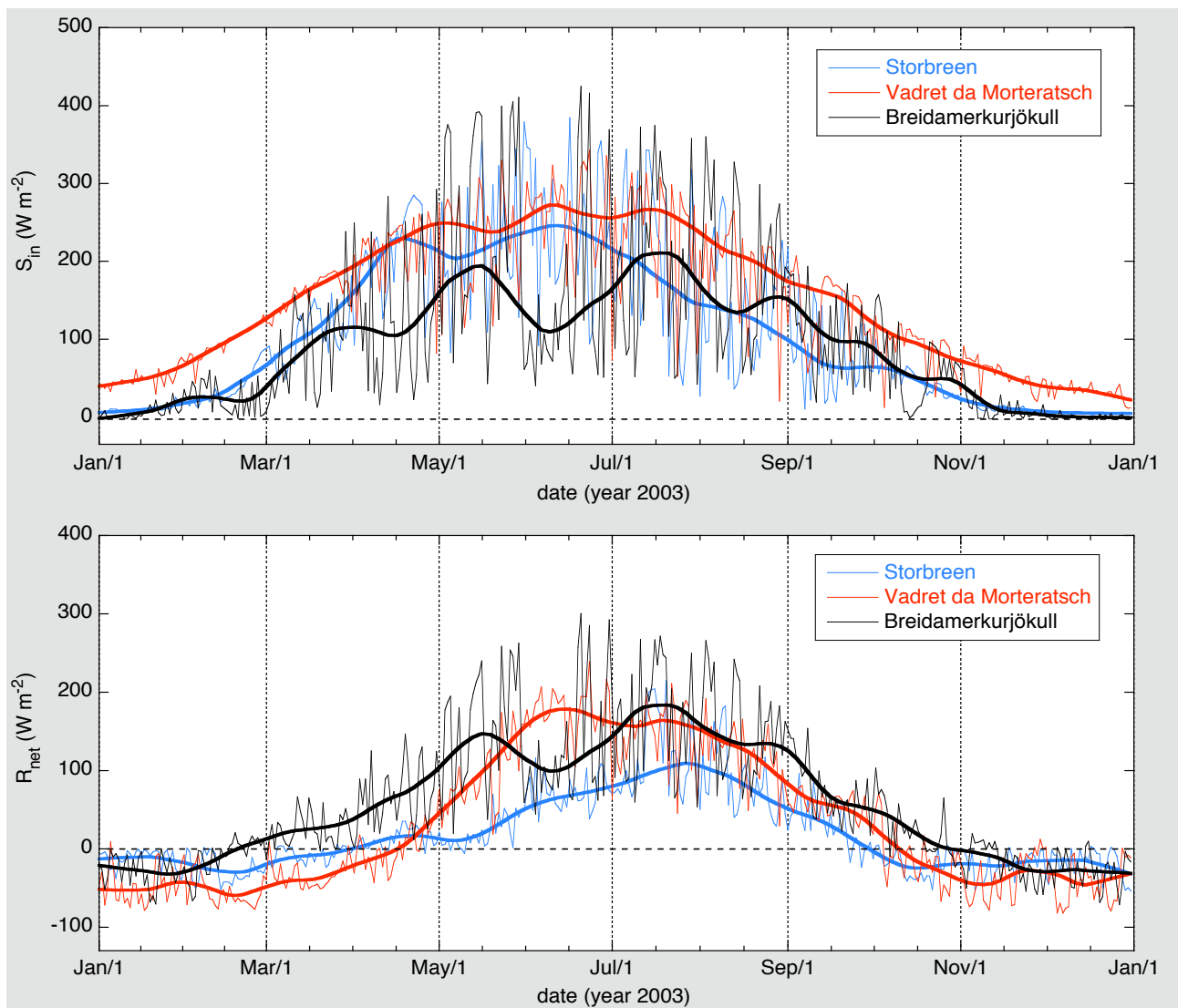

Figure 2.3. One year of daily mean values of incoming shortwave radiation (upper panel) and net radiation (lower panel), as measured by AWS on three different glaciers. Smooth curves show low-pass filtered data.

	Coordinates	Altitud. range (m)	h_{AWS} (m)	Slope (deg)	Aspect
Storbreen, Norway	61°34'N 8°8'E	1390 – 2090	1570	7	NE
Vadret da Morteratsch, Switzerland	46°24'N 9°55'E	2000 - 4049	2100	5	N
Breidamerkurjökull, Iceland	64°15'N 16°40'W	0-1600	220	4	SE

Table 2.1. Some information about the glaciers from which we study AWS data. The altitude of the AWS is denoted by h_{AWS}. The slope is the approximate slope of the glacier surface at the AWS site.

Figure 2.3 shows a selection of the radiation data (all daily mean values based on 2-minute sampling). Perhaps the most striking feature is the very large day-to-day variation in the incoming shortwave radiation (S_{in}) on Breidamerkurjökull. Peak values in summer are up to 400 W m^{-2}, which is larger than the peak values on Storbreen and significantly larger than the peak values on the Vadret da Morteratsch. This can be understood from the fact that Breidamerkurjökull is located at the highest latitude. The substantial daily variation must be related to the large average optical thickness of clouds in the wet and maritime climate of Iceland.

In contrast to the Vadret da Morteratsch, Storbreen and Breidamerkurjökull have very little shortwave radiation in wintertime. The daily variation on the Vadret da Morteratsch is small, especially in the winter half year. This is due to the combined effect of optically thin clouds and multiple reflections between the glacier surface, clouds and the snow-covered valley walls (of the three glaciers studied here, the Vadret da Morteratsch is surrounded by the steepest and highest mountains). When we look at the low-pass filtered data it becomes clear that the annual amount of incoming shortwave radiation is by far the largest on the Vadret da Morteratsch, apparently due to the combined effect of the lower latitude and fewer (and probably thinner) clouds.

Breidamerkurjökull has the largest values of net radiation. This is due to the relatively large amount of incoming longwave radiation (not shown) associated with high air temperature and humidity, and in particular to the very low surface albedo. The continuous melt out of black tephra (volcanic ash) on the tongue of Breidamerkurjökull leads to low albedos (typically 0.1 – 0.2, Figure 2.4). Consequently, the absorption of the incoming shortwave radiation is very effective.
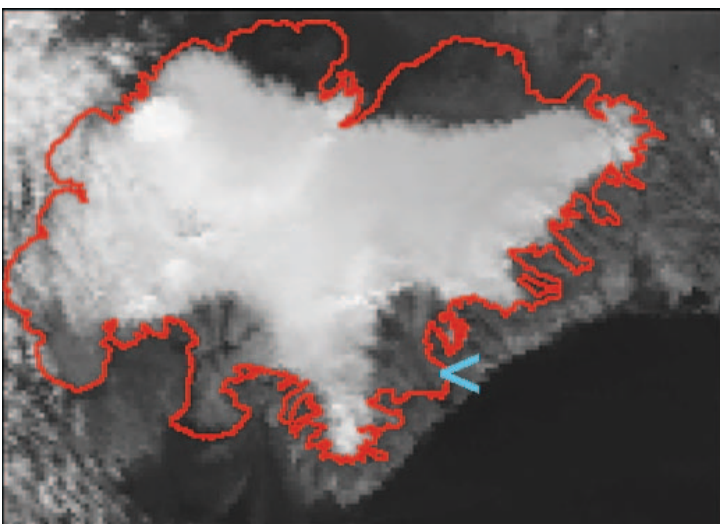

Figure 2.4. NOAA-AVHRR (Channel-2) image of Vatnajökull (25 August, 1996), The red contour indicates the approximate margin of the ice cap. The blue arrow points to Breidamerkurjökull and the location of the AWS.

Figure 2.4 shows that the ablation zones of Vatnajökull are as dark as the surrounding land, but not as dark as the ocean. The transition from the snow/firn surface to the dirty ice surface is remarkably sharp.

Storbreen shows significantly smaller values of the net radiation. The annual mean flux is only about 1/3 of that at Breidamerkurjökull. The day-to-day variation is comparable to that of the Vadret da Morteratsch. For a more extensive analysis, see Andreassen et al. (2008).

Although turbulent heat fluxes also play a significant role, the differences in net radiation measured for the three glaciers are certainly in line with the differences in summer balance rates at the AWS sites: typically -2 mwe for Storbreen, -6 mwe for the Vadret da Morteratsch and -10 mwe for Breidamerkurjökull.

Daily mean air temperature and relative humidity are shown in Figure 2.5. The difference between the maritime climate at Breidamerkurjökull (annual temperature range ~8 K) and the more continental climate at the Vadret da Morteratsch (annual temperature range ~20 K) is striking.
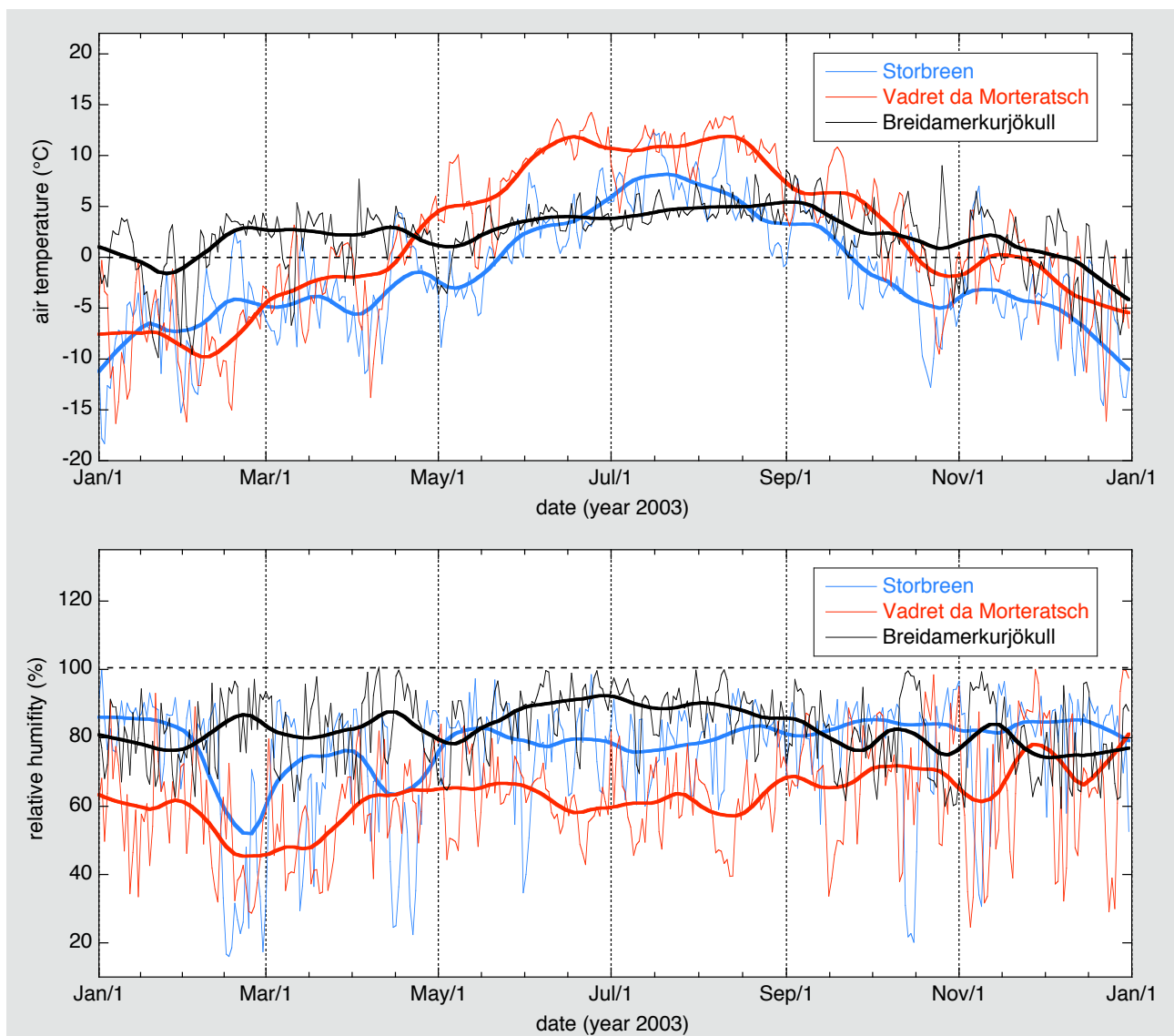

Figure 2.5. One year of daily mean values of air temperature (upper panel) and relative humidity (lower panel), as measured by AWS on three different glaciers. Smooth curves show low-pass filtered data.

       2 - A basic survey of data

The humidity data show that climate at the Vadret da Morteratsch is much drier than at Breidamerkurjökull and Storbreen. Relative dry conditions are typical for the inner Alpine valleys, and the region of the Vadret da Morteratsch is no exception.

At the Vadret da Morteratsch as well as at Storbreen (in winter) an appreciable number of days has very low humidity (between 20 and 40%). This can be attributed to situations in which the rapid descent of air past a mountain crest leads to a strong decrease in relative humidity (frequently associated with föhn winds). The immediate surroundings of Breidamerkurjökull have a smoother topography and days with a very low humidity are rare.

The data discussed above only cover one year and it is not feasible to draw very general conclusions. However, the data show that operating AWS on glaciers is rewarding and provides valuable insight into the meteorological conditions found on glaciers in different climatic regimes.

2.5 Elevational gradients in radiation and air temperature

Large vertical gradients in temperature and humidity characterize the earth's atmosphere. The existence of such gradients is most apparent in mountain regions, where everyone can observe the rapid changes in vegetation when going upward. For typical conditions in the 'free atmosphere', a commonly used value for the temperature lapse rate is -0.0065 K m^{-1}. When the earth's surface is persistently cold and drawing energy from the overlying air, like in the polar regions or at the midlatitudes in winter, smaller absolute values are normally found (at least in the lower troposphere).

Humidity varies much more than temperature because it is so strongly affected by atmospheric motion. Relative humidity is more constant than absolute humidity, because it is not affected by adiabatic motion (no phase transitions). The saturation specific humidity decreases rapidly with temperature according to the Clausius-Clapeyron equation (e.g. Tsonis, 2007). The scale height for atmospheric moisture, defined as the height at which the specific humidity is reduced to e^{-1} times the humidity at sea level, is typically 1.5 km. This should be compared to the scale height for atmospheric mass, which is about 8 km.

When we consider 'elevational gradients along glaciers', we have to be careful about what we actually mean. The *vertical* temperature gradient above a melting glacier surface can be very large – of the order of several degrees K per metre. This implies that the magnitude of the elevational temperature gradient along a melting glacier surface depends very much on the height considered. Actually, at the melting surface the gradient is zero! When we would measure the elevational gradient with a series of identical weather stations, the gradient will be larger when the instruments are higher above the surface. We may expect that when the instruments are sufficiently high above the surface, the temperature gradient will approach the free atmospheric lapse rate. However, in that case the masts would have to be higher than the glacier boundary layer, which is not feasible.

The meteorological experiment carried out on the Pasterze was designed (i) to investigate the structure of the boundary layer over the glacier during conditions of melt, and (ii) to study elevational gradients in meteorological quantities and the components of the surface energy budget. During a period of 46 days in the summer of 1994 five energy balance stations were operated along a flowline of the Pasterze (Figure 2.6, see also Figure 1.5). Stations 1, 2 and 3 were in the ablation
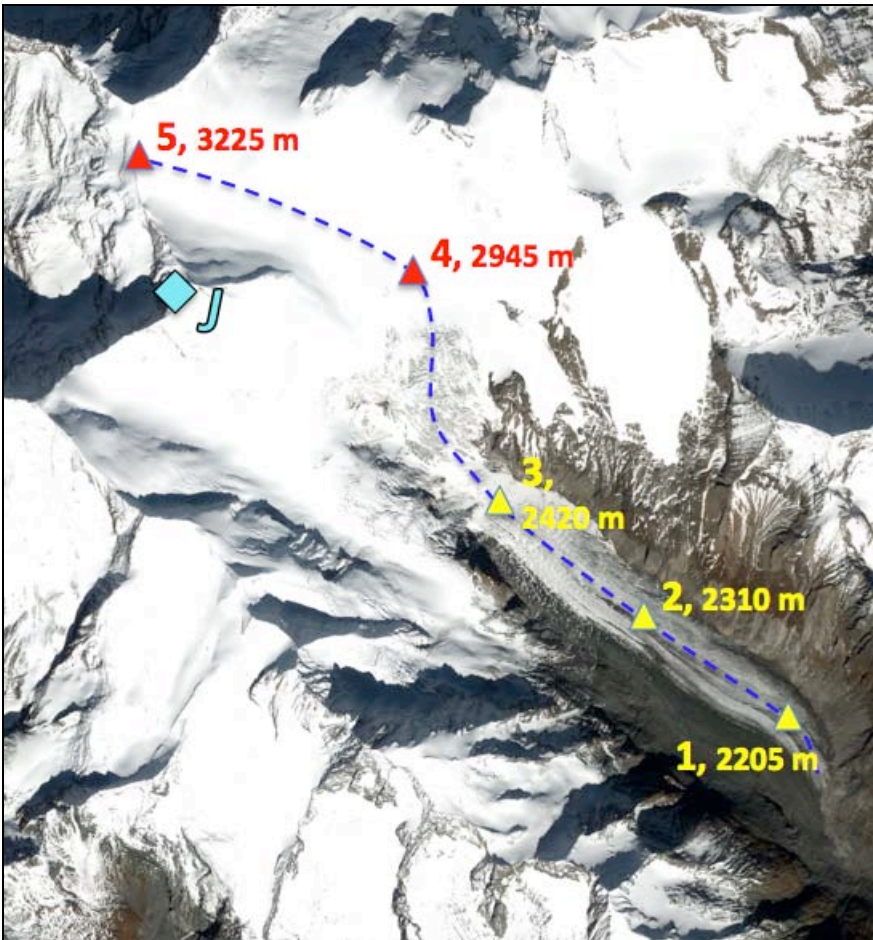
Figure 2.6. Location of the weather stations on the Pasterze, Austria, during the 1994 summer experiment. "J" is the Johannisberg, 3463 m. The dashed blue line indicates an approximate flowline. The distance between the stations 1 and 5 along this line is 7.9 km.

The image is part of a true color image from the Ikonos satellite (October 3, 2001), prepared by Robert Simmon, NASA.

zone, stations 4 and 5 in the accumulation zone. All the measurements were done at a nominal height of 2 m. At station 1 a profile mast was also operated and cable balloon soundings were done every 3 hours to a height of about 800 m above the glacier surface (Figure 1.5). The elevational gradients were studied in detail by Greuell et al. (1997) and Greuell and Smeets (2001), and we discuss some of their results shortly.

As already mentioned in Chapter 1, another large dataset was obtained during the field campaign on Vatnajökull (Oerlemans et al., 1999). The deployment of 16 weather stations across the ice cap, at locations ranging in elevation from close to sea level up to 1210 m (Figure 2.7) also allows the study of elevational gradients. At most stations profiles of temperature and humidity and the components of the radiation budget were measured during the period 22 May – 31 August 1996.

For a further comparison, we also consider data from a meteorological experiment which was carried out in the melting zone of the Greenland ice sheet in the summer of 1991 (GIMEX; Oerlemans and Vugts, 1993). Here the geographical setting and the spatial scale is fundamentally different from valley glaciers and small ice caps, but the transition from an accumulation zone to an ablation zone with appreciable melt rates is similar.

We first consider global radiation. A survey of how global radiation in summer increases with elevation is presented in Figure 2.8. The data points give mean values over the periods indicated. First of all it is interesting to note that the values for the mean global radiation measured in high summer on the Pasterze and in Greenland are similar (260 - 300 W m^{-2}). Over the entire period of the measurements (22 May - 31 August), the values from Vatnajökull are much smaller. When the
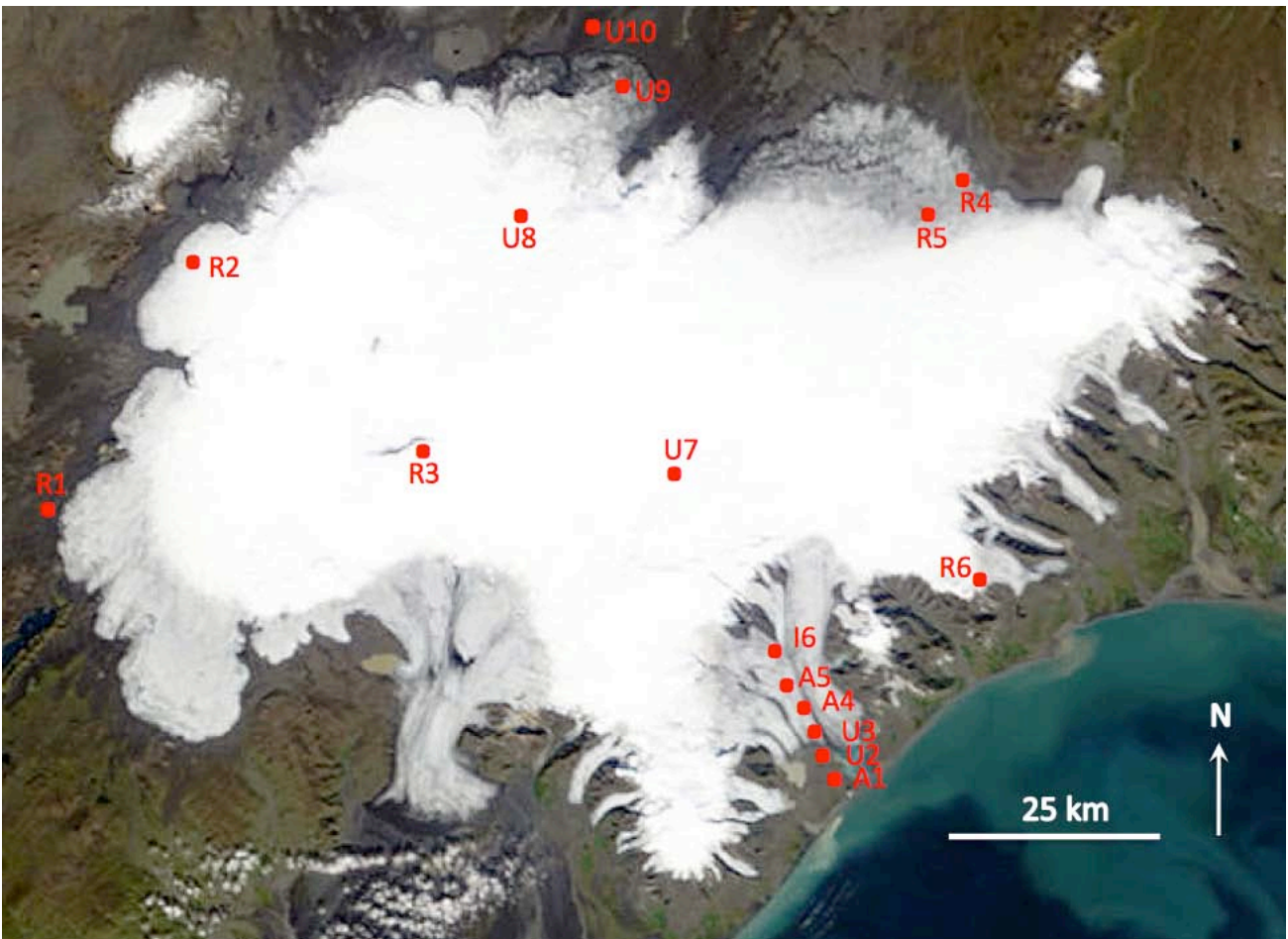
Figure 2.7. Locations of the weather stations on and near Vatnajökull, Iceland, during the 1996 summer experiment, plotted on a MODIS image (9 September 2002; courtesy of NASA).
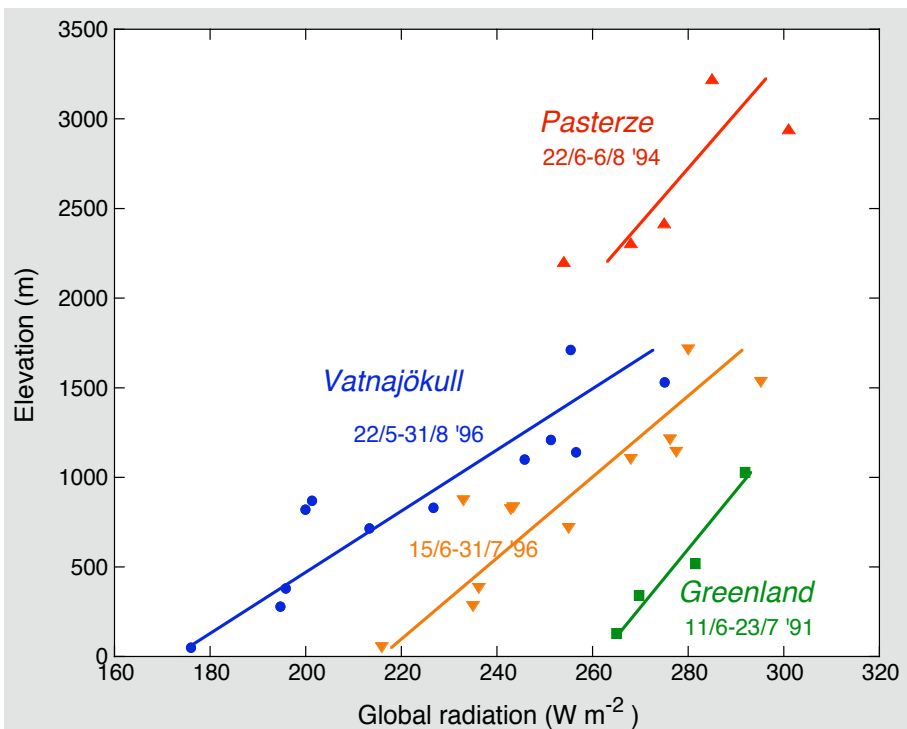

Figure 2.8. The increase in global radiation with station elevation measured during various field campaigns. Note that data for Vatnajökull are shown for a longer (blue) and shorter (orange) period.

period 15 June - 31 July is considered, a better comparison with the other data can be made. Nevertheless, the amount of global radiation in the lower reaches of Vatnajökull is relatively small (see also Figure 2.3).

A more detailed analysis of the data reveals that the differences seen are mainly due to differences in cloud amount and cloud type. This applies to the characteristic values of global radiation as well as to their altitudinal gradients. In general, clouds over the central western part of the Greenland ice sheet are optically thin and high, and the cloudiness is relatively small. This is in sharp contrast with Vatnajökull where low clouds are present most of the time and lead to a very strong increase in global radiation with altitude. The variability in the Vatnajökull data is larger anyway than for the other two data sets. This is due to the fact that the stations were widely spaced, covering the entire ice cap (area: 8100 km^2).

Clearly, all data sets show a consistent positive gradient in the global radiation with elevation. A characteristic gradient is 0.04 W m^{-3}. Although cloud characteristics are the decisive factor here, on valley glaciers the decrease in shading when going upwards may play an important role as well (e.g. Greuell et al. 1997).

A more general study of the altitude dependence of the surface radiation budget was carried out by the ASRB-project (Alpine Surface Radiation Budget; e.g. Marty et al., 2002). Based on four years of data the conclusion from this study was that elevation gradients in global radiation are rather small, with slightly negative values below 2000 m and positive values above 2800 m (in summer). The negative gradients at lower elevations are attributed to the development of convective clouds shading the middle and high parts of mountains. Marty et al. (2002) mention multiple reflection between clouds and the often snow-covered slopes as an explanation for the positive elevational gradient in global radiation in high alpine terrain. Altogether, the elevation gradients in global radiation seen on glaciers appear to be significantly larger than in the non-glaciated terrain.

In summer the net longwave radiation (L_{net}) decreases with elevation (Figure 2.9). This is due to a decrease in the incoming longwave radiation, because the outgoing longwave radiation varies little
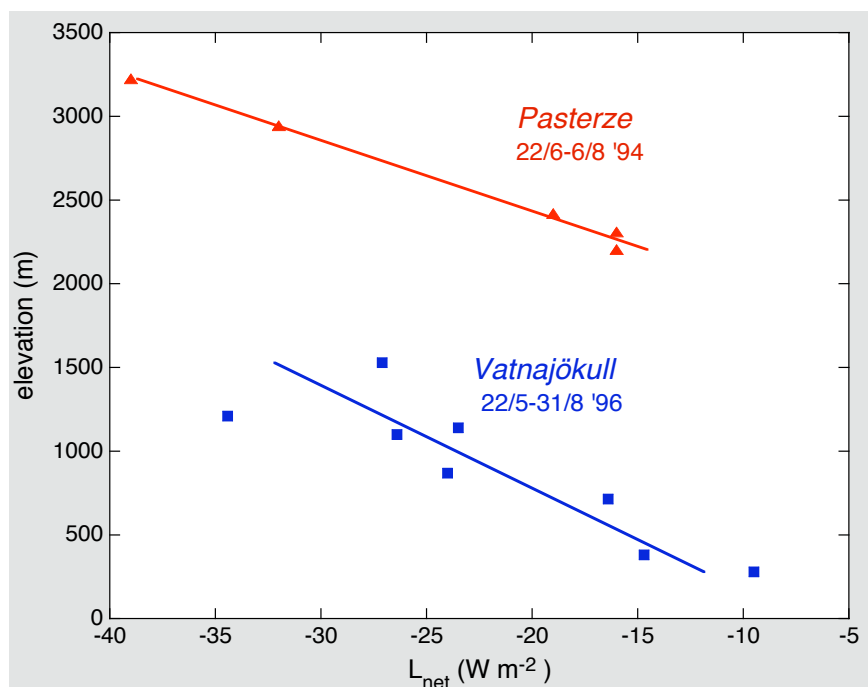

Figure 2.9. The decrease in net longwave radiation with station elevation. The number of data points is less than in Figure 2.8 because longwave radiation was measured at a selection of stations only.

(surface at the melting point most of the time). A characteristic gradient for L_{net} is -0.02 W m^{-3}. So if the albedo would be constant, the net radiation in summer would increase with elevation at a typical rate of 0.02 W m^{-3}.

As mentioned in the beginning of this chapter, elevational gradients in air temperature are somewhat problematical because the value depends very much on the reference measurement level. During the summer experiments on Greenland, Pasterze and Vatnajökull care was taken to have temperature measurements at 2 m for all stations. The stations were visited regularly to ensure that the correct measurements heights were maintained and that sensors remained horizontal (this is particularly important when global radiation from different stations is compared). For automatic weather stations running unmanned for a year this is more problematical because sensors have to be higher above the surface to avoid interference with the snowpack in winter, and because after some time the masts are slightly tilted. Therefore it is best to study elevational temperature gradients with the data from the summer experiments.

In Figure 2.10 mean 2 m air temperatures are plotted as a function of station elevation. Apparently, the elevational gradients are rather similar for the three experiments. The values are -0.0042 K m^{-1} for the ablation zone in West Greenland, -0.0041 K m^{-1} for the Pasterze, and -0.0035 K m^{-1} for Vatnajökull. This should be compared to the moist adiabatic lapse rate of -0.0065 K m^{-1} (dashed lines in Figure 2.10). We may conclude that 2 m temperatures are strongly affected by the melting surface, leading to a smaller elevation temperature gradient. Since the temperature gradient appears to differ little from glacier to glacier, it would be interesting to see whether an atmospheric boundary-layer model would be able to reproduce this!
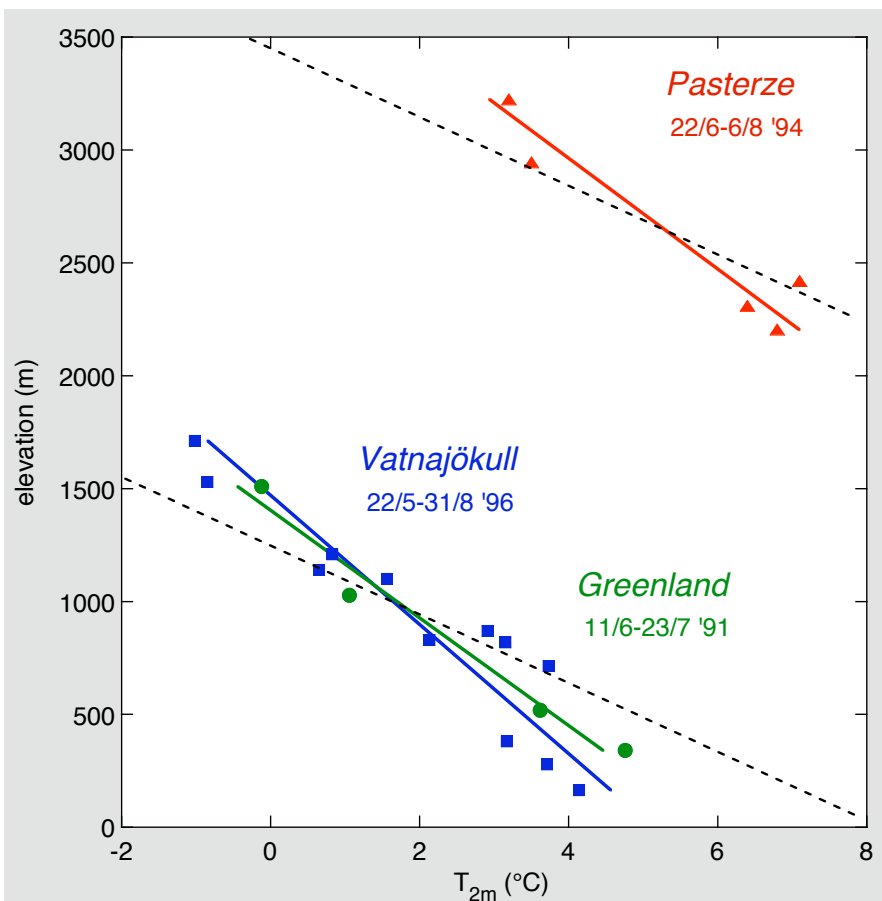
Figure 2.10. Air temperature measured at 2 m (mean values for the periods indicated). The dashed lines have lapse rates of -0.0065 K m^{-1}.
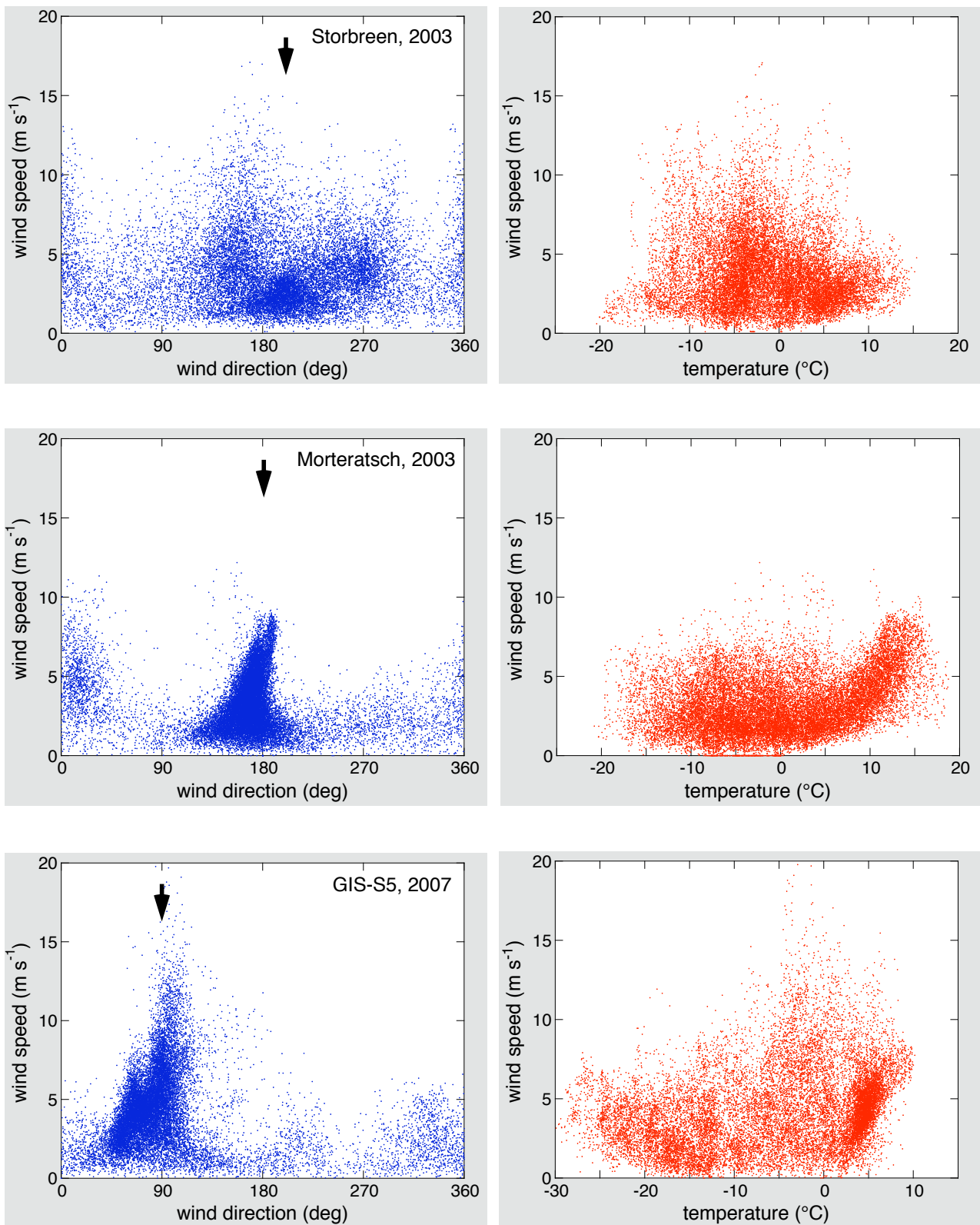
Figure 2.11. Scatter plots showing relations between wind speed, wind direction and air temperature. In all cases a full year of measurements is shown, and every dot represents a 30-min average value (so every plot contains 17520 points). The arrow indicates the direction of the local fall line of the glacier. The instrument height is 6 m for Storbreen, 3.5 m for the Vadret da Morteratsch, and 6 m in the melt zone of the Greenland ice sheet. The AWS on Storbreen and the Vadret da Morteratsch are located on the lower glacier tongue, where AWS S6 on Greenland is along the Kangerlussuaq transect, 6 km from the ice edge at an elevation of 510 m (Van de Wal et al., 2006). Note that the temperature scales are not identical.

2.6 The wind regime

A good impression of the wind regime in the glacier boundary layer is obtained from scatter plots of wind speed, wind direction and air temperature. A survey is shown in Figure 2.11, where data from Storbreen, Vadret da Morteratsch and the melting zone of the Greenland ice sheet (GIS-S6, Kangerlussuaq transect) are compared.

It is obvious that for all glaciers preferred wind directions exist. For the Vadret da Morteratsch the wind blows downglacier virtually all the time. The same is true for GIS-S6, with perhaps a slight veering of the wind with respect to the fall line. For Storbreen the clustering of the data points is less pronounced. The cluster around a wind direction of ~200° and a wind speed of a few meters per second represents the katabatic regime, but wind directions of ~270° and ~150° also occur frequently.

In the classical description of katabatic flow, the forcing is determined by the temperature deficit in the near-surface layer. This deficit is defined as the difference between the actual air temperature T_a and the temperature of the ambient atmosphere, extrapolated to the same altitude. Generally speaking, T_a measured at a few metres height above the glacier surface contains little information about the temperature deficit because the ambient temperature is not known. However, when the surface is melting and T_a is above the melting point (T_m), the temperature deficit must be negative and katabatic flow must be generated. The buoyancy forcing is proportional to the temperature deficit and we therefore expect a positive correlation between T_a and the katabatic wind speed. Such a correlation is evident from Figure 2.11. In all cases we see higher wind speeds becoming

Figure 2.12. The Vadret da Morteratsch photographed by Ch. Rothenbühler (26 June 2003). The view is towards the south. The location of the AWS on the glacier tongue is indicated by the red spot. Note the yellow-coloured Sahara dust band.

more frequent for higher temperatures when $T_a > 0\,°C$. For Storbreen the correlation is not so strong, whereas for the Vadret da Morteratsch the increase of wind speed with temperature is clearly nonlinear. The difference in wind regime for Storbreen and the Vadret da Morteratsch can be attributed to the size of the glaciers. Storbreen is a small glacier and the distance over which the katabatic flow can develop is rather short (~1 km). The Vadret da Morteratsch is 7 km long and flows into a deep valley (Figure 2.12).
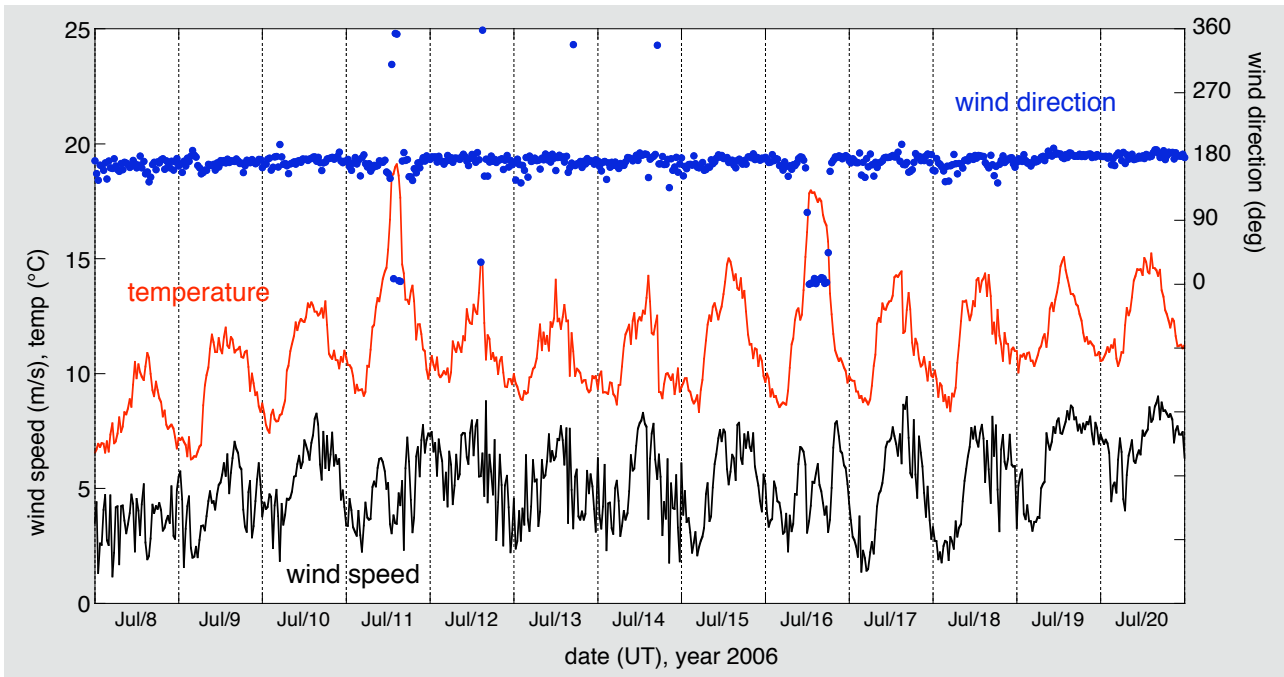

Figure 2.13. The daily rhythm of the glacier wind as observed on the Vadret da Morteratsch. The scale at the left refers to wind speed and air temperature, the scale at the right to wind direction (all measured at a height of 3.5 m). Vertical lines refer to midnight UT (in summer, LT = UT+2 hr and solar time = UT+2 hr 40 min).

Figure 2.13 illustrates the daily rhythm of the glacier wind for a fair weather period in the summer of 2006 on the Vadret da Morteratsch. The wind speed closely follows the air temperature, both reaching peak values in the afternoon. The wind direction is very constant (~180°, which is downglacier). However, there must also be a strong valley wind that blows on top of the katabatic flow in opposite direction. On two occasions the glacier wind is eroded in the afternoon by this valley wind, namely on July 11 and July 16. Then the wind direction changes over 180° to blow upglacier, the wind speed drops, and the air temperature suddenly increases by 4 to 5 degrees K. Such events happen on the warmest days, and were also observed during the summer experiments on the Hintereisferner and the Pasterze.

Perhaps one would expect that katabatic flows on glaciers occur more frequently in summer than in winter. However, the data from the Morteratsch AWS show that this is not the case (Figure 2.14). There is little difference in the histograms for wind direction. In winter the strongly negative radiation budget of the snow surface leads to cooling of the surface air, generating negative buoyancy. The mean wind speed in the winter half year is somewhat smaller than in the summer half year (not shown).
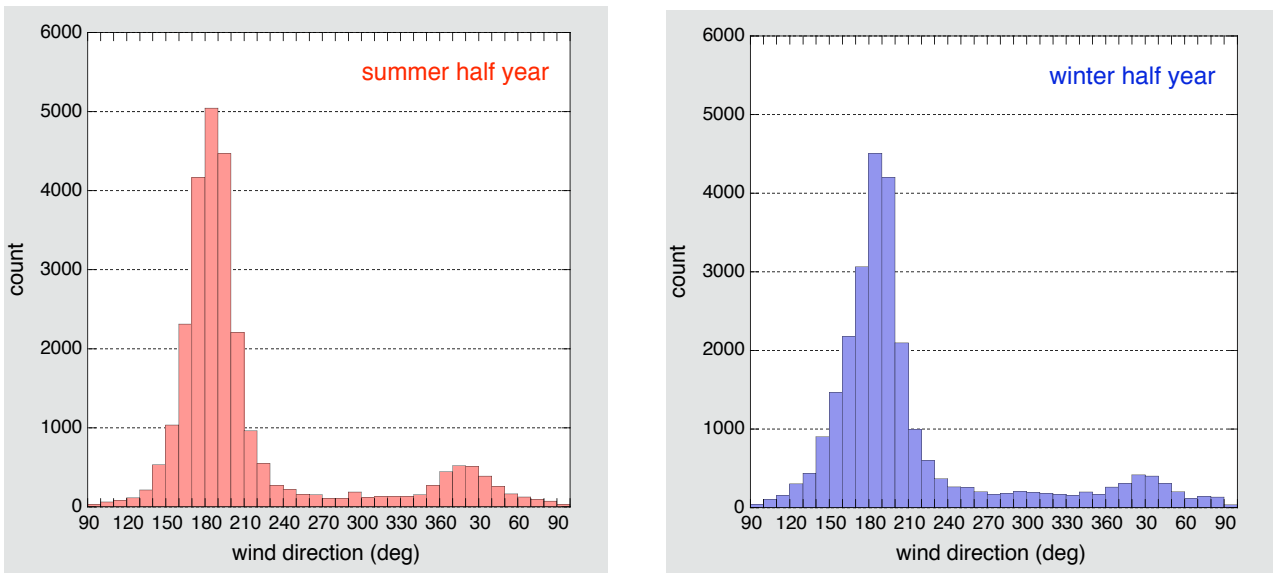
Figure 2.14. Histograms of wind direction as observed on the Vadret da Morteratsch. The summer half year is defined as 1 May – 30 October, the winter half year as 1 November – 30 April. Data are from three years of measurements (1 October 1995 – 30 November 1998). Each diagram is based on 26304 data points (half hourly values).

Altogether, it is clear that the wind regime on larger glaciers is dominated by katabatic flow. Cases with high temperature and low wind speed are very rare on all studied glaciers. Katabatic winds act as a kind of heat pump for melting glaciers. The heat flux towards the glacier surface cools the air and forces a katabatic flow. The interaction of the katabatic flow with the irregular glacier surface generates turbulence, in spite of the very stable stratification. This turbulence enhances the sensible heat flux to the surface and thereby the forcing of the katabatic flow, keeping the heat pump going. All the measurements discussed so far are surface measurements. As mentioned in Chapter 1, the vertical structure of the glacier - valley wind system has been observed with cable balloon soundings and profile masts. This will be discussed in detail later, but here we look at a single balloon sounding to illustrate the basic characteristics (Figure 2.15).

Figure 2.15. Result of a cable balloon sounding in fair weather on Pasterzen Kees, 23 July 1994, 16[h]25 LT.

The most striking feature in Figure 2.15 is the very sharp temperature inversion close to the surface. The temperature increas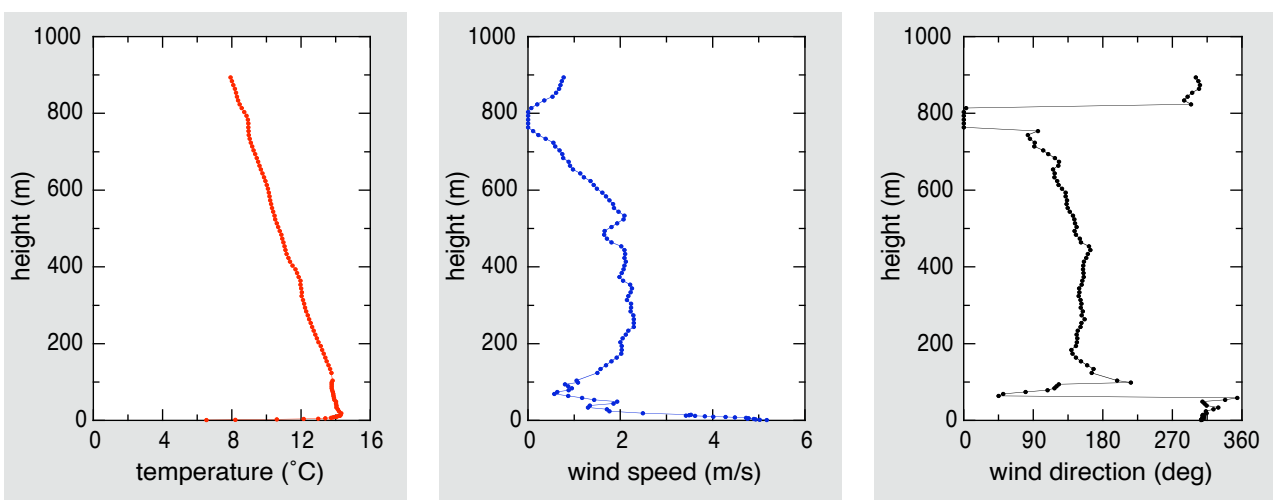es by 14 K over a vertical distance of less than 20 m. Above the inversion the lapse rate is very constant and equal to -0.0067 K m^{-1}. The windspeed maximum is very close to the surface and is about 5 m s^{-1}. The wind direction in the katabatic flow is downglacier. At a height of about 50 m the wind speed is almost zero and the wind direction changes by 180 degrees. Apparently this is the transition of the katabatic layer to the valley wind, which blows upglacier at a typical speed of 2 m s^{-1}. Simultaneous measurements with a 13-m high profile mast reveal that on this occasion the wind maximum was about 6 to 7 m above the glacier surface.

2.7 Microclimate and large scale weather

The glacier microclimate is embedded in a larger scale atmospheric system. In Section 2.6 we have seen that katabatic flow over glaciers is relatively undisturbed by the large-scale flow. So the coupling of the glacier microclimate to the synoptic scale weather conditions is first of all determined by the temperature field. This point deserves further study, because one of our goals is to relate the energy fluxes at the glacier surface to the large scale meteorological variables.
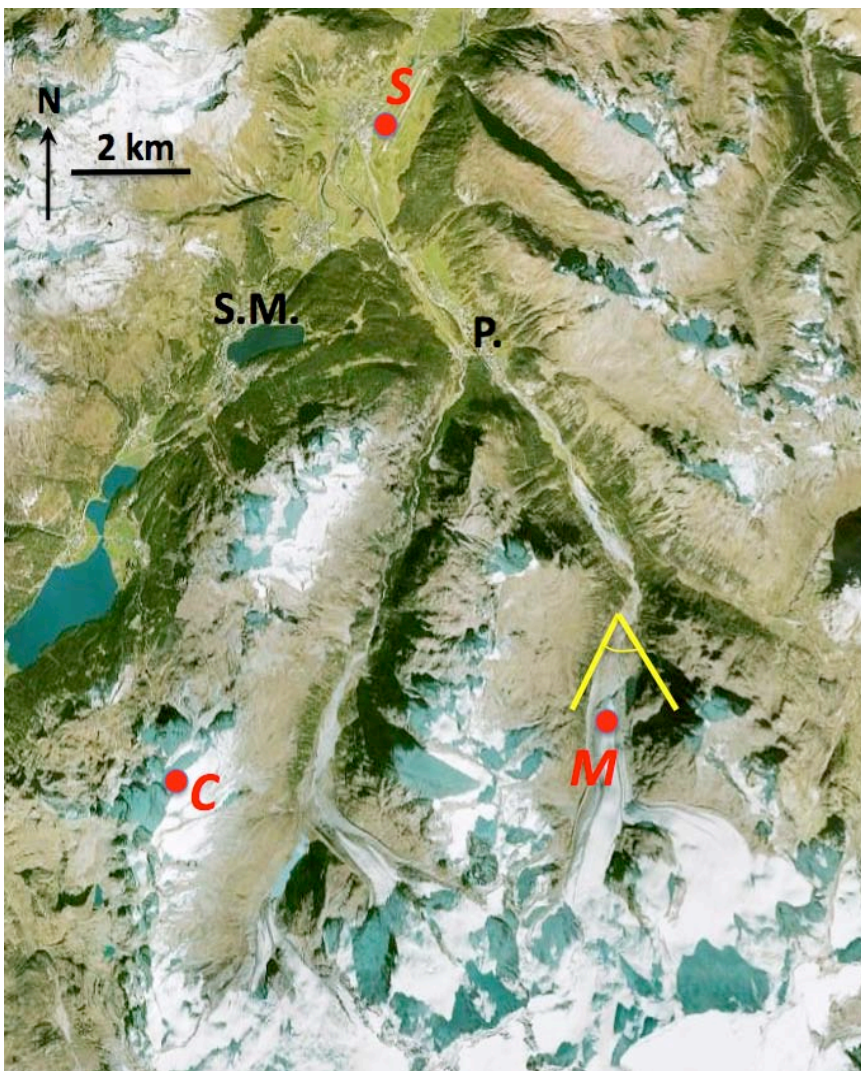

Figure 2.16. Spot image (1997) of the northern Bernina glaciers and the Oberengadin, with the weather stations indicated by red spots. *M* is the AWS on the Vadret da Morteratsch, *S* is Samedan, C is Corvatsch. Sankt Moritz (S.M.) and Pontresina (P.) are also indicated.
The yellow bars refer to the approximate direction of view of Figure 2.12.

The data from the AWS on the Vadret da Morteratsch can be used to carry out a survey. A number of synoptic weather stations operated by the Swiss Meteorological Service are located not too far from the Vadret da Morteratsch. We will look at data from Samedan, sometimes referred to as Sankt Moritz airport, and from Corvatsch (Figure 2.16). Samedan (1704 m) is located in the middle of a wide valley only 13 km north of the Morteratschgletscher. Corvatsch (3297 m) is a station on a mountain top, at a distance of about 9 km west of the Vadret da Morteratsch. These stations are ideally suited for a comparison. We first look at a period of fair weather in October 1995 (Figure 2.17; note that the curves for Samedan and Corvatsch are smoother because hourly mean values have been plotted).

The regularity of the temperature records is large. At Samedan the daily range is about 20 K, at the Morteratsch AWS about 6 K and at Corvatsch only a few degrees K. During this period the glacier wind blows steadily down the Vadret da Morteratsch (not shown). Later we will discuss whether it is possible to derive the katabatic forcing associated with these temperature records.

It is also interesting to compare daily mean temperatures at these stations for a full year (Figure 2.18). Clearly, a distinction should be made between the winter period (end of November until early March) and the rest of the year. For most of the year the correlation between the stations is very high, but in winter the temperatures for Samedan and the Morteratsch AWS tend to become decoupled. Samedan is located in a wide flat valley and has much lower temperatures, especially during clear nights. This 'cold pool effect' is not present on the tongue of the Morteratschgletscher, where katabatic flow mixes warmer air downwards all the time.

The correlation coefficient between daily mean temperature at Corvatsch and the Morteratsch AWS is quite high: 0.97 on an annual basis. This result suggests that measurements from high-altitude weather stations are very valuable for estimating the temperature conditions over nearby glaciers.

Finally, it should be emphasised again that one must take great care when discussing air temperature over a melting glacier. Since the vertical temperature gradient is so large, the reference height should always be given.
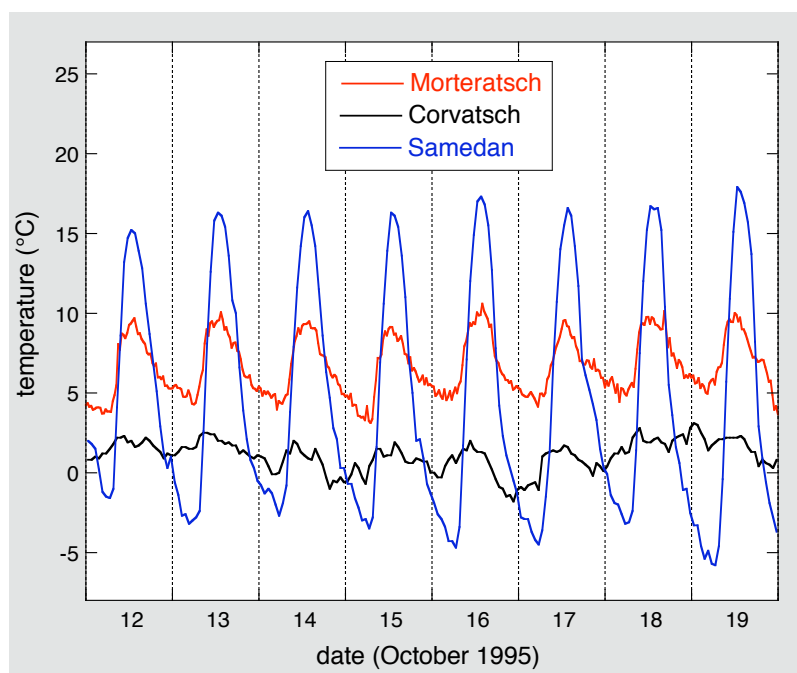

Figure 2.17. Air temperature (3.5 m) measured on the tongue of the Vadret da Morteratsch, compared with observations at other neighbouring stations.
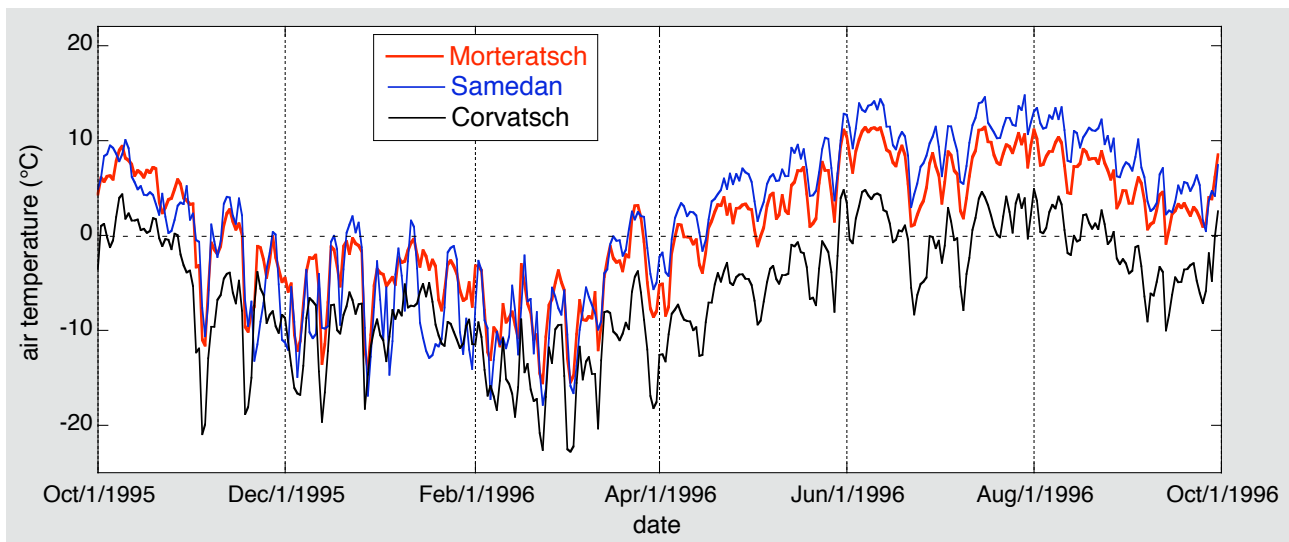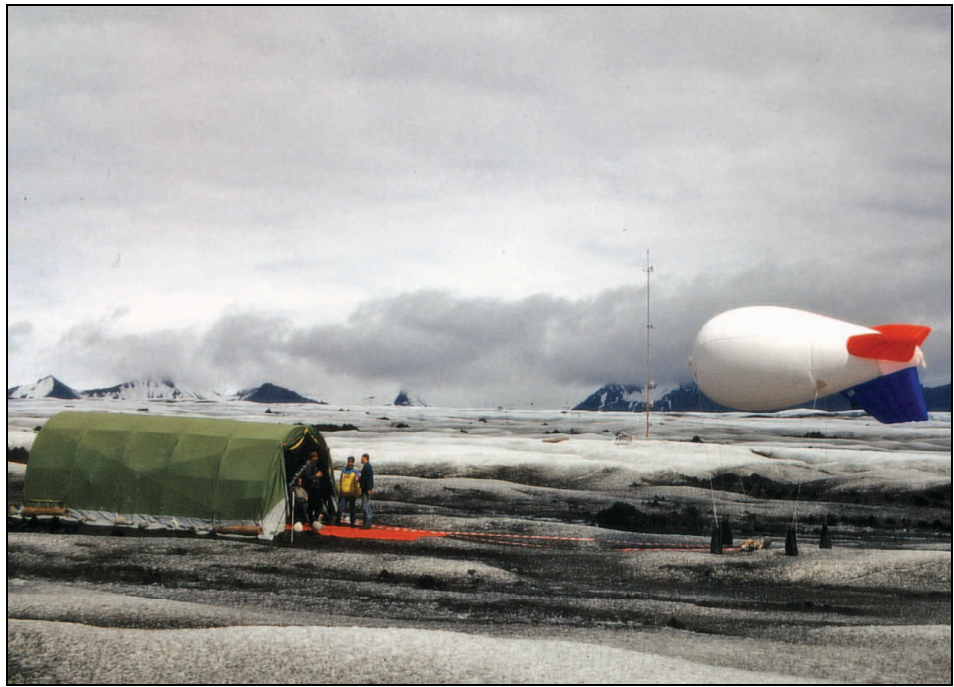
Figure 2.18. Daily mean air temperature for a full year as measured on the Vadret da Morteratsch and surrounding stations. The correlation is very high, except in the winter months.

2 - A basic survey of data

Studying katabatic flow over Vatnajökull, Iceland, June 1996.

3. The glacier wind

3.1 Introduction

A well developed glacier wind is characterised by a distinct wind maximum at a height of 5 to 10 meters. To observe the structure of the jet in detail a well equipped meteorological tower extending to a height of 20 to 30 m would be the best tool. However, well developed glacier winds occur over ablation regions where the melt rates are typically between 5 and 10 cm of ice per day and the morphology of the surface changes continuously. Therefore it is virtually impossible to build up and maintain a high tower on a melting glacier surface. An alternative approach is to use a lower mast in combination with a cable balloon system. Such a set up was used during the Pasterze experiment (operational phase 16 June – 10 August 1994). At station 1 (see Figures 1.5 and 2.6), eddy-correlation measurements of the turbulent fluxes were made at two heights. A 13 m mast was erected with temperature, humidity and wind measurements at eight levels (0.25, 0.5, 1, 2, 4, 8 and 13 m). Much of the profile data and the turbulence measurements have been analysed with traditional methods from boundary-layer meteorology (Smeets et al., 1998; Smeets et al., 2000; Denby and Greuell, 2000). These investigations have made clear that it is sometimes difficult to apply concepts developed for the stable boundary layer to study katabatic flows. Estimating surface fluxes requires more than applying stability corrections to existing schemes. In this chapter we will try to develop an alternative line of thinking, in which the nature of the katabatic flow is more directly coupled to the surface fluxes.

Concerning the vertical structure of the glacier wind on a valley glacier, the experiment carried out on the Pasterze has probably delivered the most extensive data set to date. In addition to the measurements with the profile mast, about 200 cable balloon soundings were made to a height of 500 to 1000 m above the surface. On most days the soundings were made every 3 hours. The analysis in this chapter is largely based on the data from the Pasterze experiment.

Apart from the significance with respect to climate change, the glacier wind is also interesting from a purely meteorological point of view. Over glacier tongues the surface temperature remains at the melting point for long periods of time (sometimes for several months), providing a lower boundary condition for temperature and vapour pressure that is much simpler (and constant in time) than for nocturnal drainage flows. Moreover, the flow is generally stronger with a well-defined wind maximum, and on many glaciers there is a long fetch over a nearly constant surface slope.

3.2 The observed vertical structure of the glacier wind

In the period that the Pasterze experiment was running, a wind maximum below 13 m was observed during 63% of the time. During the remaining time the wind maximum was at a greater height as observed from the balloon soundings, or there was no wind maximum at all. On days with fair weather the wind maximum was practically always below 13 m.

Figure 3.1 shows wind and temperature profiles at 3 hourly intervals for a sunny day with a relatively weak large-scale atmospheric flow. Each profile represents a 30-min average. The profiles appear to be very regular, with a limited but well defined daily cycle in the air temperature (a range of ~4 K at 13 m above the surface). The highest wind speeds are observed at 4 or 6 m above the glacier surface. The strongest winds occur for the highest temperatures, but the profile at 12 hr is an exception. The jet is lower and weaker, although the air temperature is high. Altogether, there is an apparent correlation between the height and the strength of the katabatic jet: when the maximum wind speed is larger the jet is further above the surface.

The relation between the height and the strength of the jet appears to be a fairly robust result. Denby (personal communication) has used polynomial fitting on all profiles from the Pasterze experiment to find the wind maximum in an objective way. The result is shown in Figure 3.2. The correlation coefficient between u_m (maximum wind speed) and z_m (height of the wind maximum) is 0.78. The mean height of the wind maximum is 4.4 m, but this cannot be regarded as the real mean height because all cases with a wind maximum above 11 m are not picked up by the profile mast.
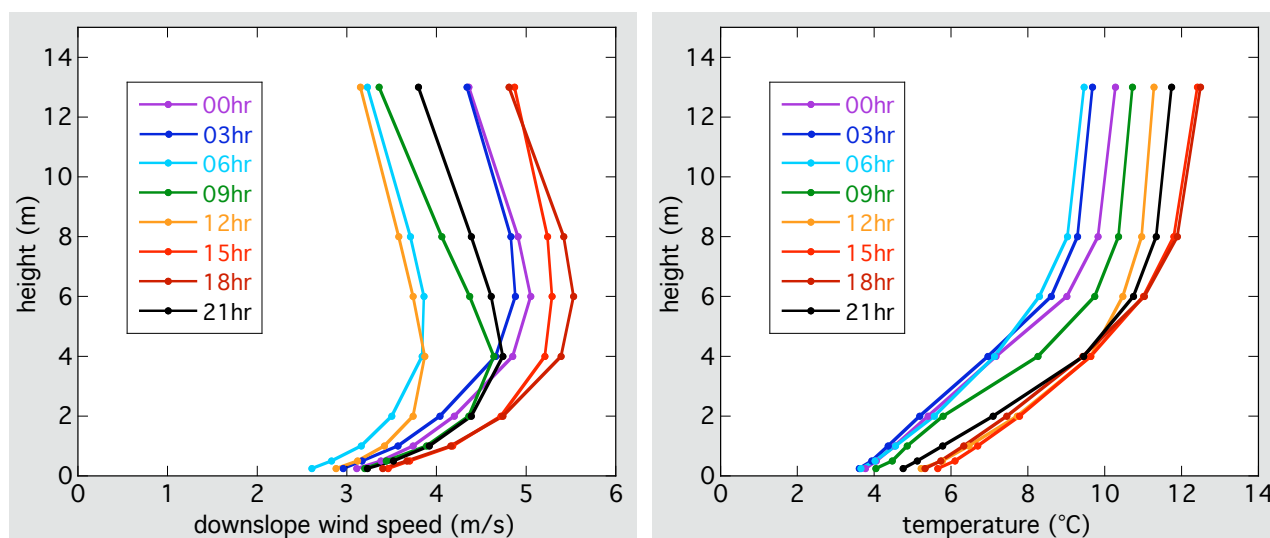

Figure 3.1. Observed wind and temperature profiles on 29 July 2007. Profiles are shown for every 3 hours (UT), but represent 30-min averages.
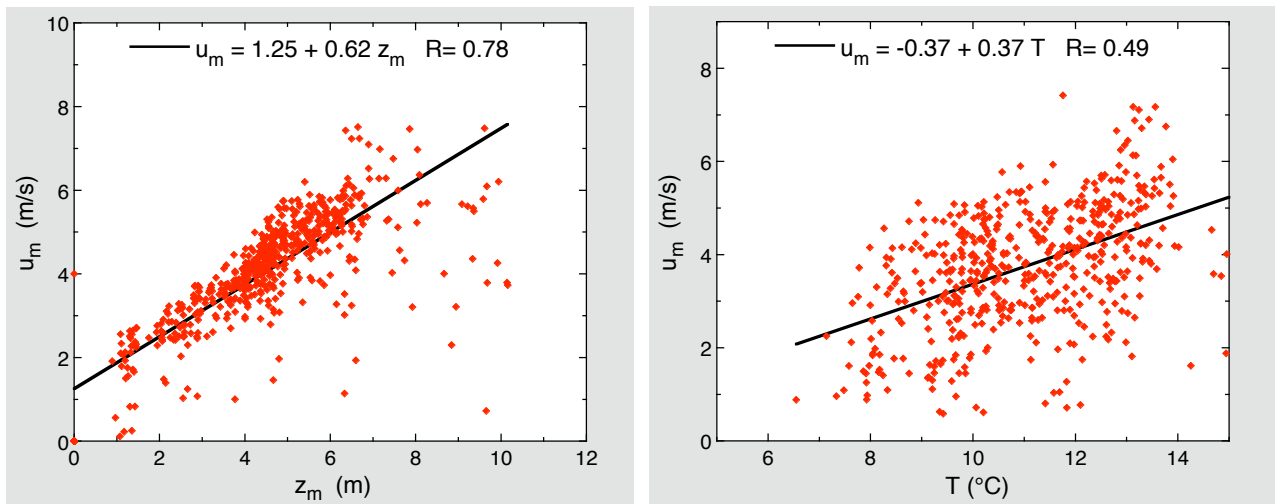
Figure 3.2. The relation between the observed strength of the wind maximum and the height of the wind maximum (left) and the 13 m temperature (right). Every dot represents a 30-min average. Prepared by B. Denby.

The correlation between temperature (measured at 13 m) and u_m is weaker, although significant. Altogether, the conclusion from the data of the profile mast is that higher air temperatures lead to a stronger katabatic jet which is higher above the glacier surface.

In July 1986 wind profiles were measured on the Hintereisferner for a short period (10 days). Two sites were studied: one with a surface slope of 4° and one with a slope of 10° (Oerlemans and Greuell, 1986, unpublished manuscript). The data from this experiment revealed a similar relation between u_m and z_m, and generally lower values of z_m for the location with the steeper slope.

The relation between u_m and z_m is a typical result that can be used to verify theoretical models. A realistic model of the glacier wind should be able to reproduce, among other things, values of $\partial u_m / \partial z_m$. The values for the field experiments discussed above are listed in Table 3.1.

	period	slope	$\partial u_m / \partial z_m$ (s^{-1})
Hintereisferner	12 – 22 July 1986	10°	1.96
Hintereisferner	12 – 22 July 1986	4°	0.88
Pasterze	16 June – 10 August 1994	5°	0.62

Table 3.1. Results from field experiments on the relation between strength and height of the katabatic jet.

Next we consider the vertical structure of the glacier – valley wind system as observed by the balloon soundings. A thorough analysis has been carried out by Van den Broeke (1997a) and we discuss a few of his results.

During the Pasterze experiment there were several spells of fair weather with relatively weak synoptic scale forcing. During one of these periods, 23 July - 3 August 1994, a complete set of 3 hr balloon soundings was obtained, and an averaged daily cycle was calculated for a height up to 500 m above the glacier surface. Figure 3.3 shows the downslope wind component and the potential temperature in time-height diagrams. Figure 3.4 shows the same in a close-up for the lower 50 m.
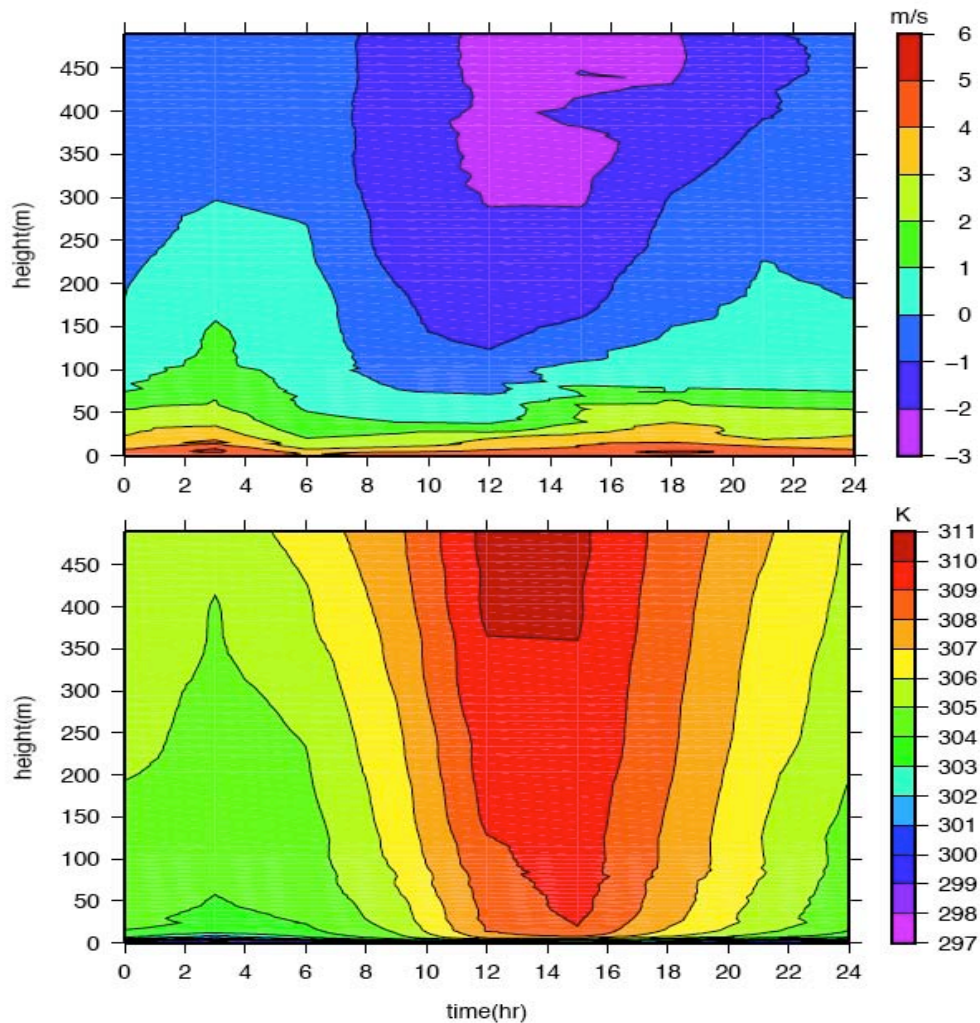
Figure 3.3. Average daily cycle of downslope wind component (upper panel), and potential temperature (lower panel) for fair weather conditions on the Pasterze. The diagrams are based on 3-hourly balloon soundings during the period 23 July - 3 August 1994.

The structure of the potential temperature field is dominated by the strong vertical gradient near the glacier surface, and by an obvious daily cycle. During daytime the valley above the glacier is filled with warm air that is advected by the valley wind (negative downslope winds of up to -3 m/s). From Figure 3.4 we can see that this leads to higher near surface temperatures, and also to a larger vertical temperature gradient near the surface. The advection of warm air has a twofold effect on the strength of the glacier wind: (i) the temperature deficit increases and implies a larger forcing to the glacier wind, (ii) the upslope valley wind tends to retard the downslope glacier wind by friction. Which process dominates is hard to say. As discussed before, on very warm days the valley wind can be so strong that the glacier wind disappears temporarily (Figure 2.13).

The mean daily cycle shows two maxima in the downslope wind component. The maximum in the night can be explained by the fact that katabatic downslope winds from the mountain walls merge with the glacier wind. The maximum at the end of the afternoon is probably related to the weakening of the valley wind, while the temperature forcing is still large (Van den Broeke, 1997a). The lower panel in Figure 3.4 shows the humidity structure of the glacier – valley wind system.

3 - The glacier wind

There is a strong relation between the specific humidity and air temperature, of course. The warm air brought upwards by the valley wind is humid, whereas the katabatic layer is relatively dry.
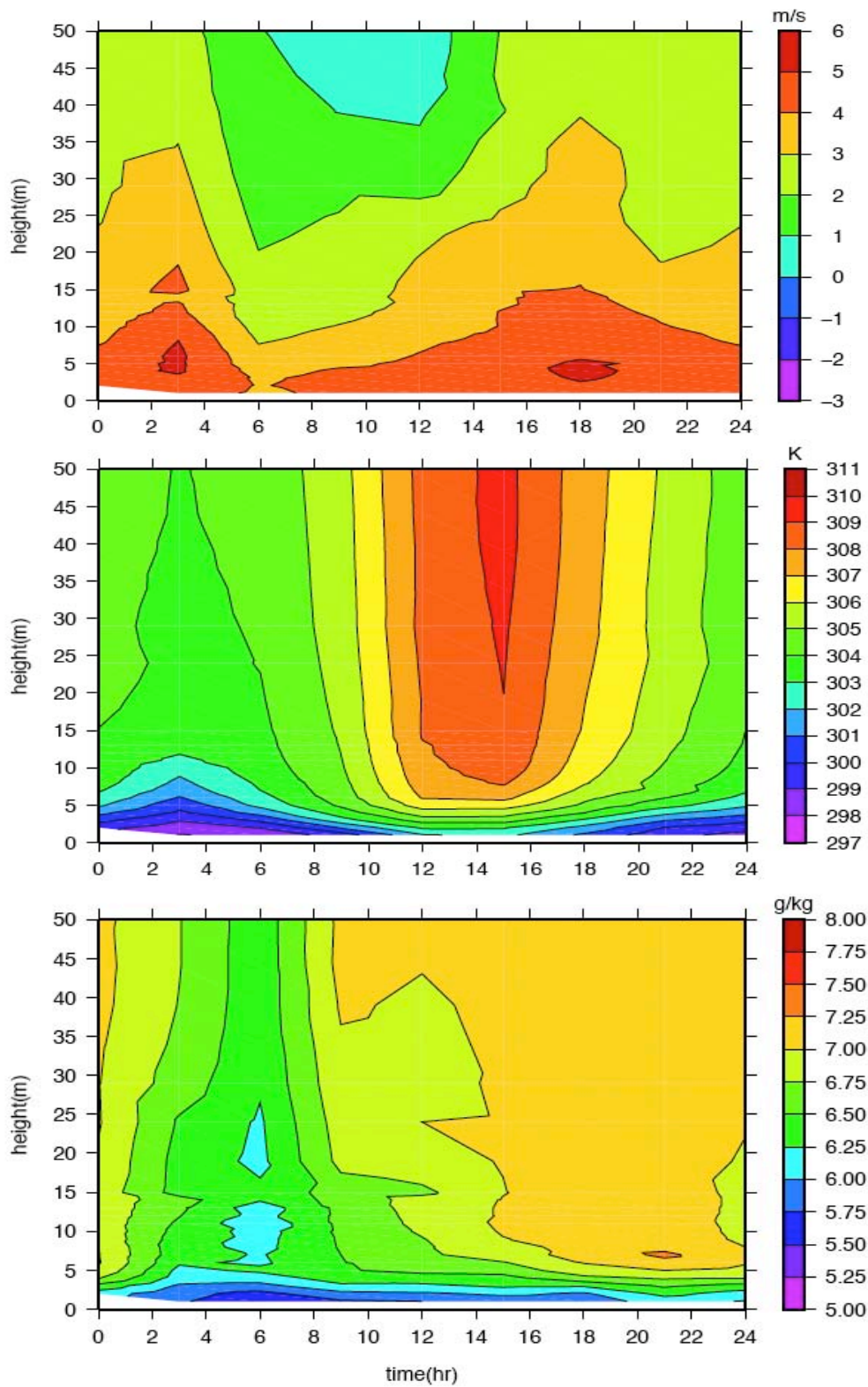

Figure 3.4. Close-ups for the lower 50 m: downslope wind component (upper panel), potential temperature (middle panel), and specific humidity (lower panel). As in Figure 3.3, the diagrams are based on 3-hourly balloon soundings during the period 23 July - 3 August 1994.

Measurements of wind, temperature and humidity profiles have been done on many glaciers. However, very few observations have been done with masts that were sufficiently tall to capture the structure of the katabatic jet. It is unfortunate that in many cases the height of the jet is too high above the surface for a standard profile mast, and too low for a balloon system. This problem was evident in particular during the experiment on Vatnajökull (Oerlemans et al., 1999).

Nevertheless, the data discussed above have revealed a number of characteristics of the glacier wind. The most outstanding results of the previous analysis are: (i) Over glaciers a katabatic flow, in the form of a low-level jet, is present most of the time; (ii) There is a clear relation between the height and the strength of the wind maximum; (iii) Vertical temperature gradients are very large and remarkably constant below the jet. A theory describing the structure of the katabatic flow should be able to reproduce these findings.

3.3 Simplified dynamic equations describing katabatic flow

Motions in the atmosphere are described by the Navier-Stokes equations. The complete Navier-Stokes equations for a rotating frame form a complicated set of mathematical expressions describing the evolution of the state of the atmosphere (e.g. Gordon et al., 1998). For the description of katabatic flow over a glacier a simplified set of equations can be used because the flow is shallow. This allows the use of the Boussinesq approximation, which implies that density fluctuations are proportional to temperature fluctuations relative to a standard temperature profile. It is also convenient to use a tilted Cartesian coordinate system in such a way that one of the axes coincides with the glacier surface in downslope direction (Figure 3.5). Clearly, such an approach only makes sense if the spatial scale over which the slope of the glacier changes is significantly larger than the depth of the katabatic flow.
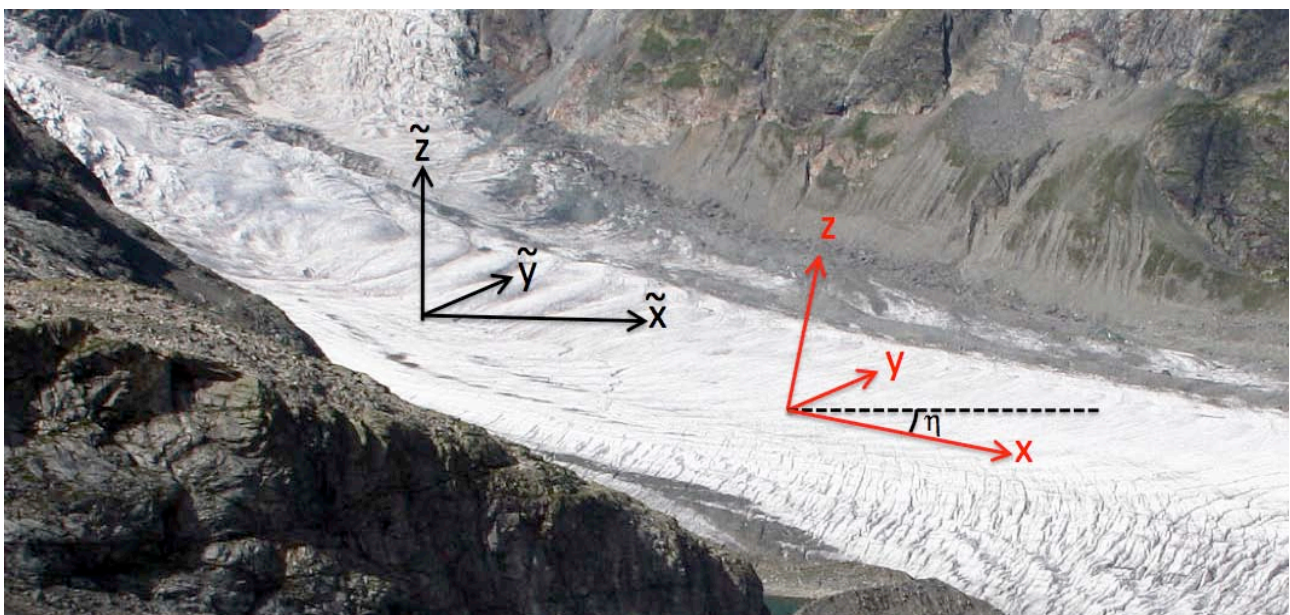

Figure 3.5. Tilted Cartesian coordinate system (red) to describe katabatic flow. The x-axis is along the fall line of the glacier and makes an angle η with the horizontal.

We assume that the flow is quasi 2-dimensional in the sense that all derivatives with respect to y are zero. This would be a very good assumption for a wide glacier like Breidamerkurjökull. For glaciers in narrower valleys the flow will be channeled by the valley walls, but this does not necessarily imply that 3-dimensional effects are insignificant. For instance, if one valley wall is heated by the sun and the opposing wall is not, a cross-valley circulation will be generated that may interfere with the glacier wind. Nevertheless, the measurements discussed so far suggest that a useful description of the glacier wind is possible with a 2-dimensional approach. In writing down the dynamic equations we follow Nappo and Rao (1987) and Denby and Smeets (2000).

In the following we make a distinction between the x,z coordinate system as defined above and the $\tilde{x},\tilde{z}$ system in which $-\tilde{z}$ is aligned along the acceleration of gravity. The first step is to describe the temperature field in a suitable way. As dependent variable we use the potential temperature perturbation θ, defined as the difference between the potential temperature Θ and a reference potential temperature Θ_{ref}. Θ_{ref} has a constant vertical lapse rate $\gamma_\theta \ (>0)$, so we write

$$\theta = \Theta - \Theta_{ref}(\tilde{x},\tilde{z}) = \Theta - \{\Theta_0(\tilde{x}) + \gamma_\theta \, \tilde{z}\} \ . \tag{3.3.1}$$

The ambient atmosphere is supposed to be in hydrostatic and geostrophic equilibrium. The x-component of the momentum equation can then be written as [note that $\eta < 0$ when the surface slopes downward in the x-direction].

$$\frac{\partial u}{\partial t} = \underbrace{-u\frac{\partial u}{\partial x} - w\frac{\partial u}{\partial z}}_{advection} \quad \underbrace{-\frac{\partial F_u}{\partial z}}_{turbulence} \quad \underbrace{+\frac{g(\sin\eta)}{T_0}\theta}_{\substack{katabatic \\ forcing}} \quad \underbrace{+\frac{g(\cos\eta)}{T_0}\frac{\partial\overline{\Theta}}{\partial x}}_{thermal\ wind} \quad \underbrace{+f(\cos\eta)(v - v_g)}_{\substack{Coriolis \\ acceleration}} \ , \tag{3.3.2}$$

$$\text{where } \overline{\Theta} = \int_{\tilde{z}}^{\infty} \Theta(z')\,\mathrm{d}z' \ . \tag{3.3.3}$$

In equation (3.3.2), u,v,w are the velocity components in the x,y,z-directions, g is the acceleration of gravity, f is the Coriolis parameter, and T_0 is a characteristic temperature. The geostrophic wind in the y-direction is indicated by v_g. With regard to the divergence of the turbulent momentum flux F_u, only the component along the z-axis is considered. Due to the use of the Boussinesq approximation and the tilting of the coordinate system, the original pressure term in the momentum equation transforms into two components: the 'katabatic forcing', proportional to the local temperature perturbation, and the 'thermal wind', set up by horizontal temperature gradients. Note that if $u = v = 0$, equation (3.3.2) reduces to the thermal wind relation (e.g. Gordon, 1998). The thermodynamic equation takes the form

$$\frac{\partial \theta}{\partial t} = \underbrace{-u\frac{\partial \theta}{\partial x} - w\frac{\partial \theta}{\partial z}}_{advection} \quad \underbrace{-\frac{\partial F_\theta}{\partial z}}_{turbulence} \quad \underbrace{-\gamma_\theta(\sin\eta)u - \gamma_\theta(\cos\eta)w}_{\substack{advection\ of\ ambient \\ temperature\ field}} \quad \underbrace{-\frac{1}{\rho c_p}\frac{\partial R_n}{\partial z}}_{radiation} \tag{3.3.4}$$

Because the temperature field has been split into an ambient field and a perturbation, advection of the ambient temperature field by the flow occurs as a separate term. The last term in equation (3.3.4) represents the divergence of the radiative flux.

The relative importance of the various terms in equations (3.3.2) and (3.3.4) can be studied by assuming characteristic numbers for the various quantities. With a horizontal length scale of 10 km, a glacier slope of 5°, a wind speed of 5 m/s and a temperature perturbation of 10 K it is easily verified that the katabatic forcing (~ 0.03 m s^{-2}) is at least an order of magnitude larger than the along-slope advection, Coriolis acceleration and horizontal pressure gradient (thermal wind) in equation (3.3.2). For advection along the z-axis this is not so clear, although we may anticipate that w will be at least an order of magnitude smaller than u. For a steady katabatic wind it thus follows that in the first-order momentum budget there must be a balance between the buoyancy forcing and friction. Similarly, for a sufficiently stable stratification of the ambient atmosphere the term $-\gamma_\theta (\sin\eta)u$ dominates [note that $-(\sin\eta)u$ is the component of the glacier wind along the $\tilde{z}$-axis, i.e. the true vertical motion]. This implies that there is a balance between the turbulent heat flux, cooling the air near the glacier surface, and the heating due to downward motion in a stably stratified atmosphere. A more detailed analysis of the momentum and heat budgets of the glacier wind, based on the data from the Pasterze-experiment, can be found in Van den Broeke (1997b).

Based on the first-order heat and momentum budgets described above, the following equations describe steady state katabatic flow:

$$\frac{g\,(\sin\eta)}{T_0}\theta - \frac{\partial F_u}{\partial z} = 0 \ , \tag{3.3.5}$$

$$-\gamma_\theta (\sin\eta)u - \frac{\partial F_\theta}{\partial z} = 0 \ . \tag{3.3.6}$$

To find a first basic solution to these equations we consider the case where the fluxes of heat and momentum are formulated with simple K-theory:

$$F_u = -K_m \frac{\mathrm{d}u}{\mathrm{d}z} \ , \quad F_\theta = -K_h \frac{\mathrm{d}\theta}{\mathrm{d}z} \ . \tag{3.3.7}$$

Here K_m and K_h are the eddy diffusivities for momentum and heat. By substituting eq. (3.3.7) into eqs. (3.3.5)-(3.3.6) we obtain

$$\frac{g\,(\sin\eta)}{T_0}\theta + \frac{\mathrm{d}}{\mathrm{d}z}\left(K_m \frac{\mathrm{d}u}{\mathrm{d}z}\right) = 0 \ , \tag{3.3.8}$$

$$-\gamma_\theta (\sin\eta)u + \frac{\mathrm{d}}{\mathrm{d}z}\left(K_h \frac{\mathrm{d}\theta}{\mathrm{d}z}\right) = 0 \ . \tag{3.3.9}$$

For convenience we write $s = -\sin\eta \ (>0)$, and we also assume that the eddy diffusivities are constant. The equations then reduce to the set that was already used by Prandtl (1942) to describe thermally induced slope flows, namely:

$$K_m \frac{d^2u}{dz^2} - \frac{gs}{T_0}\theta = 0 \ , \tag{3.3.10}$$

$$K_h \frac{d^2\theta}{dz^2} + \gamma_\theta \, su = 0 \ . \tag{3.3.11}$$

This is a system of homogeneous linear differential equations of 4th order that can be solved for $u(z)$ and $\theta(z)$ by standard methods.

3.4 The Prandtl model for glacier wind

In this section we will look at the solution of eqs. (3.3.10)-(3.3.11) and compare the result with observations fom the Pasterze-experiment.
Since the system is of fourth order, the general solution reads

$$\theta(z) = \sum_{i=1}^{4} a_i \, e^{\lambda_i z} \ , \tag{3.4.1}$$

and similarly for $u(z)$. In eq. (3.4.1), the a_i are complex constants and the λ_i are the complex eigenvalues of the characteristic equation. In the present case we are looking for a single solution that has the smallest "wavenumber" and obeys the following set of boundary conditions:

$$u(z = 0, z \rightarrow \infty) = 0 \ , \tag{3.4.2}$$

$$\theta(z \rightarrow \infty) = 0 \ , \quad \theta(z = 0) = C \ . \tag{3.4.3}$$

Here $C \, (<0)$ is the temperature perturbation at the glacier surface. It is easily verified that the following solution fulfills the boundary conditions:

$$\theta(z) = C \, e^{-z/\lambda} \cos(z/\lambda) \ , \tag{3.4.4}$$

$$u(z) = C\mu \, e^{-z/\lambda} \sin(z/\lambda) \ , \tag{3.4.5}$$

where

$$\lambda = \left(\frac{4T_0 \, K_m \, K_h}{gs^2 \, \gamma_\theta} \right)^{1/4} \ , \tag{3.4.6}$$

$$\mu = \left(\frac{g \, K_h}{T_0 \, K_m \, \gamma_\theta} \right)^{1/2} \ . \tag{3.4.7}$$

The quantity λ thus appears to be the natural length scale of the flow. To plot the solution in non-dimensional form we scale temperature with C and wind speed with μC. The resulting wind and temperature profiles are shown in Figure 3.6. The basic structure of the glacier wind is clearly present in the solution, which is a nice result.

From eq. (3.4.5) we easily derive the height z_m at which the wind maximum occurs:

$$z_m = \frac{\pi}{4}\lambda \ . \tag{3.4.8}$$

The maximum wind speed is

$$u_m = -C\mu e^{-\pi/4}\sin(\pi/4) = -0.322C\mu \ . \tag{3.4.9}$$

Obviously, the height of the wind maximum increases with eddy diffusivities and decreases with the temperature lapse rate and the surface slope, which is in broad agreement with observations. To obtain an order of magnitude for u_m we subsitute some characteristic values into eq. (3.4.7): with $g = 9.8\ \mathrm{ms}^{-2}$, $T_0 = 280\ \mathrm{K}$, $\gamma_\theta = 0.005\ \mathrm{K\,m}^{-1}$, and the turbulent Prandtl number $\mathrm{Pr}(= K_m/K_h)$ equal to unity we find

$$u_m = -0.852C \ . \tag{3.4.10}$$

Note that according to the Prandtl solution the maximum wind speed does not depend on the surface slope. For a temperature deficit of 10 K the model thus predicts $u_m \cong 8.5\ \mathrm{ms}^{-1}$, which is the right order of magnitude (although on the high side). To find the corresponding value of z_m we have to assign values to the surface slope and the eddy diffusivities. With $s = 0.05$ and $K_h = K_m = 0.1\ \mathrm{m}^2\,\mathrm{s}^{-1}$ we find $z_m \approx 8.2\ \mathrm{m}$, which is a reasonable value. The corresponding surface
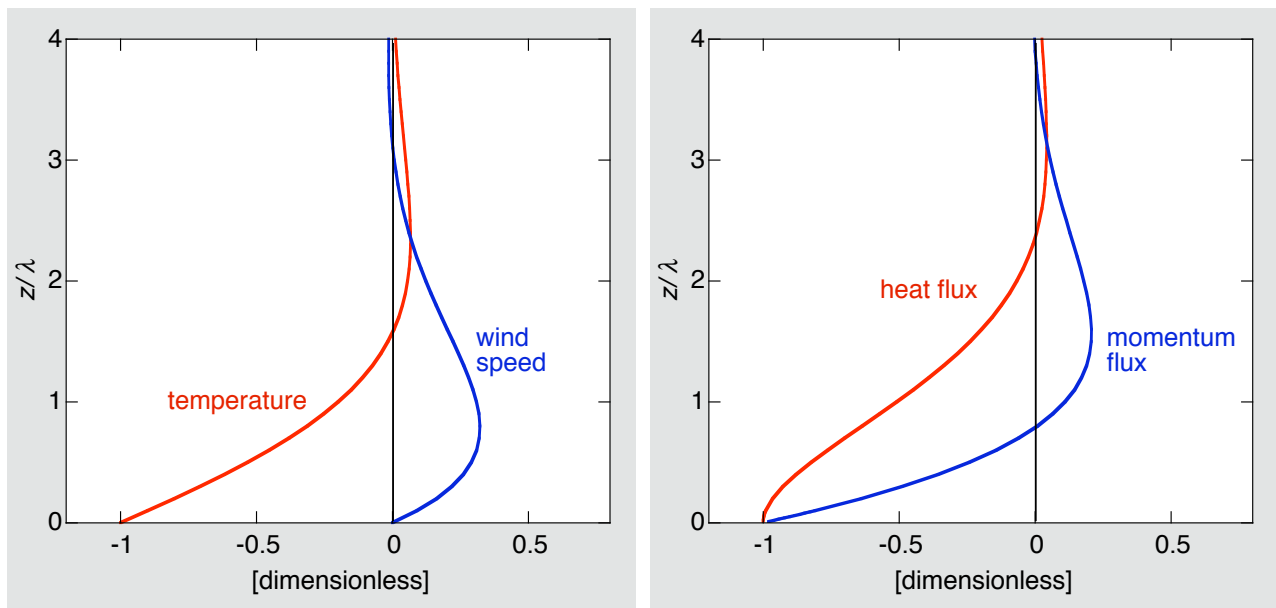

Figure 3.6. The solution of the Prandtl model for the glacier wind, plotted in nondimensional form.

heat flux is about 100 W m^{-2} [note that F_h has to be multiplied by air density and specific heat to obtain the heat flux in W m^{-2}].

It is instructive to consider the profiles of the momentum and heat flux, which are given by:

$$F_u(z) = -K_m \frac{du}{dz} = \frac{\mu C K_m}{\lambda} e^{-z/\lambda} \{\cos(z/\lambda) - \sin(z/\lambda)\} , \qquad (3.4.11)$$

$$F_h(z) = -K_h \frac{d\theta}{dz} = \frac{C K_h}{\lambda} e^{-z/\lambda} \{\cos(z/\lambda) + \sin(z/\lambda)\} . \qquad (3.4.12)$$

The (nondimensional) profiles are shown in Figure 3.6. The (downward) heat flux is largest near the surface and decreases gradually upwards. The momentum flux is downwards (<0) below the jet axis and upwards (>0) above the jet axis.

Although the Prandtl model with constant eddy diffusivities is capable of giving a broad description of the glacier wind, it has some shortcomings which become apparent when we try to match the theoretical profiles with observations (Figure 3.7). As is evident from eq. (3.4.7), for given values of the thermal stratification (γ_θ) and the temperature deficit ($-C$), the strength of the glacier wind is only determined by the eddy Prandtl number Pr. To obtain a reasonable value for u_m, it turns out that Pr has to be of order 10, which is a very large value. The height of the wind maximum is controlled by the product of K_m and K_h. We can use small values for these parameters to bring the wind maximum down and more in line with the observations, but then the modelled temperature profile gets worse. Therefore the fit shown in Figure 3.7 is about the best we can get.

A feature not reproduced by the Prandtl model is the increasing height of the wind maximum when the flow gets stronger (Figure 3.2). A stronger glacier wind due to a larger thermal forcing corresponds to a larger (negative) value of C. However, eq. (3.4.8) shows that z_m does not depend on C. In reality stronger flow has better developed turbulence and the exchange coefficients in the model should be larger. This then would produce a larger value for z_m. In view of this, it is doubtful if the Prandtl model with constant eddy diffusivities predicts the correct relation between temperature forcing and surface heat flux.
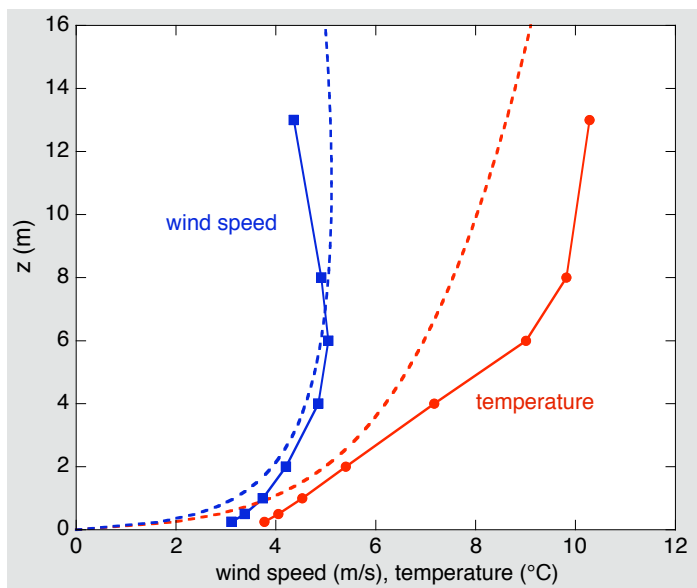

Figure 3.7. A comparison of observed and calculated profiles of wind and temperature. Data (30-minute mean values) are from the Pasterze experiment (29 July 1994, 00 UT). The parameter values are: $\gamma_\theta = 0.004 \ \mathrm{K \, m^{-1}}$. $C = -11 \, \mathrm{K}$, $K_m = 0.1 \, \mathrm{m^2 \, s^{-1}}$, Pr = 10.

3.5 Glacier wind model with height-dependent eddy diffusivity

Various attempts have been made to extend and improve the Prandtl model. Grisogono and Oerlemans (2001, 2002) have used the WKB-method (e.g. Bender and Orszag, 1978) to find a solution for a slowly varying K-profile. It turned out that the following K-profile provides a much better fit to the Pasterze-data than the constant-K model:

$$K(z) = c z e^{-(z/h)^2} .$$

(3.5.1)

Here c and h (a length scale) are constants that can be adjusted to fit the observed temperature and wind profiles (Oerlemans and Grisogono, 2001).

It is obvious that the model with $K(z)$ given by eq. (3.5.1) works better because $K(z)$ goes to zero when the surface is approached. Although the WKB-method can handle several other types of K-profiles, it is more difficult to obtain solutions for more complicated boundary conditions. For instance, it would be interesting to find a solution for the case of valley wind blowing up-glacier, or for a background state varying in time. To achieve this we design a relatively simple numerical model.

We calculate $u(z)$ and $\theta(z)$ as a function of time from

$$\frac{\partial u}{\partial t} = \frac{g(\sin\eta)}{T_0}\theta - \frac{\partial F_u}{\partial z} ,$$

(3.5.2)

$$\frac{\partial \theta}{\partial t} = -\gamma_\theta(\sin\eta)u - \frac{\partial F_\theta}{\partial z} ,$$

(3.5.3)

where, as before,

$$F_u = -K_m \frac{\partial u}{\partial z} , \quad F_\theta = -K_h \frac{\partial \theta}{\partial z} .$$

(3.5.4)

The only difference with the Prandtl model is that we include time dependency and allow K_m and K_h to vary with z (and eventually with t).

The coupled set of equations can be solved with a simple differencing scheme on a staggered grid (Figure 3.8). Since we deal with a parabolic system, forward differencing in time and central differencing in space yields a scheme that is numerically stable (e.g. Hamming, 1987).
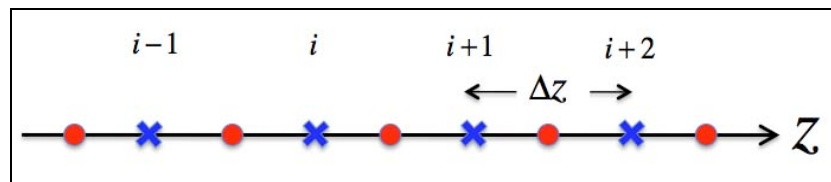

Figure 3.8. A staggered grid used to obtain a numerical solution of eqs. (3.5.2)-(3.5.3). The crosses are the 'true' gridpoints at which the dependent variables $u(z)$ and $\theta(z)$ are calculated. The turbulent fluxes are evaluated at the points in between (red dots).

We use an equidistant grid along the z-axis with gridpoint spacing Δz. Denoting the time step by Δt, the difference equations read (i and q are the discrete variables corresponding to z and t):

$$F_u^{(i+1/2,q)} = -\left(\frac{K_m^{(i+1,q)} + K_m^{(i,q)}}{2}\right)\left(\frac{u^{(i+1,q)} - u^{(i,q)}}{\Delta z}\right) , \tag{3.5.5}$$

$$F_\theta^{(i+1/2,q)} = -\left(\frac{K_h^{(i+1,q)} + K_h^{(i,q)}}{2}\right)\left(\frac{\theta^{(i+1,q)} - \theta^{(i,q)}}{\Delta z}\right) , \tag{3.5.6}$$

$$u^{(i,q+1)} = u^{(i,q)} + \Delta t\left\{\frac{g(\sin\eta)}{T_0}\theta^{(i,q)} - \frac{F_u^{(i+1/2,q)} - F_u^{(i-1/2,q)}}{\Delta z}\right\} , \tag{3.5.7}$$

$$\theta^{(i,q+1)} = \theta^{(i,q)} + \Delta t\left\{-\gamma_\theta(\sin\eta)\,u^{(i,q)} - \frac{F_\theta^{(i+1/2,q)} - F_\theta^{(i-1/2,q)}}{\Delta z}\right\} . \tag{3.5.8}$$

Note that gridpoint and time for a particular quantity are indicated by a superscript in brackets. Because the fluxes are evaluated at the staggered gridpoints it is necessary to average the turbulent exchange coefficiens of the neighbouring gridpoints. This implies some smoothing, of course.

For a *linear* parabolic differential equation with diffusivity D the scheme described above is numerically stable if (e.g. Smith, 1986)

$$\Delta t \le \frac{(\Delta x)^2}{D} . \tag{3.5.9}$$

The set of equations we are dealing with here has variable diffusivities, and the time step should be taken according to

$$\Delta t \le (\Delta x)^2 \min\left(\frac{1}{K_k(z)}, \frac{1}{K_m(z)}\right) . \tag{3.5.9}$$

Next boundary conditions have to be formulated. At the surface ($i = 0$) we set the wind speed to zero and the temperature perturbation to C. At the top of the model domain ($i = N$) the temperature perturbation is zero and the wind speed equal to u_{top}. So we have

$$u^{(0)} = 0,\ u^{(N)} = u_{top},\ \theta^{(0)} = C,\ \theta^{(N)} = 0 . \tag{3.5.10}$$

In view of the simple differencing scheme the coding of the model is straightforward.

A basic test of the numerical model is to see if it accurately reproduces the analytical solution for constant diffusivities. Figure 3.9 shows the result of a calculation with an initial state defined by $u(z) = 0$ and $\theta(z) = 0$. Profiles are shown after 30 minutes and 2 hours of integration. It is obvious that the steady-state Prandtl solution is approached very quickly. After two more hours the Prandtl and numerical solutions are virtually indistinguishable.
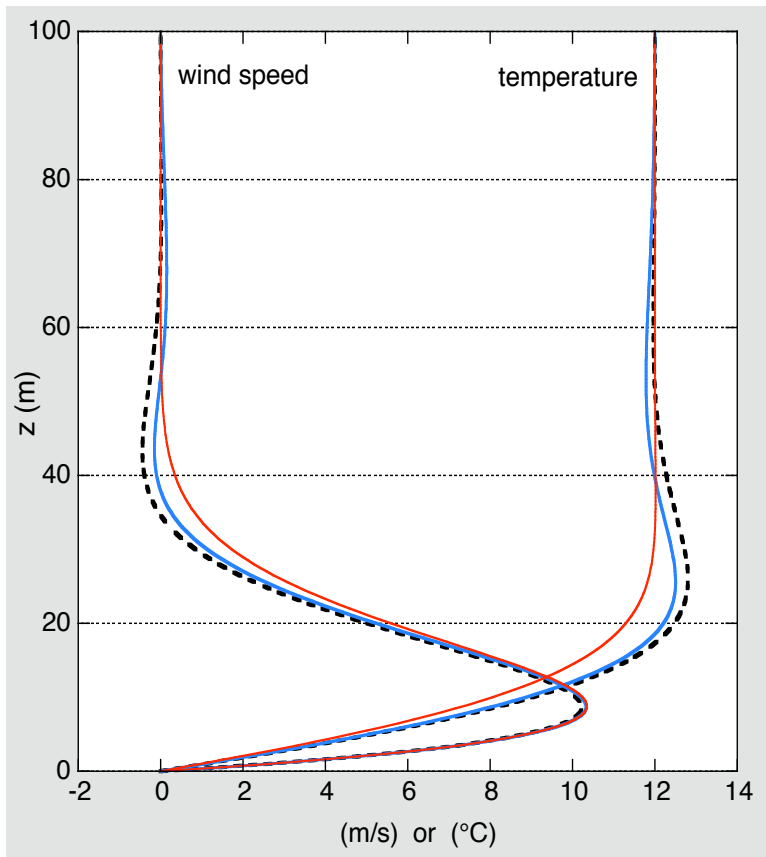
Figure 3.9. The numerical solution after 30 minutes (red) and 2 hours (blue) compared to the steady-state Prandtl solution (dashed). The grid resolution (Δz) is 0.5 m.

Parameter values:

$K_m = K_h = 0.07 \, \text{m}^2 \, \text{s}^{-1}$,

$\gamma_\theta = 0.005 \, \text{K} \, \text{m}^{-1}$,

$\eta = -5°$,

$C = -12 \, °\text{C}$,

$T_0 = 280 \, \text{K}$.

In many boundary-layer models the process of turbulent mixing is dealt with by introducing a 'closure model' to parameterize the Reynolds stresses (which arise from decomposition of the dynamic equations in a time-mean and time-varying part, e.g. Garratt, 1992). Several closure models have been introduced (e.g. Yamada, 1983; Duynkerke, 1988; Denby, 1999), and these models are all local in the sense that parameterizations of the various terms in the higher-order equations make use of local variables like wind shear, stability and turbulent kinetic energy. Since katabatic flows have a distinct wind maximum, mechanical production of turbulent kinetic energy ceases at some height above the surface and transport terms in the turbulent kinetic energy equation have to be included. A survey of the literature on modelling of katabatic flows reveals that there is no concensus about which model works best. Therefore a more heuristic approach, in which the height-dependence of the eddy diffusivity is prescribed, remains an attractive alternative.

In the atmosphere over glaciers there are basically two sources of turbulence: (i) turbulence generated by the katabatic flow, and (ii) turbulence in the layer above the katabatic jet advected by the mesoscale or large-scale circulation. Especially during daytime the valley wind advects warm turbulent air over the glacier. Also, heating or cooling of the valley walls leads to upslope or downslope winds which generate a cross-valley circulation and associated turbulence. Then, the large-scale circulation generates turbulence at the mountain crests, associated with breaking gravity waves and related phenomena. Altogether the picture is fairly complex and it is not so clear that a formulation like eq. (3.5.1) is the best choice.

We first investigate what kind of results can be obtained with a very simple formulation of the K-profile, given by:

$$K(z) = 1 - \exp\left[-(z+\delta)/p\lambda\right] , \tag{3.5.11}$$

$$K_m(z) = k_m K(z) , \quad K_h(z) = k_h K(z) \tag{3.5.12}$$

This formulation implies that the turbulent Prandtl number is independent of z. Since the only intrinsic length scale of the katabatic system is λ, see eq. (3.4.6), it is natural to let λ play a role. With the parameter p the K-profile can be adjusted. It turns out that the height of the wind maximum is to a large extent determined by the value of p, which will therefore be used as a tuning parameter. Obviously, eq. (3.5.11) ignores the fine-scale structure around the katabatic jet, but for the moment we assume that this is not needed for a simulation of the wind and temperature profiles. In eq. (3.5.11), a (small) quantity δ has been introduced to avoid a singularity in the diffusion equations at $z = 0$. In view of eq. (3.5.9), a zero diffusivity at the boundary of the domain may generate numerical instability.

It is not difficult to find model parameters that generate realistic profiles of temperature and windspeed (Figure 3.10). Although a detailed inspection of the data points reveals that the simulated gradients are still too small very close to the surface, the overall agreement with the observations is good. An interesting result is that a good match with the observational data cannot be achieved with a turbulent Prandtl number of unity. For the fit shown in Figure 3.10 the turbulent Prandtl number is about 1.7.
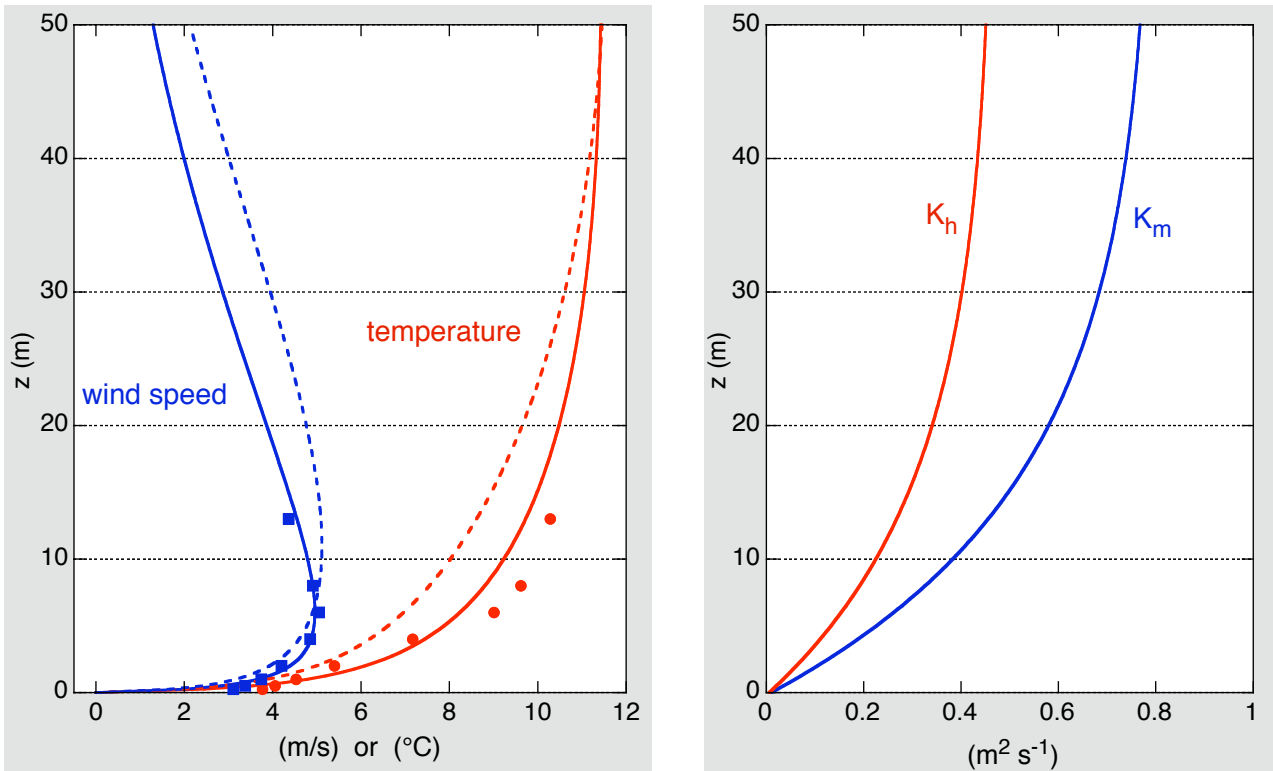
Fig 3.10. The numerical solution of the katabatic wind model compared to observations from the Pasterze experiment (29 July 1994, 00 UT). The Prandtl solution for constant eddy diffusivity is shown by dashed lines. Model parameters: $k_m = 0.80 \, \text{m}^2 \, \text{s}^{-1}$, $k_h = 0.47 \, \text{m}^2 \, \text{s}^{-1}$, $\delta = 0.2 \, \text{m}$, $p = 0.5$, $\gamma_\theta = 0.004 \, \text{K m}^{-1}$, $\eta = -5°$, $C = -11°\text{C}$, $T_0 = 280 \, \text{K}$, $\Delta z = 0.25 \, \text{m}$.

With respect to the temperature profile, some discrepancy between simulation and observations is still evident. In the first five meters above the surface, the observed temperature profile is fairly linear. According to Figure 3.1 this is a rather general feature. Several attempts were made to find out if a more accurate temperature profile could be simulated with different K-profiles, but this did not work. More generally speaking, from the available observational data it cannot be demonstrated that a more sophisticated formulation of the K-profile than the one described by eq. (3.5.11) is useful.

Tuning the model revealed that the value of p in eq. (3.5.11) should be smaller than one. The value of p determines to a large extent the height of the wind maximum. When p is too large the wind maximum is lower than observed. This result suggests that most of the turbulence is generated in the shear layer just below the katabatic jet.

3.6 Further calculations with the numerical glacier wind model

A question of particular interest is how the sensible heat flux at the glacier surface $F_{\theta,s}$ depends on the temperature deficit $(-C)$. As shown in Figure 3.11, the numerical model predicts a linear relation between $-C$ and $F_{\theta,s}$ (as does the Prandtl model). However, this result should be considered with caution because the turbulent exchange coefficients are assumed to be independent of the flow. In the case of katabatic flow this is probably a poor representation of what actually happens. Turbulence is generated by the shallow katabatic layer flowing over a relatively bumpy surface (Figure 1.3). A possible approach is to assume that the relevant length and velocity scales are the characteristic obstacle height λ_{obs} and the intrinsic velocity scale as defined by eq. (3.4.9). We therefore write:
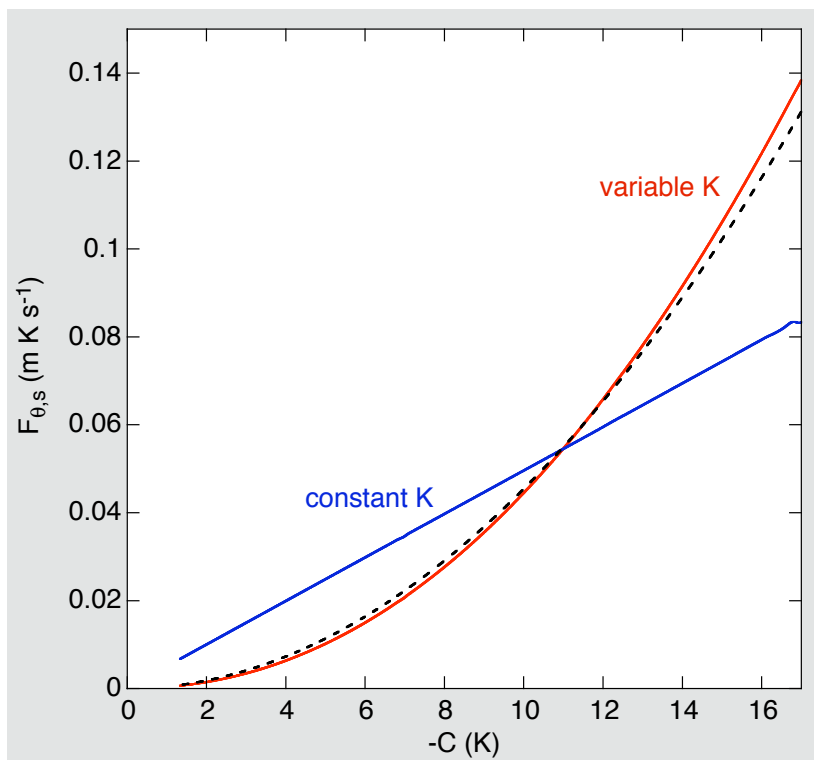

Figure 3.11. Blue line: the relation between the surface temperature deficit (-C) and the surface heat flux ($F_{\theta,s}$). Parameter values as in Figure 3.10.
Red line: The surface heat flux for the model in which the turbulent exchange coefficients depends on the strength of the katabatic flow.
Dashed line: The result from the scaling analysis of Oerlemans and Grisogono (2002).

$$k_m = c_m \lambda_{obs} u_m \ , \ k_h = c_h \lambda_{obs} u_m \ , \tag{3.6.1}$$

where c_m and c_h are appropriate constants. By using k_m and k_h in the expression for the intrinsic length scale, the K-profile also depends implicitly on the strength of the katabatic flow, i.e.

$$K(z) = 1 - \exp\left[-(z + \delta)/p\lambda\right] \ , \text{ where} \tag{3.6.2}$$

$$\lambda = \left(\frac{4T_0 \, k_m \, k_h \, K_\infty^2}{g s^2 \, \gamma_\theta}\right)^{1/4} . \tag{3.6.3}$$

K_∞ denotes the asymptotic value of $K(z \to \infty)$, which equals unity.

With this formulation of the turbulent exchange coefficients the flow depends on $-C$ in a different way. The height of the wind maximum (z_m) now increases with $-C$ (note that for the simple Prandtl model z_m is independent of C). At the same time the strength of the wind maximum increases nonlinearly with $-C$, as illustrated in Figure 3.12. The relation between height and strength of the wind maximum is in qualitative agreement with the observations shown in Figures 3.1 and 3.2, and with the data in Table 3.1. The surface heat flux now increases nonlinearly with $-C$ (Figure 3.11). The physical interpretation of this result is straightforward: a larger surface heat flux leads to a stronger density perturbation and accelerates the flow, which in turn leads to larger eddy diffusivities enhancing the heat flux. This positive feedback results in a 'heatpump' that increases the sensitivity of the ablation rate to the ambient air temperature.
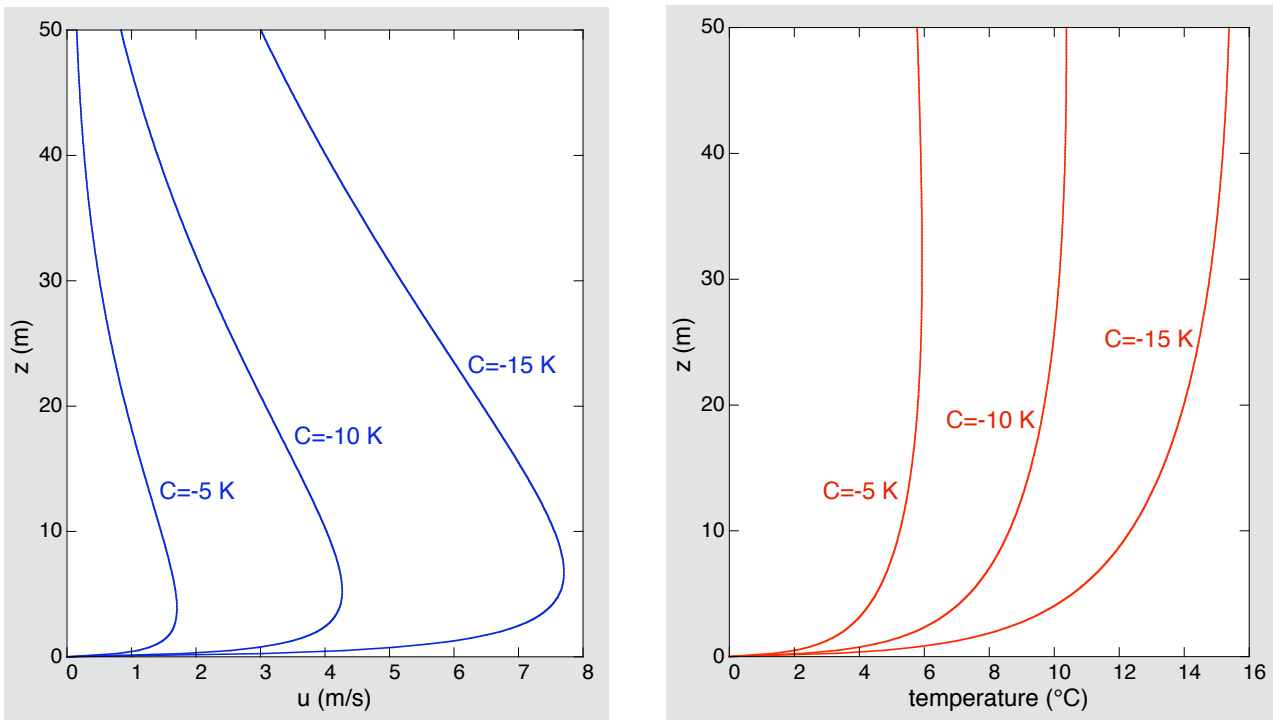

Figure 3.12. Downslope velocity and temperature profiles as calculated with the numerical katabatic flow model with flow-dependent eddy diffusivities. Parameter values as in Figure 3.10, and $c_m = 0.072$ and $c_h = 0.043$ (for $C = -11$ K this gives the same result as the model with flow-independent diffusivities).

It should be noted that the result found here is very similar to that of a scaling analysis of the Prandtl-model in which the eddy diffusivity is also related to the strength of the katabatic flow (Oerlemans and Grisogono, 2002). They found:

$$F_{\theta,s} = k\,C^2 \sqrt{\frac{g}{T_0\,\gamma_\theta\,\mathrm{Pr}}} \quad , \qquad\qquad\qquad (3.6.4)$$

where k is a dimensionless constant. The heat flux according to eq. (3.4.12) is also plotted in Figure 3.11. The constant k was chosen in such a way that the heat flux for $C = -11\,\mathrm{K}$ equals the result from the numerical model.

The numerical model can be used to perform a whole series of calculations for different boundary conditions and parameter values. It is also straightforward to include the Coriolis acceleration and study katabatic flows on a larger scale like those found on medium-size ice caps or in the ablation zone of the Greenland ice sheet. However, it should be remembered that advection of u and θ is assumed to be negligible.

To conclude this section a few results are shown for different values of the slope and the ambient potential temperature lapse rate. In all cases $C = -10\,\mathrm{K}$. Figure 3.13a shows that for an increasing slope the glacier wind becomes shallower and the height of the wind maximum decreases. At the same time the maximum wind speed increases slightly, in spite of the fact that the buoyancy forcing is proportional to the sine of the slope. Here the compensating effect is the more efficient downward heat advection because the flow has a larger vertical component (it should be noted that in the original Prandtl model with constant eddy diffusivities the maximum wind speed does not depend on the slope at all).
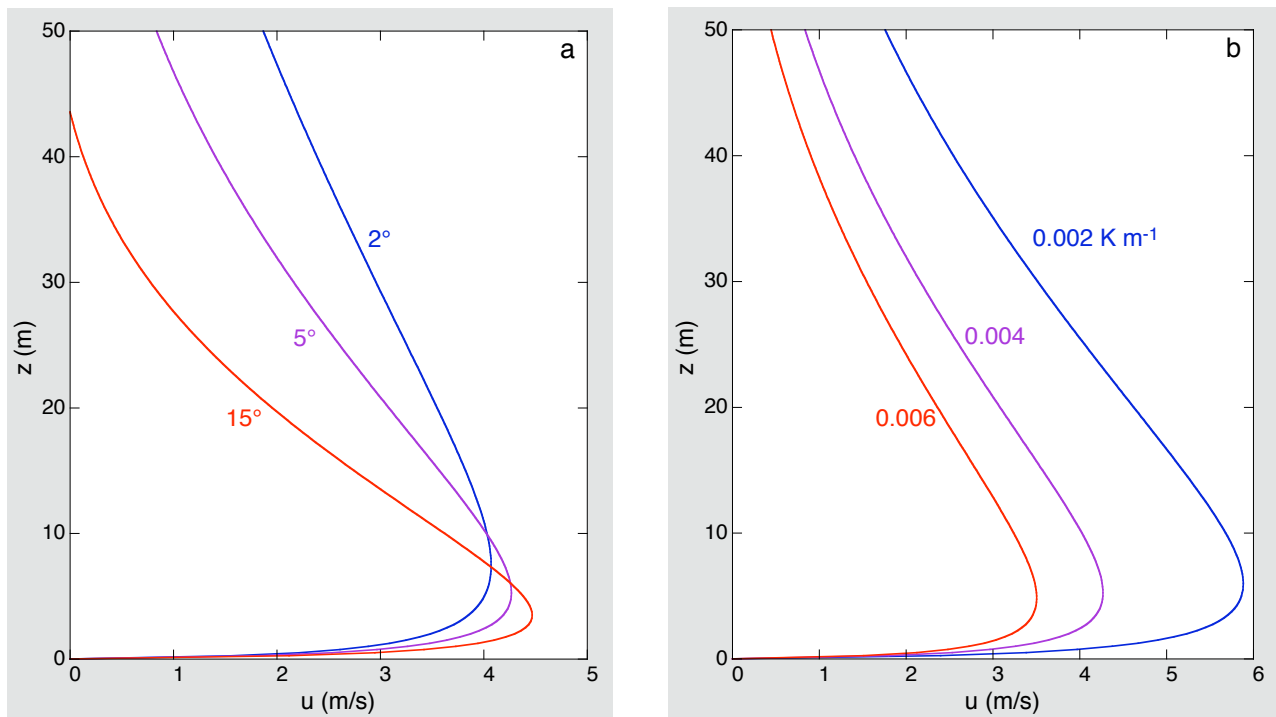

Figure 3.13. The structure of the glacier wind for different values of the slope (a) and the atmospheric stability (b). Note the difference in horizontal scale.

The role of the atmospheric stratification γ_θ is illustrated in Figure 3.13b. The maximum wind speed increases strongly with decreasing γ_θ, which is also obvious from eqs. (3.4.7)-(3.4.9).

3.7 Validation and implications for parameterization of the surface heat flux

The results described in the previous section all seem plausible, but it is very hard to get a sound experimental verification. Even the most detailed field experiments carried out to date do not deliver all the input parameters with a sufficient accuracy. Additionally, the direct measurement of the surface heat flux over a melting glacier surface by eddy-correlation techniques remains challenging (e.g. Munro, 1989; Smeets et al., 1998). A fundamental problem is the rapid variation of the heat flux with height just above the glacier surface. In contrast to boundary layers that are driven by a large-scale pressure gradient that depends only weakly on height, the glacier wind has no constant flux layer (or it is very thin, i.e. has a thickness comparable to the obstacle height). The application of standard boundary layer theory, in which the mechanics and thermodynamics of the flow are essentially decoupled, is therefore limited.

In many field studies the turbulent surface fluxes have been calculated with the bulk method (e.g. Denby and Greuell, 2000; Oerlemans and Grisogono, 2002; Smeets and Van den Broeke, 2008). The expressions normally used are

$$H_s = \rho c_p C_s u(T - T_s) , \tag{3.7.1}$$

$$H_l = \rho L_v C_l u(q - q_s) , \tag{3.7.2}$$

$$H_m = \rho C_m u^2 . \tag{3.7.3}$$

Here H_s, H_l, and H_m are the surface fluxes of sensible heat, latent heat and momentum, respectively. The corresponding nondimensional transfer coefficients are C_s, C_l and C_m (the latter is also referred to as drag coefficient). Furthermore, ρ is air density, c_p is the specific heat, L_v the latent heat of vapourisation, u the wind speed, T the air temperature, T_s the surface temperature, q the specific humidity, and q_s the surface specific humidity. The transfer coefficients depend on the height at which u, T and q are measured! Note that the sensible heat flux H_s differs from the sensible heat flux F_s as defined earlier by a factor ρc_p (and similar for the other fluxes).

When evaluating fluxes from AWS data, it is general practice to apply Monin-Obukhov theory to take into account the effect of stratification. However, there is evidence that the stability correction has to be limited because otherwise the fluxes are underestimated in the case of a well developed glacier wind (Van den Broeke et al., 2005). Calculating the fluxes from eqs. (3.6.1)-(3.6.3) with observed temperature and wind speed implies that the correlation between ambient temperature and wind speed is included implicitly. In fact, it is impossible to use fluxes calculated in this way to verify the relation between *ambient* temperature and surface heat flux (Figure 3.11), because the relation between the ambient temperature and the temperature at a certain height above the surface depends on the flow itself. Altogether, it is obvious that the evaluation of the surface fluxes from AWS data and the parameterization of the fluxes for use in a mass balance model are different issues. Mass balance models for valley glaciers are driven by data from nearby weather stations, or by output from climate models. In both cases it is inappropriate to use the available wind data as

input, because then the presence of the glacier wind is not taken into account. A possible pragmatic approach suggested by the theory discussed above is to parameterize the turbulent fluxes as

$$H_s = \rho c_p C^* (T_a - T_s) \; , \tag{3.7.4}$$

$$H_l = \rho L_v C^* (q_a - q_s) \; , \tag{3.7.5}$$

where

$$C^* = C_b + C_{kat} = C_b + k(T_a - T_s)\sqrt{\frac{g}{T_0 \, \gamma_\theta \, \mathrm{Pr}}} \quad \text{for} \quad T_a - T_s > 0 \; , \tag{3.7.6}$$

$$C^* = C_b \quad \text{for} \quad T_a - T_s \leq 0 \; . \tag{3.7.7}$$

There are two contributions to the turbulent exchange coefficient (denoted now by C^*, taken equal for the latent and sensible heat flux). C_b represents a 'background contribution' associated with the turbulence generated by the atmospheric circulation on a synoptic/regional scale, and C_{kat} represents the contribution from the katabatic wind system as formulated by eq. (3.4.16). This approach was used by Klok and Oerlemans (2002) in a mass balance modelling study for the Vadret da Morteratsch. The parameterisation appeared to work well, although it is hard to demonstrate that it is superior over an approach in which the turbulent exchange coefficient is simply constant.
Figure 3.14 shows an example of the relation between the surface heat flux and the ambient atmospheric temperature for the parameterisation described above. The parameter values used are:

$$C_b = 0.003 \, , \quad k\sqrt{\frac{g}{T_0 \, \gamma_\theta \, \mathrm{Pr}}} = 0.0002 \, \mathrm{K}^{-1} \tag{3.6.8}$$
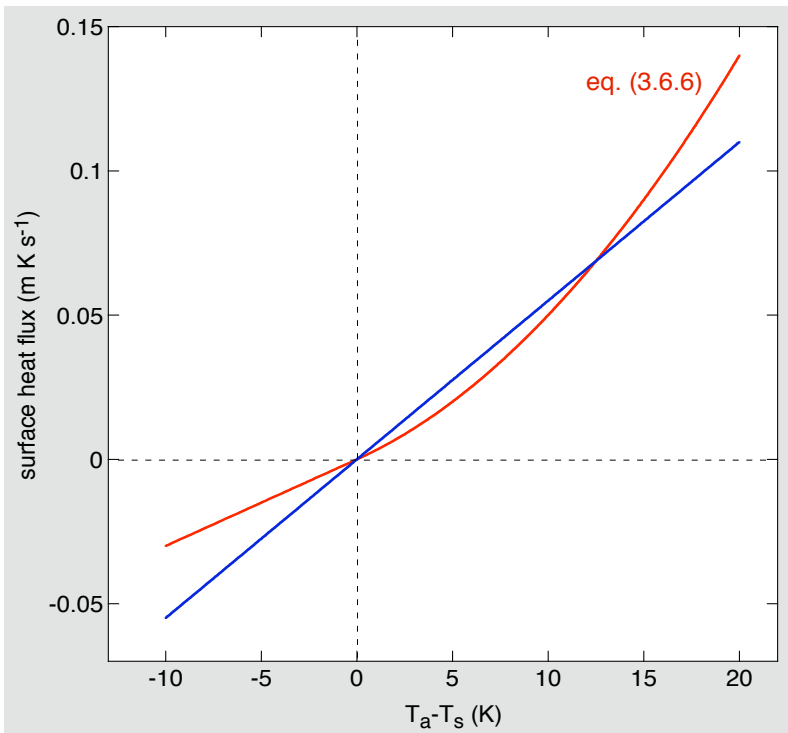
Figure 3.14. Sensible heat flux [$F_s = H_s/(\rho c_p)$] at the glacier surface as parameterised by eqs. (3.7.4)-(3.7.7).

For comparison, the heat flux for a constant turbulent exchange coefficient is also shown. In general it is not difficult to obtain overall agreement between measured melt and melt calculated from the surface energy flux by adjusting the turbulent exchange coefficients. This applies to the simple approach as well as to the use of eq. (3.7.6). With regard to the climate sensitivity of glacier mass balance there is a fundamental difference, of course. The 'heat pump effect' as expressed by eq. (3.7.6) makes the net balance of a glacier more sensitive to temperature change. This point will be taken up again in the chapter on simple mass balance models.

Dirty ice with an albedo of about 0.28 (photo by Irina Gorodetskaya).

4. The surface albedo of glaciers

4.1 Introduction

Many studies have shown that solar radiation makes a large contribution to the surface energy flux when melting occurs. In most cases this contribution is even larger than that of the turbulent heat flux, which makes the surface albedo a particular important quantity deserving a great deal of attention. The albedo of a glacier depends in a complicated way on crystal structure, surface morphology, dust and soot concentrations, morainic material, the presence of liquid water in veins and at the surface, solar elevation, cloudiness, etc. (e.g. Takeuchi, 2002; Brock, 2004). It appears to be a fairly hopeless task to quantify and model all these factors, but maybe the most important can be captured by looking carefully at the data available.

The definition of albedo is based on the concept of irradiance, i.e. the total energy flux coming in through a hemisphere. The albedo is then defined as

$$\alpha = \int_{solspec} \frac{S^{\uparrow}}{S^{\downarrow}} \, , \tag{4.1.1}$$

where $S^{\uparrow}$ and $S^{\downarrow}$ refer to solar radiation received by a downward-facing sensor and an upward-facing sensor, respectively. The radiative flux is integrated over the entire solar spectrum. In the case that the fluxes are integrated over specific wavelength bands, it is common practice to speak about 'band albedos'. The albedo as defined in eq. (4.1.1) is frequently referred to as 'broadband albedo'. Satellite instruments normally measure radiances in certain spectral channels, from which band albedos can in principle be obtained. Band albedos are of interest because the comparison of reflectance for different wavelengths contains information about the nature of the reflecting surface.

When the instrument is not too far above the surface, the radiation received by the downward-facing sensor is actually the radiation reflected by the surface, and the contribution related to scattering in the layer of air between instrument and surface can normally be neglected. Only during foggy conditions we can expect a significant contribution from cloud droplets in the air just above the surface.

The reflection of solar radiation by the glacier surface is the outcome of a complicated scattering process in the upper layers of the glacier. The theory of radiative transfer in scattering media is well developed (e.g. Liou, 1980; Mishchenko, 2008). For an application like modelling the surface albedo of a glacier, the problem is the specification of the input parameters (concentration and geometric properties of impurities, spacing and size of air bubbles, and, when snow is considered, all the information needed to characterize the structure of the snow).

Especially when the ice is clean, solar radiation can penetrate to an appreciable depth. However, this depends very much on the wavelength. It is instructive to consider the outcome of some calculations with a radiative transfer model for the upper layer of a glacier. Figure 4.1a shows the net radiative flux as a function of depth in clean ice, for blue light and averaged over the entire solar spectrum ('broadband'). The fluxes have been normalized with the surface values. The curves are based on a calculation with a radiative transfer model (P. Kuipers Munneke, personal communication). The net flux for blue light decreases much slower with depth than for other colours, which explains why the ice in a glacier cave, or in a crevasse, appears to be blue.

With respect to thermodynamic processes in the upper layers of a glacier, the divergence of the radiative flux (div S) is the important quantity. It represents absorption of energy, which is either used to increase the ice temperature or to cause internal melting (e.g. Van den Broeke et al., 2008). Figure 4.1b shows div S as a function of depth in snow and ice (broadband). In this calculation the net solar flux at the surface was equal to 147 W m^{-2}. It is evident that most of the solar energy is absorbed in the upper centimeter of a snowpack, and in the upper few cm of an ice surface. For many applications it is therefore justified to treat the glacier surface as a simple reflecting surface as far as solar radiation is concerned.
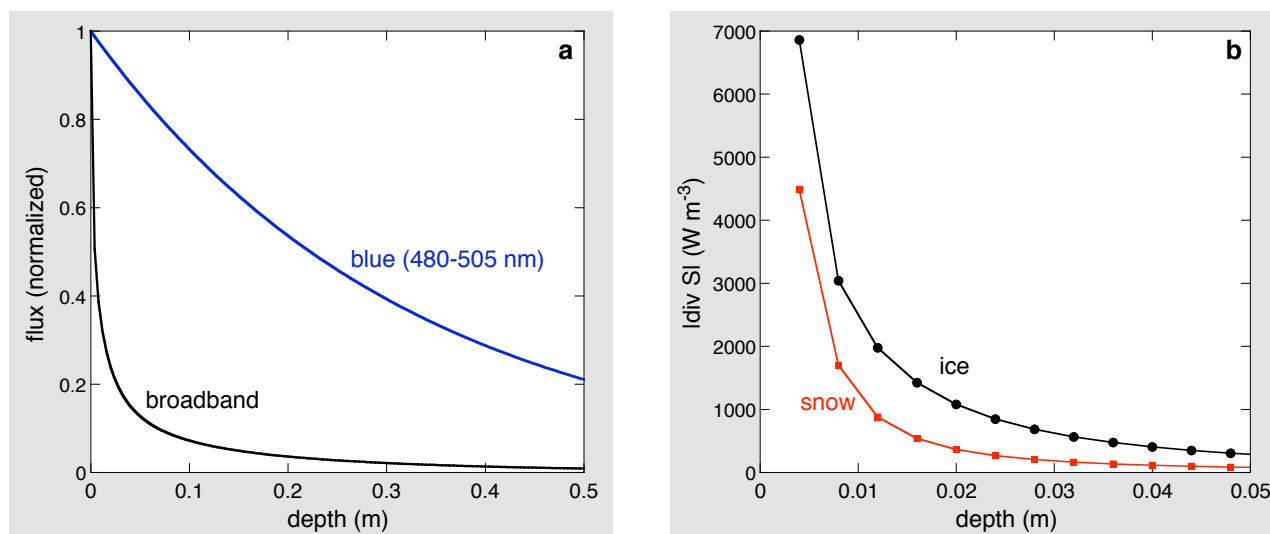

Figure 4.1. (a) Net solar radiative flux as a function of depth (normalized with the value at the surface). (b) Divergence of the broadband flux for snow and ice (P. Kuipers Munneke, personal communication).

4.2 Measurements from automatic weather stations

Figure 4.2 shows scatter plots of incoming versus reflected solar radiation for two-year periods as measured on Midtdalsbreen, Norway, and Vadret da Morteratsch, Switzerland.

There is a clear grouping in the diagram and characteristic albedos for snow/firn and ice are emerging. Occasionally albedo values >1 occur (points located in the upper triangle). Closer inspection of the data in relation to the snow depth records shows that this happens during snowfall and is the result of snow flakes sticking on the upward looking sensor whereas the downward looking sensor remains free of snow.

Figure 4.2 also shows that the snow albedo tends to decrease for larger values of the incoming radiation. This mainly concerns data points from late spring/early summer, when incoming radiation is large, air temperatures are high and snowfall rarely occurs. The snow structure has now been transformed into large grains and there is normally some accumulation of dust on the surface.
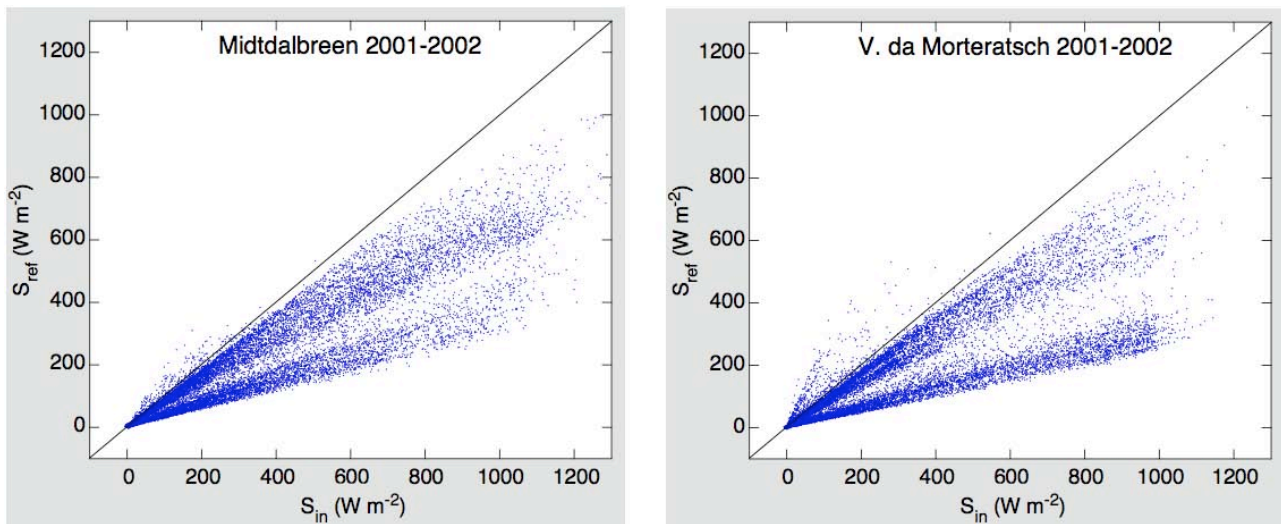
Figure 4.2. Scatter plots of incoming versus reflected solar radiation for two years from the AWS on Midtdalsbreen, Norway, and on the Vadret da Morteratsch, Switzerland. Every point represents a 30-min average.

On most days albedo shows short-term variations. A detailed study by Brock (2004) has revealed that such variations are first of all related to fluctuations in cloud cover, whereas solar elevation and changes in the concentration of fine debris on the glacier surface turned out to be of secondary importance. It is not appropriate to use data from *automatic* weather stations for the analysis of short-term (<1 day) albedo variability. Since these stations are not guarded, there are too many uncertain factors (varying tilt of sensors, riming, snow drift, no manual cloud observations). As concluded by Brock (2004), short-term variations in albedo are probably not so relevant for the energy budget of a glacier.

We will now consider daily albedos. Firstly, daily albedo α_d is defined as the ratio of the daily amount of reflected solar radiation to the daily global radiation:

$$\alpha_d = \int_{day} S^{\uparrow} / \int_{day} S^{\downarrow} \tag{4.2.1}$$
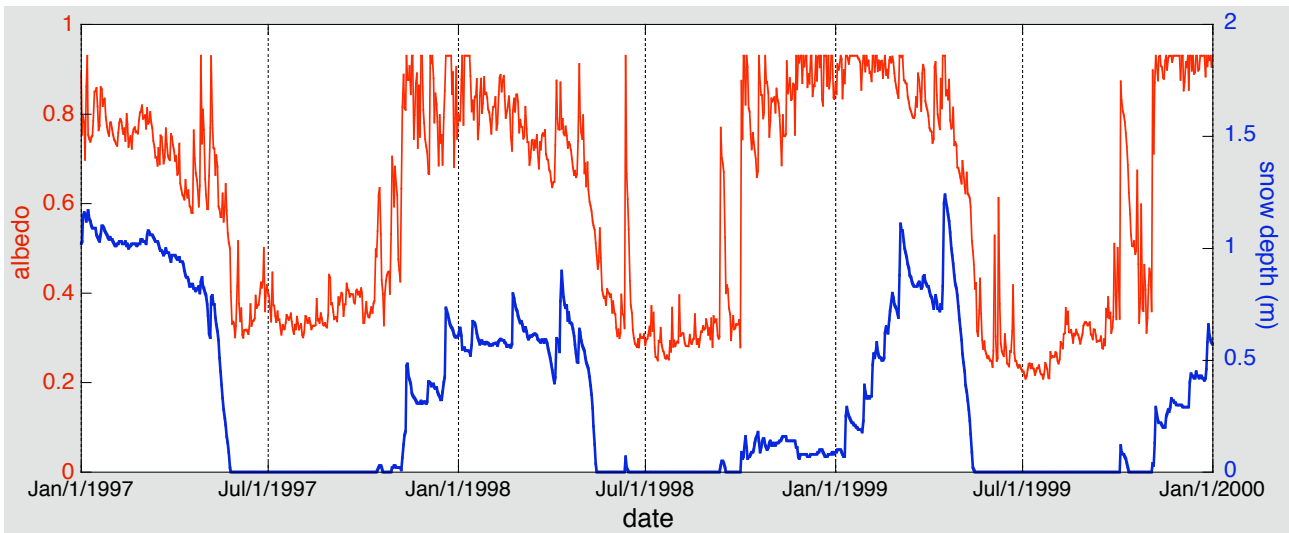
Figure 4.3. A 3 year record of daily albedo (red) and snow depth (blue) from the AWS on the Vadret da Morteratsch. An upper limit of 0.95 has been imposed on the albedo.

Note that this differs from the daily mean albedo, which is the mean of all instantaneously determined albedo values during daylight. However, this quantity may be influenced greatly by measuring errors when the sun is very low. In view of this, daily mean albedo is not a very useful quantity in analysing measurements.

Figure 4.3 shows daily albedos from the Vadret da Morteratsch AWS for a 3 year period. Also shown is the snow depth as measured by the acoustic sensor. In the albedo record the switch from winter conditions to summer conditions is very obvious, and there can be no doubt that the presence or absence of snow is the most important factor in determining albedo variations on a time scale of days and longer.

Figure 4.4. Snow with a low albedo due to accumulation of dust and growth of algae, which significantly accelerates the disappearance of the snowpack.

The picture shows the AWS on Storbreen, Norway, July 2008. Photo by Liss Andreassen.

4 - The surface albedo of glaciers

The snow albedo is by no means constant. Aging of the snow and the related change in crystal structure normally leads to a decline of the albedo by typically 0.1 to 0.2 in a couple of days. In springtime when the snow melts the accumulation of impurities and the growth of algae causes a further lowering of the snow albedo (Figure 4.4).

The ice albedo also shows large variations on time scales from days to years. Weathering crusts with a relatively high albedo form during dry and sunny conditions, when there is a lot of internal melt (i.e. below the surface). Variations in the concentrations of mineral dust and of humic material, being the residue of bacterial decomposition of organic matter (Takeuchi, 2002), also contribute to albedo variability. Figure 4.5 shows daily albedo as measured by the Morteratsch AWS for 11 years. The curves shown are for the period May-October, when the glacier surface consists of ice for most of the time. First of all it is clear that summer snowfalls create peaks in the albedo that typically last for a few days. A particularly strong snowfall occurred in July 2000, and the implications of this event will be discussed later.

During the period 1996 – 2006 the ice albedo on the snout of the Vadret da Morteratsch decreased significantly. This is mainly due to the accumulation of dust and humic material, and it has been shown that the reduced ice albedo enhances the summer ablation in a systematic way (Oerlemans et al., 2009). For retreating glaciers, the darkening of the glacier snout due to accumulation of dust is rule rather than exception (e.g. Paul et al., 2005). Exposed side moraines form a large source of unconsolidated material that is easily taken up by the wind and deposited elsewhere. Altogether, this process can be regarded as a positive feedback mechanism that makes valley glaciers more sensitive to climate warming.

In mass balance models the parameterisation of the albedo is an important element, and it is not so clear what level of complexity is justified in view of all the other uncertainties. Certainly, a basic model should deal with the transition from snow to ice and reversed. The simplest possible model should thus have two values for the surface albedo, according to:

$$\alpha = \alpha_{snow} \qquad \text{if snowdepth} > 0$$

(4.2.2)

$$\alpha = \alpha_{ice} \qquad \text{if snowdepth} = 0$$
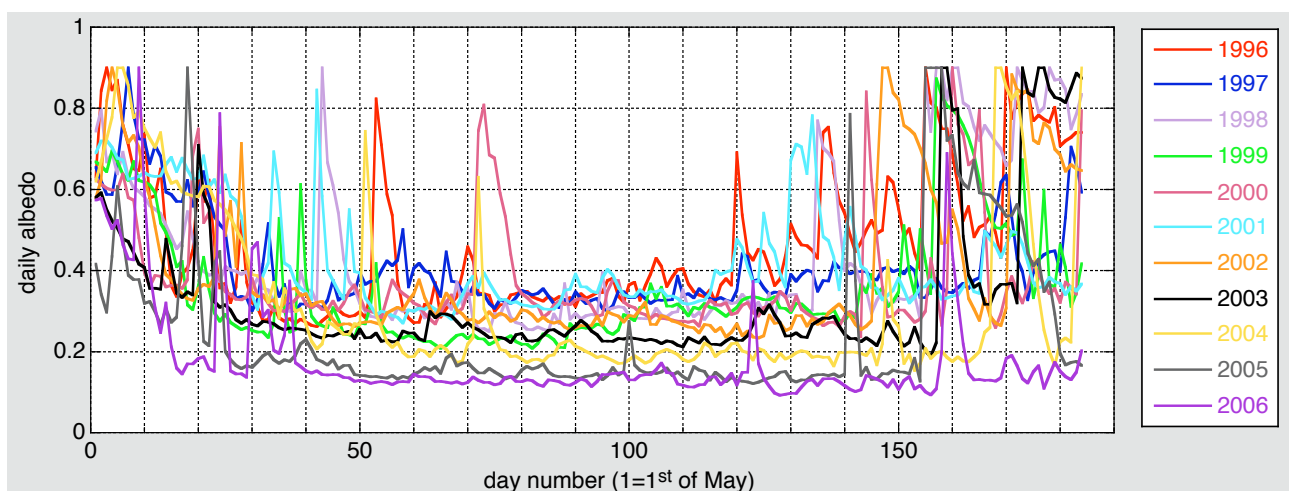
Figure 4.5. Summertime albedo for different years as measured by the AWS on the Vadret da Morteratsch. All curves start on the first of May.

In a later chapter we will test this scheme in a simple mass balance calculation. A slightly more sophisticated model would take the aging of the snow into account, but this requires information on the snowfall record. In the following section this is investigated for a 1 year record from the Morteratsch AWS.

4.3 A simple albedo model

The analaysis described here is based on Oerlemans and Knap (1998). The data used are from the Morteratsch AWS for the period 1 October 1995 – 30 September 1996, and the radiation data were corrected for the (small) tilt of the instrument.

Figure 4.6. Illustration of the simple albedo model. The upper panel shows global radiation and the extra-terrestrial irradiance (in red). The second panel shows snowfall events as derived from the sonic altimeter measurements. The snow depth is plotted in the third panel. A comparison between the observed (blue) and modelled albedo (red) is shown in the lower panel.

4 - The surface albedo of glaciers

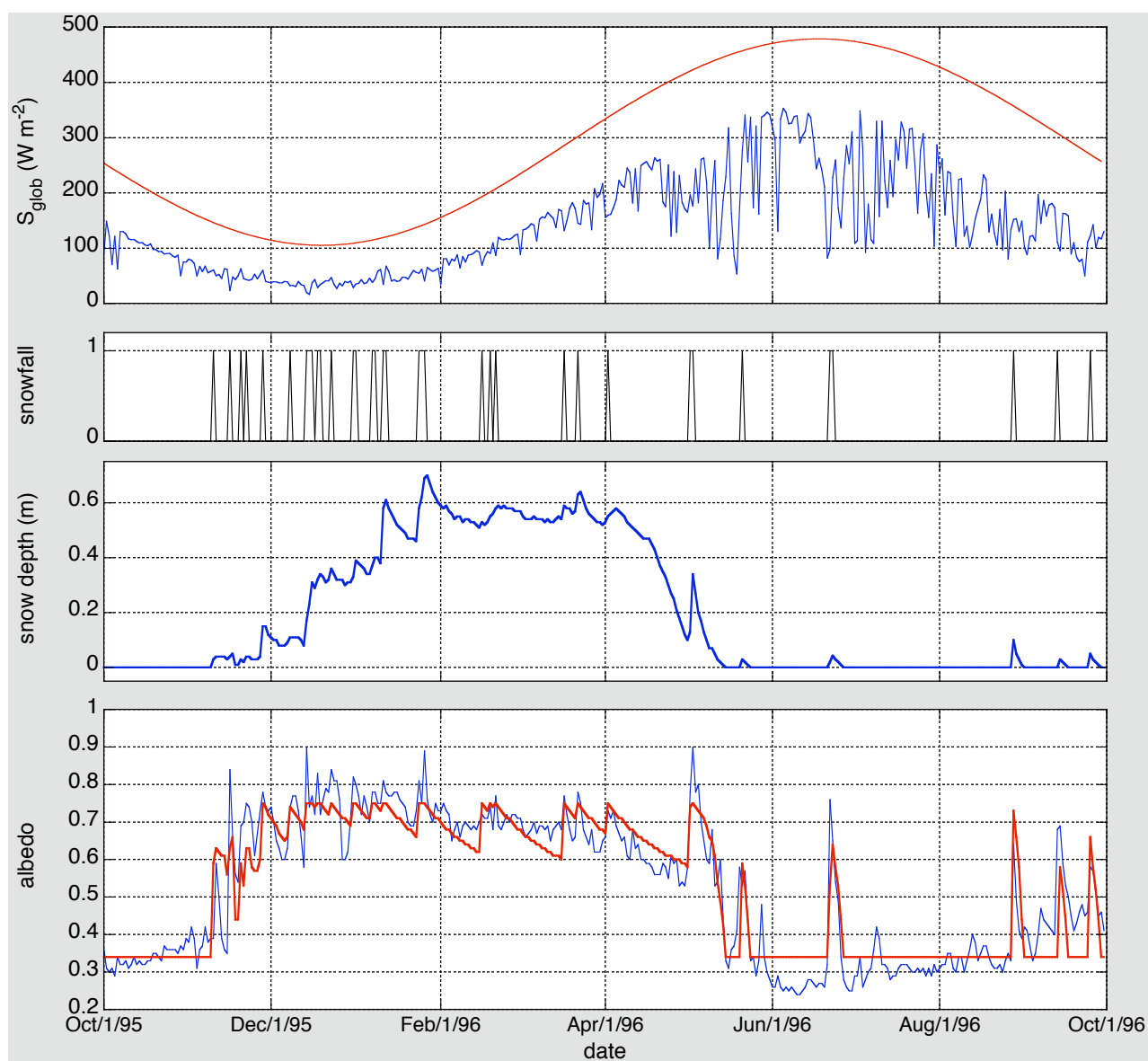The model, described shortly, has five parameters for which best values are determined by minimizing the root-mean-square difference (σ) between observed and simulated daily albedos. The 366 albedo values and the snow depth record serve as input (Figure 4.6).

First of all the albedo of the snow-covered glacier site at day j depends on the age of the snow at the surface, so

$$\alpha_{snow}(j) = \alpha_{firn} + [\alpha_{frsno} - \alpha_{firn}(j)]\ \exp\{-(J-j)/\tau*\} \qquad (4.3.1)$$

This expression introduces three parameters: a characteristic albedo for firn (α_{firn}), for fresh snow (α_{frsno}) and a time scale $\tau*$ determining how fast the snow albedo approaches the firn albedo after a snowfall. In this equation J is the number of the day on which the last snowfall occurred. Because of the daily resolution used here, the albedo of fresh snow should be interpreted as the characteristic albedo for snow that is not more than one day old. So it may (and does) differ from the albedo of a snow surface during or immediately after snowfall.

Next we require that a smooth transition to the characteristic ice albedo α_{ice} occurs when snow depth (d) is small. This can be achieved by writing for the final albedo

$$\alpha(j) = \alpha_{snow}(j) + [\alpha_{ice} - \alpha_{snow}(j)]\ \exp\{-d/d*\} \qquad (4.3.2)$$

Here $d*$ is a characteristic scale for snow depth. When snow depth equals $d*$, the snow cover contributes 1/e to the albedo, the underlying surface (1-1/e).

So there are five control parameters now: α_{frsno}, α_{firn}, α_{ice}, $\tau*$ and $d*$. Calculating the optimal values for these parameters is not difficult. It appeared that the mutual dependence of optimal control parameters is small and a unique solution minimizing σ exists. The results are given in Table 4.1 (full model). Although the correlation coefficient is significant (0.93), σ is still fairly large (0.067). We should realise that the seasonal cycle makes a major contribution to the correlation coefficient. In Figure 4.6 a comparison between observed and calculated albedo is shown, and inspection of the curves reveals some significant discrepancies. One possible reason is that light snowfall is not always picked up by the analysis of the sonic altimeter data. Another factor contributing significantly to σ is the tendency of the observed ice albedo to increase from the beginning of June to the end of September. However, as is obvious from Figure 4.5 this does not occur every year.

	α_{frsno}	α_{firn}	α_{ice}	$d*$ (cm)	$\tau*$ (days)	r	σ
full model:	**0.75**	**0.53**	**0.34**	**3.2**	**21.9**	**0.931**	**0.067**
one albedo for snow:	0.70	-	0.34	2.9	-	0.912	0.076
$d*$=0	0.71	0.54	0.34	0	21.3	0.891	0.084
two albedo values only:	0.67	-	0.34	0	-	0.882	0.087

Table 4.1. Results of fitting the simple albedo scheme. For each model the best values for the control parameters are listed, as well as the root-mean-square difference (σ) between simulated and observed albedo and corresponding correlation coefficient (r).

The question can be asked whether simpler albedo models would give a simulation of comparable quality. In Table 4.1 the results of a calculation with simpler models are summarized. Firstly, we consider a model without aging effect of the snow, implying that a single value for snow albedo is used. The best result is obtained with a snow albedo of 0.70, the resulting value of σ being 0.076. So one may conclude that the simulation without an aging effect is significantly, although not dramatically, worse.

Another simplification would be to leave out the snow depth (i.e. put d^* to zero). This leads to an optimal simulation with $\sigma = 0.084$, clearly demonstrating that it makes sense to take snow depth into account explicitly. Finally, a run was done in which only two albedo values are used: one for snow and one for ice, without any effects of snow depth or aging. Now the best simulation that can be achieved has $\sigma = 0.087$, which is 30% larger than the result for the full model.

Much detailed models of snow albedo have been published (e.g. Melloh et al., 2002; Pedersen and Winther, 2005) in which many other factors are taken into account. However, attempts to improve the model presented here by including air temperature and solar elevation as additional control parameters were not successful, i.e. did not lead to a significant reduction of σ.

The analysis of point measurements focuses on the temporal variability of the surface albedo. However, this temporal variability should be judged against the spatial variability that is so evident in summer for almost all glaciers. This can hardly be done without the help of satellite remote sensing. In a later section satellite images will therefore be used to study spatial patterns in glacier albedo and their temporal evolution.

4.4 In situ observations of band albedos

With respect to the melting process on a glacier, the full-spectrum albedo α as defined in eq. (4.1.1) is the most relevant quantity. However, sensors on space platforms measure band albedos. To map α from satellite radiance data it is thus necessary to convert band albedos into a broadband albedo.
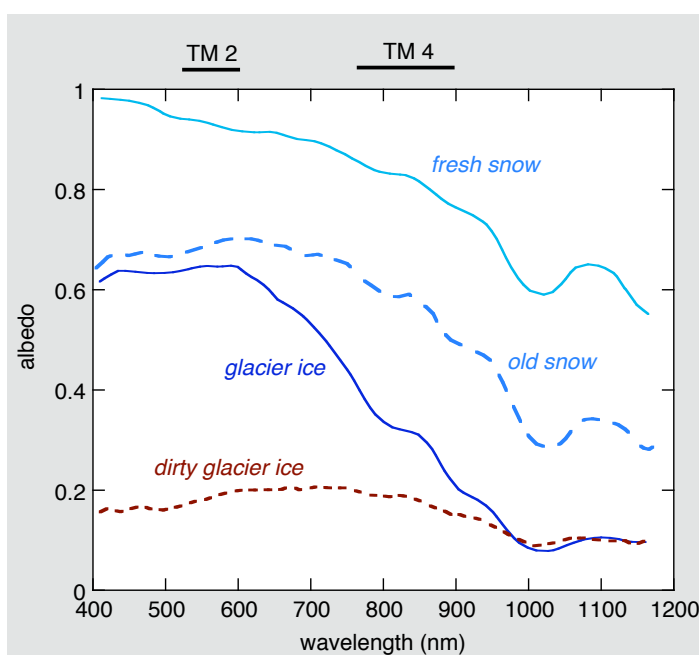

Figure 4.7. Spectral reflectance curves for ice and snow (modified after Zeng et al., 1984). The curves give the characteristic patterns only. The spectral width of the Landsat Thematic Mapper bands 2 (visible) and 4 (near-infrared) are shown at the top.

Figure 4.8. Field campaign on Iceland to measure band albedos. The instrument beam is indicated by the arrow. It has sensors to measure reflected radiation in the NOAA-AVHRR Channels 1 and 2, and in the Landsat TM bands 2 and 4.

Figure 4.7 gives an impression of how the spectral reflectance depends on the type of surface. Compared to snow, the reflectance of glacier ice drops off much more rapidly with wavelength. For dirty glacier ice the spectral dependence of the reflectance is weak.

Although theoretical models have been developed to calculate spectral reflectance curves for snow and ice, in situ measurements of band albedos (preferably in the spectral bands corresponding to those of satellite sensors) are very useful to construct and verify conversion schemes. Several field experimens on glaciers have been carried out to measure band albedos, either by mounting instruments underneath a low flying helicopter to obtain a large spatial coverage (Figure 4.8; Greuell et al., 2002), or by deploying instruments in a frame on a glacier to get time series.

Many instruments onboard of satellites measure reflectance in optical and near-infrared channels, but not all of these have appropriate characteristics for the study of glaciers. NOAA-AVHRR and MODIS images have a resolution that is useful for the study of ice caps, but too poor to map the albedo of typical valley glaciers. For valley glaciers the Landsat archive forms a very large source of information, and we therefore focus on a discussion of the Landsat instruments.

Figure 4.9 and 4.10 show long-term measurements of band albedos on the tongue of the Vadret da Morteratsch. In collaboration with Kipp & Zonen, special global radiometers were constructed with response characteristics that are very similar to the Landsat Thematic Mapper band 2 (TM-2, visible, 520-600 nm) and band 4 (TM-4, near-infrared, 760-900 nm), see Knap et al. (1999a). The bands are indicated in Figure 4.7.

Figure 4.9 shows daily band albedos and the broadband albedo during a period in late winter/early spring 1997, when a thick snowpack of about 1 m was present. First of all we note that there is a clear trend from higher to lower values of the snow albedo, which is associated with the gradual metamorphosis of the snowpack (larger grains). The decrease of the broadband snow albedo is substantial: from about 0.85 in the beginning of the period to about 0.65 at the end of the period. The TM-2 albedo is always higher than the TM-4 albedo, but the difference is smaller for fresh snow (major snowfalls are indicated by arrows). After snowfalls the snow grains become larger and
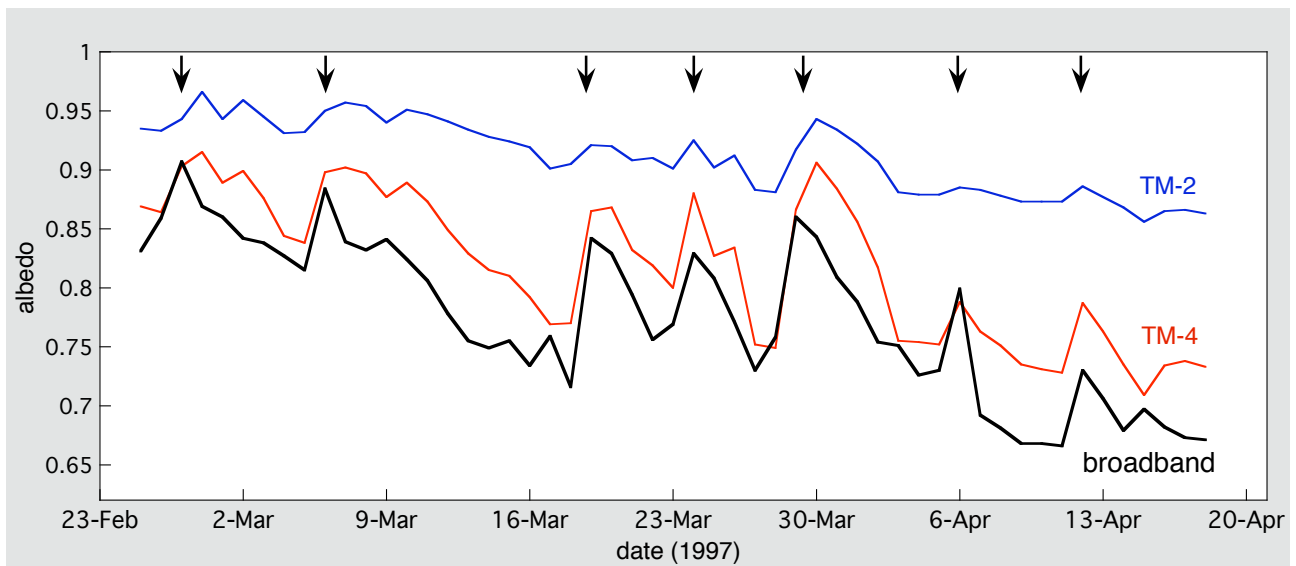
Figure 4.9. Spectral daily albedos as measured on the Vadret da Morteratsch during a period in 1997 when the glacier was covered by a thick snowpack. The albedos for the Landsat Thematic Mapper bands 2 and 4 (in blue and red) are compared to the broadband albedo. Major snowfalls are indicated by arrows. From Knap et al. (1999).
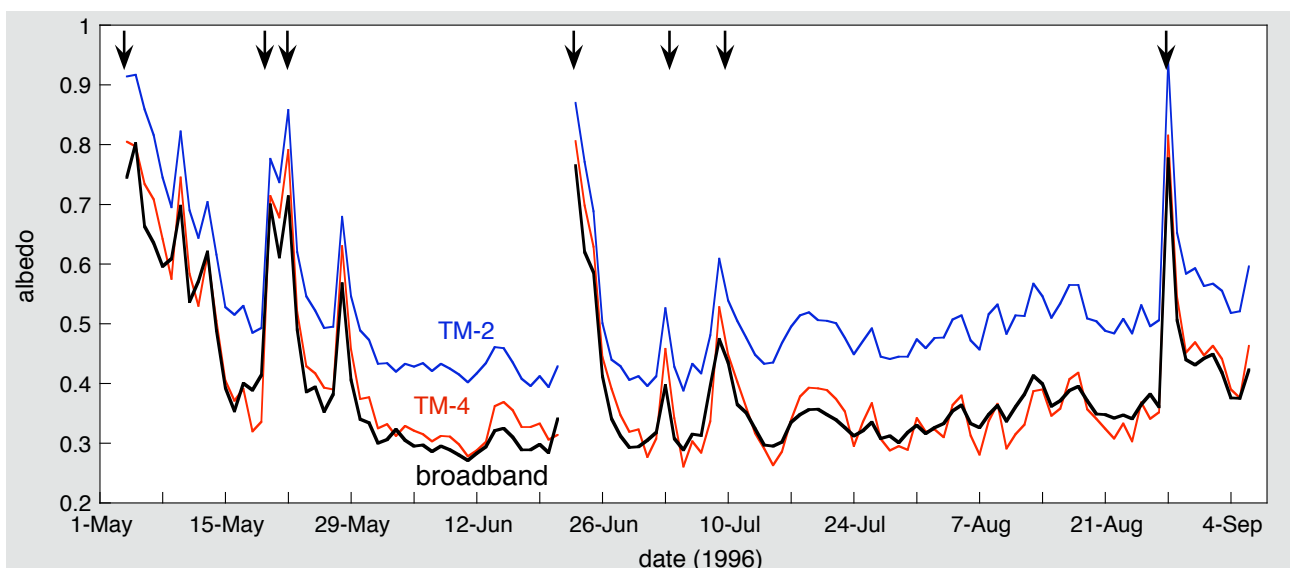
Figure 4.10. Spectral daily albedos as measured on the Vadret da Morteratsch during a large part of the melt season in 1996. The albedos for the Landsat Thematic Mapper bands 2 and 4 (in blue and red) are shown together with the broadband albedo. Snowfalls are indicated by arrows. From Knap et al. (1999).

the difference between the TM-2 and TM-4 albedos increases, up to about 0.2 towards the end of the investigated period. These findings are in agreement with earlier model studies of the spectral dependence of snow albedo (e.g. Wiscombe and Warren, 1980; Davis et al., 1993).

The transition from a snow-covered surface to an ice surface is shown in Figure 4.10. For an ice surface there is a rather constant difference between the visible and near-infrared albedo. The measurements shown in Figure 4.10 were made over relatively clean ice. Measurements at other locations on the glacier with more dust at the surface revealed that the presence of dust tends to decrease the difference between the TM-2 and TM-4 albedos. On at least three days in the summer

snowfall occurred, and it can be seen that in these cases the relative increase in albedo is smallest in the visible band.

On the basis of the measurements described above, Knap et al. (1999a) derived equations for the conversion of narrowband to broadband albedo. It appeared to be possible to fit the data with one equation for the entire range of albedo values from dirty ice to fresh snow. The equation reads

$$\alpha = 0.726\alpha_2 - 0.322\alpha_2^2 - 0.051\alpha_4 + 0.581\alpha_4^2 \qquad (4.4.1)$$

As shown in Figure 4.11, the correlation between the measured broadband albedo and the albedo calculated from the TM-2 and TM-4 sensors, denoted by α_2 and α_4 respectively, is very high ($r^2 = 0.998$; standard deviation of the residuals is 0.009). However, the TM-2 band frequently saturates over snow. The albedo can then be obtained from

$$\alpha = 0.782\alpha_4 + 0.148\alpha_4^2 \ . \qquad (4.4.2)$$
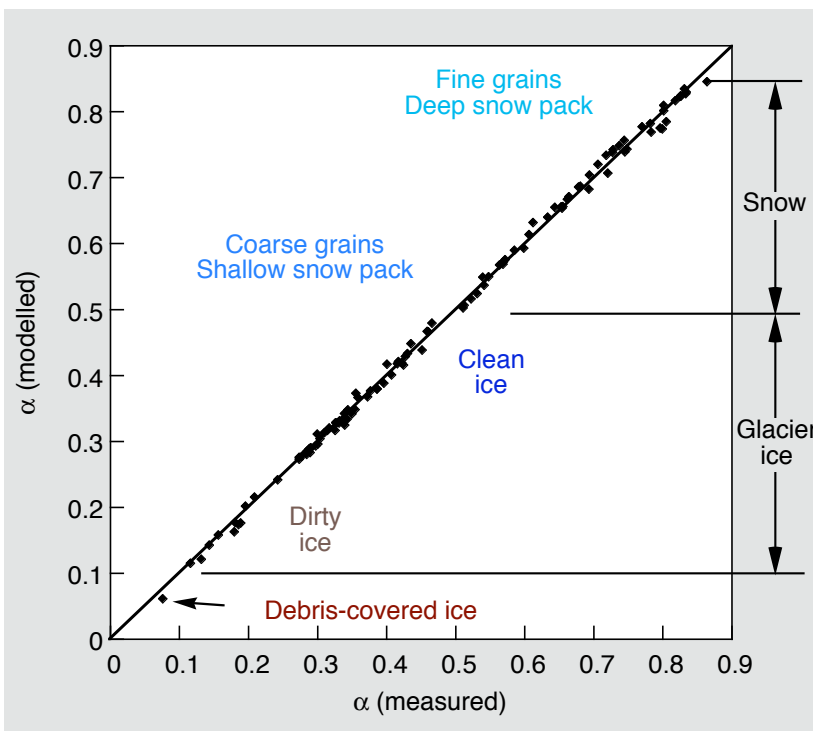
Figure 4.11. The performance of a model for the conversion of narrowband to broadband albedo (from Knap et al., 1999a).

4.5 Anisotropic reflection

In general, the radiation field reflected by a surface is not isotropic (Figure 4.12). The implication of this fact may be limited for in situ measurements of the albedo with a conventional instrument, which has a half dome collecting radiation from every direction. However, when the surface is observed from far away, like from a space platform, the viewing angle is small. When the reflected radiation is anisotropic, this implies that the measured radiance depends on the view geometry and the directional reflectance characteristics of the surface.

Figure 4.12. Anisotropic reflection of incoming solar radiation (direct and diffuse) by a glacier surface. The sketches only show the reflection in the plane of the solar beam. In both cases the solar elevation is the same, but the slope and aspect of the surface differs. For case (b) the apparent solar elevation is much larger than for case (a), which results in different reflectance characteristics.

We define a hemispherical-directional reflectance function $r(\theta,\phi)$ as

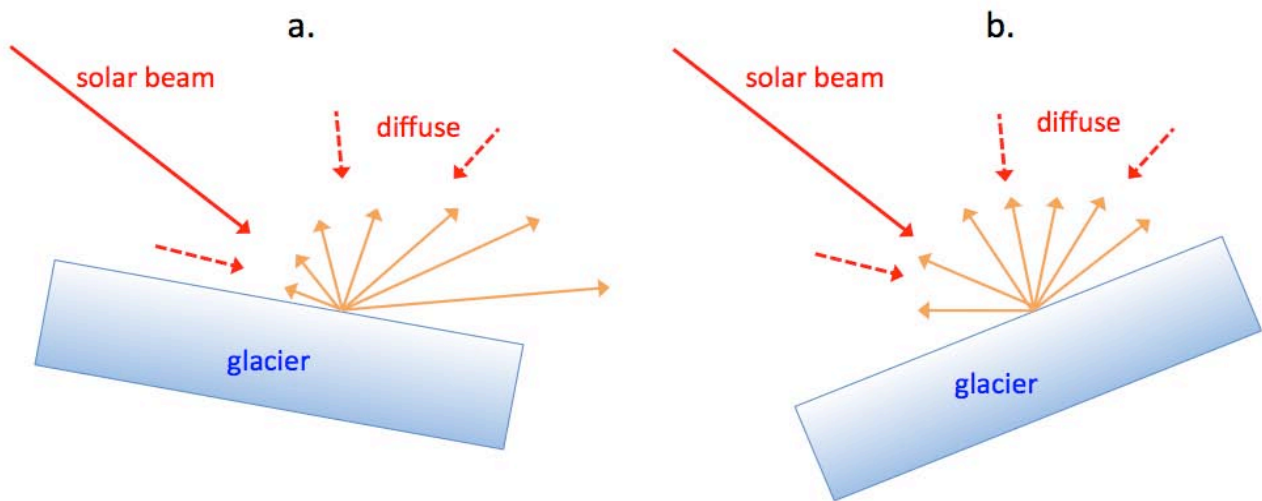$$r(\theta,\phi) = \frac{R(\theta,\phi)}{S^{\downarrow}/\pi} \, , \qquad\qquad\qquad (4.5.1)$$

where θ is the view zenith angle and ϕ the view azimuth angle (Figure 4.13). The view azimuth angle is defined relative to the solar principle plane, implying that forward scattering corresponds to $\phi = 180°$ and backward scattering corresponds $\phi = 0$. $R(\theta,\phi)$ denotes the radiance of the reflected signal (unit: W m^{-2} sr^{-1}).

The term 'hemispherical-directional' refers to the fact that we consider reflected radiation in one particular direction, but originating from incoming radiation through a hemisphere. The incoming radiation consists of direct radiation (the solar beam) and diffusive radiation. The definition of $r(\theta,\phi)$ is not meaningful if all incoming radiation is diffuse, because in that case the solar principal
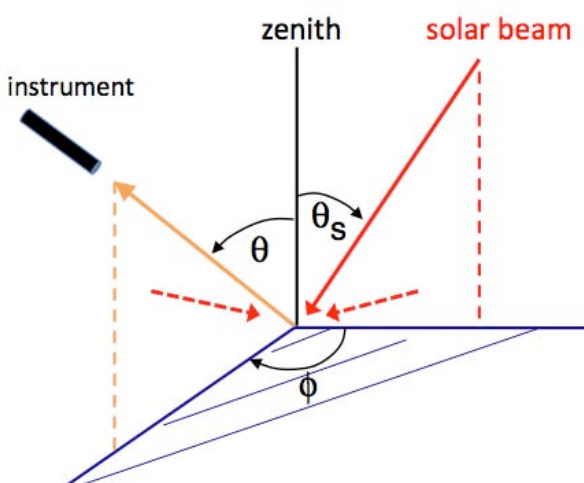

Figure 4.13. Geometrical set-up used to define the hemispherical-directional reflectance function.

4 - The surface albedo of glaciers

plane cannot be defined. However, in the application to be discussed here, namely the mapping of surface albedo from satellite data, images for (almost) clear-sky conditions are normally used.

The hemispherical-directional reflectance factor is now defined as the ratio of the reflectance function to the albedo

$$f(\theta,\phi) = \frac{r(\theta,\phi)}{\alpha} \ . \tag{4.5.2}$$

If the reflected radiation is isotropic (Lambertian surface), we have $f = 1$. On a real glacier surface the variation of f is smallest during or shortly after fresh snow has fallen. Melting and refreezing of the surface creates large variations in f, which can readily be observed when looking in the direction of the sun (forward scattering much larger than backward scattering). At this point it should also be mentioned that $f(\theta,\phi)$ depends on the solar zenith angle θ_s. We expect the degree of anisotropy to be larger when the (apparent) solar elevation is lower.

It should be noted that in the literature the term bi-directional reflectance factor has been used frequently to describe the anisotropic reflection in the situation discussed above. Strictly speaking this is not correct, because the incoming radiation does not hit the surface from a single direction. A detailed discussion on the various definitions and general nomenclature in describing reflectance can be found in Schaepman-Strub et al. (2006).

How can a hemispherical-directional reflectance function be measured in the field? There are essentially two different approaches. One approach is to measure in different directions from the same site (possibly from a tower), but thus requires a surface that is homogeneous over large distances. This method might work over the Greenland ice sheet (e.g. Nolin et al., 1994), but is not suitable for smaller glaciers. The second approach is to measure the same target from different positions of the instrument.

Figure 4.14 shows a device that has been developed at IMAU (Knap and Reijmer, 1998; Greuell and De Ruyter de Wildt, 1999). The target area is inside the ring, and radiometers with a viewing angle of 5° in the Landsat TM-2 and TM-4 bands are mounted on a support that can be moved in all directions relatively easy. In this way the radiance of the reflected radiation can be measured as a

Figure 4.14. Studying the reflectance characteristics of firn in the accumulation zone.

function of θ and ϕ within a reasonable time interval (this is required because the solar elevation should not change too much during the measurement period). To obtain the hemispherical-directional reflectance function the incoming irradiance also has to be measured.

Figure 4.15 shows an example. The pattern is characterised by a minimum value of $r(\theta,\phi)$ in the nadir direction and relatively large values in the forward limb. It is clear that the degree of anisotropy in the reflection patterns is quite large. Greuell and De Ruyter de Wildt (1999) measured a large number of reflectance distributions and concluded that the anisotropy becomes larger for increasing wavelength and increasing solar zenith angle. They also found a relation between the anisotropy and the albedo: for smaller albedos the anisotropy tends to be larger. Greuell and De Ruyter de Wildt also developed parameterisations for $f(\theta,\phi)$ that have been used for the retrieval of albedo from Landsat radiance measurements.

It should be noted that the view zenith angle of many spaceborn sensors is not very large. For the Landsat Thematic Mapper, for instance, the view zenith angle does not exceed 8° and the corresponding variation of $f(\theta,\phi)$ will be small. However, in the case of glaciers the surface slope of larger areas is typically 5° to 25°, which implies that values of $f(\theta,\phi)$ may be quite different from those over horizontal terrain. Therefore it is advisable to use a digital elevation model to determine the appropriate view angle for individual pixels in satellite scenes. In such a procedure accurate geolocation of the satellite images is essential.
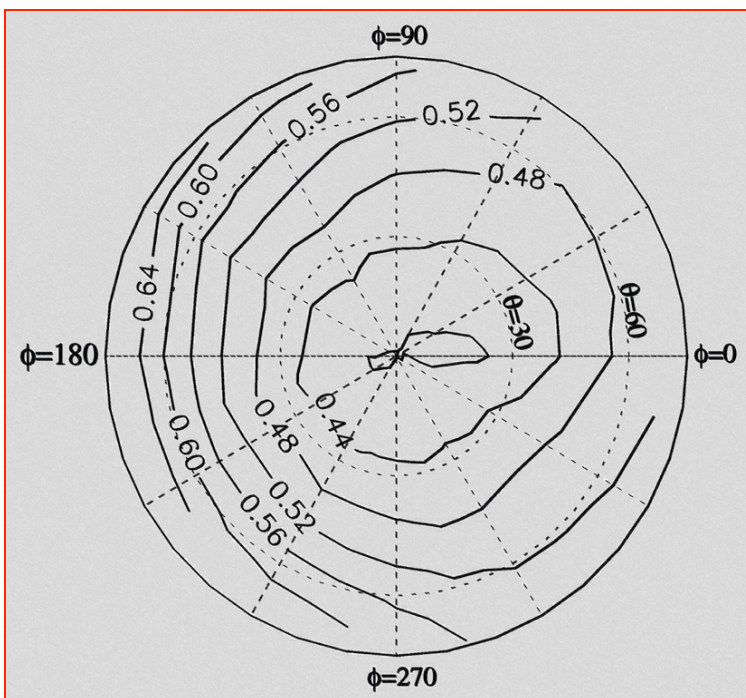
Figure 4.15. Hemipsherical-directional reflectance function for the Landsat TM-4 band measured over glacier ice with the equipment shown in Figure 4.14. The solar zenith angle was 50° and the TM-4 albedo about 0.5.

Detailed studies of the hemispherical directional reflectance factors over snow have also been studied by Bourgeois et al. (2006) at the Greenland Summit Environmental Observatory (72°35′N, 34°30′W, 3203 m above sea level). They found a strong forward scattering peak for larger solar zenith angles, whereas at noon the reflection pattern tended to become more isotropic. It also appeared that the forward scattering peak is stronger when the snow surface is smoother.

4.6 Spatial variability of glacier albedo

From visual inspection of glaciers in summer it is immediately obvious that the spatial variability of the albedo is very large. Mapping the albedo by in situ measurements is a tedious task and can normally only be done for pars of a glacier. The construction of albedo maps from radiances measured by a satellite sensor is a more attractive approach, but requires a large number of steps. First (almost) cloud-free scenes have to be selected and accurate geolocation with control points has to be carried out. When considering optical sensors there is a certain relation between image repeat time and spatial resolution. For instance, the NOAA-AVHRR (Advanced Very High Resolution Radiometer) instruments provide images every day, but these have a resolution of about 1 km at nadir. This is clearly not good enough to map mountain glaciers, but can be used for the study of ice caps with a characteristic length scale of 50 km, like Austfonna or Vatnajökull (e.g. De Ruyter de Wildt and Oerlemans, 2003). NOAA-AVHRR images are available since 1978. In contrast, the thematic mapper (TM) on the Landsat satellites has delivered a large number of scenes with high resolution (~20 m), but with a repeat time of typically 14 days one has to be lucky to get four or five cloud-free scenes of a particular glacier in a summer. For the study of mountain glaciers ASTER (Advanced Spaceborne Thermal Emission and Reflection Radiometer), onboard of the Terra satellite, has proven to deliver very useful images. The resolution is 15-90 m and data are available since the year 2000.

After selection and geolocation of images, the radiometric calibration has to be considered. More recently launched instruments normally have onboard calibration, but for NOAA-AVHRR and Landsat TM radiances this is not the case. Since the pre-launch calibration may not be valid any more after some time, it is wise to use targets having a well known and rather constant albedo for a test of the calibration (e.g. the dry snow zone of the Greenland ice sheet, a desert, and an ocean surface in calm conditions).

Next a correction has to be made to the radiance data because of interference with the atmosphere. Detailed radiative transfer models for the atmosphere exist, but the accuracy of calculations with such models depends mainly on the quality of the input, notably the vertical profiles of type and concentration of aerosol particles. Normally standard profiles are used because detailed information is not available. Two important steps remain to be taken: (i) conversion of band albedos to broadband albedo, and (ii) conversion of radiance measurements to irradiance, taking into account the anisotropic reflectance characteristics of the surface as discussed earlier.

A comprehensive study with twelve Landsat images of the Vadret da Morteratsch (Figure 2.12) was carried out by Klok et al. (2003). Maps of the surface albedo were constructed following the method described above. The necessary topographic input was obtained from a digital elevation model with a resolution of 25 m, which is comparable to the resolution of Landsat images. The Vadret da Morteratsch has a complicated and rugged topography in the upper reaches. Since the glacier flows essentially in a northerly direction, the apparent solar elevation is small for many pixels. In view of these complicating factors, the analysis can be seen as a real test case.

A selection of five maps for the year 1999 is shown in Figure 4.16. In March the glacier was entirely covered by snow. Due to the low solar elevation many pixels were in the shade at the time that the satellite was passing. The typical surface albedo derived from the images was 0.9. The image of 24 June 1999 shows the characteristic pattern for early summer: low albedos (0.2 to 0.5) on the glacier tongue where bare ice is at the surface, and higher albedos (0.6 to 0.7) in the accumulation zone. In the course of the summer there is a further lowering of the albedo (except for

the lower part of the glacier). The maps for 26 July and 13 September show remarkably low albedo values in the higher accumulation zone, which is probably unrealistic. The most plausible explanation for this is that the anisotropy correction introduces a large error in the case of rugged snow-covered mountains combined with a low solar elevation.

In October the albedo has been raised again by new snow, although the effect is small on the glacier tongue (probably because the amount of snow was small or melting proceeded more quickly here).

All albedo maps, including those for the year 2000 (not shown), reveal that the snow-free surface albedo in the lower part of the glacier has a band structure. Cleaner glacier ice in the middle is surrounded by debris-covered ice with a much lower albedo ~(typical value 0.15). In the ablation area, the lateral variations in the albedo are much larger than the altitudinal variations. This has also been found for Haut Glacier d'Arolla, Switzerland (Knap et al., 1999b) and Pasterzenkees, Austria (Greuell et al., 1997). In contrast, for the Hintereisferner, Austria, the ice albedo appeared to increase slightly when going up-glacier (Koelemeijer et al., 1992).
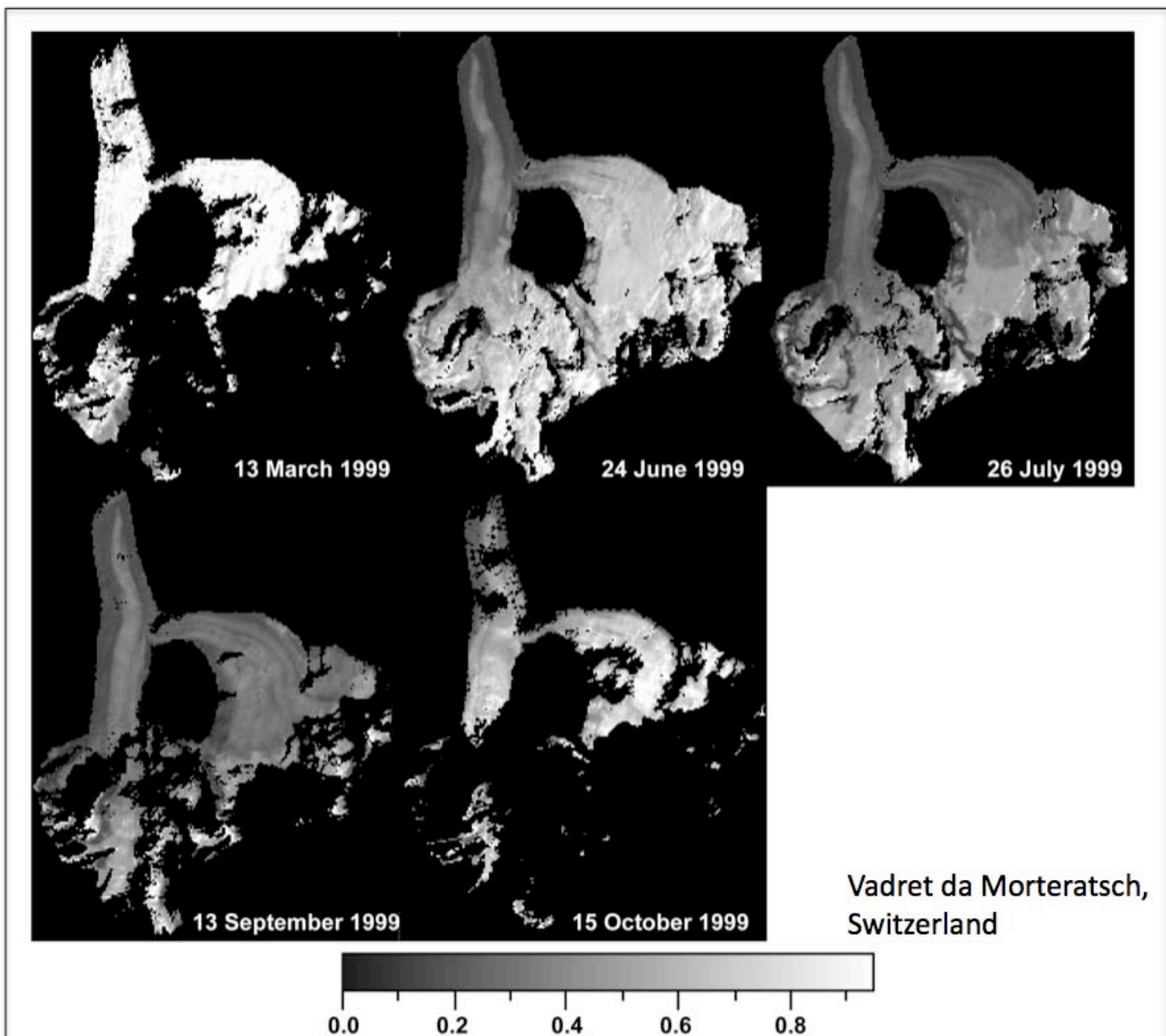

Figure 4.16. Spatial distribution of the satellite-derived albedo of the Vadret da Morteratsch during the melt season of 1999. Regions outside the glacier or in the shade during the satellite overpass are black.
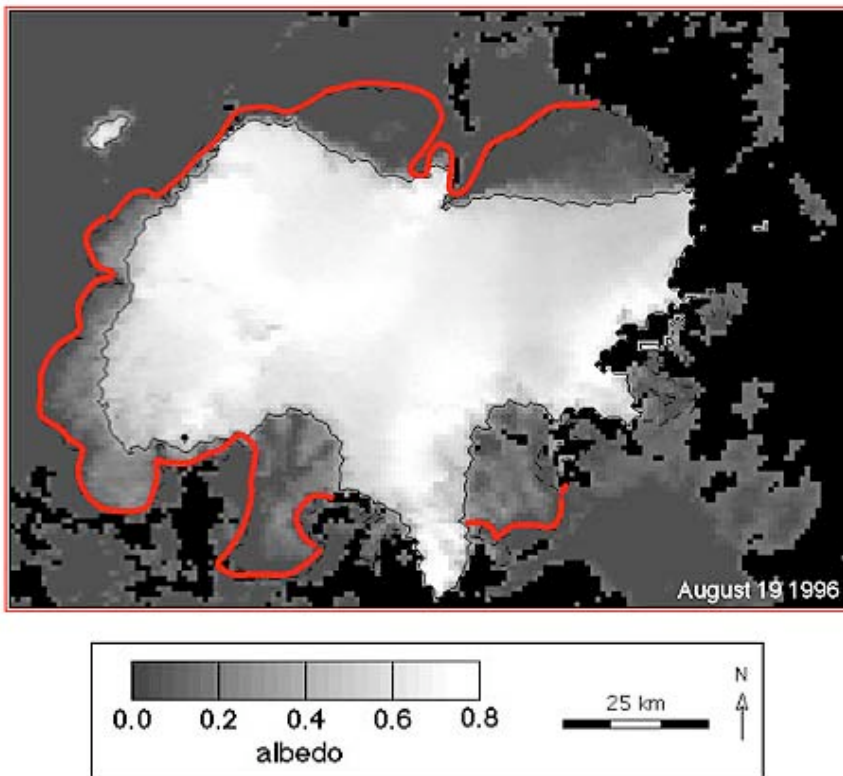
4 - The surface albedo of glaciers

Figure 4.17. Albedo map of Vatnajökull, Iceland, based on NOAA-AVHRR data (August 19, 1996).
Cloud cover is shown in black. The red line depicts the outline of the ice cap (only shown in non-cloudy regions). A thin black line marks the transient snowline.

To illustrate the contrast between ice caps and valley glaciers, Figure 4.17 shows an albedo map derived for Vatnajökull, Iceland, from a NOAA-AVHRR image (De Ruyter de Wildt and Oerlemans, 2003). The spatial resolution (~1 km) is not as good as for the Landsat scenes. Because the topography is generally smoother, the effect of anistropy in the reflected signal varies less across the ice cap. There is a distinct structure in the albedo map, with a significant albedo difference between the ablation zones and the firn area. Due to the abundant presence of tephra the albedo in the ablation zones is very low, especially in the northern part of the ice cap. In fact, here a difference between the albedo of the ice cap and the surrounding terrain is hard to detect.

The reconstruction of albedo maps for Vatnajökull was part of a project in which the relation between annual mass balance and temporal evolution of the albedo was studied. In total 107 images from the period 1991-1999 were analysed. It appeared to be possible to reconstruct annual mass-balance anomalies on the basis of the NOAA-AVHRR images. This conclusion was also reached by Greuell et al. (2007), who applied a similar analysis to 18 large glaciers on Svalbard.

4.6 The effect of clouds

Clouds may have a significant effect on the albedo, because they change the spectral distribution of the solar radiation reaching the surface. Clouds filter out radiation in the near-IR part of the spectrum (wavelength > 800 nm), where the albedo of snow and ice is generally lower than in the visible range (see Figure 4.7). The spectrally integrated albedo is therefore larger in the presence of clouds. The effect is larger when multiple reflections occur between surface and cloud, i.e. when the surface albedo is large (Wiscombe and Warren, 1980).
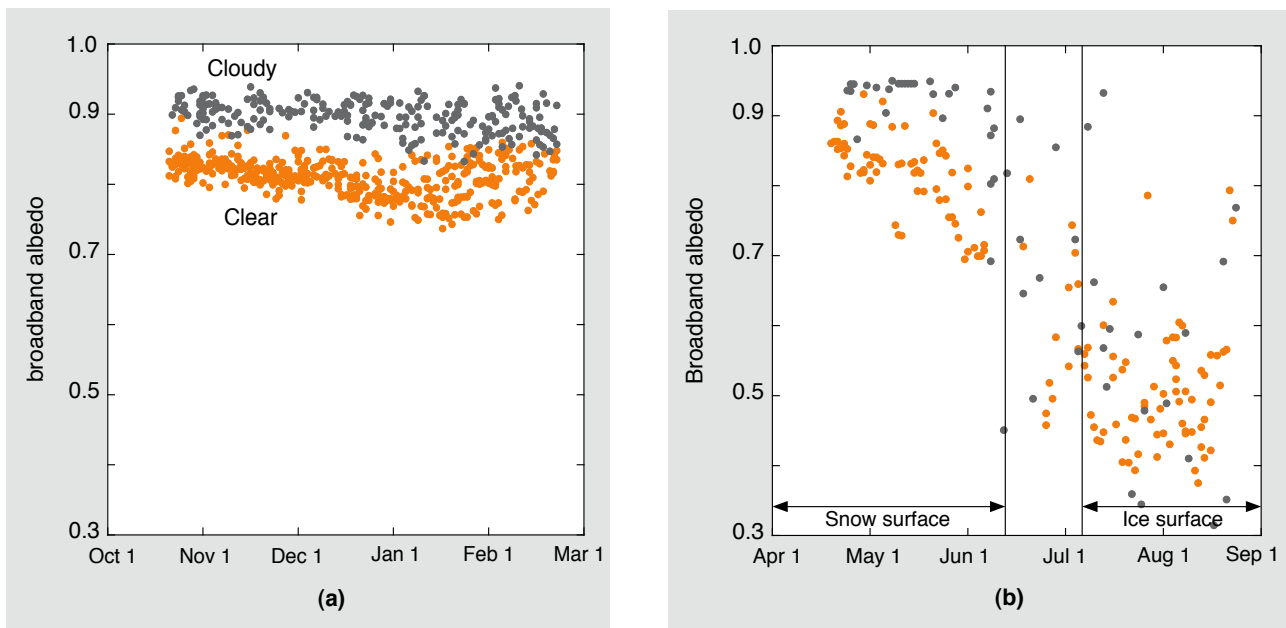
Figure 4.18. Daily mean values of broadband albedo for clear (orange) and cloudy (black) days: (a) at Neumayer station, Antarctica; (b) at station S6, K-transect, West Greenland. Data in (a) are for the period 1995-2004; data in (b) for the period 2003-2007. From Kuipers Munneke et al. (2009).

A detailed study of the dependence of the surface albedo on clouds was carried out by Kuipers Munneke et al. (2009). Their analysis is based on observations with AWS, and here we consider a few results. Figure 4.18a shows data from a location where the surface is always snow-covered: the Neumayer research station in Dronning Maud Land, Antarctica. All the data points shown are daily averages. There is a clear and systematic difference between the albedo during clear and cloudy conditions. Note that in the second half of the summer snow albedo is lower due to snow methamorphosis, which is more pronounced when temperatures are higher.

Similar data from the melting zone of the Greenland ice sheet show a different picture. Observations shown in Figure 4.18b are from a location along the K-transect in central West Greenland (Van den Broeke et al., 2008). Here the transition from a snow surface to an ice surface takes place in the second half of June. For the snow surface the difference in albedo for clear and cloudy conditions is evident. However, the scatter is much larger now than in the data from the Neumayer station, which is understandable because the surface is subject to melting. For the period with an ice surface there seems to be no significant difference between the albedo for clear and cloudy conditions. This is in agreement with observations carried out by Brock et al. (2000) on Haut Glacier d'Arolla and by Jonsell et al. (2003) on Storglaciären. Altogether, for an ice surface the correlation between cloud cover and albedo appears to be weak. We therefore conclude that multiple reflections between surface and clouds play a key role. A significant effect of clouds on albedo can therefore only be expected when the surface reflectivity is high.

Ablation stake on the Vadret da Morteratsch, with a GPS receiver on top.

5. The surface energy flux, ablation, and balance rate

5.1 The surface energy flux

In the preceding chapters different aspects of the glacier microclimate have been analysed. The process of ablation, in which snow and ice is removed from the glacier surface, is governed by thermodynamic processes acting at and just below the glacier surface. An overview of these processes has been given in section 1.4. Here we expand the discussion and look at more data from weather stations.

When going through the literature it appears that both the terms surface energy balance and surface energy flux are used to describe the thermodynamic processes. There is some confusion about the definition of energy flux and energy balance, depending on whether processes in the upper layers of the glacier are taken into account explicitly, or in a schematic way, or not at all. In some papers the terms flux and balance are used to described the same quantity. Therefore, it is useful to define once more the energy flux and the energy balance as it is referred to in this text.

The surface energy *flux* ψ at the air-glacier interface is defined as

$$\psi = S_{in} + S_{ref} + L_{in} + L_{out} + H_s + H_l \; , \tag{5.1.1}$$

where S_{in} is the incoming solar radiation, S_{ref} the reflected solar radiation, L_{in} the incoming longwave radiation, L_{out} the outgoing longwave radiation, H_s the turbulent sensible heat flux and H_l the turbulent latent heat flux.

If we denote the energy involved in all subsurface processes by G and in melting of snow and ice by M, the energy *balance* can be written as

$$\psi = M + G \, . \tag{5.1.2}$$

With subsurface processes we mean first of all *storage of energy* by convergence of the heat flux due to conduction, and possibly due to air motion in a loose snowpack. Meltwater forms a complicating factor when it does not run off, but refreezes in the snowpack. The energy consumed by the process of melting is then released again during refreezing of the meltwater. If this happens at the same location, there is no net gain or loss of energy in a vertical column. However, if the meltwater runs to another location through the snowpack or over the ice surface, a spatial redistribution of energy is implied. It is questionable if such processes are significant on temperate alpine glaciers. On cold subarctic ice caps and the Greenland ice sheet the refreezing process is more important, both with respect to the balance rate and to the energy budget.

It should be noted that the surface energy *flux* refers to the flow of energy through an interface, whereas the energy *balance* refers to a layer of a certain thickness with a heat capacity.

At this point a note about *tilted* glacier surfaces is in order. For a particular point (or 'pixel') on a glacier, the balance rate is defined with respect to the vertical. This implies that for a given area on a map (in plan view) the amount of mass added or removed is independent of the slope of the glacier surface (Figure 5.1). However, we should note that the real area in contact with the atmosphere does depend on this slope. In the formulation of the energy budget, the components of the radiation budget and the turbulent fluxes should therefore be multiplied by a correction factor $f_{sl} = (\cos \eta)^{-1}$. The value of f_{sl} is 1.0154 for a slope of 10°, 1.0642 for a slope of 20°, 1.155 for a slope of 30°, and 1.305 for a slope of 40°. So for steep glaciers the effect of an enlarged exposed area on the energy fluxes is not negligible. For large valley glaciers with, on average, surface slopes in the ablation zone of the order of 10°, the effect is limited. In the following we will assume that slopes are small and that $f_{sl} \approx 1$.
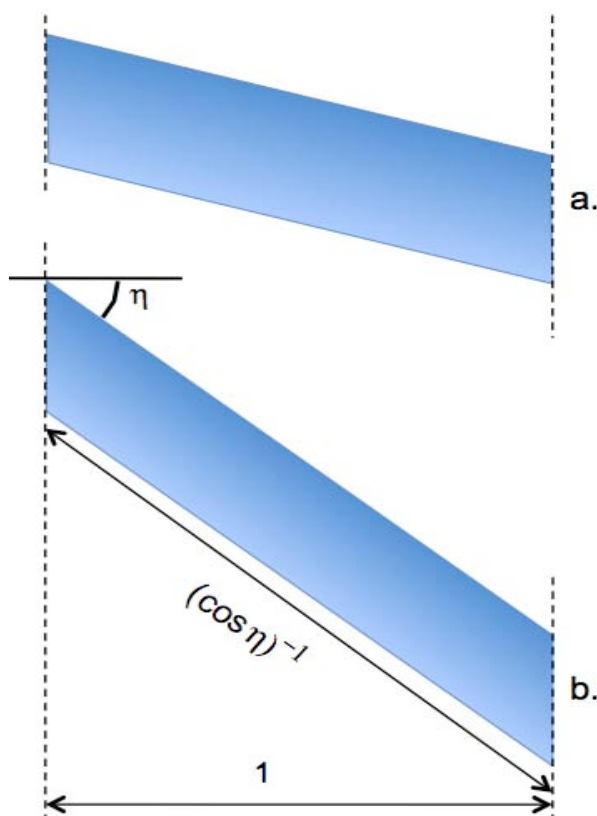

Figure 5.1. For a given unit area in map projection, the area of the glacier surface exposed to exchange processes with the atmosphere depends on the surface slope η. However, for a given balance rate, measured along the vertical, the amount of mass involved is independent of η (the area of the slabs in cases **a** and **b** is the same).

5.2 Observations of the daily mean surface energy flux

The energy flux ψ as defined in eq. (5.1.1) can be evaluated from meteorological measurements. Four years of daily mean values for AWS on three different glaciers are shown in Figure 5.2 (for details about the glaciers, locations of the weather stations, and analysis of the data, see: Andreassen et al., 2008; Giesen et al., 2008; Oerlemans et al., 2009).

For all locations there is a marked difference between the winter season, when ψ is small, and the melt season. On the Vadret da Morteratsch ψ reaches higher values in mid-summer than on the glaciers in southern Norway. This is partly related to a higher solar elevation, but also to higher air temperatures. Due to the different scale of the glaciers, the altitudinal difference between the location of the AWS and the equilibrium line is about 200 m for Storbreen, about 250 m for Midtdalsbreen, and about 900 m for the Vadret da Morteratsch. It can thus be expected that the temperature-dependent part of the surface energy flux (longwave radiation and turbulent fluxes) is significantly larger on the Vadret da Morteratsch.
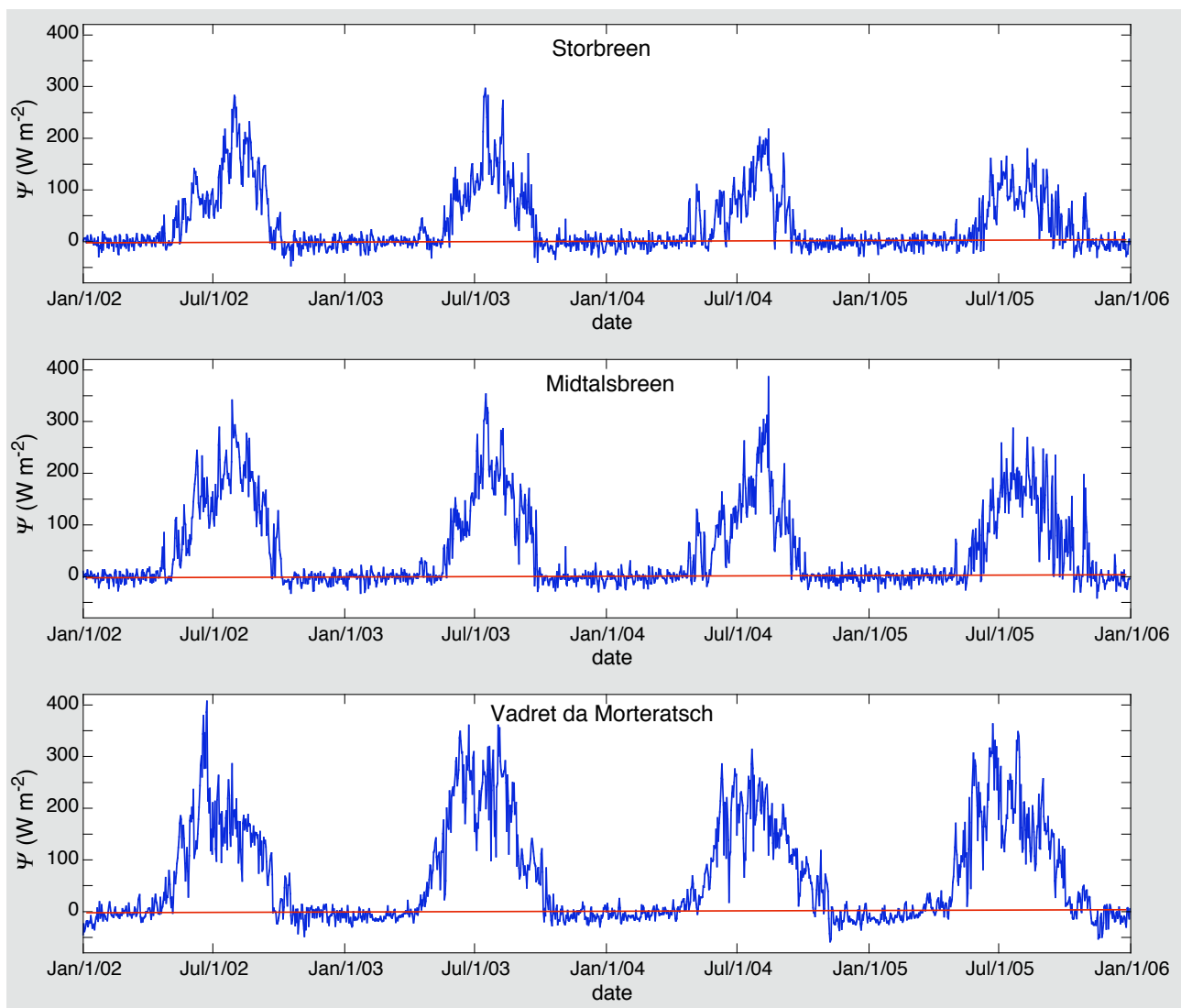

Figure 5.2. The surface energy flux (daily mean values) as measured during four years by automatic weather stations on Storbreen (Norway, 1570 m a.s.l.), Midtdalsbreen (Norway, 1449 m a.s.l.) and Vadret da Morteratsch (Switzerland, 2116 m a.s.l.).

In a global sense, and irrespective of the fluctuations on a time scale from days to a few weeks, the surface energy flux through the year can schematically be described as

$$\psi_c(t) = \max\left\{0;\; A_0 + A_1 \cos\frac{2\pi(t - t_m)}{T}\right\},$$ (5.2.1)

where A_0 and A_1 (> 0) are appropriate constants, t_m is the time at which the daily mean surface energy flux reaches a maximum, and T is the period (set to 1 year). The parameters A_0, A_1 and t_m can be found by minimizing

$$D(A_0, A_1, t_m) = \sqrt{\frac{1}{n}\sum[\psi(t) - \psi_c(t)]^2}.$$ (5.2.2)

The optimal parameter values can easily be found by a random-walk method. Values of the parameters are perturbed at random, and the new values are retained when the corresponding value of D is lower than its value in the previous step. Convergence appears to be very rapid because the parameters are almost independent. Using different initial values of the control parameters ensures the existence of a unique solution.

The best values of A_0, A_1 and t_m for the records shown in Figure 5.2 are listed in Table 5.1. The numbers are rather similar for all glaciers, except for the value of A_0 for the Vadret da Morteratsch. This is understandable in the light of the much lower altitude relative to the equilibrium-line altitude.

	A_0 (W m^{-2})	A_1 (W m^{-2})	t_m (°)	D (W m^{-2})
Storbreen	-67	200	208	32
Midtalsbreen	-56	241	207	36
Vadret da Morteratsch	-15	239	195	43

Table 5.1. Optimal parameter values for fitting a piecewise constant-cosine function to the observed records of the surface energy fluxes shown in Figure 5.2.
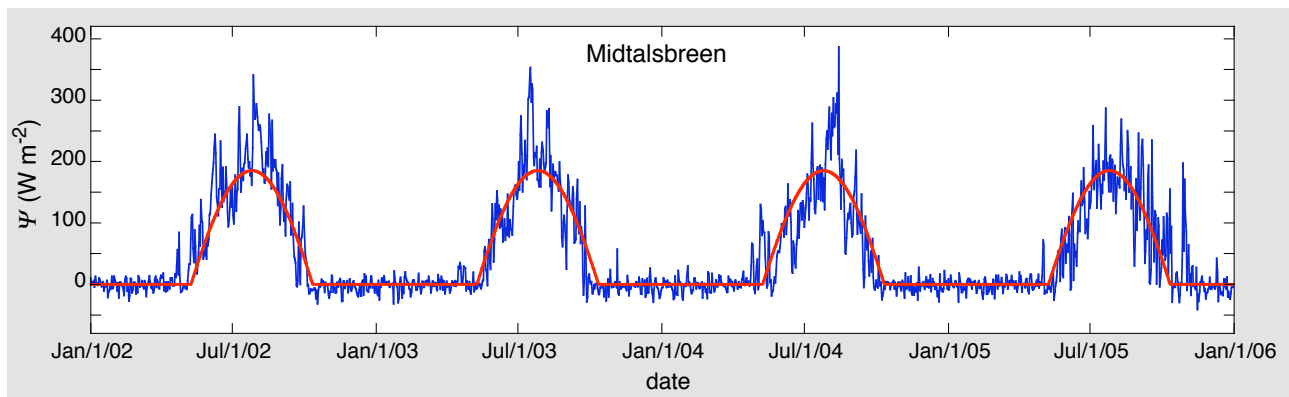

Figure 5.3. The daily mean surface energy flux as measured on Midtdalsbreen and the best fit according to eq. (5.2.1).

5 - The surface energy flux, ablation, and balance rate

In view of the large day-to-day variation in the surface energy flux, it is not surprising that values of D are large (last column in Table 5.1). Because the same parameters are used for all summers, the year-to-year variation also contributes significantly to the root-mean-square difference between observations and fit. In Figure 5.3 the fit for Midtdalsbreen is shown together with the observed record. The schematic representation of the surface energy flux by eq. (5.2.1) will be used later in a simple mass-balance calculation.

5.3 The components of the energy balance

There are different approaches in analysing the components of the energy balance of a glacier's surface layer. The classical approach is to try to estimate all components directly from the measurements. For some components this is straightforward (e.g. for shortwave radiation), for other components a scheme is needed to derive the fluxes from the meteorological observations (e.g. for the turbulent fluxes). The storage term G and the melt M are more difficult to determine. An alternative approach is to use an energy-balance model, which is driven by the meteorological observations and then calculates all components of the energy balance in an internally-consistent way (Van den Broeke and others, 2005). This approach has been used to analyse the records of the AWS on Storbreen, Midtdalsbreen and the Vadret da Morteratsch described above. Here we discuss the results for the Vadret da Morteratsch (see also Oerlemans et al., 2009).

In the model S_{in}, S_{ref} and L_{in} are taken directly from the measurements, and the other fluxes are formulated as functions of the surface temperature T_s. The model time-step is only 10 minutes to keep changes in T_s between time-steps small and to determine accurately when the surface is melting. To obtain model input for every time-step, the AWS data have been linearly interpolated between half-hourly values. Using an iterative procedure, the surface energy balance is solved for T_s. If T_s found by the model is higher than the temperature of the melting point, T_s is set back to 0°C and the excess energy is used for melting. The amount of melt W in meters water equivalent (mwe) is calculated by dividing M by the latent heat of fusion ($3.34 \cdot 10^5$ J kg^{-1}) and the density of water (1000 kg m^{-3}). The turbulent fluxes are calculated with the bulk method, based on differences in wind speed, potential temperature and specific humidity between a measurement level and the surface (for a detailed description, see Van den Broeke and others, 2005). On glaciers, katabatic winds often have a wind speed maximum within the first meters above the surface. Assumptions made in Monin-Obukhov similarity theory, on which the bulk method is based, are not valid in the presence of a wind speed maximum. Still, the bulk method has been found to give good results when the measurement level is below the wind speed maximum (Denby and Greuell, 2000). For the surface roughness length for momentum a value of 0.13 mm is used when the surface is covered by snow, and a value of 0.75 mm is used when the surface consists of ice. The calculation of the scalar roughness lengths for heat and moisture is done with the method of Andreas (1987).

The subsurface heat conduction is computed from the one-dimensional heat-transfer equation for 0.04 m thick layers down to a depth of 20 m. The temperature at the lowest level is assumed to remain constant. The initial temperature profile is generated by running the model in a continuous loop over the measurement period until the 20 m temperature becomes stationary within 0.01 K. The number of snow layers in the model is determined by dividing the observed snow depth by the model layer thickness. Melt water is routed vertically through the snowpack and refreezes where snow temperatures are below the melting point. Snow density is kept constant at 300 kg m^{-3}, based

on measurements in snowpits around the AWS. Hence refreezing only affects the temperatures in the snowpack, not the density. When the snowpack is saturated with melt water, the remaining melt water is assumed to run off. The model does not keep track of the changing depth of the snowpack, the record from the sonic ranger is used instead. When the snow has disappeared, input from the height sensor is not needed anymore and model and measurements are independent. For this snow-free period, the melt W computed by the model can be compared with the surface lowering registered by the sonic ranger and the ablation stakes by dividing W by 0.9, the ratio of the ice and water densities used here.

Figure 5.4 shows the calculated ice ablation and the surface height as measured by the sonic ranger. When the observed surface height is divided by 0.9 (dotted blue curve), a good agreement with the calculated ice ablation is obtained. Also for the records of Storbreen and Midtdalsbreen a good agreement has been found between measured and calculated ablation (Giesen et al., 2009).

The components of the energy balance are shown in Figure 5.5 (daily mean values). It is clear that in the summer halfyear the net shortwave radiation is the largest component. Globally speaking, net shortwave radiation, net longwave radiation and the turbulent sensible heat flux are an order-of magnitude larger than the other components, but on individual days this can be very different, of course.

The loss of energy by net longwave radiation is generally smaller in summer, because the air temperature is high. Moreover, the outgoing longwave radiation is limited because the surface temperature cannot exceed the melting point. The daily mean longwave radiation varies typically between 0 and -100 W m^{-2}. The large fluctuations from day to day are mainly related to cloudiness, especially in wintertime. Days with little clouds in winter show values of between -50 and -100 W m^{-2}. During cloudy days net longwave radiation is close to zero.
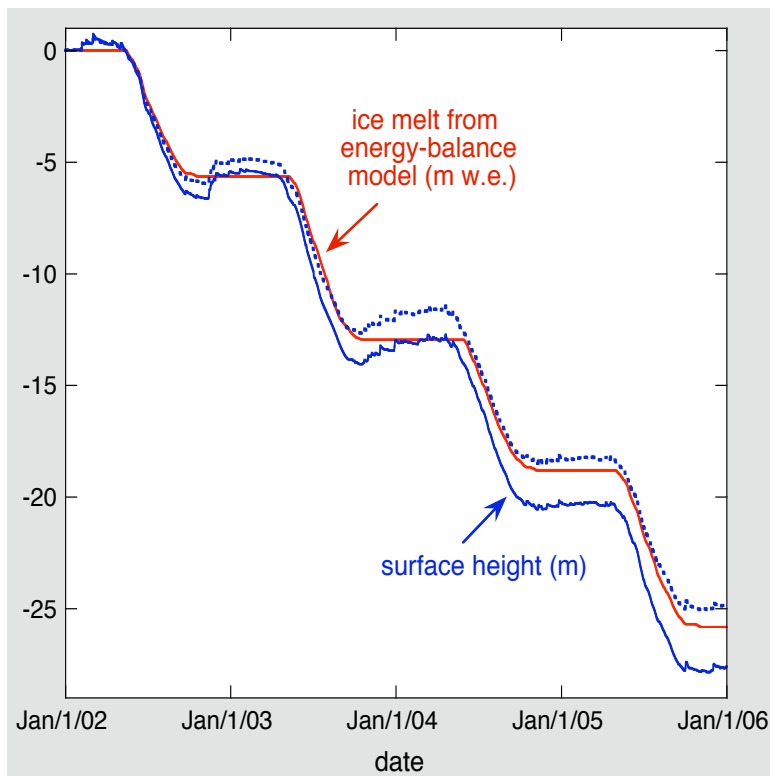

Figure 5.4. A comparison between the measured surface height and the ablation calculated from the analysis of the energy balance (data from the AWS on the tongue of the Vadret da Morteratsch).

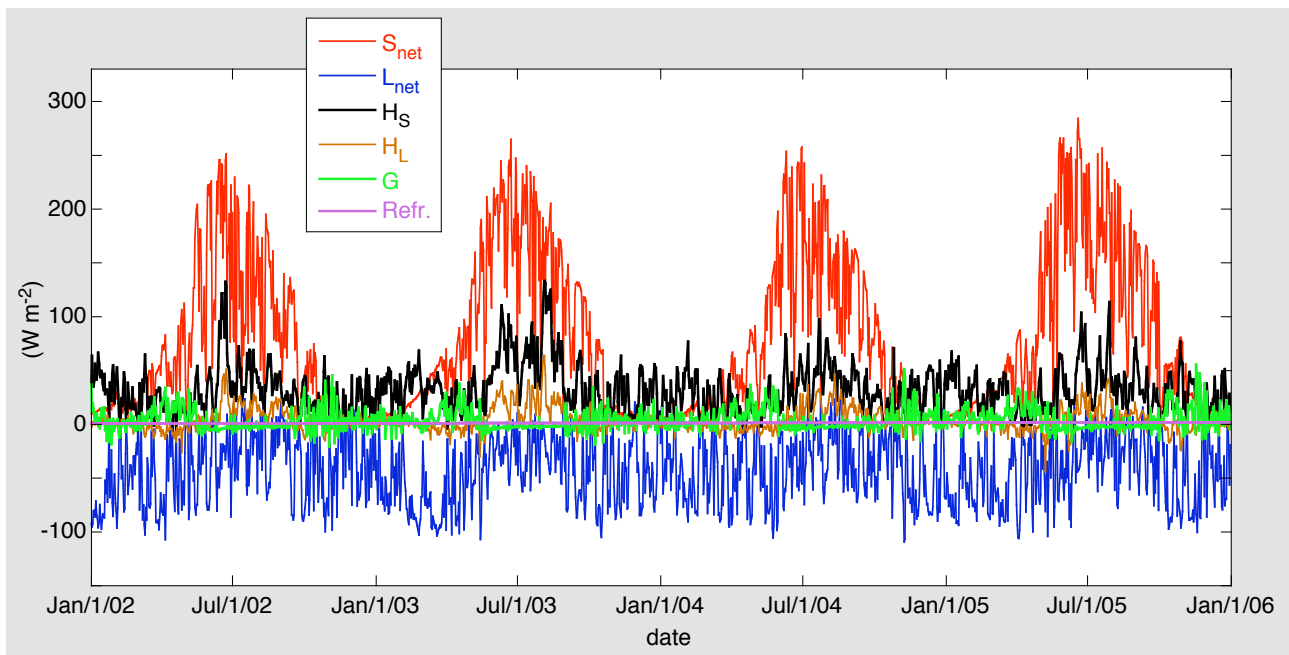*5 - The surface energy flux, ablation, and balance rate*

Figure 5.5. Components of the daily mean surface energy balance at the tongue of the Vadret da Morteratsch, as calculated with the energy balance model. Shown are net shortwave radiation, net longwave radiation, sensible and latent turbulent heat flux, heat storage and energy released by refreeezing of meltwater.

Another interesting feature seen in Figure 5.5 is the asymmetry in the net shortwave radiation with respect to the summer solstice. The lowering of the albedo (transition from snow to ice) occurs when the flux of incoming solar radiation is large, which causes a very steep increase in the net solar radiation. The decrease in net solar radiation in fall is more gradual.

For the AWS site on the Vadret da Morteratsch refreezing of meltwater does not appear to be very important. Although the refreezing process is responsible for heating up the snowpack in late spring, the amount of energy involved is small with respect to the total amount of energy consumed by the melt process during the ablation season. However, this cannot be regarded as a general result. It is well known that on glaciers in colder and drier conditions the refreezing process is more important (e.g. Wright et al., 2007).

Since air temperature generally decreases when going upward, the incoming longwave radiation as well as the turbulent heat fluxes will decrease. At the same time, the incoming solar radiation increases significantly with height (Figure 2.8). It can therefore be expected that the relative contribution of solar radiation to the melt energy increases with altitude, although an increasing albedo works in the opposite direction. The Vatnajökull experiment (Oerlemans et al., 1999), during which many meteorological stations were operated at different altitudes in the summer of 1996, provides an oppertunity to investigate this. In Figure 5.6 the total melt energy, obtained from the measured amount of ablated firn and ice, is shown for a number of stations on the ice cap, ordered with respect to altitude.

In a relatively simple analysis (Oerlemans et al., 1999), the contribution of the turbulent fluxes to the melt energy was calculated by subtracting the measured net solar and net longwave radiation from the total melt energy. The effects of refreezing and storage in the upper layers were neglected. For the investigated period these effects are certainly small on a maritime glacier. The result is shown in Figure 5.6.
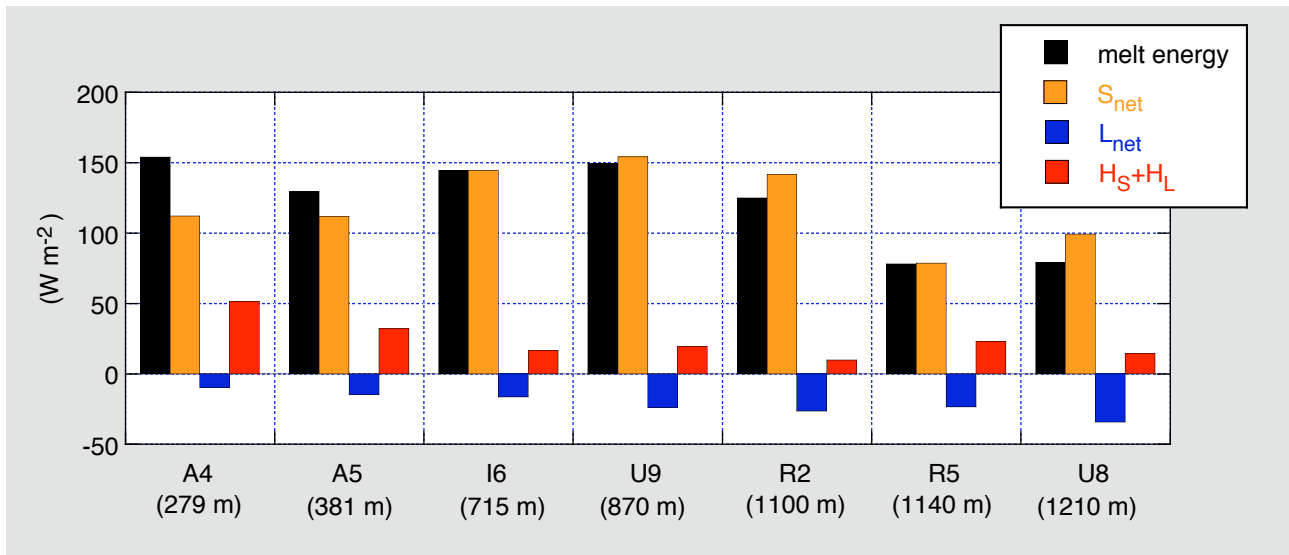
Figure 5.6. Contributions of solar radiation, longwave radiation and turbulent fluxes to the melt energy as observed on Vatnajökull (mean values for the period 22 May – 31 August 1996). See Figure 2.7 for the location of the stations.

First we note that the total melt at stations I6, U9 and R2 is larger, in spite of the relatively high altitude. This is caused by the larger amount of incoming solar radiation and the low albedo (tephra on the glacier surface). At R5 and U8 the surface albedo is higher and average cloudiness is much larger. The components of the energy balance that are directly related to temperature show a more consistent picture. The turbulent fluxes and the net longwave radiation decrease steadily with altitude. The sum of the turbulent fluxes and the net longwave radiation can be related to the 2 m air temperature as measured at the stations. It turns out that this sum increases by 10.7 W m^{-2} K^{-1}. However, it should be noted that the 2 m air temperature is not equal to the ambient temperature. If the altitudinal gradient of the stations would be converted to an air temperature by using a lapse rate of -0.0065 K m^{-1}, the increase would be 8.0 W m^{-2} K^{-1}.

5.4 A simple mass balance calculation

The diagnosis of the surface energy flux discussed above makes it possible to construct a simple mass balance scheme (see also Oerlemans, 2001; section 4.4). We assume that:

$$\text{ablation rate} = \min\{0; -\psi_c / L_m\} ,$$
(5.4.1)

where L_m is the latent heat of melting and ψ_c is defined by eq. (5.2.1). Since we will integrate ψ_c over a full year to obtain the total ablation, we may set $t_m = 0$ without loss of generality. So we have

$$\psi_c(t) = \max\left\{0; A_0 + A_1 \cos\frac{2\pi t}{T}\right\} .$$
(5.4.2)

Note that there is never any ablation when $A_0 < -A_1$, and that there is ablation all year round when $A_0 > A_1$. Accumulation is prescribed in a simple way as well: we assume that the accumulation rate

is constant when $\psi_c = 0$, and zero otherwise. The model is illustrated in Figure 5.7. The figure depicts the case when $-A_1 < A_0 < A_1$. There is ablation from $t = 0$ onwards and it will stop at time t_e, given by

$$t_e = \frac{T}{2\pi} \arccos\left(\frac{-A_0}{A_1}\right).$$

(5.4.3)

The total ablation W_c (≤ 0) is thus obtained from (note that now the ψ_c curve is symmetrical with respect to $t = T/2$):

$$W_c = -\frac{2}{L_m} \int_0^{t_e} \left[A_0 + A_1 \cos\left\{\frac{2\pi t}{T}\right\} \right] dt = -\frac{2A_0 t_e}{L_m} - \frac{A_1 T}{\pi L_m} \sin\left\{\frac{2\pi t_e}{T}\right\},$$

(5.4.4)

and the total accumulation A_c is given by

$$A_c = 2(T/2 - t_e)P .$$

(5.4.5)

In eq. (5.4.5) P is the precipitation rate, assumed to be constant throughout the year.
With the expression for melt and accumulation given above it is now possible to formulate a mass balance model. As a first step we divide an imaginary glacier in three zones: (i) a zone without any ablation, (ii) a zone where there is ablation during part of the year, and (iii) a zone where there is ablation all year round. A real glacier does not necessarily have all these zones. In fact, many glaciers will be entirely in zone (ii).
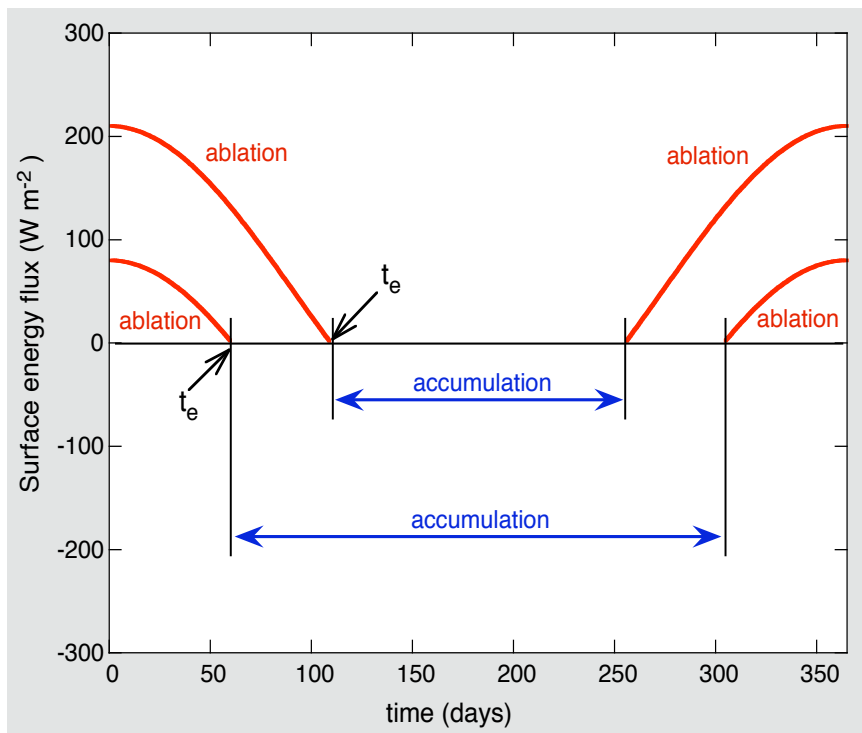The mass balance model can now be formulated as:

Figure 5.7. Illustration of the simple mass balance model for two points on a glacier. The lower curves correspond to a higher location on the glacier.

(i) $A_0 < -A_1$ (no ablation)   (5.4.6)

$$A_c = TP \ ,$$

$$W_c = 0 \ .$$

(ii) $-A_1 < A_0 < A_1$ (ablation during part of year)   (5.4.7)

$$A_c = 2(T/2 - t_e)P \ ,$$

$$W_c = -\frac{2A_0 t_e}{L_m} - \frac{A_1 T}{\pi L_m}\sin\left\{\frac{2\pi t_e}{T}\right\} \ .$$

(iii) $A_0 > A_1$ (continuous ablation)   (5.4.8)

$$A_c = 0 \ ,$$

$$W_c = -\frac{A_0 T}{L_m} \ .$$

In these equations t_e is given by eq. (5.4.3). The specific balance rate is obtained from

$$\dot{b} = A_c + W_c \ . \qquad\qquad\qquad\qquad\qquad\qquad\qquad\qquad\qquad\qquad (5.4.9)$$

The calculation of the balance described above is for a single point. If we want to calculate a balance profile, we have to specify how A_0, A_1 and P depend on altitude. We assume that A_1 is constant, and that A_0 and P vary linearly with altitude h according to:

$$A_0 = -\gamma_E (h - h_{ref}) \ , \qquad\qquad\qquad\qquad\qquad\qquad\qquad\qquad (5.4.10)$$

$$P = P_{sl} + \gamma_P h \ . \qquad\qquad\qquad\qquad\qquad\qquad\qquad\qquad\qquad (5.4.11)$$

The constants γ_E (< 0) and γ_P (normally > 0) indicate how the surface energy flux and precipiation rate change with altitude, respectively. The reference altitude h_{ref} can be interpreted as the height at which the ablation season lasts six months. For precipitation we take zero altitude (sea level) as a reference point (P_{sl}).

Five parameters thus need to be specified to calculate a balance profile. First we consider a case typical for the Alps. We choose $A_1 = 230\,\mathrm{W\,m^{-2}}$ (compare with Table 5.1), $\gamma_E = 0.15\,\mathrm{W\,m^{-3}}$, $P_{sl} = 1\,\mathrm{m}$, $\gamma_P = 0.0005$ and $h_{ref} = 2200\,\mathrm{m}$. The value of γ_E was estimated from the results of the Pasterze experiment (Greuell and Smeets, 2001; Table I). The other parameter values are characteristic numbers that match the observations on the Vadret da Morteratsch (notably the surface energy flux at the AWS site).

The result from a calculation with these parameter values is shown in Figure 5.8. In this case the 'no ablation zone' is above 3750, and the equilibrium is at about 3000 m. The small kink in the balance curve at an altitude of 3650 m is due to the cut-off of ablation at the top of the sine function. If we were to construct an ensemble mean balance profile over a number of years, where A_0 varies slightly from year to year, the kink would be smoothed out.
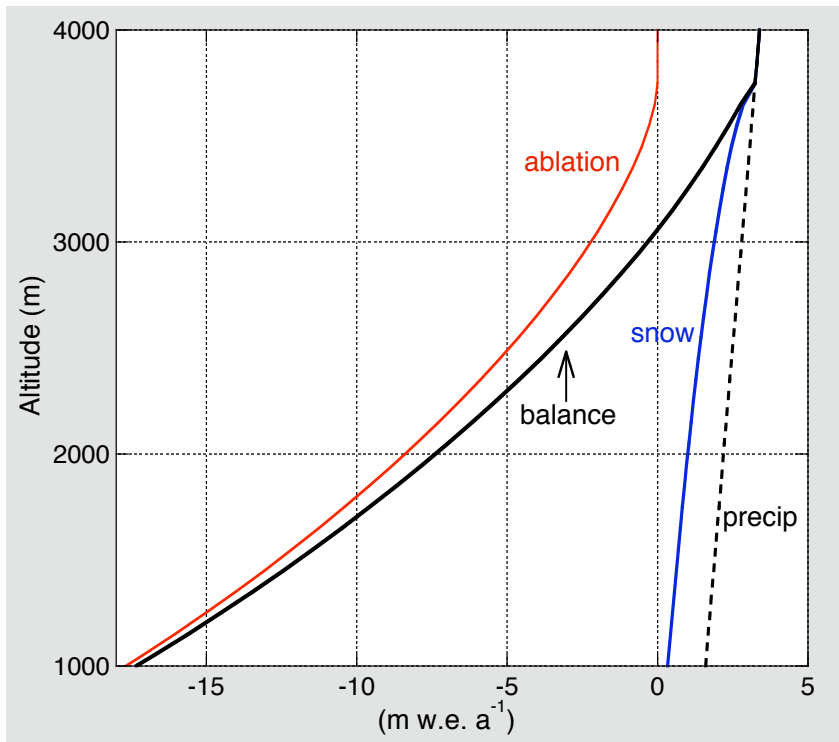
Figure 5.8. Result of the mass balance model with parameters typical for the Alps.

5.5 A calculation for Nigardsbreen, Norway

The simple mass balance model can be applied to glaciers that have a reasonably smooth balance profile, like Nigardsbreen (Østrem et al., 1977; Kjøllmoen, 2008). Nigardsbreen is an outlet glacier of Jostedalsbreen, the largest ice cap in mainland Norway. Nigardsbreen has an area of about 48 km^2 and spans an altitudinal range from 320 to 1960 m a.s.l. Mass balance measurements have been carried out on this glacier since 1963. The historcial length variations of Nigardsbreen have been studied with numerical glacier flow models (Oerlemans, 1997b).

We apply the simple mass balance model to this glacier by adjusting a few of the parameters used in section 5.4. We take $A_1 = 200 \, \mathrm{W \, m^{-2}}$ (because Storbreen is not so far from Nigardsbreen; Table 5.1), $\gamma_E = 0.15 \, \mathrm{W \, m^{-3}}$, $P_{sl} = 1.5 \, \mathrm{m}$, $\gamma_P = 0.0015$ and $h_{ref} = 880 \, \mathrm{m}$. The result is shown in Figure 5.9. The mean observed balance profile over the period 1989-2004 is also plotted, together with the corresponding winter balance. The difference between the observed and simulated balance profile is small, in spite of the simplicity of the model and the limited amount of input data. We may also compare the calculated accumulation with the observed winter balance. In the upper half of the glacier the correspondence is good, but in the lower part of the glacier the winter balance is significantly smaller than the calculated snow accumulation. This is due to the fact that the winter balance is normally measured in May, when the snow on the glacier tongue has already (partly) melted. Therefore the discrepancy has little meaning with regard to the performance of the model.

It is interesting to use the simple mass balance model for a climate sensitivity test. In order to calculate the response of the balance profile to a uniform change in ambient air temperature (ΔT_a), we first have to relate A_0 to ΔT_a. The effects on the turbulent heat flux and net longwave balance should both be included. In earlier work it was argued that for the sum of these fluxes a value of 10 W m^{-2} K^{-1} is a reasonable value (Oerlemans, 2001; p. 47). In section 5.3 we found from the

Vatnajökull experiment a value of 8 W m^{-2} K^{-1}. In the simple mass balance model the albedo feedback is not included. In reality a higher temperature leads to a longer ablation season, and thus to a lower mean albedo. The resulting increase in net solar radiation is not taken into account in the model formulated in section 5.4. In view of this we prefer to use the higher value of 10 W m^{-2} K^{-1}. To calculate the changes in the net balance rate $\dot{b}_n$, the net gain or loss in a certain height interval k has to be weighted by the corresponding surface area. So

$$\dot{b}_n = \frac{1}{S_{tot}} \sum_{k=1}^{K} \dot{b}_k \, S_k \; .$$

(5.5.1)

Here S_{tot} is the total glacier area, S_k the surface area of height interval k, and $\dot{b}_k$ the balance rate of height interval k. In the following the area data have been taken from Kjøllmoen, 2008.

First we look at changes in the balance profile (Figure 5.10). For a 1 K temperature increase the decrease in the balance rate varies from about -0.6 m w.e. a^{-1} at the glacier snout to about -0.3 m w.e. a^{-1} in the highest parts of the glacier. For a 10 % increase in precipitation the change in the balance rate also depends strongly on altitude. The black curve in Figure 5.10 shows the change in the balance rate when perturbations of temperature and precipitation are applied simultaneously. There is only compensation of the temperature and precipitation effects on the balance rate for the highest part of the glacier. On the glacier tongue the effect of increasing precipitation is really small.
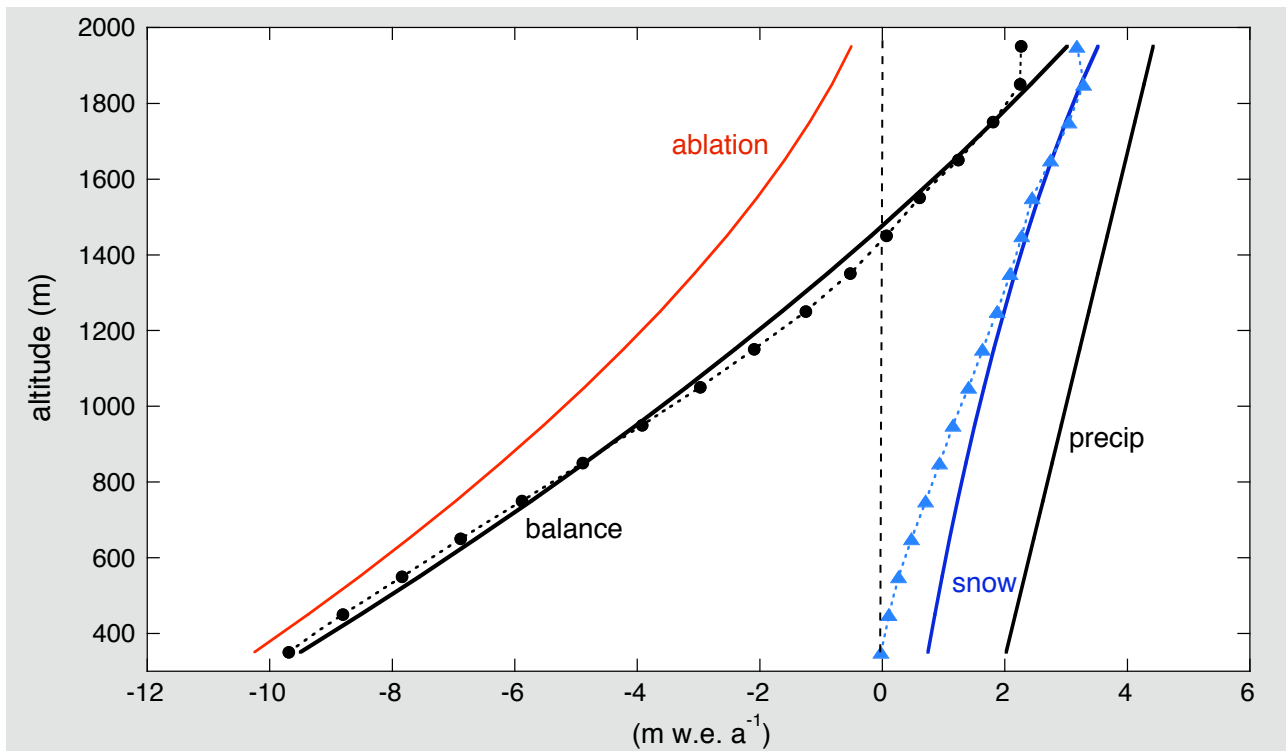

Figure 5.9. The simple mass balance model applied to Nigardsbreen, Norway. Dotted lines with symbols show observations (for 100 m altitude bands): black dots refer to the balance rate, blue triangles to the winter balance.

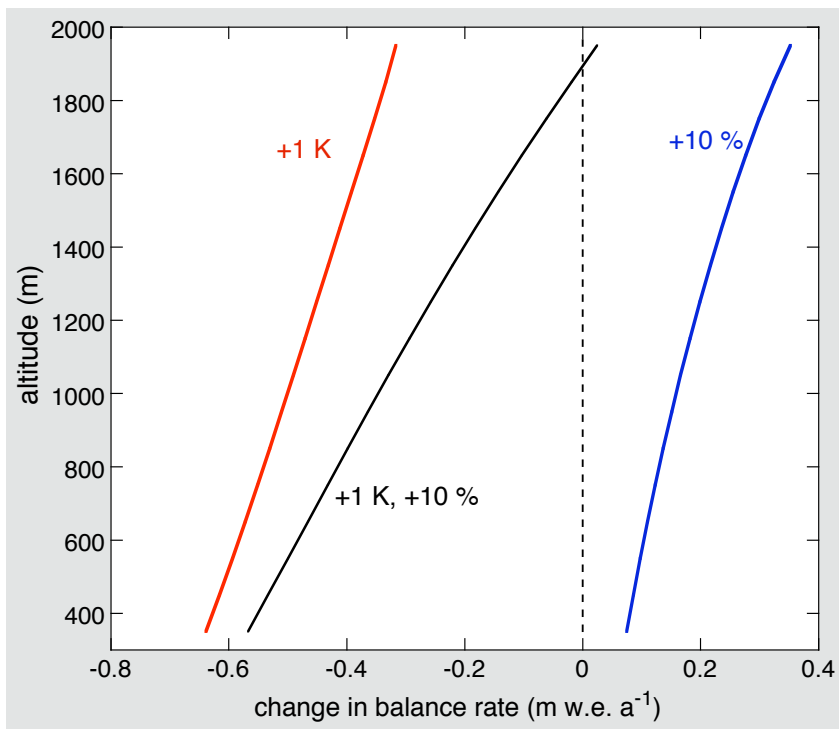*5 - The surface energy flux, ablation, and balance rate*

Figure 5.10. Changes in the calculated balance profile for Nigardsbreen for a temperature increase of 1 K (red) and a precipitation increase of 10 % (blue). The black curve shows the combined effect.

The observed value of $\dot{b}_n$ is 0.66 m w.e. a^{-1} and the simulated value for the reference case is 0.59 m w.e. a^{-1}. These values could be made identical by adjusting the model parameters, but that would not be a very meaningful exercise. For a 1 K temperature increase $\dot{b}_n$ changes by -0.39 m w.e. a^{-1}. This is a rather small value compared to the value obtained with a more sophisticated energy balance model (namely -0.66 m w.e. a^{-1}; Oerlemans, 2001). The difference is most likely due to the lack of albedo feedback in the simple model. For a 10 % precipitation increase $\dot{b}_n$ changes by -0.26 m w.e. a^{-1}. The combined effect of the temperature and precipitation increase is a change in $\dot{b}_n$ of about -0.31 m w.e. a^{-1}.

5.6 More sophisticated mass balance models

The fact that a simple model can be calibrated to produce a realistic balance profile does not necessarily imply that results from a sensitivity analysis are reliable. A useful model does not need to be complex, but it should deal with all processes that are known to be important. The knowledge about which processes really matter normally stems from scaling arguments of the relevant mathematical description in combination with observational evidence.

The most obvious process missing in the simple mass balance model of section 5.4 is the coupling between the accumulation/ablation history and the surface albedo. Geometric factors affecting the amount of solar radiation received by the glacier surface can also be very important (e.g. slope and aspect of the surface, shading by surrouding mountains).

It is probaby fair to say that pioneering work on glacier mass balance modelling, based on a year-round consideration of the surface energy balance and an interactive albedo scheme, was carried out by Greuell and Oerlemans (1987), and Oerlemans and Hoogendoorn (1989). Profiles of the balance rate were obtained by evaluating the energy balance at gridpoints spaced at equal differences in altitude (like in section 5.5). Simulations with these models have generally been successful in the

sense that it was not difficult to reproduce observed balance profiles after calibration. Model calibration is necessary, because it is not possible to calculate the absolute mean specific balance of a glacier from meteorological input data, simply because the accuracy of such data is limited. Or, formulated in another way, glacier mass balance is too sensitive to meteorological input data. However, if this were not the case the response of glaciers to climate change would be very slight and of limited interest.

Further application to real glaciers (e.g. Oerlemans, 1991, 2001) lead to a few outstanding conclusions, namely that (i) the net balance of maritime glaciers is much more sensitive to temperature changes than the net balance of continental glaciers, (ii) to compensate for the effect of a 1 K temperature increase, an increase in precipitation of 20 to 40 % is needed. More recently, the energy balance approach has been extended to spatially-distributed mass-balance modelling (e.g. Klok and Oerlemans, 2002; Reijmer and Hock, 2008).

At this point it should also be mentioned that another class of mass balance models is based on a simpler concept, namely the temperature index method to calculate ablation (e.g. Braithwaite and Zhang, 2000; De Woul and Hock, 2005). In this approach the basic idea is that ablation can be parameterized entirely in terms of air temperature. The total ablation in a summer is then for instance assumed to be proportional to the cumulative sum of positive temperatures (the 'temperature index'). Constants of proportionality ('melt factors') are chosen differently for snow and ice surfaces, thus implicitly taking into account the effect of differences in surface albedo. In view of the results from energy balance studies on glaciers, as summarized in e.g. Figures 5.4 and 5.5, the validity of a temperature index method must be questioned. Although in most cases the melt factors can be determined in such a way that observed balance profiles are reproduced, this does not necessarily imply that the model can provide a realistic estimate of the sensitivity of the balance rate to temperature change. Because all the ablation due to net solar radiation is assigned to the temperature index, it is implicitly assumed that, when temperature changes, the net solar radiation changes in proportionality. This may sometimes be the case (if warm summers are sunnier), but it is unlikely that net solar radiation and air temperature are always positively correlated when long-term climate change is considered. Therefore it remains unclear whether temperature index models provide a reliable estimate of the sensitivity of glacier mass balance to temperature change.

It has been argued that the use of energy balance models is cumbersome because so many input variables and parameters are required. To some extent this is a valid argument. Even if the meteorological input data are available, there is still uncertainty about the various parameters in the fomulations of the energy fluxes. To give an example, Klok and Oerlemans (2002) use the following equations to calculate the incoming longwave radiation:

$$L_{in} = \varepsilon \sigma T_a^4 = \left[\varepsilon_{cs} (1 - n^p) + \varepsilon_{cl} n^p \right] \sigma T_a^4 \ , \tag{5.6.1}$$

$$\varepsilon_{cs} = a + b (e_v / T_a)^\kappa \ . \tag{5.6.2}$$

Here ε is an effective atmospheric emissivity, made up of a contribution from the cloud-free part of the sky (ε_{cs}) and a contribution from the cloudy part of the sky (ε_{cl}). Furthermore, T_a is the air temperature, n the fractional cloudiness and e_v the vapour pressure. Altogether the parameterisation involves 5 empirical constants (p, ε_{cl}, a, b, κ). When data from an AWS are available, these constants can be determined individually. But even then further complications are normally

encountered: some of the constants appear to vary through the year. Moreover, altitudinal gradients have to be dealt with (for instance, the clear-sky emissivity decreases with altitude).

In view of this, it remains attractive to search for simplification. In Oerlemans (2001) a model was proposed based on a simple parameterization of the daily mean surface energy flux:

$$\dot{b}_{cum}(t+1) = \dot{b}_{cum}(t) + \Delta t \left\{ \min(0; -\psi_d(t)/L_m) + \dot{a}(t) \right\} , \tag{5.6.3}$$

$$\psi_d = \tau_e(1-\alpha)Q_E + c_0 + c_1 T_d . \tag{5.6.4}$$

Now t is the discrete time variable in days and Δt the time step (1 day). The mean daily surface energy flux is denoted by ψ_d. T_d is the daily mean free air temperature and c_0 and c_1 are suitable constants. The model formulated by eqs. (5.6.3)- (5.6.4) has been successfully applied to a number of glaciers (e.g. Nigardsbreen).

An alternative approach, in which the daily cycle can be retained, is to use an equation similar to eq. (5.6.3) with a much smaller time step (e.g. 15 minutes). So all energy fluxes not directly related to solar radiation are expressed in terms of air temperature only. Using a small time step makes it possible to study the effects of shading and sloping surfaces on the net solar radiation in a relatively simple way. In the next chapter we will explore the possibilities of such an approach.

Albedo variations over the Vadret da Morteratsch, September 2005.

6. A mass balance model for valley glaciers

6.1 Introduction

Mass balance models generate the balance rate from meteorological input data. A consideration of the energy budget of the glacier surface is central to the whole procedure. We define the cumulative balance rate as

$$\dot{b}_{cum}(t) = \int_0^t \{\dot{a}(t') - \dot{m}(t') + \dot{a}_{Hl}(t')\} \, \mathrm{d}t' \ , \tag{6.1.1}$$

where $\dot{a}(t')$ and $\dot{m}(t')$ are the time-dependent accumulation rate and ablation rate, respectively. Mass exchange associated with the latent turbulent heat flux (sublimation, riming) is denoted by $\dot{a}_{Hl}$. The balance refers to the total mass change in a vertical column. The lower boundary of this column can be regarded as a material surface at a few meters depth. Apart from the more obvious processes like snowfall and runoff, sub-surface melting, refreezing meltwater or rain, snowdrift, etc., can also make a contribution to the balance rate.

Modelling the ablation can be done in many ways. A frequently made assumption is that melting and runoff occurs whenever the surface energy flux is positive. In such an approach the surface temperature is at the melting point all the time and refreezing is not considered. The implications of this were studied in some detail by Greuell and Oerlemans (1987). By comparing simulations with and without a temperature calculation in the upper layers of the glacier, they concluded that the simple approach with a perpetual melting surface works well for glaciers with a large mass turnover. However, for drier and colder conditions, like on subpolar glaciers or in the upper parts of midlatitude glaciers, the refreezing process is significant. In a recent study, Wright et al. (2007)

made a thorough study of different schemes to deal with refreezing and internal acumulation. At a later stage we will come back to this.

If processes in the upper layers of the glacier are neglected [$G = 0$ in eq. (5.1.2)], and the term $\dot{a}_{Hl}$ is supposed to be small, the cumulative balance can be calculated from

$$\dot{b}_{cum}(t) = \int_0^t \left[\dot{a}(t') + \min\{0; -\psi(t')/L_m\} \right] dt \; , \tag{6.1.2}$$

where

$$\psi = \tau_e (1 - \alpha) Q_E + f(T_a) \; . \tag{6.1.3}$$

Here Q_E is the extra-terrestrial irradiance, τ_e the effective atmospheric transmissivity for solar radiation, and $f(T_a)$ is a suitable function of the atmospheric temperature T_a. The reflected solar radiation is now taken into account by introducing the (full-spectrum) albedo α. As argued before, in a mass balance model it is important to generate the albedo within the model, because the albedo feedback is an essential process. To deal with geometric effects on the amount of solar radiation received by a tilted surface, it is useful to make a distinction again between direct radiation and diffuse radiation (see Figure 4.12).

First we consider solar radiation, and develop a scheme with which the effects of a sloping surface and shading can be taken into account in a relatively simple way. After that we study the temperature dependent part of the surface energy flux. We will try to find a suitable expression for $f(T_a)$ by looking at the data from the automatic weather stations discussed before.

6.2 Solar radiation – geometric effects

The amount of solar energy that is intercepted by the earth is determined by the solar constant S^*. The solar constant is defined as the energy flux through a unit area perpendicular to the solar beam, at the mean earth-sun distance. Its value is $1367 \pm 3 \, \mathrm{W\,m^{-2}}$. At present, the earth-sun distance varies little over the year, because the eccentricity of the earth orbit around the sun is small (currently 0.0167). We define the extra-terrestrial irradiance on a horizontal surface as

$$S_E = S^* (\bar{r}/r)^2 \sin e \; . \tag{6.2.1}$$

Here e is the solar elevation, r the actual sun-earth distance and $\bar{r}$ its annual mean value. The quantity $(\bar{r}/r)$ can be approximated by the following expansion:

$$(\bar{r}/r)^2 = 1.0011 + 0.034221 \times \cos(2\pi N/365) + 0.00128 \times \sin(2\pi N/365) +$$
$$+ 0.000719 \times \cos(4\pi N/365) + 0.000077 \times \sin(4\pi N/365) \; . \tag{6.2.2}$$

N is the day of the year (1st January=1).
The solar elevation is given by (e.g. Walraven, 1978)

$$\sin e = \sin\phi \sin\delta + \cos\phi \cos\delta \cos\omega_h \; , \tag{6.2.3}$$

where ϕ is latitude, δ the solar declination (0° at the vernal and autumnal equinoxes, 23.45° at the NH summer solstice, -23.45° at the SH solstice), and ω_h the hour angle (here taken as positive in the morning, zero at noon, negative in the afternoon; decreasing by 15° per hour). The declination angle (in radians) can be calculated to a sufficiently good approximation from

$$\delta = 23.45 \frac{\pi}{180} \sin\left\{2\pi \frac{284+N}{365.25}\right\} . \tag{6.2.4}$$

The solar illumination on a horizontal surface for a transparent atmosphere can now be calculated from eqs. (6.2.1)-(6.2.4) for any latitude and any time of the day. More details can be found in textbooks on radiation. Special methods have been developed to obtain daily totals in an efficient way (e.g. Allen et al., 2006).

It is instructive to consider the effect of latitude on the extra-terrestrial irradiance, because it is one of the basic factors determining the length and intensity of the ablation season. Increasing latitude implies a smaller annual mean value, a larger seasonal amplitude and a smaller daily amplitude of S_E. Figure 6.1 shows how the daily mean value of S_E varies through the year. In summer, there is little change with latitude. Furthermore the well-known features are seen: the double maximum in the equatorial regions and the polar night at high latitudes. At this point we should realize that there is no simple relation between S_E and global radiation at the surface. Because the mean solar elevation is less at higher latitudes, the apparent optical mass of the atmosphere is larger and absorption and reflection of solar radiation are stronger.

The seasonal cycle in S_E increases strongly with latitude, but at the same time the daily cycle decreases. Figure 6.2 shows S_E calculated for some selected latitudes on a day in summer. For very high latitudes the daily cycle becomes really small.
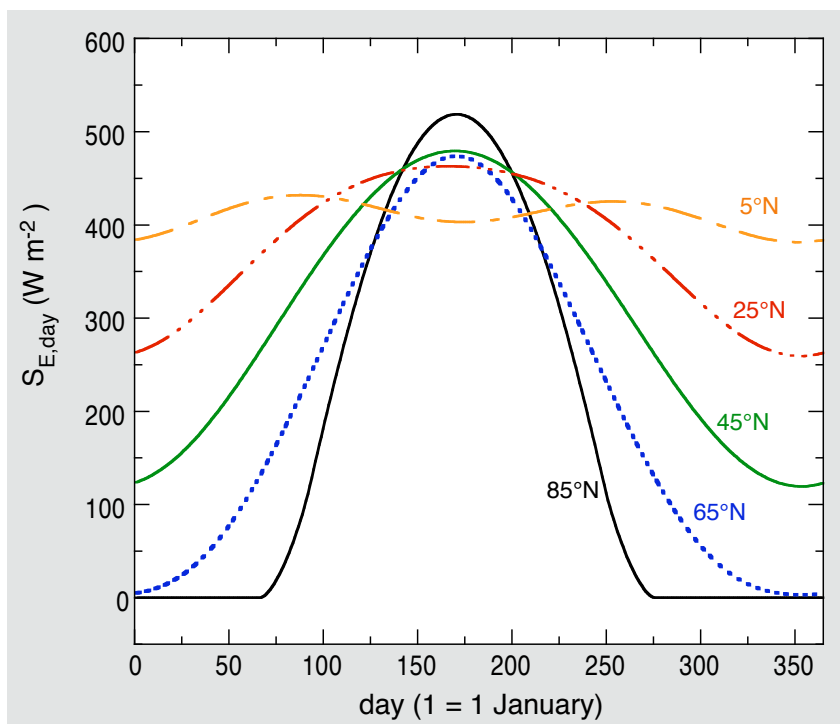

Figure 6.1. Daily mean values of the extra-terrestrial irradiance for a horizontal surface.
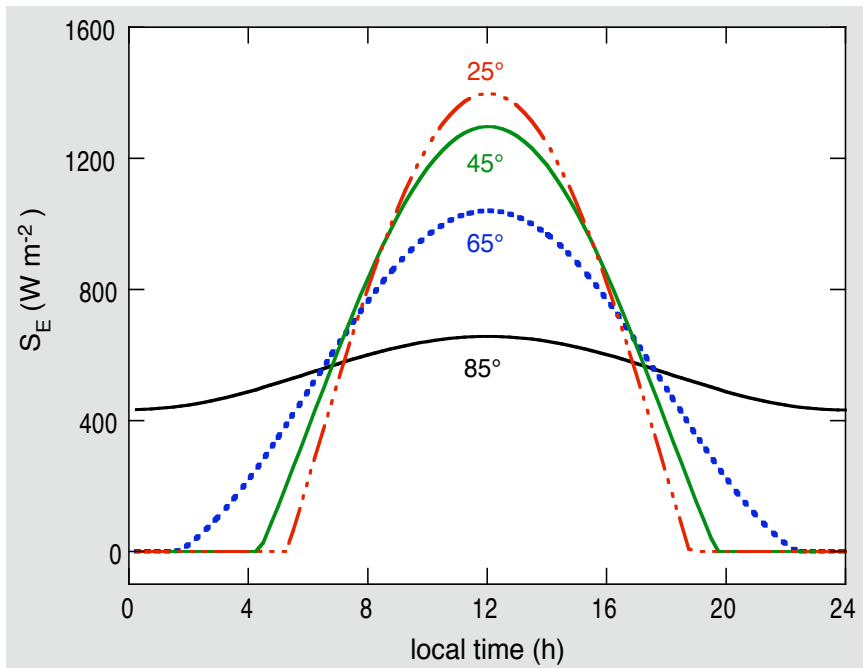
Figure 6.2. The extra-terrestrial irradiance for 29 June at some selected latitudes (Northern Hemisphere).

A number of steps are needed to relate S_E to the solar radiation that may become available at a glacier surface. First of all there are local geometric factors like shading by mountains, and the slope and aspect of the surface and reflection from surrounding slopes.

To calculate the effect of geometry, the modification of the solar beam in the atmosphere has to be considered. Sophisticated methods have been devised to deal with this; the ultimate method for a valley with a complicated geometry in which scattering clouds are present is a Monte-Carlo technique which traces the path of billions of photons interfering with aerosol, clouds, mountain walls, etc. With a considerable computational effort the distribution of solar radiation can then be obtained from a statistical analysis of the photon paths. It is obvious that such a method is not very suitable for mass balance modelling. Simpler schemes that deal with geometric effects in a schematic way are nomally preferrred.

First we assume that the relation between incoming solar radiation and the extra-terrestrial irradiance can be written as

$$S_{in} = \tau_e \, S_E = \tau_{cl} \, \tau_a \, \tau_g \, S_E \; . \tag{6.2.5}$$

Here τ_e is the total effective transmissivity, τ_{cl} the cloud transmissivity, τ_a the transmissivity related to absorption and scattering by air molecules, water vapour and aerosol. The geometric effects (shading, reflections from surrounding slopes) are represented by τ_g. Eq. (6.2.5) looks simple because the problems are hidden: the transmissivities are not independent. Geometric effects depend on the cloud conditions and it is difficult to disentangle all the possible interactions. Nevertheless, to arrive at a workable approach that can be used in mass-balance models, eq. (6.2.5) is a useful representation of the reduction of the solar flux by atmospheric processes.

To investigate the implications of a sloping glacier surface we assume that S_{in} consists of direct radiation, which comes from a single direction, and diffusive radiation, which is isotropic:

$$S_{in} == f_{dir} \, S_{in} + f_{dif} \, S_{in} \qquad (f_{dir} + f_{dif} = 1) \; . \tag{6.2.6}$$

For clear-sky conditions in mountain regions f_{dif} is typically 0.15, for an overcast sky 0.85. But this really depends on the type of clouds: e.g. for a uniform layer of cirrostratus f_{dif} can be 0.5. The values of f_{dir} and f_{dif} also depend on other atmospheric constituents (notably aerosol). Over lowlands and industrial areas the diffusive radiation in clear-sky conditions may be much larger. However, in mountain regions with a relatively small aerosol loading of the atmosphere it is mainly the cloudiness that determines the variation of f_{dir} and f_{dif}.

We can now develop a formulation for the amount of solar radiation impinging on a *sloping* surface. We denote the flux by $S_{in,S}$, to distinguish it from the flux received by a horizontal surface. In our approach slope and aspect only affect the direct radiation because the diffusive part is assumed to be isotropic. Denoting the *apparent* solar elevation with respect to the sloping surface by e' we then have

$$\text{if } e > 0 \wedge e' > 0: \quad S_{in} = \tau_e \, S_E \, (f_{dir} \, \sin e' + f_{dif} \, \sin e) \; ,$$

$$\text{if } e > 0 \wedge e' \leq 0: \quad S_{in} = \tau_e \, S_E \, f_{dif} \, \sin e \; , \tag{6.2.7}$$

$$\text{if } e < 0: \quad S_{in} = 0 \; .$$

The calculation of the apparent solar elevation e' for given slope s and surface azimuth γ_s can be done with the following equation (Garner and Ohmura, 1968; Allen et al., 2006):

$$\sin e' = \sin\delta \, \sin\phi \, \cos s + \sin\delta \, \cos\phi \, \sin s \, \cos\gamma_s + \cos\delta \, \cos\phi \, \cos s \, \cos\omega_h +$$
$$- \cos\delta \, \sin\phi \, \sin s \, \cos\gamma_s \, \cos\omega_h - \cos\delta \, \sin\gamma_s \, \sin s \, \sin\omega_h \; . \tag{6.2.8}$$

The surface slope is always taken positive. The surface azimuth γ_s is measured clockwise from north (so an eastward facing slope has $\gamma_s = \pi/2$, southward facing slope has $\gamma_s = \pi$, etc.). In the literature one can find different versions of eq. (6.2.8), depending on the definition of the geometry and whether the solar azimuth angle appears in the equation or has been eliminated (as is the case for eq. (6.2.8)). The solar azimuth angle γ_{sol} can be obtained from (also measured clockwise from north):

$$\sin\gamma_{sol} = \frac{\cos\delta \, \sin\omega_h}{\cos e} \; . \tag{6.2.9}$$

The procedure described above is about the simplest way in which the geometric effect of a sloping surface on the incoming solar radiation can be calculated. Now we turn to shading by surrounding mountains (Figure 6.3). The shading angle ϕ_s, defined as the angle between the horizontal and the skyline, varies with the azimuth, of course. For many glaciers shading is a significant factor, or, put the other way round, glaciers tend to form in shaded places. Glaciers flowing into narrow deep valleys away from the sun can penetrate to much lower altitudes.

How can shading be dealt with? The approach in which the solar radiation is split into a direct and diffusive part is again useful. When the sun is behind the mountain rim the direct flux must vanish,

Figure 6.3. For glaciers in steep mountain terrain shading may strongly affect the surface enery budget.

but there will still be diffusive radiation as long as $e > 0$. So shading can be taken into account by setting direct radiation to zero when $\phi_s > e$.

The geometric effects discussed above are illustrated in Figure 6.4. For the example shown in Figure 6.4a the values of f_{dir} and f_{dif} were set to 0.85 and 0.15, respectively. The attenuation of the solar radiation in the atmosphere was not taken into account. This is somewhat inconsistent because it implies the presence of diffusive radiation in a fully transparent atmosphere ($\tau_e = 1$). However, it allows us to study purely geometric effects. In the example shown the shading angle is 25° and the slope 10° to the north. Clearly, a considerable part of the extra-terrestrial irradiance does not reach the surface. For the selected parameter values the effect of shading on the daily total incoming radiation is larger than the effect of the slope.
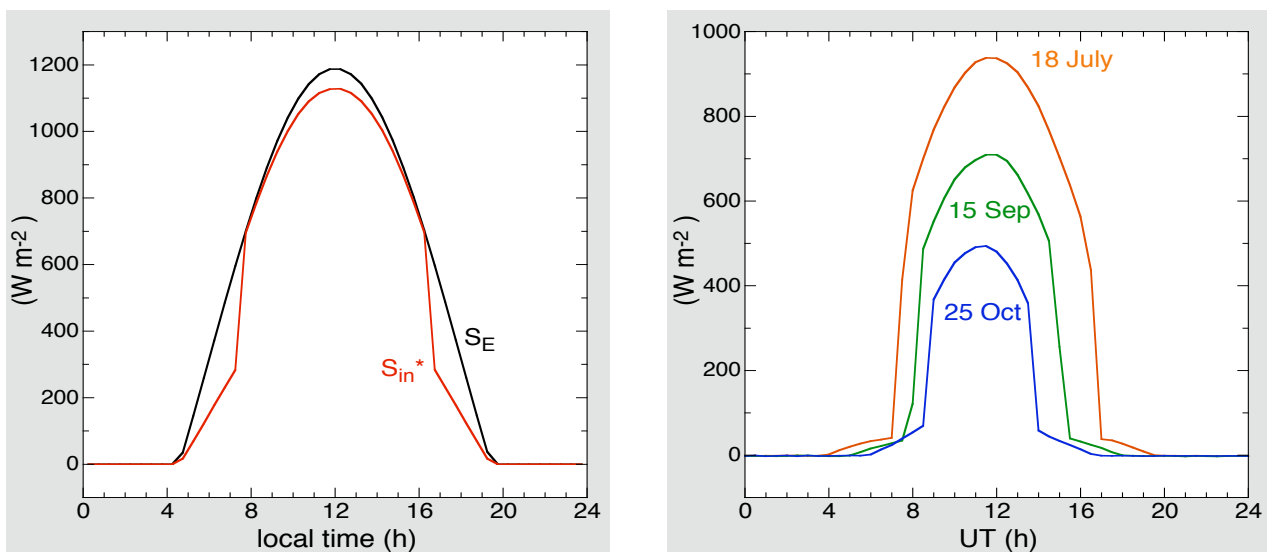

Figure 6.4. (a) The effect of slope and shading calculated for 20 July at 45°N. The shading angle is 25° and the surface slopes 10° to the north. S_E is the extra-terrestrial irradiance. The atmospheric transmissivity (τ_e) has been set to unity. (b) Incoming solar radiation as measured by the AWS on the Vadret da Morteratsch for three different days in 2003. The curves are based on 30-min average values.

6 - A mass balance model for valley glaciers

Figure 6.4b shows observed incoming solar radiation as measured by the AWS on the Vadret da Morteratsch. Three cloudless days have been selected in summer and fall (18 July, 15 September and 25 October, 2003). Because there was very little snow cover, the effect of reflection from the surrounding slopes was limited. The curves show the typical shape expected when shading is important. In contrast to the theoretical case of Figure 6.4a, the shading angle is not constant but varies with the sun's azimuth. Therefore the curves are not perfectly regular nor symmetrical. Nevertheless, the observed data for the Vadret da Morteratsch suggest that on clear days the diffusive radiation is really very small when the sun is still behind (very high) mountains. It is likely that f_{dif} is smaller when the shading angle is larger, because the scattering process creating the diffusive radiation occurs higher in the atmosphere. However, data on which a parameterisation of this effect could be based hardly exist.

6.3 Solar radiation – atmospheric effects

The theory of scattering and absorption of solar radiation in the atmosphere is well developed (e.g. Liou, 1992; Zdunkowski et al., 2007). Many algorithms have been constructed to calculate solar fluxes for a prescribed composition of the atmosphere. In general, the accuracy of calculations performed with such algorithms is limited by the quality of the input data, not by deficiencies in the radiative transfer theory and its numerical implementation.

Clouds form a particularly difficult aspect. In recent years, the application of satellite data has led to substantial progress in the quantification of cloud distribution and cloud physical properties. However, glacio-meteorology has not benefitted much. The detection of clouds over highly reflective surfaces from satellite data is much more difficult. For ice sheets and ice caps some information can be obtained, but there is a lack of data about valley glaciers. Weather satellites are not really helpful because the scale of valley glaciers is too small.

Greuell et al. (1997) analysed the PASTEX-94 data and considered the radiation balance in detail. On the basis of 3-hourly cloud observations (208 data points in the period June 18 to August 9, 1994), the following relation was found for the cloud transmissivity at an altitude of 2205 m (n is the fractional cloud cover):

$$\tau_{cl} = 1 - 0.233\,n - 0.415\,n^2 \tag{6.3.1}$$

This relation is in very good agreement with an analysis of global radiation data from Austrian climate stations carried out by Sauberer (1955). His tables can be fitted well with (h is altitude):

$$\tau_{cl} = 1 - (0.41 - 6.5 \times 10^{-5}\,h)\,n - 0.37\,n^2 \ . \tag{6.3.2}$$

Eqs. (6.3.1) and (6.3.2) are illustrated in Figure 6.5. For comparison, a parameterisation of cloud transmissivity for the Greenland ice sheet is also shown, taken from Konzelmann et al. (1994). This parameterisation is also based on in situ measurements of solar radiation and manual cloud observations. The relation proposed by Konzelmann et al. (1994) is

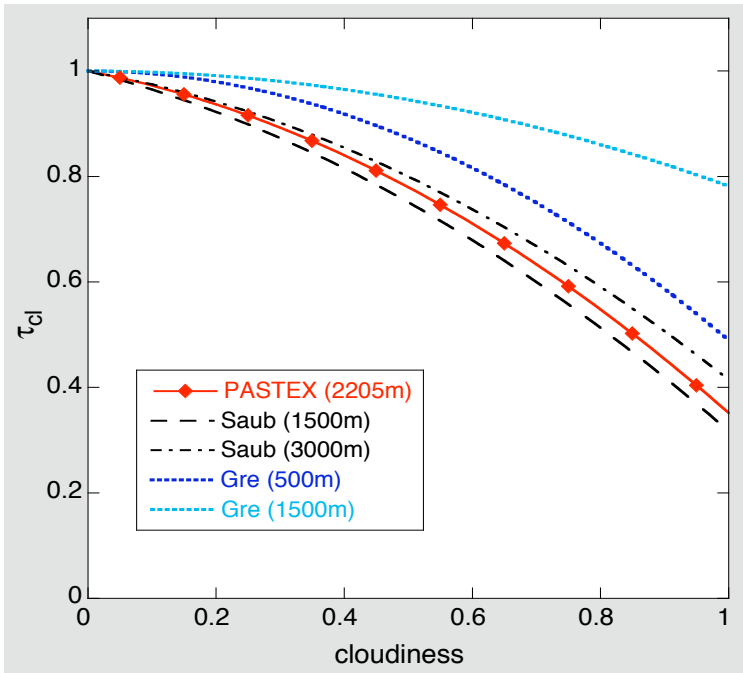$$\tau_{cl} = 1 - 0.78\,n^2 \exp(-0.00085\,h) \ . \tag{6.3.3}$$

Figure 6.5. Parameterisation of cloud transmissivity based on the PASTEX-94 data. The fit to the Sauberer (1955) data is shown for two altitudes.
For comparison, the parameterisation for the Greenland ice sheet derived by Konzelmann et al. (1994) is also shown.

From the curves in Figure 6.5 it is quite clear that clouds on the Greenland ice sheet are optically thinner, especially at higher elevation. There is little effect of such clouds up to a fractional cloud cover of 0.3. Altogether, Figure 6.5 gives a good impression of how global radiation depends on cloudiness. The analysis is still primitive, because no distinction is made between different cloud types. Moreover, cloud transmissivity does not depend on the solar elevation, see e.g. Fitzpatrick et al. (2004). There are practical reasons why a more refined analysis is not feasible, at least not for valley glaciers. For larger ice masses like the Greenland and Antarctic ice sheets more detailed analysis is possible, because there is more horizontal homogeneity in atmospheric conditions.

Next we consider the clear-sky transmissivity τ_a (see eq. 6.2.5). As discussed in section 2.5, global radiation increases strongly with altitude (Figure 2.8). The reasons for this are decreasing cloud amount and decreasing optical mass, including a reduction in constituents that absorb and scatter solar radiation. However, it is very difficult to disentangle the various contributions on the basis of the scarce observations available. In earlier work (Oerlemans, 1992), the following relation appeared to perform satisfactorily:

$$\tau_a = (0.79 + 2.4 \times 10^{-5} h) \left\{ 1 - 0.08 \frac{(\pi/2 - e)}{\pi/2} \right\} . \tag{6.3.4}$$

The solar elevation e is now measured in radians. In this simple formulation the only parameters are altitude and solar elevation, and the variation of atmospheric constituents like aerosol and water vapour is not considered. The bulk effect of all scatterers and absorbers except clouds is contained in the coefficients. Figure 6.6 shows how this works out for some values of the solar elevation. Although f_{dir} and f_{dif} will also vary with solar elevation (more diffusive radiation when the sun is low) and other factors, further parameterisations are not developed. We should also keep in mind that situations with a low sun are not very significant with respect to the melting process because the amount of energy involved is limited.
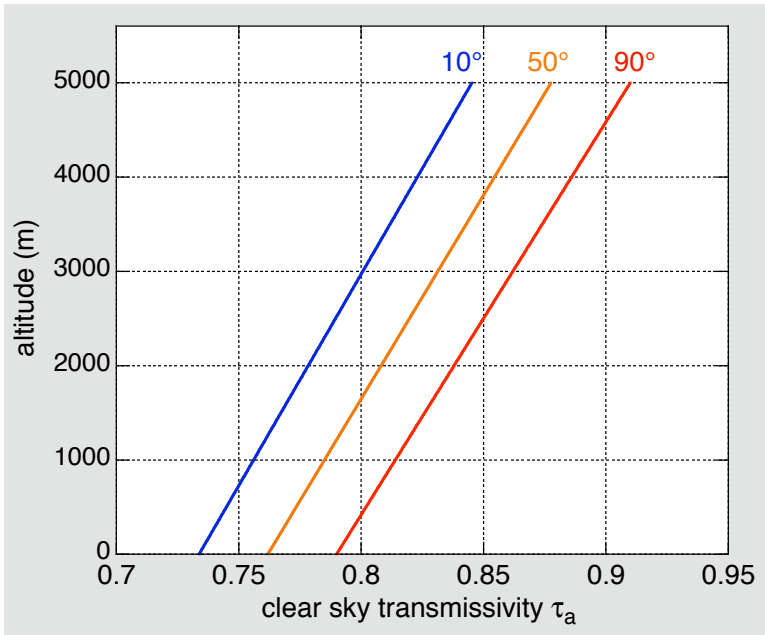
Figure 6.6. Clear-sky transmissivity according to eq. (6.3.4). The labels refer to the solar elevation angle e.

This concludes the description of a scheme to calculate the solar radiation impinging on a glacier surface. However, we should remain aware of the simplifications that have been made. As stated earlier, the basic eq. (6.2.5) is simple because the interactions are not formulated explicitly. As a final illustration we note that multiple reflection between glacier surface and atmosphere is even important in clear-sky conditions. In the absence of geometric factors and clouds the incoming solar radiation can be written as

$$S_{in} = \tau_a \left[\frac{1}{1 - \alpha \, \alpha_{air}} \right] S_E \; . \tag{6.3.5}$$

The term within brackets, containing the surface albedo α and the clear-sky albedo α_{air}, is the correction to the atmospheric transmissivity due to multiple reflection. With characteristic values of 0.60 and 0.07 for α and α_{air}, it amounts to 1.044. In many studies this correction factor is simply absorbed in the transmissivity, giving a slightly larger value of τ_a. In conditions with high surface albedo and low stratus clouds the correction will be much larger. Since the surface albedo normally increases when going up-glacier, the increase in global radiation will be enhanced by the process of multiple reflection.

6.4 The temperature-dependent part of the surface energy flux

We now consider the temperature-dependent part of the surface energy flux $f(T_a)$, as defined in eq. (6.1.3). The analysis of data from AWS on glaciers should provide guidance. Figure 6.7 shows scatter plots of the temperature-dependent part of the surface energy flux (denoted by ψ_T), defined as the surface energy flux minus the net solar radiation. In the plots 30-minute values are shown for longer periods of time, for AWS on the glaciers Midtdalsbreen, Storbreen and Vadret da Morteratsch. Note that scales in these plots are the same for an easy comparison.
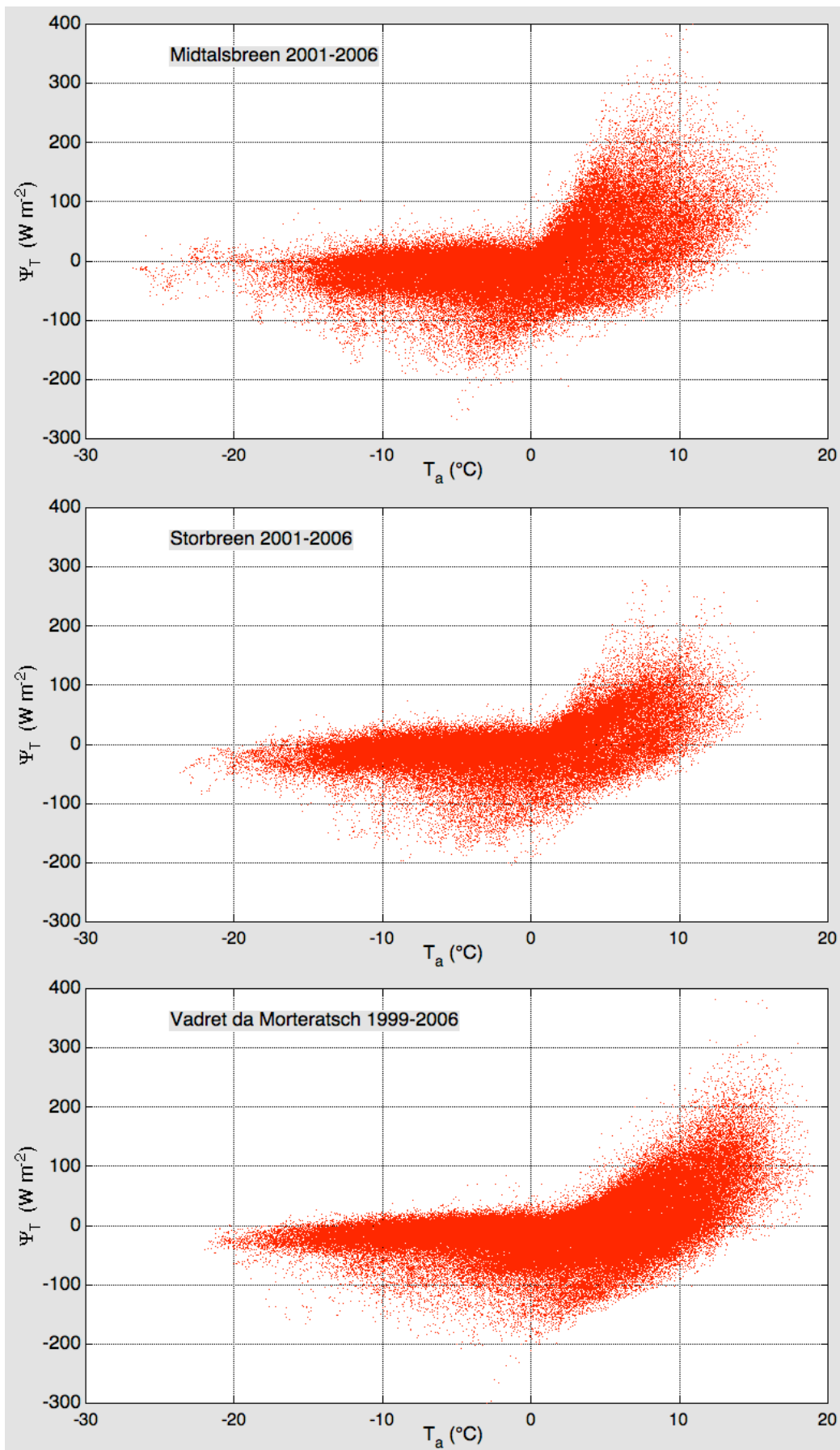
Figure 6.7. Scatter plots of the temperature-dependent part of the surface energy flux ψ_T versus air temperature T_a, obtained from AWS on three glaciers. Each dot represents a 30-minute average.

6 - A mass balance model for valley glaciers

First of all we note that the scatter plots have common structure: for $T_a < 0\,°C$ there is no clear relation between ψ_T and T_a, whereas for $T_a > 0\,°C$ the flux clearly increases with T_a. On Midtdalsbreen values of ψ_T increase more strongly with temperature than on Storbreen and on the Vadret da Morteratsch. This is to a large extent caused by the much higher wind velocities on Midtdalsbreen, implying a more important role of the turbulent heat fluxes.

Closer inspection of the data reveals that the spread in ψ_T for a given temperature is almost entirely due to variations in cloudiness. Note that the distribution of ψ_T for a given temperature is strongly asymmetric for lower temperatures. For temperatures below the melting point the relation between ψ_T and T_a is weak. For temperatures above the melting point ψ_T increases strongly with T_a. For the data shown in Figure 6.8, $f(T_a) = c_0 + c_1 T_a + c_2 T_a^2$ can be used as a fitting function, with the requirement that $c_1 = c_2 = 0$ for $T_a < 0$. The outcome depends on the fitting procedure, of course (least squares or otherwise). In the next chapter, $f(T_a)$ with appropriate coefficients will be used to simulate the mass balance of Nigardsbreen.

The data shown in Figure 6.7 refer to point measurements. In a mass-balance model the altitudinal dependence of $f(T_a)$ is essential to obtain a realistic change of the melt energy with altitude. It appears that the altitudinal dependence of air temperature (through the atmospheric lapse rate) can only partly generate the variation of the melt energy as observed. After experimentation with field data and output from more sophisticated energy balance models, it became clear that a linear decrease of c_0 with altitude works well.

6.5 Refreezing

Refreezing of meltwater in the snowpack in late spring / early summer is generally thought to be insignificant for glaciers with a large mass turnover, because the amount of energy involved is quite small compared to the total melt energy in the ablation season. Such glaciers are normally found in (sub)maritime climates with relatively mild winters. The snowpack therefore does not get very cold and a relatively small amount of energy is needed to bring the snow temperature to the melting point. As already pointed out by Ambach (1963), for glaciers in drier and more continental climates refreezing may be more important.

The way in which meltwater refreezes depends on the local conditions at the glacier surface (e.g. Braithwaite et al., 1994; Schneider and Jansson, 2004). Refreezing of percolating meltwater in cold snow occurs on almost all glaciers until the snowpack has been heated up to the melting point. Capillary water trapped in the firn can refreeze at the end of the summer or in fall at locations where the snowpack survived the ablation season. Yet another process is the direct refreezing of percolating meltwater onto the impermeable ice (forming superimposed ice).

A detailed treatment of refreezing and related processes requires a calculation of the temperature and density structure of the snowpack as a function of time. However, when the interest only concerns the bulk effects of refreezing on the mass and energy budget, a simpler approach is possible. Here we describe the method introduced in Oerlemans (1992).

The method is based on the idea that the fraction of melt energy involved in run-off, denoted by $\dot{r}$, increases when the snow/ice temperature approaches the melting point. This is formulated as

$$\dot{r} = \frac{\psi}{L_m} \exp(c_r T_{sn}) \,, \tag{6.5.1}$$

$$G_{refr} = \psi \left[1 - \exp(c_r \, T_{sn}) \right] , \qquad\qquad (6.5.2)$$

$$C_{sn} \frac{dT_{sn}}{dt} = G_{refr} \quad (T_{sn} \leq 0) . \qquad\qquad (6.5.3)$$

Here G_{refr} is the heat added to the upper snow/ice layer. This layer has a heat capacity C_{sn} and a mean temperature T_{sn} (here in °C). The constant c_r determines how fast the fraction of melted snow that runs off approaches 1.

A comprehensive test of six refreezing models, including the one described above, was carried out by Wright et al. (2007). The comparison was done for high Arctic conditions (Midre Lovénbreen, Svalbard). One of the conclusions of this study was that a scheme with a detailed englacial temperature calculation performs only marginally better than the bulk models. This is understandable, because it is the surface energy flux and the winter cold wave that dictate the total possible amount of refreezing; the details of the vertical density and temperature structure and how these evolve in time matter less.
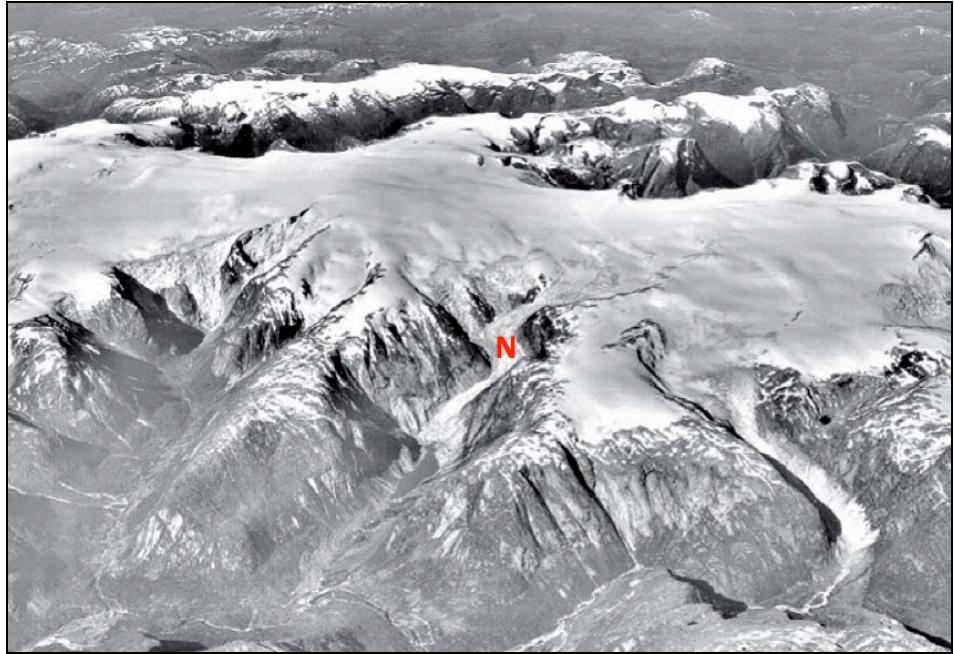
Nigardsbreen (N) as a part of Jostedalsbreen, Norway (1982; NVE, Oslo).

7. Application to Nigardsbreen, Norway

7.1 Introduction

Most valley glaciers on which long-term mass balance measurements are carried out are small or do not span a large altitudinal range. Nigardsbreen is a clear exception: it covers an area of about 48 km^2 and there is an altitude difference of 1700 m between the glacier snout (at ~320 m) and the highest point of the accumulation basin (~1960 m). Mass balance observations on this glacier were initiated in 1961 and have been conducted ever since. The data (and those for other Norwegian glaciers) can be found in the annual reports of the Norwegian Water Resources and Energy Directorate (NVE, Oslo). Because the measurements span a considerable period of time and meteorological data are available from weather stations not too far away, Nigardsbreen is an interesting target for a study in mass-balance modelling. In addition, a long record on glacier length is available (from 1748, e.g. Østrem et al., 1977) and the dynamic response of Nigardsbreen to climate change has been studied with numerical glacier models (e.g. Oerlemans 1997b).

In Chapter 5 a simple mass balance calculation was done for Nigardsbreen, and it turned out to be easy to match the observed balance profile for a reasonable set of parameters (Figure 5.9). However, since the albedo feedback was not present in this simple model, doubts were raised that the sensitivity of the balance rate to climate change is not estimated correctly. The mass-balance model described in the previous chapter is a better tool and here it will be applied to Nigardsbreen. A mass balance model can be driven by a climatology, or by a set of observed meteorological data, or by a combination. Here we will use temperature and precipitation data from a nearby weather station (daily mean values), combined with standard climatological parameters like lapse rates of temperature and precipitation, characteristic daily temperature range, etc.

After inspection of meteorological records from a number of weather stations in the larger Jostedalen region, it was decided to use data from only one station (i.e. no combination of different

stations to achieve a longer time span). The selected station is Bjørkehaug (i Jostedal), which was in operation from 1964 till 2003. Bjorkhaugen is located about 20 km south south-east from Nigardsbreen. Since the balance year starts on the 1st of October, the period 1 October 1964 – 30 September 2003 was used for the model study. The meteorological input data are shown in Figure 7.1. Although not so obvious from the graphs, the main features in this record are (i) slightly colder weather in the period 1979 – 1989, and significantly more precipitation in the period 1981-2000 (as compared to the average conditions over the 40 year period).
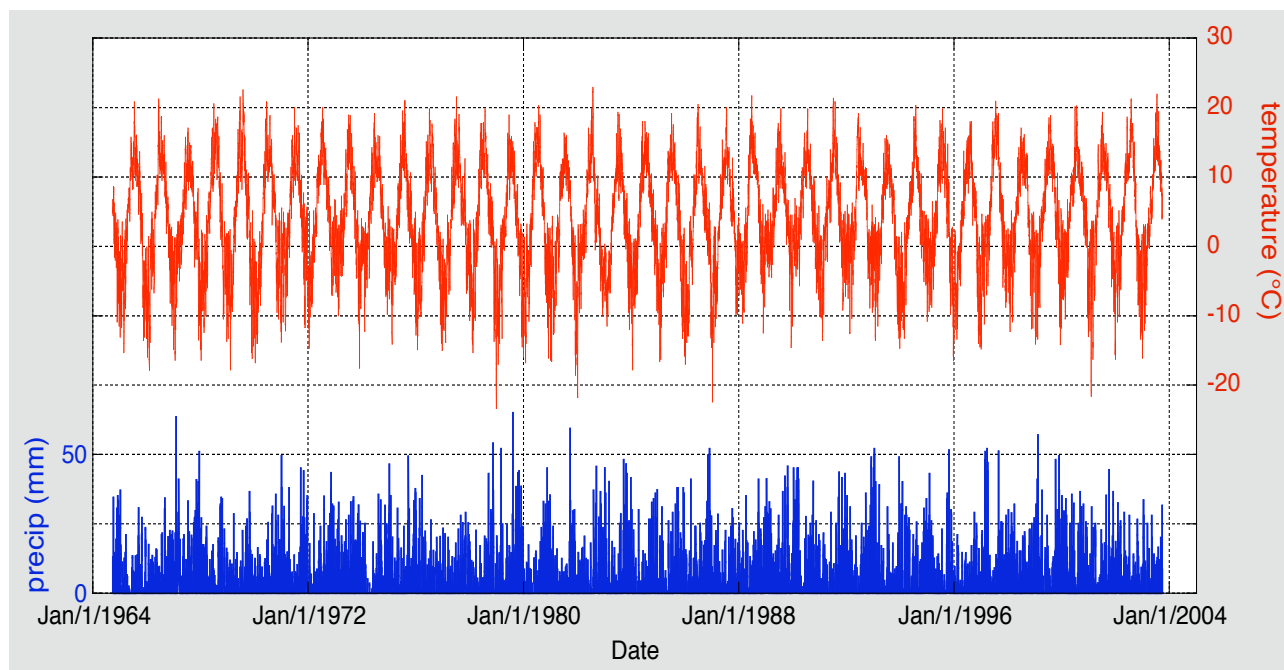

Figure 7.1. Daily precipitation and daily mean temperature as measured at Bjørkehaug in Jostedalen. Data shown are for the period 1 October 1964 – 30 September 2003.

7.2 Preparing the mass balance model for Nigardsbreen

The model described in the previous chapter is easily coded and adjusted for the typical geometry of Nigardsbreen. As in section 5.5, a grid is used with altitudinal increments of 100 m. These coincide with the 100 m intervals used by NVE for the presentation of the observations, which facilitates a comparison of observed and simulated balance rates. The integration in time is done with a 15 minute time step, which should be small enough to resolve the daily cycle.

The calculation of the solar radiation follows the description given in sections 6.4-6.5. No adjustments were made to the parameters given there. Tilting of the surface and shading is taken into account in a schematic way (a detailed treatment is not possible because the model is not spatially-distributed). For cloudiness a constant value of 0.7 was taken, because detailed information is not available. The albedo model of section 4.3 was used, but now applied to 15 min time steps (which requires different values for the various parameters). Compared to the Vadret da Morteratsch, the ablation zone is relatively clean and the ice albedo higher. Good results were obtained with $\alpha_{ice} = 0.40$, $\alpha_{firn} = 0.55$ and $\alpha_{frsno} = 0.85$.

For the temperature dependent part of the surface energy flux the approach described in section 6.6 was followed, e.g.

$$f(T_a) = c_0 + c_1 T_a + c_2 T_a^2 \text{ , with} \tag{7.2.1}$$

$$c_1 = 0 \text{ if } T_a \leq 0; \quad c_1 = 15 \text{ W m}^{-2} \text{K}^{-1} \text{ if } T_a > 0 \text{ ,}$$

$$c_2 = 0 \text{ if } T_a \leq 0; \quad c_2 = 0.12 \text{ W m}^{-2} \text{K}^{-2} \text{ if } T_a > 0 \text{ ,}$$

$$c_0 = -50 - 0.018\,h \text{ W m}^{-2} \text{ .}$$

Here h is the surface elevation in m. The balance gradient β is affected significantly by the altitudinal dependence of c_0. Other factors that determine β are the increase of precipitation with height and the difference between the ice and firn albedo.

The refreezing scheme described in section 6.7 is included, but sensitivity tests reveal that for a maritime glacier like Nigardsbreen the effect of refreezing on the net balance is limited ($< 2\%$). The reason for this is that the winter cold wave is not very strong and the surface energy flux in summer is large, even on the highest part of the glacier.

The temperature forcing of the model was formulated as

$$T_a = T_{Bj} + A_d \cos\{(2\pi t - 2)/24\} + \gamma_T (h - h_{Bj}) + \varepsilon_T \tag{7.2.2}$$

Here T_{Bj} is the daily temperature as measured at Bjørkehaug, A_d is the amplitude of the daily cycle (kept constant at a value of 3 K), t is local time in hr, γ_T is the atmospheric temperature lapse rate (kept constant at a value of -0.007 K/m), h_{Bj} is the altitude of Bjørkehaug (327 m above sea level) and ε_T is a tuning parameter. Further refinements are possible, e.g. a decreasing daily cycle with altitude or a smaller lapse rate in wintertime, but there is little data on which such refinements can be based.

The precipitation on the glacier is assumed to be equal to that in Bjorkhaugen, with an altitudinal gradient γ_P. Precipitation is assumed to fall as snow when the air temperature is below 2 °C. The formulation for the accumulation rate thus becomes

$$\dot{a} = \frac{P_{Bj}\{1 + \gamma_P(h - h_{Bj})\}}{N_d} \quad \text{if } T_a < 2\,°\text{C ,} \tag{7.2.3}$$

$$\dot{a} = 0 \quad \text{if } T_a \geq 2\,°\text{C .} \tag{7.2.4}$$

N_d is the number of seconds in a day. The accumulation rate is thus kept constant through the day. Altitudinal precipitation gradients in southern Norway appear to increase towards the east, because the valleys are more sheltered (Østrem et al. 1988; Oerlemans, 1992). A typical value for the mountains of central southern Norway is 0.001 m^{-1}. This value appeared to give satisfactory results and is therefore used in all calculations.
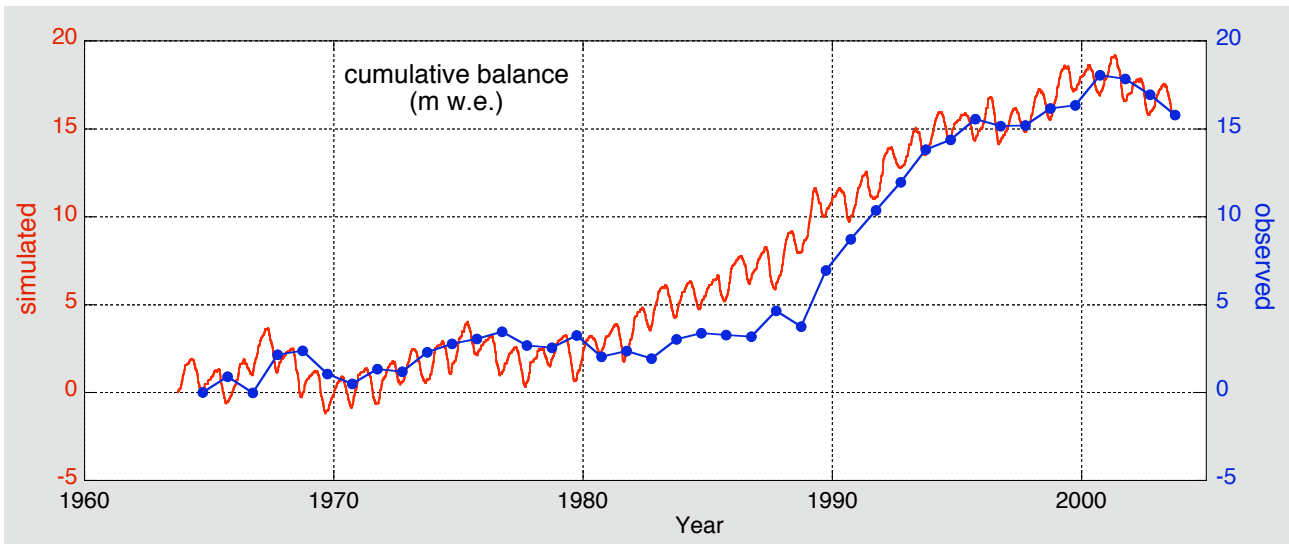
Figure 7.2. A comparison between simulated (red) and observed (blue) cumulative balance for Nigardsbreen. Note that the blue dots are shifted, e.g. the 2000 net balance is plotted on the time axis at 2000.65 years.

7.3 Calculating the mass balance of Nigardsbreen

In Figure 7.2 the simulated net balance of Nigardsbreen is compared to the observations. The quantity ε_T in eq. (7.2.2) was used as a tuning parameter. For $\varepsilon_T = 0.52\,\mathrm{K}$ the calculated and observed cumulative balance are identical (namely 15.78 m w.e.). Apparently, only a small correction to the measurements made at Bjorkhaugen is needed to simulate the observed total balance. Also, the observed and simulated cumulative balances compare well throughout the period of 40 years considered.
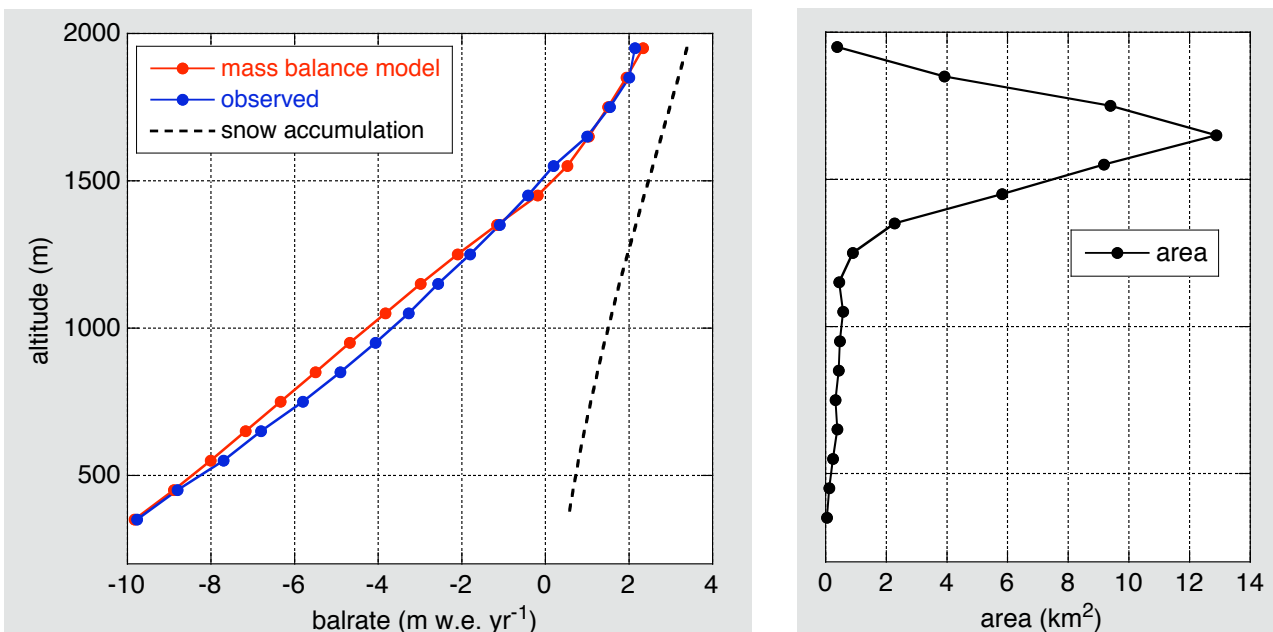

Figure 7.3. Left panel: A comparison between simulated (red) and observed (blue) balance profiles for Nigardsbreen. The dashed curve shows the simulated mean snow accumulation. Right panel: the corresponding surface area of the 100 m altitude bands used to compute the total mass balance.

7 - Application to Nigardsbreen, Norway

The balance profile is shown in Figure 7.3a. There is a good correspondence between the simulated and observed profiles (mean values over the 40 yr period). Around the equilibrium line the simulated balance gradient is larger than the observed gradient. This appears to be related to the evolution of the albedo. Experimentation with different albedo models revealed that a better match can be obtained if the ice albedo is not taken constant but made dependent on the altitude or distance to the equilibrium line (as was actually done in Oerlemans, 1992). However, there are no observational data for Nigardsbreen on which a more refined parameterization of the ice albedo could be based.

The calculated and observed balance profiles yield the same mean balance over the period studied. This can be understood by considering the hypsometry of Nigardsbreen (Figure 7.3b). The lower calculated balance in the mid-elevation range is compensated by the slightly larger balance around 1500 m where the glacier area is relatively large.

Figure 7.4 provides a further illustration of how the albedo is generated by the model. It shows the albedo for three gridpoints, at altitudes of 450, 1250 and 1950 m. It can be seen that at 450 m the surface consists of ice for about half of the time. During many periods the albedo at 1250 m equals the albedo at 1950 m, because snowfall occurs at the same days and the snow aging process does not depend on the temperature. In the year 1993 the amount of snow falling on the glacier was large, and at 1250 m the ice never came at the surface.
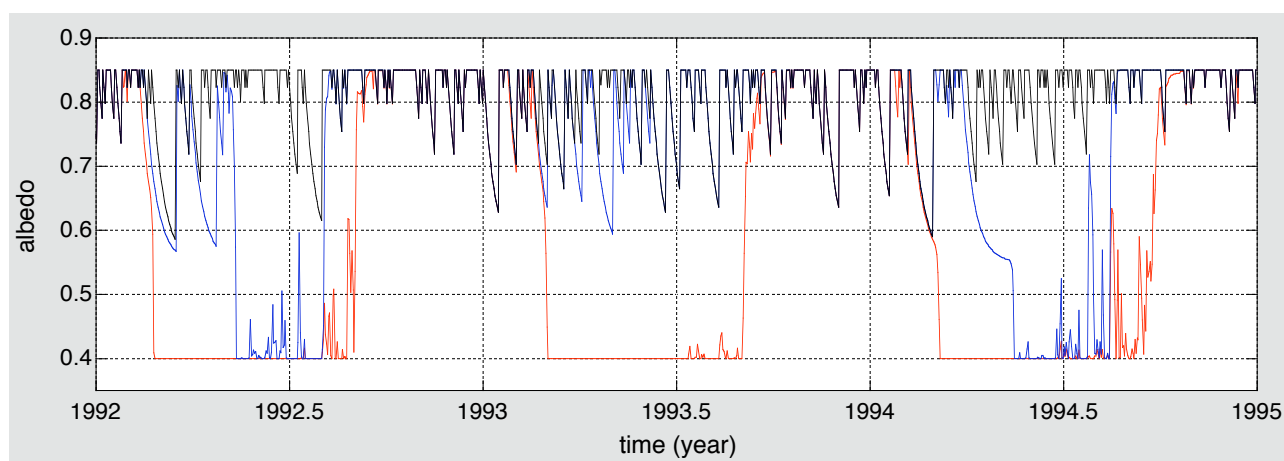

Figure 7.4. The albedo as generated by the mass balance model for a 3 yr period, at altitudes of 450 m (in red), 1250 m (in blue), and 1950 m (in black).

7.4 Sensitivity experiments

The model is able to simulate the mass balance of Nigardsbreen in a satisfactory way, and it is interesting to calculate how the balance changes for small changes in temperature and precipitation. Figure 7.5 shows balance profiles for various perturbations in the prevailing climate. In all cases the imposed changes in air temperature and precipitation do not depend on time and altitude. Precipitation anomalies are prescribed as a percentage of the precipitation in the reference case (the 40 year period), so the change in absolute precipitation increases with altitude. It should be noted that a temperature change affects the ablation as well as the amount of snowfall (because the fraction of the precipitation falling as rain changes).
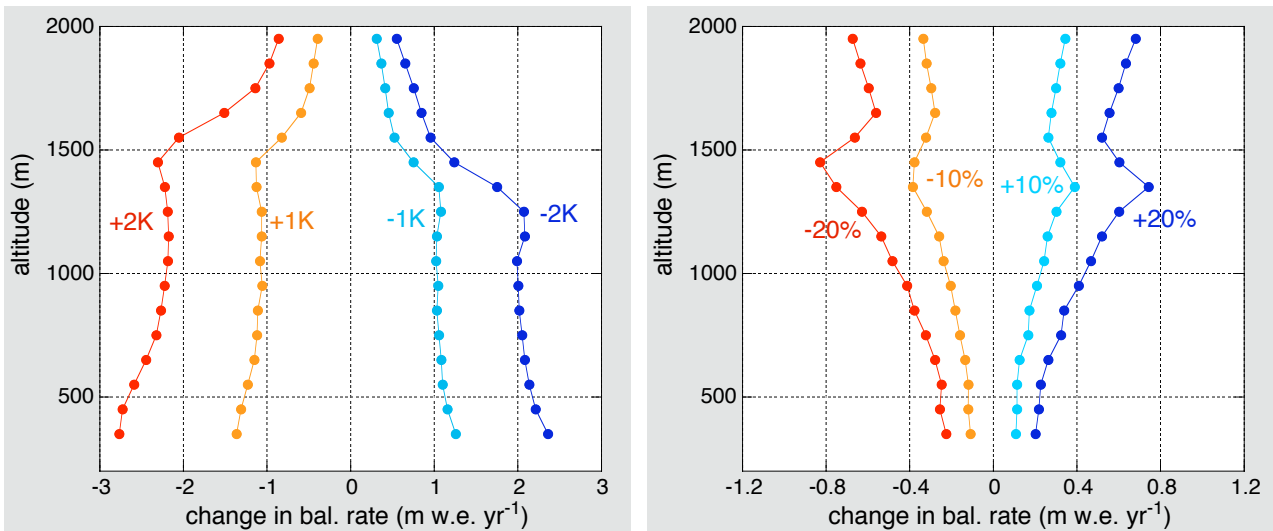
Figure 7.5. Calculated changes in balance profiles for Nigardsbreen for changes in temperature (left) and precipitation (right). Note that horizontal scales differ by a factor of two.

The curves in Figure 7.5 show that a large sensitivity of the balance rate is found in the vicinity of the equilibrium line, especially for changes in precipitation. This is a direct consequence of the albedo feedback. The altitude of relative maximum sensitivity depends on the temperature anomaly: for a larger temperature change the zone of maximum sensitivity shifts upwards. For a temperature change the sensitivity also increases steadily towards the lowest parts of the glacier. Here the ablation season is longer and the temperature change thus has a larger impact on the annual balance. The response of the equilibrium-line altitude and the mean balance rate for changes in temperature and precipitation are shown in Figure 7.6. The response of the mean balance to temperature perturbations is clearly nonlinear: the sensitivity is larger for a larger temperature change. However, when interpreting this result it should be kept in mind that in all calculations the geometry of the glacier is fixed.
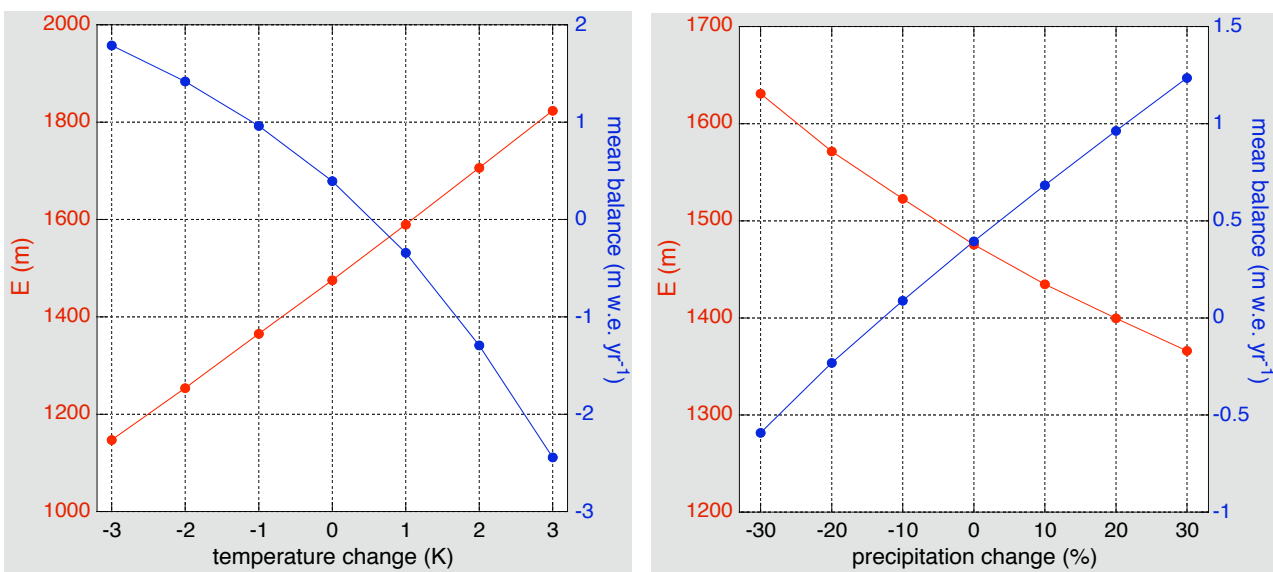

Figure 7.6. Equilibrium-line altitude (red) and mean balance rate (blue) for changes in temperature and precipitation.

7 - Application to Nigardsbreen, Norway

Characteristic values for the climate sensitivies are ($\dot{b}_m$ is the balance rate averaged over the entire glacier):

$$\frac{\partial E}{\partial T_a} = 113 \, \mathrm{m\,K^{-1}} \, , \qquad\qquad \frac{\partial E}{\partial P} = -4.38 \, \mathrm{m\,\%^{-1}} \, , \qquad\qquad (7.3.1)$$

$$\frac{\partial \dot{b}_m}{\partial T_a} = -0.693 \, \mathrm{m\,w.e.\,K^{-1}} \, , \qquad \frac{\partial \dot{b}_m}{\partial P} = 0.0302 \, \mathrm{m\,w.e.\,\%^{-1}} \, . \qquad (7.3.2)$$

These values are in line with earlier modelling studies with energy-balance models (e.g. Greuell and Oerlemans, 1987; Kuhn, 1989; Oerlemans, 2001).

It is also interesting to look at the influence of seasonal variations in temperature and precipitation. For instance, a temperature decrease in summer will have a different effect on the balance rate than a similar temperature decrease in winter. To illustrate this, Oerlemans and Reichert (2000) introduced the Seasonal Sensitivity Characteristic (SSC), which summarizes the effect of monthly perturbations in temperature and precipitation on $\dot{b}_m$. They suggested that the annual balance rate can be calculated in the following way:

$$\dot{b}_m = \sum_{k=1}^{12} \left[C_{T,k}(T_k - T_{ref,k}) + C_{P,k}\left(\frac{P_k}{P_{ref,k}} - 1\right)\right]. \qquad (7.3.3)$$

The index k refers to the month. $C_{T,k}$ is the change in the balance rate due to a 1 K temperature perturbation in month k. Similarly, $C_{P,k}$ is the change in the balance rate related to a change in precipitation rate in month k. Note that the monthly precipitation is normalised with a reference value, whereas the temperature is taken relative to a reference value. The SSC thus consists of a 12x2 matrix that characterizes the sensitivity of the balance rate to seasonal changes in the weather.
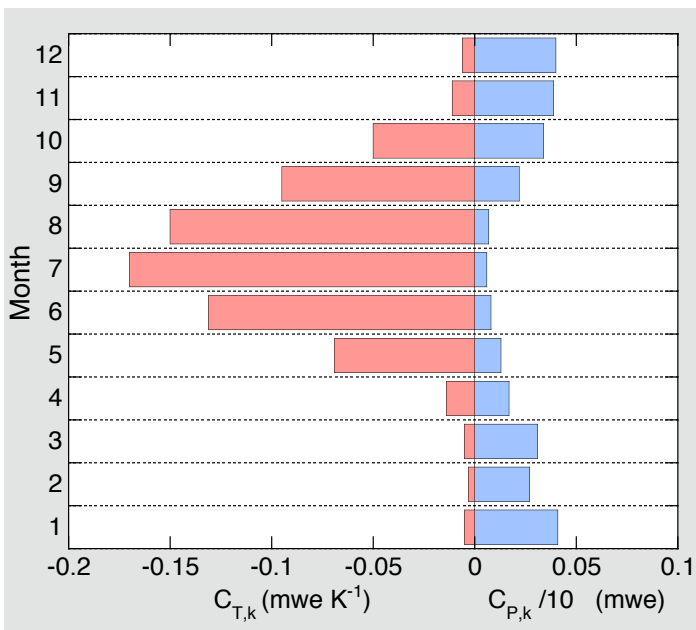

Figure 7.7. Seasonal Sensitivity Characteristic (SSC) for Nigardsbreen.

The SSC for Nigardsbreen is shown in Figure 7.7. The red bars show the change in balance rate for a 1 K temperature increase, the blue bars the change in the balance rate for a 10% increase in precipitation. It is is clear that temperature changes in the winter months matter little, as do precipitation changes in the summer months. However, precipitation and temperature fluctuations in spring and autumn can be quite significant. For an annual temperature increase of 1 K, the summer (June-July-August) contributes 60 % to the decrease in the balance rate, implying that there is still a 40 % contribution from the other seasons. This is typical for a maritime glacier with a large mass turnover. The lower ablation zone is far below the equilibrium line and therefore subject to relatively high air temperatures. As a consequence there is significant ablation on the glacier snout in spring and autumn, which explains the sensitivity of the balance rate for temperature changes in these seasons.

Briksdalsbreen, a maritime glacier in Norway, in 1996.

8. Maritime and continental glaciers

8.1 Introduction

As briefly discussed in section 2.1, maritime glaciers are located in a climate with a small seasonal temperature range (10 to 15 K), high humidity and a large mean fractional cloudiness (0.6 to 0.9), and large amounts of precipitation (1.5 to 5 m yr^{-1}). In contrast, continental glaciers are subject to a large seasonal temperature range (20 to 50 K), lower humidity and a lower mean fractional cloudiness (0.3 to 0.7), and small amounts of precipitation (0.3 to 1 m yr^{-1}). Many glaciers are neither really maritime nor continental. For example glaciers in the Alps, in the central Rocky Mountains, or in northern Scandinavia are located in a transitional climate.

Several authors have suggested that maritime glaciers are more sensitive to climate change than continental glaciers. Meier (1984) argues that glaciers with a large mass turnover respond more strongly to changes in the input. From mass-balance modelling studies it appears that the change in the mean specific balance due to a rise in temperature is indeed strongly related to the annual precipitation (e.g. Oerlemans and Fortuin, 1992, Oerlemans, 2001; De Woul and Hock, 2005). There are also geometric effects making maritime glaciers more sensitive: on average maritime glaciers are longer and have smaller surface slopes, which implies a stronger response of glacier length to changing mass-balance conditions (for a discussion on the relation between glacier geometry and response to climate forcing, see Oerlemans, 2008).

The nourishment of glaciers depends almost entirely on snowfall. With respect to glaciation in mountain regions, the precipitation regime is a decisive factor. Annual precipitation varies typically by one order of magnitude, and it is interesting to study the response of a mass balance model to such large variations in climatic setting. In the next section we will look at the relation between continentality and equilibrium-line altitude; later in this chapter we consider geometric effects.

8.2 Continentality and balance rate

For all calculations discussed in this chapter, the input data for Nigardsbreen were used with some modifications. First of all, the annual precipitation was changed by just scaling all the daily values with the same factor. The altitudinal profiles were scaled in proportion (i.e. *relative* changes are independent of altitude). When all other input data and model parameters are kept the same, the red curve in Figure 8.1 results. It shows the dependence of the equilibrium-line altitude E (40 year mean values) on the annual amount of annual precipitation. This dependency is clearly nonlinear: E increases more and more rapidly when the climate gets drier. Broadly speaking, reducing the annual precipitation from 5 m to 0.5 m implies a 1000 m rise of the equilibrium line.

As mentioned earlier, glaciers in a continental climate are subject to a much larger seasonal temperature range (the mean temperature difference between the warmest and the coldest month). This may also have a large effect on the altitude of the equilibrium line. We can study this by modifying the temperature input of the mass balance model. First we adopt a simple relation between annual precipitation and seasonal temperature range (ΔT):

$$\Delta T = \Delta T_0 \exp\left(-P_{ann}\big/P_0\right) \tag{8.2.1}$$

With $\Delta T_0 = 65 \text{ K}$ and $P_0 = 2.5 \text{ m}$ the resulting relation, shown in Figure 8.2, is broadly in line with the climatological evidence (e.g. Müller, 1987). The seasonal temperature range is more than 50 K for extremely dry conditions, and about 10 K in very maritime climates. It should be noted that there are many other factors affecting ΔT, notably latitude. For instance, in the dry subpolar regions like the Canadian arctic, values of ΔT are normally larger than in the dry climates of central Asia, simply because the seasonal variation in the incoming solar radiation increases strongly with latitude. Nevertheless, making ΔT dependent on the annual precipitation implies a reasonable characterisation of the degree of continentality.
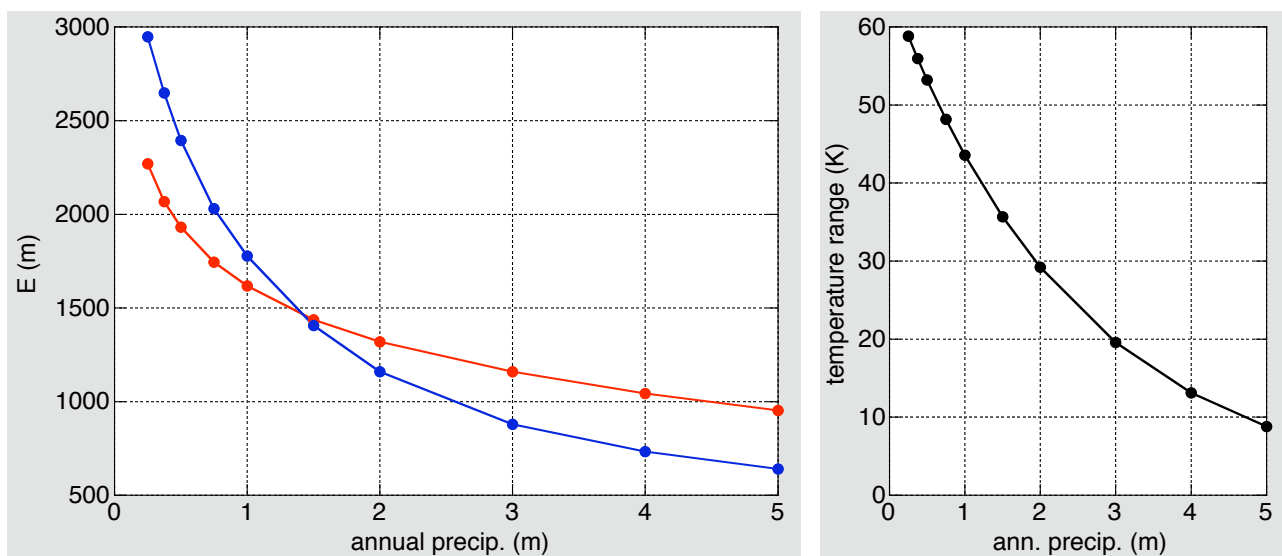

Figure 8.1. The dependence of the equilibrium line altitude E on the annual precipitation (in red). The blue curve is for the case in which the seasonal temperature change has been adjusted. The adopted relation between precipitation and seasonal temperature range is shown at the right.

To accommodate changes in the seasonal temperature range the daily temperature forcing of the model has to be adopted. The simplest approach is to scale all temperatures relative to the mean value by a constant factor f_T. So a new temperature series T' is generated by:

$$T' = \overline{T} + f_T (T - \overline{T}) .$$ (8.2.2)

Here T is the observed temperature from the Bjørkehaug series discussed before, and $\overline{T}$ is the 40 year mean value. The reference simulation for Nigardsbreen thus corresponds to $f_T = 1$.

The blue curve in Figure 8.1 shows how the equilibrium line altitude changes when ΔT is allowed to vary with precipitation. It is obvious that changes in the seasonal temperature range are very important. The range over which E varies has now increased to about 2500 m. Because the annual mean temperature has been kept constant, the summer temperature is directly related to ΔT. We may conclude that the variations in P_{ann} are of roughly equal importance as the variations in ΔT. On the basis of Figure 8.1 we may understand that many mountain regions in eastern Siberia have no or very few glaciers: the combination of low precipitation and large seasonal temperature cycle make the equilibrium line rise to high altitudes. In contrast, extensive glaciation is found in southern Alaska, Iceland, and in the western Patagonian ice fields, in spite of rather high annual mean temperatures. Here the combination of a small seasonal temperature range and large amounts of precipitation implies a low equilibrium line altitude.

Balance profiles for three values of P_{ann} are shown in Figure 8.2. Note that the profiles all have the same altitudinal range. It is noteworthy that the balance gradient increases with P_{ann}, which is in broad agreement with observations. The accumulation profiles are also shown, and in all simulated cases there is significant melt even in the highest part of the profile. However, this depends on the altitude of the highest point with respect to the equilibrium line altitude, of course.
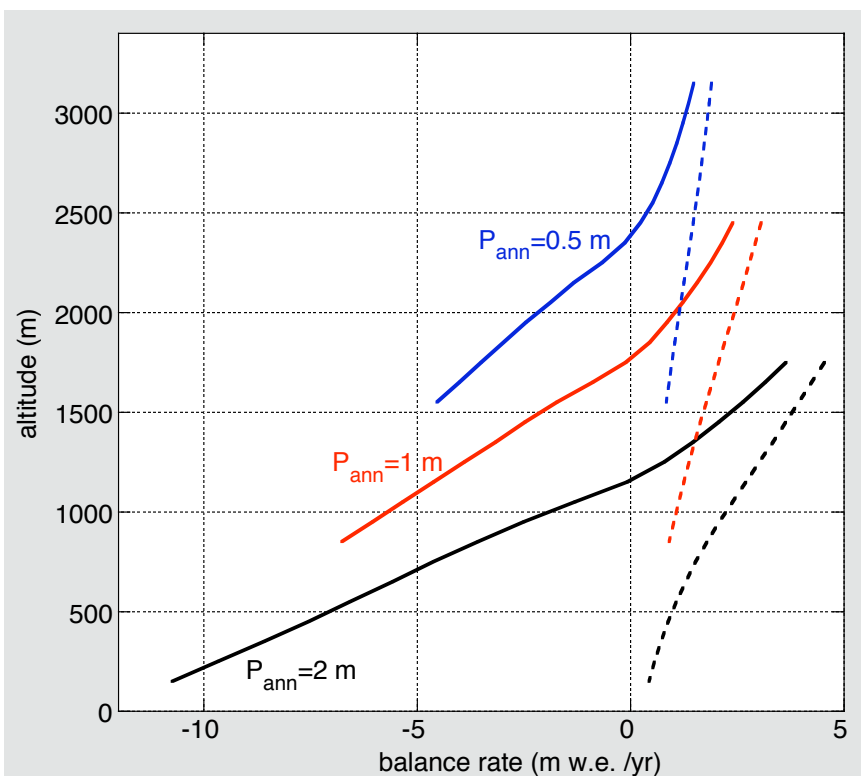

Figure 8.2. Profiles of the balance rate and accumulation (dashed) for three values of the annual precipitation.

8.3 Sensitivity to climate change

The mass balance model can be used to study the relation between continentality and sensitivity of the balance rate to climate change. As mentioned in section 8.1, maritime glaciers are thought to be more sensitive to changes in temperature and precipitation. Calculations with the current model support this view, as discussed below.

Figure 8.3 shows the change in balance rate ($\Delta \dot{b}$) calculated for a uniform 1 K warming (solid lines), and for a uniform 20% increase in precipitation (dashed lines). Concerning the 1 K warming, it is immediately obvious that values of $\Delta \dot{b}$ are more negative for larger values of P. This finding is largely due to the albedo feedback, which is more effective when the amount of snow deposited annually on the surface is larger. For a maritime glacier ($P_{ann} = 2$ m), the value of $\Delta \dot{b}$ below the equilibrium line is typically -1.5 m w.e. yr^{-1}, twice as large as for a continental glacier with $P_{ann} = 0.5$ m. With respect to changes in precipitation we observe similar differences, but we should remember that the increase in precipitation is fractional, i.e. larger for larger values of P_{ann}. Figure 8.3 also reveals that the climate sensitivity of the balance rate has a (relative) maximum in the vicinity of the equilibrium line, where the albedo feedback is particularly effective. This applies to temperature changes as well as changes in precipitation.

In Chapter 7 we briefly discussed the Seasonal Sensitivity Characteristic (SSC; Oerlemans and Reichert, 2000) for Nigardsbreen. A similar exercise can be done for the equilibrium line altitude E, which has the advantage that a glacier geometry does not need to be specified. The disadvantage is that the balance gradient close to the equilibrium line is large, and depending quite a bit on how the surface energy balance is formulated. Therefore, the SSC for E (denoted by SSC_E), is not so well defined as for $\dot{b}_m$, which is more like an integral quantity. Nevertheless, in Figure 8.4 the SSC_E is
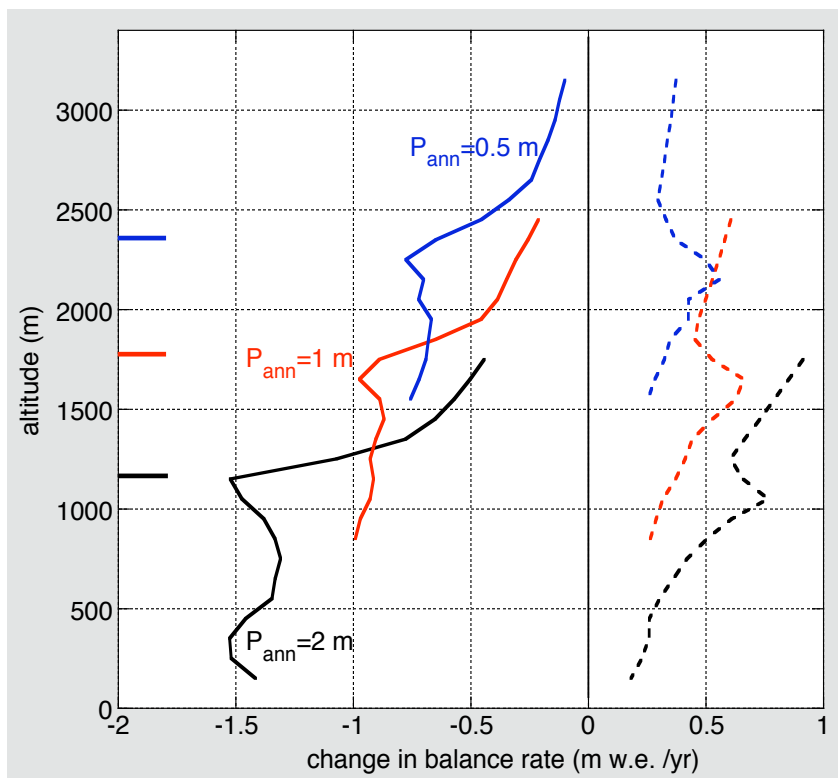

Figure 8.3. Changes in the balance profiles (relative to those shown in Figure 8.2) for a 1 K higher temperature (solid) and a 20 % increase in annual precipitation (dashed).
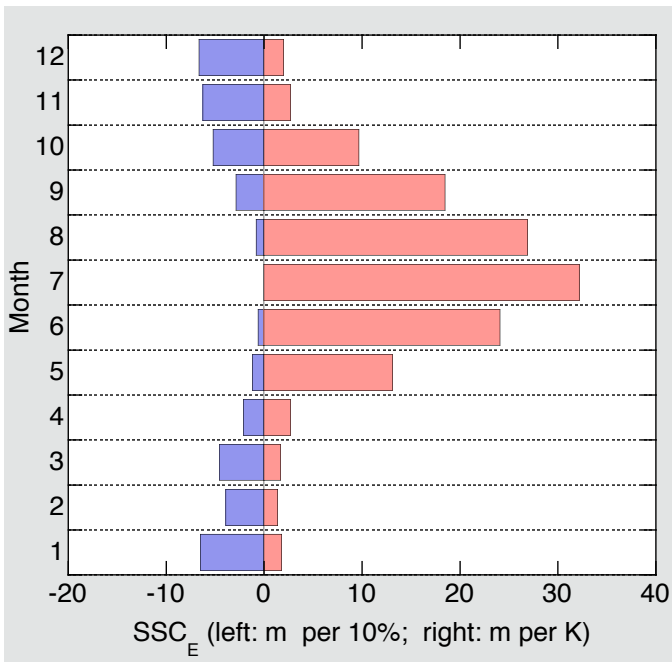
Figure 8.4. The SSC_E for the case with $P_{ann}=2$ m. Note the difference in units for the blue and red bars.

shown for the case with $P_{ann} = 2$ m. As expected, changes in summer precipitation have no effect on the equilibrium line, because at this altitude all precipitation then falls as rain. We can also see that temperature changes in fall and spring are quite important. If we sum up the monthly changes for a 1 K temperature increase to obtain a value for the entire year, a large number results: 136 m. Running the model for a constant 1 K temperature increase through the year yields an increase in E of 117 m. Apparently the effect of a temperature perturbation in a single month is relatively large, because it has some influence on what happens in the next month, even when the temperature perturbation in that month is zero.
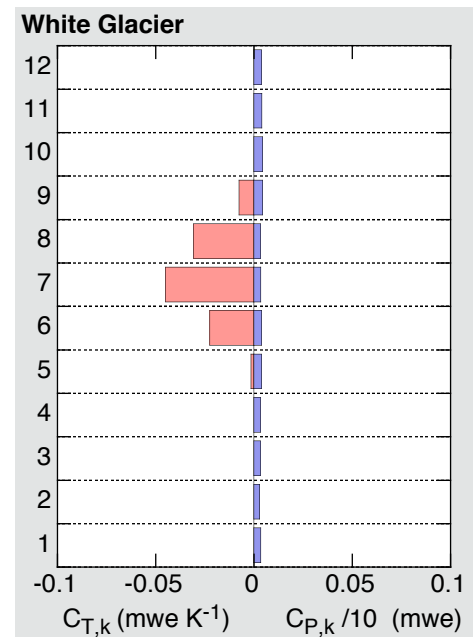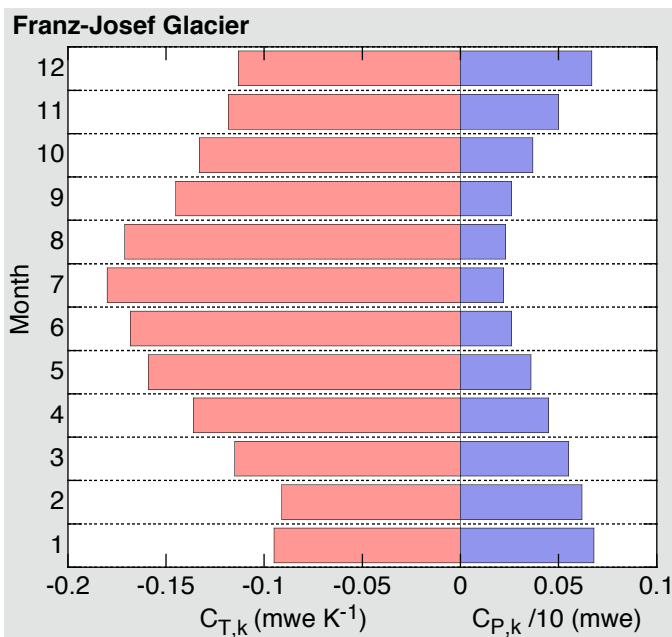

Figure 8.5. Modelled SSC's for Franz-Josef Glacier, New Zealand, and White Glacier in the Canadian Actic. Note that the horizontal scales are the same. From Oerlemans (2001).

For an individual glacier, changes in the net balance depend on its hypsometry. It should be recalled that differences in the typical geometry of continental and maritime glaciers may play an important role in determining the climate sensitivity of the net mass balance (e.g. Oerlemans, 2001). It is therefore interesting to compare the SSC for glaciers in different climates. In Figure 8.5 two really extreme cases are considered: Franz-Josef Glacier is located in a very maritime climate and the balance rate on the snout is estimated to be of the order of -25 m w.e. yr^{-1}. In contrast, White Glacier in Canada experiences very dry conditions and a huge temperature difference between summer and winter. For this glacier only changes in summer temperature matter. Most glaciers are in between the extreme cases shown in Figure 8.5, of course.

The difference between maritime and continental glaciers can be illustrated further by considering a seasonality index (SI), defined as

$$SI = \left(C_{T,6} + C_{T,7} + C_{T,8}\right) \Big/ \sum_{k=1}^{12} C_{T,k} \ . \tag{8.3.1}$$

This index measures the relative importance of summer temperature for a glacier's net balance. We expect that SI has a high value for continental glaciers and a low value for maritime glaciers. If only the summer months would matter SI would be equal to 1. If all months would be equally important SI would be 0.25.

In Figure 8.6 the SI for a set of glaciers is plotted as a function of the annual precipitation. There is a very clear relation. Most of the glaciers shown have an SI in the 0.5 to 0.7 range, implying that the three summer months account for about half of the sensitivity to temperature change.
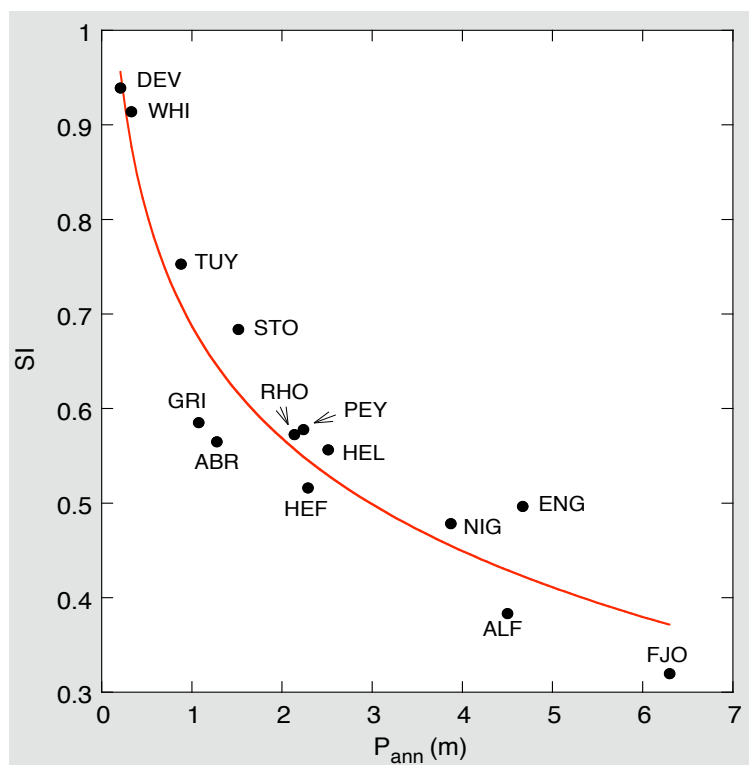

Figure 8.6. The seasonality index SI for a number of glaciers, as obtained from mass-balance modelling, plotted against annual precipitation. The curve shows a logarithmic fit.

The acronyms refer to the following glaciers: FJO: Franz-Josef Glacier; ALF: Alfotbreen, NIG: Nigardsbreen; ENG: Engabreen; HEF: Hintereisferner; ABR: Abramov glacier; HEL: Hellstugubreen; PEY: Peyto Glacier; RHO: Rhone-gletscher; GRI: Griesgletscher; STO: Storglaciären; TUY: Tuyuksu glacier; WHI: White Glacier; DEV: Devon Ice Cap.
From Oerlemans (2001).

The first IMAU weather station, used to study the microclimate of the beach in the early 1970's.

Epilogue

During the past decades our knowledge of the microclimate of glaciers has increased tremendously. The notion that on the global scale glaciers shrink and sea level rises has stimulated the interest. The growing awareness that anthropogenic forcing of the climate system may play an important role in the current evolution of glacier systems has made it easier to acquire funds for costly field programmes and space missions for earth observations. With respect to in situ measurements on glaciers, new battery technology and reliable solid-state logging systems have made the difference and stimulated the deployment of AWS on glaciers. We now have data sets from the melting zones of glaciers that span many years and allow thorough testing and calibration of models.

In this book I have given an account of various aspects of the microclimate of glaciers. The focus has been on valley glaciers, not on the big ice sheets. The story is certainly biased towards the work carried out at or coordinated by the IMAU. Apart from giving an overview of the main data sets and the related development of theory, the book is also meant to give a flavour of the historical development of the subject at IMAU. I apologize to those who feel their work should have got a more prominent place in this text.

We have acquired a good understanding of the microclimate of glaciers and how the exchange of mass and energy between glacier surface and atmosphere actually works. The knowledge of the micro-meteorological processes has made it possible to develop mass balance models. With these models the sensitivity of the balance rate to climate change can be studied. Perhaps the most remarkable result is the large difference between continental and maritime glaciers: the sensitivity of the balance rate to temperature change varies by one order of magnitude. Another result from the data analysis which I found remarkable is the strong increase of global radiation with altitude found on glaciers and ice caps. With respect to the glacier wind (katabatic flow) it has become obvious that its occurrence is widespread and persistent, even on such exposed ice caps like Vatnajökull.
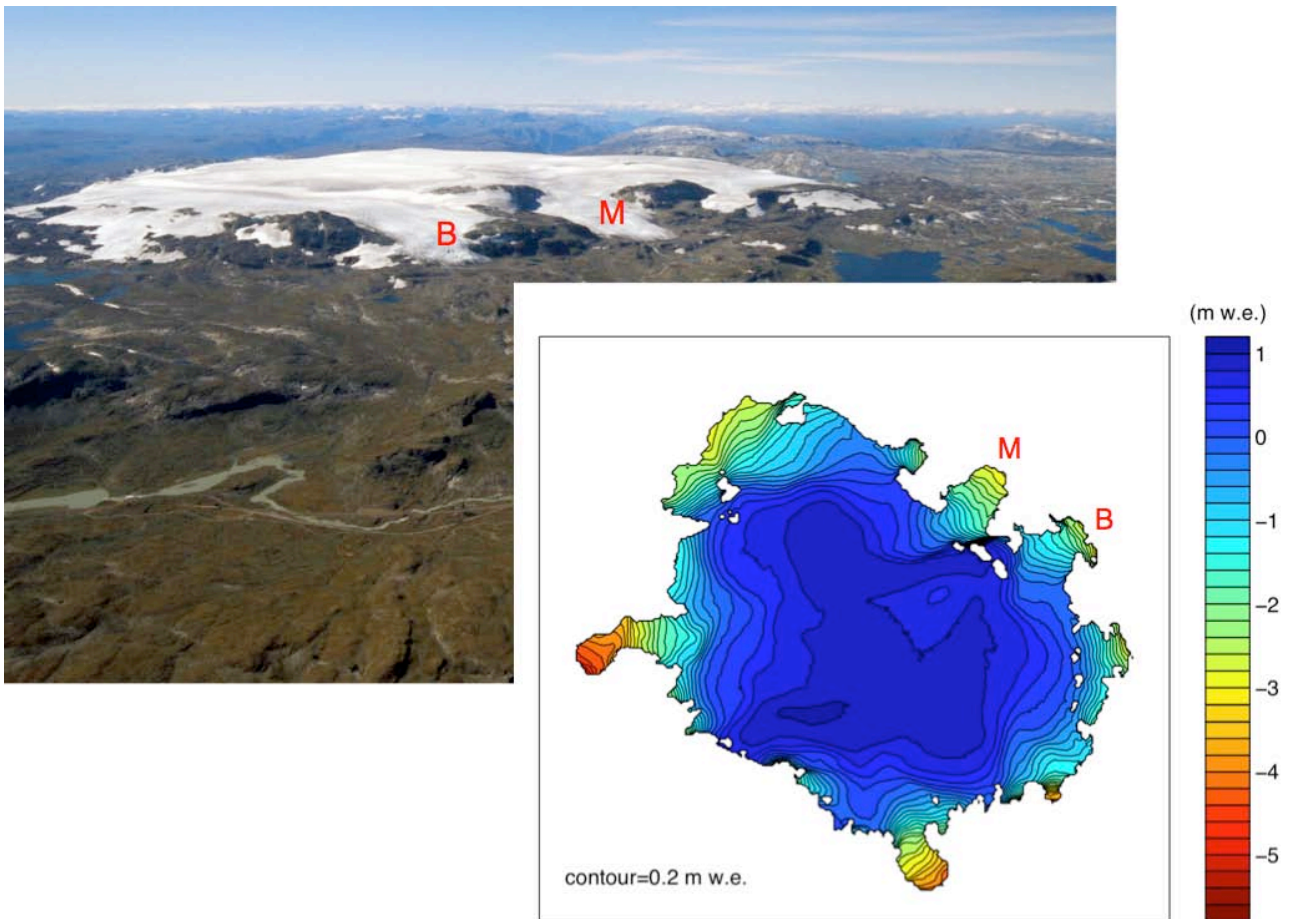
The balance rate of Hardangerjøkulen for the period 1958-2005, simulated with a spatially distributed mass balance model (Giesen and Oerlemans, 2010). Midtdalsbreen is indicated by M, Blåisen by B. The scale on the right is in mwe per year. Photo by Sven Dahlgren.

Spatially distributed mass balance models are now used more and more. These models are attractive because the effect of a complicated topography on the depletion of solar radiation can be calculated explicitly. The figure above shows an example. The distribution of the balance rate on Hardangerjøkulen, Norway, has been calculated from climatological data on a grid with 50 m resolution. This particular model has also been coupled to a 2-dimensional ice flow model, making it possible to study the interaction of a changing glacier geometry and the balance rate in great detail (Giesen and Oerlemans, 2010). In the case of Hardangerjøkulen strong nonlinear effects are apparent. There appears to be a range of climatic conditions for which there are two stable geometries for the ice cap which are very different.

Spatially distributed models also have a great potential for palaeoclimate studies. The initial glacierization of mountainous terrain may depend critically on the distribution of solar radiation and snow accumulation. Energy balance models should therefore be superior to more traditional methods of determining former equilibrium-line altitudes (e.g. Rea, 2008). However, modelling the distribution of snow accumulation in complex terrain remains a critical issue and a subject for further research. The same applies to the ice albedo.

Assessing the impact of climate change on glaciers on the global scale remains a challenge. This applies to the contribution of glacier shrinkage to sea level rise over the past centuries, as well as to the state of the cryosphere in the future. We have to find efficient methods that can deal with all

glaciers on one hand, and incorporate the important local processes on the other hand. Some critical issues and questions are:

- Downscaling of climate model output for use in glacier mass balance models;
- The interplay of satellite data and models on a larger scale;
- The feedback between changing glacier geometries and balance rates;
- How can mass-balance observations be used to calibrate a global scale model?
- How can historical glacier length records be used to constrain a global scale model?

Ideally, the balance rate at a glacier surface should be an inherent project of a climate model. For the Greenland and Antarctic ice sheets, regional climate models provide sufficient resolution to study the distribution of the balance rate (e.g. Van de Berg et al., 2006; Fettweis, 2007; Van den Broeke et al., 2009). However, for valley glaciers and smaller ice caps highly parameterized models will be needed for a long time to come.

Acknowledgements

References

Allen R.G., R. Trezza and M. Tasumi (2006): Analytical integrated functions for daily solar radiation on slopes. *Agricultural and Forest Meteorology* **139**, 55–73.

Ambach W. (1963): Untersuchungen zum Energieumsatz in der Ablationszone des Grönlandischen Inlandeises. *Meddelelser om Grønland* **174** (4), 311 pp.

Ambach W. (1974): The influence of fractional cloud cover on the net radiation balance of a snow surface with high albedo, *Journal of Glaciol*ogy **67**, 73-84.

Anderson B., W. Lawson, I. Owens and B. Goodsell (2006): Past and future mass balance of Ka Roimata o Hine Hukatere (Franz Josef Glacier). *Journal of Glaciology* **52**, 597-607.

Andreas E. L. (1987): A theory for the scalar roughness and the scalar transfer coefficients over snow and sea ice. *Boundary-Layer Meteorology* **38**, 159–184.

Andreassen L.M., M.R. van den Broeke, R.H. Giesen and J. Oerlemans (2008): A 5 year record of surface energy and mass balance from the ablation zone of Storbreen, Norway. *Journal of Glaciology* **54**, 245-258.

Bender C. and S. Orszag (1978): *Advanced mathematical methods for scientists and engineers*. McGrawHill (1978), Springer (1999).

Benson C.S. (1962): *Stratigraphic studies in snow and firn on the Greenland ice sheet*. SIPRE Research Report 70, U.S. Army Corps of Engineers, Wilmette, Illinois, 93 pp.

Björnsson H. (1972): 'Bægisarjökull, North Iceland. Results of Glaciological Investigations 1967–1968, Part II. The Energy Balance'. *Jökull* **22**, 44–59.

Braithwaite R. J., M. Laternser and W. T. Pfeffer (1994): Variations of near-surface firn density in the lower accumulation area of the Greenland ice sheet, Pâkitsoq, West Greenland. *Journal of Glaciology* **40**, 477-485.

Bourgeois C.S, P. Calanca and A. Ohmura (2006): A field study of the hemispherical directional reflectance factor and spectral albedo of dry snow. Journal of Geophysical Research **111**, D20108, doi:10.1029/2006JD007296.

Box J.E., D.H. Bromwich and L.-S. Bai (2004): Greenland ice sheet surface mass balance for 1991–2000: Application of Polar MM5 mesoscale model and in-situ data. *Journal of Geophysical Research* **109,** D16105, doi:10.1029/2003JD004451.

Braithwaite R.J. and Y. Zhang (2000): Sensitivity of mass balances of five Swiss glaciers to temperature changes assessed by tuning a degree-day model. *Journal of Glaciology* **46**, 7-14.

Brock B.W. (2004): An analysis of short-term albedo variations at Haut Glacier d'Arolla, Switzerland. *Geografiska Annaler* **A86**, 53-65.

Brock B.W., I.C. Willis and M.J. Sharp (2000): Measurement and parameterisation of albedo variations at Haut Glacier d'Arolla, Switzerland. *Journal of Glaciology* **46**, 675-688.

Cogley J.G. and W.P. Adams (1998): Mass balance of glaciers other than the ice sheets. *Journal of Glaciology* **44**, 315–25.

Davis R.E., A.W. Nolin, R. Jordan, and J. Dozier (1993): Towards predicting temporal changes of the spectral signature of snow in visible and near-infrared wavelengths. *Annals of Glaciology* **17**, 143–148.

Defant F. (1949): Zur Theorie der Hangwinde, nebst Bemerkungen zur Theorie der Berg- und Talwinde. *Archiv für Meteorologie, Geophysik und Bioklimatologie* **A1**, 421-450.

Denby B. (1999): Second-order modelling of turbulence in katabatic flows. *Boundary-Layer Meteorology* **92**, 67-100.

Denby B. and J.W. Greuell (2000): The use of bulk and profile methods for determining the surface heat fluxes in the presence of glacier winds. *Journal of Glaciology* **46**, 445-452.

Denby B. and C.J.P.P. Smeets (2000): Derivation of turbulent flux profiles and roughness lengths from katabatic flow dynamics. *Journal of Applied Meteorology* **39**, 1601-1612.

De Ruyter de Wildt M. and J. Oerlemans (2003): Satellite retrieval of mass balance: comparing SAR images with albedo images and in situ mass-balance observations. *Journal of Glaciology* **49**, 437-448.

De Woul M. and R. Hock (2005): Static mass balance sensitivity of Arctic glaciers and ice caps using a degree-day approach. *Annals of Glaciology* **42**, 217-224.

Duynkerke P. G. (1988): Application of the *e*-turbulence closure model to the neutral and stable atmospheric boundary layer. *Journal of Atmospheric Sciences* **45**, 865–880.

Egger J. (1987): Simple models of the valley-plain circulation, Part II: Flow resolving model. *Meteorology and Atmospheric Physics* **36**, 243-254.

Fettweis X. (2007): Reconstruction of the 1979–2006 Greenland ice sheet surface mass balance using the regional climate model MAR. *The Cryosphere* **1**, 21-40.

Fitzpatrick M.F., R.E. Brandt and S.G. Warren (2004): Transmission of solar radiation by clouds over snow and ice surfaces: a parameterization in terms of optical depth, solar zenith angle, and surface albedo. *Journal of Climate* **17**, 266-275.

Garner B.J. and A. Ohmura (1968): A method for calculating direct shortwave radiation income of slopes. *Journal of Applied Meteorology* **7**, 796–800.

Garratt J. (1992): *The Atmospheric Boundary Layer*. Cambridge University Press, 316 pp.

Giesen R.H., L.M. Andreassen, M.R. van den Broeke and J. Oerlemans (2009): Comparison of the meteorology and surface energy balance on Storbreen and Midtdalsbreen, two glaciers in southern Norway. *The Cryosphere* **3**, 57-74.

Giesen R.H., M.R van den Broeke, J. Oerlemans and L.M. Andreassen (2008): Surface energy balance in the ablation zone of Midtdalsbreen, a glacier in southern Norway: Interannual variability and the effect of clouds. *Journal of Geophysical Research* **113** (D21111), doi: 1029/2008JD010390.

Giesen R.H. and J. Oerlemans (2010): Response of the ice cap Hardangerjøkulen in southern Norway to the 20th and 21st century climates. *The Cryosphere*, submitted.

Gordon A., W. Grace, P. Schwerdtfeger and R. Byron-Scott (1998): *Dynamic Meteorology – A Basic Course*. Oxford University Press, 344 pp.

Greuell W., W.H. Knap and P.C. Smeets (1997): Elevational changes in meteorological variables along a midlatitude glacier during summer. *Journal of Geophysical Research* **102** (D22), 25,941-25,954.

Greuell W. and J. Oerlemans (1987): Sensitivity studies with a mass balance model including temperature profile calculations inside the glacier. *Zeitschrift für Gletscherkunde und Glazialgeologie* **22**, 101-124.

Greuell W. and M. de Ruyter de Wildt (1999): Anisotropic reflection by melting glacier ice: measurements and parameterizations in Landsat TM bands 2 and 4. *Remote Sensing of Environment* **70**, 265-277.

Greuell W. and P.C. Smeets (2001): Variations with elevation changes in the surface energy balance on the Pasterze (Austria). *Journal of Geophysical Research* **106** (D23), 31,717-31,727.

Greuell W., C.H. Reijmer and J. Oerlemans (2002): Narrowband-to-broadband albedo conversion for glacier ice and snow based on aircraft and near-surface measurements. *Remote Sensing of Environment* **82**, 48-64.

Greuell W., J. Kohler, F. Obleitner, P. Glowacki, K. Melvold, E. Bernsen and J. Oerlemans (2007): Assessment of interannual variations in the surface mass balance of 18 Svalbard glaciers from the Moderate Resolution Imaging Spectroradiometer/Terra albedo product. *Journal of Geophysical Research* **112**, D07105, doi:10.1029/2006JD007245.

Grisogono B. and J. Oerlemans (2001): Katabatic flow: analytic solution for gradually-varying eddy diffusivities. *Journal of the Atmospheric Sciences* **58**, 3349-3354.

Grisogono B. and J. Oerlemans (2002): Justifying the WKB approximation in pure katabatic flows. *Tellus* **A 54**, 453-463.

Hamming R. (1987): *Numerical Methods for Scientists and Engineers*. Dover Publ., 2nd edition, 721 pp.

Hay J.E. and B.B. Fitzharris (1988): A comparison of the energy-balance and bulk-aerodynamic approaches for estimating glacier melt. *Journal of Glaciology* **34**, 145-153.

Hock R. (2005): Glacier melt: A review on processes and their modelling. *Progress in Physical Geography* **29**, 362-391.

Hock, R. and H. Jensen (1999): Mass balance computations using kriging interpolation. *Geografiska Annaler* **81A**, 611-619.

Hoinkes H. (1954): Beiträge zur Kenntnis des Gletscherwindes. *Archiv für Meteorologie, Geophysik und Bioklimatologie* **B6**, 36–53.

Jonsell U., R. Hock and B. Holmgren (2003): Spatial and temporal variations in albedo on Storglaciären, Sweden. *Journal of Glaciology* **49**, 59-64.

Kaser G., I. Juen, C. Georges, J. Gomez and W. Tamayo (2003): The impact of glaciers on the runoff and the reconstruction of mass balance history from hydrological data in the tropical Cordillera Blanca, Peru. *Journal of Hydrology* **282**, 130–144.

Kaser G. and H. Osmaston (2002): *Tropical Glaciers*. Cambridge University Press, 207 pp.

Kjøllmoen B., Editor, (2008): *Glaciological investigations in Norway in 2007*. The Norwegian Water Resources and Energy Directorate, Oslo, Norway.

Klok E.J., J.W. Greuell and J. Oerlemans (2003): Temporal and spatial variation of the surface albedo of the Morteratschgletscher, Switzerland, as derived from 12 Landsat images. *Journal of Glaciology* **49**, 491-502.

Klok E.J. and J. Oerlemans (2002): Model study of the spatial distribution of the energy and mass balance of Morteratschgletscher, Switzerland. *Journal of Glaciology* **48**, 505-518.

Knap W.H. and C.H. Reijmer (1998): Anisotropy of the reflected radiation field over melting glacier ice: measurements in Landsat-TM bands 2 and 4. *Remote Sensing of Environment* **65**, 93-104.

Knap W.H., C.H. Reijmer and J. Oerlemans (1999a): Narrowband to broadband conversion of Landsat TM glacier albedos. *International Journal of Remote Sensing* **20**, 2091-2110.

Knap W.H., B.W. Brock, J. Oerlemans and I.C. Willis (1999b): Comparison of Landsat TM derived and ground-based albedo of Haut Glacier d'Arolla. *International Journal of Remote Sensing* **20**, 3293-3310.

Koelemeijer R., J. Oerlemans and S. Tjemkes (1992): The surface reflectance of the Hintereisferner from Landsat 5 TM imagery. *Annals of Glaciology* **17**, 17-22

Konzelmann T., R.S.W. van de Wal, W. Greuell, R. Bintanja, E.A.C. Henneken and A. Abe-Ouchi (1994): Parameterization of global and longwave incoming radiation for the Greenland ice sheet. *Global and Planetary Change* 9, 143-164.

Kuhn M. (1979): On the computation of heat transfer coefficients from energy-balance gradients on a glacier. *Journal of Glaciology* 22, 263-272.

Kuhn M. (1987): Micro-meteorological conditions for snow melt. *Journal of Glaciology* **33**, 24–26.

Kuhn M. (1989): The response of the equilibrium-line altitude to climate fluctuations: theory and observations. In: *Glacier Fluctuations and Climate Change* (ed. J. Oerlemans), 407-417, Kluwer Academic Publishers.

Kuipers Munneke, P., C. H. Reijmer and M. R. van den Broeke. 2009. Assessing the retrieval of cloud properties from radiation measurements over snow and ice. *Submitted to International Journal of Climatology*.

Liou K.N. (1992): *Radiation and Cloud Processes in the Atmosphere*. Oxford University Press, 504 pp.

Marty C., R. Philipona, C. Fröhlich and A. Ohmura (2002): Altitude dependence of surface radiation fluxes and cloud forcing in the Alps: Results from the alpine surface radiation budget network. *Theoretical and Applied Climatology* **72**, 137–155.

Meier M.F. (1984): Contribution of small glaciers to global sea-level. *Science* **226**, 1418–1421.

Melloh R.A., J.P. Hardy, R.N. Bailey and T.J. Hall (2002): An efficient snow albedo model for the open and sub-canopy. *Hydrological Processes* **16**, 3571 – 3584.

Mishchenko M.I. (2008): Multiple scattering, radiative transfer, and weak localization in discrete random media: Unified microphysical approach. *Reviews of Geophysics* **46**, RG2003, doi:10.1029/2007RG000230.

Munro D. (1989): Surface roughness and bulk heat transfer on a glacier: comparison with eddy correlation. *Journal of Glaciology* **35**, 343-348.

Munro D. and J.A. Davies (1978): On fitting the log-linear model to wind speed and temperature profiles over a melting glacier. *Bounary-Layer Meteorology* **15,** 423–437.

Müller M.J. (1987): *Handbuch ausgewählter Klimastationen der Erde.* Universität Trier, 346 pp.

Nappo C.J. and K.S. Rao (1987): A model study of pure katabatic flows. *Tellus* **39A**, 61–71.

Nolin A.W., K. Steffen and J. Dozier (1994): Measurement and modeling of the bidirectional reflectance of snow. *Surface and Atmospheric Remote Sensing: Technologies, Data Analysis and Interpretation* **4**, 1919 - 1921 (doi: 10.1109/IGARSS.1994.399611).

Oerlemans J. (1991): A model for the surface balance of ice masses: Part I: alpine glaciers. *Zeitschrift für Gletscherkunde und Glazialgeologie* **27/28**, 63-83.

Oerlemans J. (1992): Climate sensitivity of glaciers in southern Norway: application of an energy-balance model to Nigardsbreen, Hellstugubreen and Alfotbreen. *Journal of Glaciology* **38**, 223-232.

Oerlemans J. (1997a): Climate Sensitivity of Franz-Josef Glacier, New Zealand, as revealed by numerical modelling. *Arctic and Alpine Research* **29**, 233-239.

Oerlemans J. (1997b): A flow-line model for Nigardsbreen: projection of future glacier length based on dynamic calibration with the historic record. *Annals of Glaciology* **24**, 382-389.

Oerlemans J. (2001): *Glaciers and Climate Change*. A.A. Balkema Publishers, 148 pp. ISBN 9026518137.

Oerlemans J. (2008): *Minimal Glacier Models*. Igitur, Utrecht University, 90 pp. ISBN 978-90-6701-022-1.

Oerlemans J., H. Björnsson, M. Kuhn, F. Obleitner, F. Palsson, P. Smeets, H.F. Vugts and J. de Wolde (1999): A glacio-meteorological experiment on Vatnajökull, Iceland. *Boundary-Layer Meteorology* **92**, 3-26.

Oerlemans J., M. Dyurgerov and R.S.W van de Wal (2007): Reconstructing the glacier contribution to sea-level rise back to 1850. *The Cryosphere* **1**, 59-65.

Oerlemans J. and J.P.F. Fortuin (1992): Sensitivity of glaciers and small ice caps to greenhouse warming. *Science* **258**, 115-117.

Oerlemans J. and B.K. Reichert (2000): Relating glacier mass balance to meteorological data using a Seasonal Sensitivity Characteristic (SSC). *Journal of Glaciology* **46**, 1-6.

Oerlemans J., R.H. Giesen and M.R. van den Broeke (2009): Retreating alpine glaciers: increased melt rates due to accumulation of dust (Vadret da Morteratsch, Switzerland). *Journal of Glaciology* **55**, 729-736.

Oerlemans J. and B. Grisogono (2002): Glacier wind and parameterisation of the related surface heat flux. *Tellus* **A 54**, 440-452.

Oerlemans J. and N.C. Hoogendoorn (1989): Mass balance gradients and climatic change. *Journal of Glaciology* **35**, 399-405.

Oerlemans J. and W.H. Knap (1998): A one-year record of global radiation and albedo from the ablation zone of the Morteratschgletscher, Switzerland. *Journal of Glaciology* **44**, 231-238.

Oerlemans J. and H.F. Vugts (1993): A meteorological experiment in the melting zone of the Greenland ice sheet. *Bulletin of the American Meteorological Society* **74**, 355-365.

Ohmura A., P. Kasser and M. Funk (1992): Climate at the equilibrium line of glaciers. *Journal of Glaciology* **38**, 397-411.

Østrem G., K.D. Selvig and K. Tandberg (1988): *Atlas over breer i Sør-Norge*. Norges 'Vassdrags- og Energiverk. Hydrologisk' Avdeling. Meddelelse 61.

Østrem G. and M. Brugman (1991): *Glacier mass-balance measurements: a manual for field and office work*. NHRI Science Report No. 4. Saskatoon: National Hydrology Research Institute.

Østrem G., O. Liestøl and B. Wold (1977): Glaciological investigations at Nigardsbreen, Norway. *Norsk Geografisk Tidsskrift* **30**, 187-209.

Paul F., H. Machguth and A. Kääb (2005): On the impact of glacier albedo under conditions of extreme glacier melt: the summer of 2003 in the Alps. EARSeL Workshop on Remote Sensing of Land Ice and Snow, Berne, 21.-23.2. 2005. *EARSeL Proceedings* **4**, 139-149.

Pedersen C.A. and J.-G. Winther (2005): Intercomparison and validation of snow albedo parameterization schemes in climate models. *Climate Dynamics* **25**, 351-362.

Pettersson R., P. Jansson and P. Holmlund (2003): Thinning of the cold surface layer on Storglaciären, observed by repeated ground penetrating radar surveys. *Journal of Geophysical Research* **108** (F1), 6004, doi:10.1029/2003JF000024.

Prandtl L. (1942): *Führer durch die Strömungslehre*. Vieweg und Sohn, Braunschweig.

Rea B.R. (2009): Defining modern day Area-Altitude Balance Ratios (AABRs) and their use in glacier-climate reconstructions. *Quaternary Science Reviews* **28**, 237-248.

Reijmer C.H. and R. Hock (2008): Internal accumulation on Storglaciären, Sweden, in a multi-layer snow model coupled to a distributed energy- and mass balance model. *Journal of Glaciology* **54**, 61-72.

Sauberer F. (1955): Zur Abschätzung der Globalstrahlung in verschiedenen Höhenstufen der Ostalpen. *Wetter und Leben* **7**, 22-29.

Schaepman-Strub G., M.E. Schaepman, T.H. Painter, S. Dangel and J.V. Martonchik (2006): Reflectance quantities in optical remote sensing – definitions and case studies. *Remote Sensing of Environment* 103, 27-42.

Schneider T. and P. Jansson (2004): Internal accumulation in firn and its significance for the mass balance of Storglaciären. *Journal of Glaciology* **50**, 25-34.

Smeets C.J.P.P., P.G. Duynkerke and H.F. Vugts (1998): Turbulence characteristics of the stable boundary layer over a mid-latitude glacier. Part I: A combination of katabatic and large-scale forcing. *Boundary-layer Meteorology* **87**, 117-145.

Smeets C.J.P.P., P.G. Duynkerke and H.F. Vugts (2000): Turbulence characteristics of the stable boundary layer over a mid-latitude glacier. Part II: Pure katabatic forcing conditions. *Boundary-layer Meteorology* **97**, 73-107.

Smeets C.J.P.P. and M.R. van den Broeke (2008): The parameterisation of scalar transfer over rough ice. *Boundary Layer Meteorology* **128**, 339-355.

Smith G.D. (1986): *Numerical Solution of Partial Differential Equations: Finite Difference Methods*, 3rd Edition. Oxford University Press, 350 pp.

Takeuchi N. (2002): Optical characteristics of cryoconite (surface dust) on glaciers: the relationship between light absorbency and the property of organic matter contained in the cryoconite. *Annals of Glaciology* **34**, 409-414.

Tsonis A.A. (2007): *Introduction to Atmospheric Thermodynamics*. Cambridge University Press, 187 pp.

Van de Berg W.J., M.R. van den Broeke, C.H. Reijmer and E. van Meijgaard (2006): Reassessment of the Antarctic surface mass balance using calibrated output of a regional atmospheric climate model. *Journal of Geophysical Research* **111**, D11104, doi:10.1029/2005JD006495.

Van den Broeke M.R. (1997a): Structure and diurnal variation of the atmospheric boundary layer over a mid-latitude glacier in summer. *Boundary-Layer Meteorology* **83**, 183-205.

Van den Broeke M.R. (1997b): Momentum, heat and moisture budgets of the katabatic wind layer over a mid-latitude glacier in summer. *Journal of Applied Meteorology* **36**, 763-774.

Van den Broeke M.R., J. Bamber, J. Ettema, E. Rignot, E. Schrama, W.J. van de Berg, E. van Meijgaard, I. Velicogna and B. Wouters (2009): Partitioning recent Greenland mass loss. *Science* **326**, 984-986.

Van den Broeke M.R., C.H. Reijmer, D. van As, R.S.W. van de Wal and J. Oerlemans (2005): Seasonal cycles of Antarctic surface energy balance from Automatic Weather Stations. *Annals of Glaciology* **41**, 131-139.

Van den Broeke M.R., C. Smeets, J. Ettema, C. van der Veen, R.S.W. van de Wal, and J. Oerlemans (2008): Partitioning of melt energy and meltwater fluxes in the ablation zone of the West Greenland Ice Sheet. *The Cryosphere* **2**, 179-189.

Van de Wal R.S.W., W. Boot, M.R. van den Broeke, C.J.P.P. Smeets, C.H. Reijmer, J.J.A. Donker and J. Oerlemans (2008): Large and rapid velocity changes in the ablation zone of the Greenland ice sheet. *Science* **321**, 111-113.

Van de Wal R.S.W., W. Greuell, M.R. van den Broeke, C.H. Reijmer and J. Oerlemans (2006): Surface mass-balance observations and automatic weather station data along a transect near Kangerlussuaq, West Greenland. *Annals of Glaciology* **42**, 311-316.

Van de Wal R.S.W., J. Oerlemans and J.C. van der Hage (1992): A study of ablation variations on the tongue of Hintereisferner, Austria. *Journal of Glaciology* **38**, 319-324.

Walraven R. (1978): Calculating the position of the sun. *Solar Energy* **20**, 393-397.

Wiscombe W.J. and S.G. Warren (1980): A model for the spectral albedo of snow, I, Pure snow. *Journal of Atmospheric Sciences* **37**, 2712– 2733.

Wright A.P., J.L. Wadham, M.J. Siegert, A. Luckman, J. Kohler, and A.M. Nuttall (2007): Modeling the refreezing of meltwater as superimposed ice on a high Arctic glacier: A comparison of approaches. *Journal of Geophysical Research* **112**, F04016, doi:10.1029/2007JF000818.

Yamada T. (1983): Simulations of nocturnal drainage flows by a q^2l turbulence closure model. *Journal of the Atmospheric Sciences* **40**, 91-106.

Zeng Q., C.M. Cao, X. Feng, F. Liang, X. Chen and W. Sheng (1984): Study on spectral reflectance characteristics of snow, ice and water of northwest China. *Science Sinica (Set B)* **27**, 647-656.

Zdunkowski W., Th. Trautmann and A. Bott (2007): *Radiation in the Atmosphere*. Cambridge University Press, 496 pp.